MODELLING OF FLOW DURING FRACTURE GROWTH DRIVEN BY MULTIPLE FLUID STAGES USING HIGH-PERFORMANCE PARALLEL COMPUTING ALGORITHMS

by

Amaury Fonseca Junior

Engenheiro Mecânico/Nuclear, Pontifícia Universidade Católica do Rio de Janeiro (1981)
Mestre em Mecânica/Matemática Aplicada, Pontifícia Universidade Católica do Rio de Janeiro (1984)

Submitted to the Department of Mechanical Engineering
in Partial Fulfillment for the Requirements for
the Degree of

Doctor of Philosophy
at the
Massachusetts Institute of Technology

June 1992

Signature of Author _____
Department of Mechanical Engineering
May 12, 1992

Certified by _____
Professor Michael P. Cleary
Thesis Supervisor

Signature of Author _____
Professor Ain A. Sonin
Chairman, Department Committee on Graduate Studies

Modelling of Flow During Fracture Growth Driven by Multiple Fluid Stages Using High-Performance Parallel Computing Algorithms

by

Amaury Fonseca Junior

Submitted to the Department of Mechanical Engineering
in Partial Fulfillment for the Requirements for
the Degree of Doctor of Philosophy

Abstract

The present work addresses a particular problem in Hydraulic Fracturing, i.e., characterization of gravity-driven motion of multiple stages of immiscible fluids, with various rheologies, within a narrow fracture cavity. The following capabilities were developed to address the present problem:

1) An analytical algorithm to predict the size and characteristics of encapsulated multiple fluid layers;

2) A semi-analytical algorithm to predict effects on in-plane fluid motion due to finite end-boundaries (e.g., the fracture perimeter), and wedging (crack-width variation) for a two-stage flow;

3) A suite of numerical algorithms, named *PARFES* (acronym for *PAR*allel *F*inite *E*lement *S*olvers) —designed specially to take advantage of highly parallel computer environments— based on an Euler-Lagrangian approach (e.g., nodes delineating the injection region are constrained while other nodes are free to move, according to the coupling of flow field variables with the elastic stress field). *PARFES* is composed of three modules:

3.1) *PARFES1* – tracks the interface motion and mesh nodal distribution of a given fluid stage;

3.2) *PARFESAX* – models the axisymmetrical multiple stage flow problem;

3.3) *PARFES2* – a modified nonlinear Newton-Raphson algorithm to determine non-symmetrical motions.

4) An experimental apparatus, named *TARG-DECH* (acronym for *T*est *A*pparatus for *R*esponse to *G*ravity-*D*riven *E*ffects in *C*onvective *H*ydraulics) designed to study the gravity-driven flow regimes at low Reynolds number. *TARG-DECH* is also used to experimentally verify the results from algorithms *1)* and *2)* above. In addition, a number of experimental measurements were conducted to characterize properties (e.g., viscosity, density, surface/interfacial tension, wettability and spreading) of the fluids and apparatus used.

Based on results of the above projects, it is established that the following two phenomena dominate the placement of fluids and solids (proppant) in uncontained fractures:

I. Convective motion, due to gravity-driven forces, predominate over particle-settling forces and (often) even over pumping-pressure-driven flows.

II. The tendency of higher viscosity fluids to migrate to regions of lower shear rates (and vice-versa) may dramatically alter the (wetting) conditions at the fracture walls, often giving rise to a transverse instability termed encapsulation, in addition to in-plane instabilities, usually referred to as fingering.

Both of these findings have direct practical relevance. Due to a lack of recognition of convective motion, and without consideration of encapsulation, current designs for (expensive) commercial oil and gas fracture treatments tend to greatly overestimate effective propped fracture length. To make this point clear: it is found, in many instances, that all of the proppant-laden fluid goes very quickly to the bottom of (relatively uncontained) fractures, instead of being ideally distributed over the fracture length opposite the target "pay" zone.

The work in this thesis should form the basis for correcting this primary (among many) discrepancies in current practice.

THESIS COMMITTEE: Prof. Michael P. Cleary (Thesis Supervisor)
Prof. Herbert H. Einstein
Prof. Harry Kytömaa

Acknowledgements

This work was supported by the Gas Research Institute.

I would like to thank the following colleagues and friends for invaluable discussions, criticism and support: Fouad Ahmad; Dave Barr; Alan Brik; Marie Dokoupil; Beatrice Kleppner; Eric Montagut; Sundar Narasimhan; David Otis; Peter Poole; Nasser Rabbat; Michael Ullman; Mark West and Wael Yared.

I had a chance to interact with brilliant undergraduate students, under my supervision, over the past two years: Yitwah Cheung; Natalie Henry; Mike Schmanske; Adeeb Shana'a; Ben Yau and Lisa Zhang. They helped me with a lot of the hard work in this thesis. Also under my supervision, the following undergraduate students, Ashanthi, Andy Frakes, Anne Guy and Rob Polansky, have helped me with various tasks.

Professors Herbert Einstein, Harry Kytömaa and Anthony Patera (on sabbatical leave this semester), my thesis committee members, were extremely helpful and provided me with a balanced amount of criticism and enthusiasm. Their guidance was invaluable. Also Leslie Regan, administrative officer of our department, was very supportive.

A special thanks to Professor Michael Cleary. He is one of the most demanding thesis advisors one can have. However, after passing this test, I think I will be able to handle any professional obstacle in my future career. I admire and respect you a lot.

Finally, I dedicate this thesis to my mother Maria Regina Gallo and my stepfather Luiz Mario Sá Freire. They gave me all the love and care one can have. In special, I will never forget the endless effort my mother dedicated to give me a solid education and ethical values.

Table of Contents

List of Figures

1 Background and Literature Overview

1-1 Introduction

Hydraulically-driven fracture growth in porous-elastic media (e.g., underground strata), can be found in various applications. Some of these applications include petroleum recovery, Barr and Cleary (1992), geothermal energy and nuclear waste disposal.

In such applications a liquid slurry is pumped into a wellbore, through producing strata, forcing the growth of a fracture. This technique is used to increase access to the strata (over half of oil and gas production wells in the US are hydraulically fractured). Not only must the fracture achieve the desired dimensions but, proppant (a mixture of solid particles within a fluid) must be pumped inside to keep the fracture open against the high ambient confining stresses. Following a successful hydraulic fracture operation, petroleum productivity may increase many-fold, especially in the early operational lifetime of the well. However, true optimization of the operation requires (real-time) processing of large amounts of physical data, most effectively achieved through simplified numerical algorithms, Cleary, Wright et al. (1991). In turn, these simplified numerical codes rely on results obtained through simulations performed with more detailed and accurate numerical algorithms, Cleary and Junior (1992).

Although a variety of such detailed numerical models have been developed, the level of realism has been completely unsatisfactory until recently, Barr (1991); Cleary, Wright et al. (1991). Indeed, a number of issues still remain to be resolved, even in such more realistic simulators. Primary among these issues is the complex problem of convective proppant transport within such fractures, driven by the gradients of density, created by variation of injected proppant concentrations and also strongly affected by leak-off.

The proper placement of proppant laden fluids within a fracture is the ultimate design goal in Hydraulic Fracturing. Due to a lack of consideration of convective gravity-

driven motion and encapsulation, current commercial fracture designs often overestimate final propped fracture length. In this regard the following two issues are the focus of this work:

1.1) **How fast** the **proppant-carrying fluid moves downward** within a cavity with variable length, height and width (crack opening).

2.1) To **what extent encapsulation occurs** and **affects** the process of motion of multiple fluid stages.

These issues are addressed by means of: *i)* analytical and semi-analytical mathematical models; *ii)* a suite of numerical algorithms named **PARFES** (**PAR**allel **F**inite **E**lement **S**olvers); and, *iii)* experiments using an apparatus developed in our laboratory, named **TARG-DECH** (**T**est **A**pparatus for **R**esponse to **G**ravity-**D**riven **E**ffects in **C**onvective **H**ydraulics).

1-2 Mathematical Modeling of Hydraulic Fractures

Detailed mathematical modeling of hydraulic fracturing (See **Figure 1-1** on **Page 29**) requires a collection of submodels:

I. partial differential equations (PDEs), e.g., describing fluid transport;

I.A. *local and global volume conservation* — the volume of injected fluid stages equals to the volume of the channel, delimited, in the transverse direction, by the crack opening, $\pm\delta(x,y,t)/2$, and, in the fracture plane, by the effective wellbore radius, R_W, and the crack tip perimeter, $R_T(x,y,t)$. Δ, ω, L, and H are, respectively, the characteristic scales for crack opening, non-wetted crack-tip zone, length and height, with typical ratios: $\Delta/\omega \sim 1$ and $\Delta/L \sim \Delta/H \sim 10^{-4}$. The global mass conservation provides a constraint for all possible configurations of the fluids interface and crack front at any given time.

I.B. *momentum conservation* — coupling of the local volume conservation with the momentum conservation, provides a set of PDEs that

characterize the fluid stages motion within a planar Three-Dimensional fracture cavity.

II. integral equations, e.g., elastic displacement and fracture mechanics, and history dependent equations, e.g., for fluid losses to porous strata;

II.A. *elastic displacement* — a set of integral equations relating the crack opening displacement (displacement discontinuities) to the change in the Three-Dimensional stress field. The change in the stress field involves distinct contributions: from the fluid(s) pressure field (within the fracture cavity); from the confining stresses; and from the backstresses (due to fluid and heat exchange with the porous matrix).

II.B. *stress intensity factor* — K_{IC} the critical stress intensity factor in mode I, which may be assumed of order zero for most large-scale operations, nevertheless serves as an integral constraint to balance the local distribution on the wetted (e.g., excess stress field), and non-wetted (e.g., confining stresses) regions of the fracture cavity. The effect of incorporating the K_{IC} criterion into the model, is to determine the ratio $R_F(x,y,t)/R_W(x,y,t)$, where $R_F(x,y,t)$ represents the perimeter of the outermost fluid stage. Both integral equations, described in **II.A** and here, have singular integral kernels, and special numerical integration techniques are required to solve them.

II.C. *fluid and heat exchange* — the effective permeability (connected porosity) of the stratum(a) surrounding the fracture, and a variety of conditions (e.g., viscosities of fluids inside and outside the fracture, BCs at the fracture walls, etc.) determine the amount of fluid and heat transfer through the fracture walls (transverse direction–z plane) to the adjacent stratum(a).

III. a variety of boundary conditions (BCs) for flow and fracture perimeters, fluid rheologies, and equations of state.

III.A. *Boundary Conditions* — BCs are, in general, either the weakest or

the strongest point of a fracture simulator. A typical example is the uncertainty about an adequate boundary condition for the near-the-crack-tip region (which has been under scrutiny for many years). For instance, in earlier models, Lam (1985), and some current industry models, Clifton and Wang (1991), the excess stress field is assumed to be zero at the fluid front, and to be the (negative) value of the confining stresses within the non-wetted region. That assumption has been shown to be erroneous, Barr (1991), and leads to unacceptable results, Cleary, Wright et al. (1991).

III.B. *Fluid Rheology (and Equations of State)* — The most common fluid rheology equations are the Newtonian linear approximation and a Power-Law, for simple Non-Newtonian fluids. Although the Power-Law equation is often used for any fluid that presents a Non-Newtonian behavior, it is doubtful, for instance, that it could adequately simulate the flow of some more complex gels (and effects of associated breaker agent). Nevertheless, such a simplified fluid model is adopted here for first-order characterization and, especially, for comparison with laboratory experiments (where such simple fluids are employed).

1-2.1 Difficulties Associated With Numerical Modeling

Difficulties associated with the numerical solution of hydraulic fracture models are related to the unique physical behavior of the system. For instance:

- change of fluid pressure, within the crack, at any point affects the displacement field (crack opening) everywhere (global data structure);
- the integral constraint, K_{IC}, is satisfied continuously in time, so pressure must change throughout the crack when a local perturbation is introduced;
- one free external moving boundary, the perimeter of the fracture, and one partially constrained internal moving boundary, the perimeter of the fluid front,

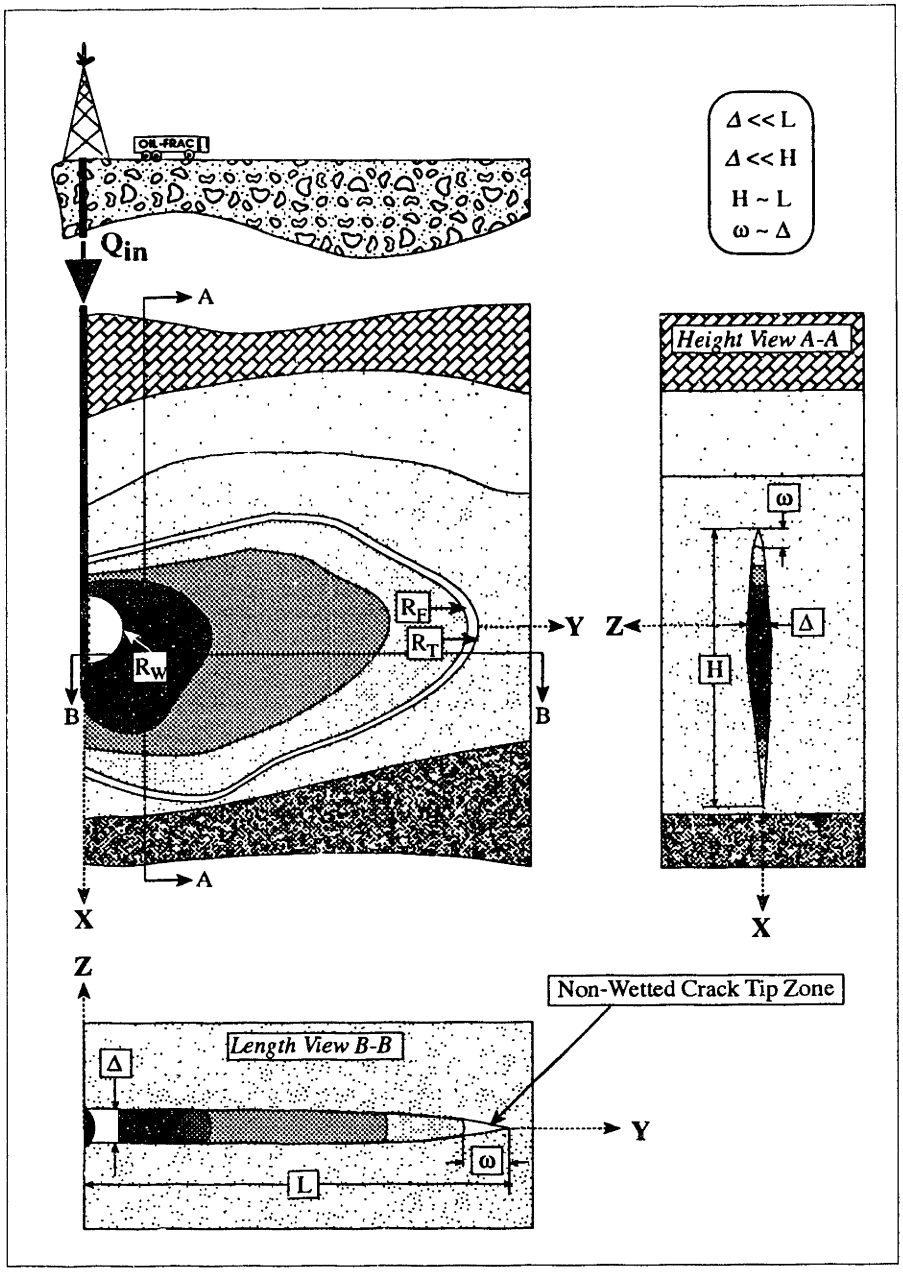

FIGURE 1-1: Sketch of hydraulic fracture growth driven by multiple fluid stages

are simultaneously controlled by mass conservation, fluid(s) rheology, the critical stress intensity factor and elastic behavior of the porous matrix;

- chemical/kinetic characterization of the fluids, gels and proppants injected

into the fracture is quite complex. In addition, fluid losses, to the surrounding stratum(a), can alter the relative composition of an injected mixture;

- the convective motion of fluid stages within the fracture can be affected by two instabilities mechanisms: fingering (in-plane – x and y directions), and encapsulation (transverse – z direction). Although fingering can modify the morphology of the fluid stages' interfaces, encapsulation instabilities are more important in the more common practical circumstances of increasing fluid viscosity in successive stages. Encapsulation instabilities can substantially affect the average velocity of the heavier fluid(s) carrying the proppant. For instance, if most of the proppant is carried directly to the bottom of the fracture, post-fracturing oil/gas production can be significantly reduced.

A hydraulic fracture simulator that can successfully handle the above mentioned numerical difficulties is still not available. Currently available simulators, Barr (1991); Cleary, Wright et al. (1991), address, in detail, the first three items above and, in a simplified manner, the last two items.

1-2.2 Numerical Modeling — Parallelization Issues

Adequate numerical simulation of each submodel should take into account the locality/non-locality of the data structure. By local data structure it is meant that the immediate effect of perturbations in a certain degree of freedom at a particular node is localized to the neighboring nodes; whereas in a global data structure the immediate effect of perturbations is non-local, i.e., it can directly affect all degrees of freedom at all nodes in the model, Junior (1989); Mathur (1989).

Equations in items ***I.A*** and ***I.B*** render good numerical discretization with local data structures algorithms (e.g., Finite Element Method with low order interpolation base) but, the coupling of the stress field with the crack opening (vide items ***II.A*** and ***II.B***), requires a global data structure algorithm. However, there are ways to overcome this disparity (one possibility is presented later in the description of PARFES2 in **Chapter 3**).

1-3 Fingering, Encapsulation, Settling, and Convection

Fingering instabilities have been under scrutiny for many years, Bensimon, Kadanoff et al. (1986); Chuoke, Meurs et al. (1958); Coyne and Elrod (1970); Homsy (1987); Saffman and Taylor (1958); Taylor and Saffman (1958); Weinstein, Dussan et al. (1990), but few of the results have been useful in hydraulic fracture designs, Barr and Cleary (1984); King (1985); Paterson (1981).

Encapsulation instabilities were initially studied in multi-layer/stratified flows Yih (1967); Yu and Sparrow (1967). Later they were addressed in polymeric flows, Everage (1973); Everage (1975); Lee and White (1974); Lee and White (1975); MacLean (1973); White and Lee (1975); Williams (1975), and, recently, in lubricated flows, Anturkar, Papanastasiou et al. (1990a); Anturkar, Papanastasiou et al. (1990b); Hooper and Boyd (1983); Hu and Joseph (1989); Joseph, Nguyen et al. (1984); Joseph and Preziosi (1987); Joseph, Renardy et al. (1984); Pradhan and Tripathy (1986); Schwartz and Michaelides (1988); Shibata and Mei (1986a); Shibata and Mei (1986b); Than, Rosso et al. (1987). However, to our knowledge, in hydraulic fracturing the onset of encapsulation instabilities, its development, and quantitative characterization have been neither known nor studied.

In typical hydraulic fractures, the average convective to settlement (particles settling within a fluid stage) velocity ratio can be shown (See **Section 2-2** on **Page 41**) to be of order

$$\frac{V_{convection}}{V_{settling}} \approx \left[\frac{crack\ opening}{particle\ diameter}\right]^2 \approx \left[\frac{\delta}{D}\right]^2 \approx 10^2 \Leftrightarrow 10^4$$

Hence, the proppant settling velocity within the gel is few orders of magnitude slower than the mixture's overall convective drop velocity. However, curiously, only the settling mechanism is well studied and characterized in hydraulic fracturing.

1-4 Convective In-Plane Motion

Assuming the displacement of a lighter and less-viscous bath of fluid, with density

ρ_1 and dynamic viscosity μ_1, by a heavier and more-viscous *blob* of fluid (ρ_2,μ_2), the in-plane motion of the blob is associated to the pair of coordinates x-y, (vide **Figure 1-2**).

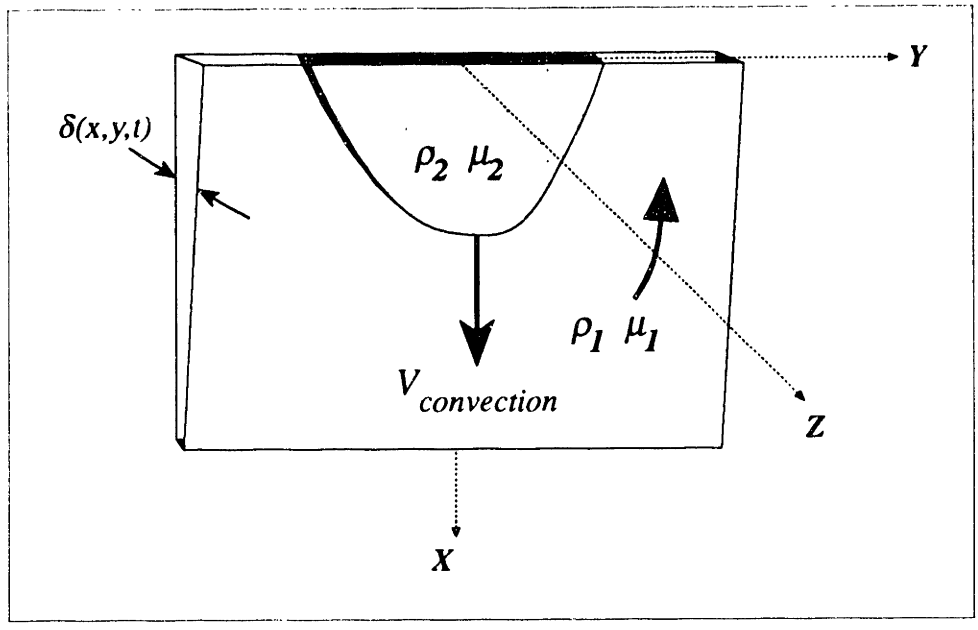

FIGURE 1-2: Convective motion — heavier and more viscous (blob of) fluid 2, displacing lighter and less viscous (bath of) fluid 1. Motion can be decomposed into two components: in-plane (x-y plane); and, transverse (z direction), assuming that the ratio of the characteristic crack width to the in-plane *blob* dimensions is small (less than 10^{-3})

Part of the work presented in **Chapter 2** characterizes two boundary effects on the in-plane convective motion:

- The presence of an end-boundary in the direction of motion (an arbitrary plane with normal in the x direction, located at the "bottom" of the fracture, e.g., the bottom fracture perimeter);
- The effect of varying the crack opening along the x direction (denominated wedging effect).

In addition, the suite of algorithms, presented in **Chapter 3**, and part of the experiments, described in **Chapter 4**, are designed to study in-plane interface(s) motion.

1-5 Convective Transverse Motion

The transverse motion (associated to variations in the z direction – vide **Figure 1-2**) is analyzed by means of an analytical algorithm, presented in **Chapter 2**. This algorithm, devised to find the thickness of the encapsulated fluid layers in the transverse direction, minimizes the total viscous dissipation energy and uses a criteria (based on maximization of the flow field velocity of the displacing fluid) to predict the flow field final transverse configuration. Causes leading to the onset of encapsulation instabilities are briefly discussed in both **Chapters 2** and **4**.

1-6 Wetting Conditions at the Fracture Walls

TARG-DECH, the experimental apparatus described in **Chapter 4**, provides a basis for analysis of the influence of wall effects on the motion of the downwards fluid *blob*. Among these effects, the wall wetting characteristics seems to play a fundamental role on the onset and development of encapsulation instabilities.

By varying TARG-DECH's container walls, dramatic changes on overall motion behavior were observed (e.g., variations of two orders of magnitude on the downwards convective *blob* velocities). In response to this experimental evidence (of the importance of wetting conditions at the fracture walls) a number of tests were carried to characterize the:

- wettability of the container walls, with respect to the fluids used;
- spreading rate of the displacing fluid for both dry and wet conditions, i.e., walls contaminated (wet), or not contaminated (dry), by the displaced fluid;
- surface tension of each fluid used;
- interfacial tensions for each displacing/displaced fluid combination.

The term *surface affinity* is used, throughout this work, to loosely describe adhesion properties of the combined displacing/displaced fluid system to the TARG-DECH's container walls.

1-7 Literature Overview

A fascinating (but time consuming) task, during the development of this thesis, was to gather and relate information from completely different areas of research to this study. It would be rewarding to see some of the initial interdisciplinary links established herein, to be further developed and analyzed in future research work.

To facilitate the connection between references cited in this thesis and different research areas, the following sections present a classification scheme. Also, the primary review references for each area are noted.

1-7.1 Hydraulic Fracture

- *Primary review references* — Cleary (1988), Barr (1991), Cleary, Wright et al. (1991), Barr and Cleary (1992).

Nilson (1981); Nilson (1986); Nilson and Griffiths (1982); Nilson and Griffiths (1986); Nilson and Morrison (1986); Nilson, Proffer et al. (1985); Abé, Keer et al. (1979); Abé, Mura et al. (1976); Bui and Parnes (1982); Cleary, Kavvadas et al. (1983); Cleary, Barr et al. (1988); Griffiths, Nilson et al. (1986); Johnson and Cleary (1991); Lam (1985); Clifton and Wang (1991).

1-7.2 Fingering and Hele-Shaw Flows

- *Primary review references* — Homsy (1987), Saffman (1986), Weinstein, Dussan et al. (1990).

Barr and Cleary (1984); Ben-Amar, Hakim et al. (1991); Bensimon, Kadanoff et al. (1986); Brener, Levine et al. (1991); Chuoke, Meurs et al. (1958); Coyne and Elrod (1970); Howison (1986); Hu and Joseph (1990); Joseph (1990); King (1985); Lacey, Howison et al. (1990); Park, Gorell et al. (1984); Park and Homsy (1984); Paterson (1981); Reinelt and Saffman (1985); Reinelt (1987); Saffman and Taylor (1958); Taylor and Saffman (1958); Thomé, Rabaud et al. (1989); Zimmerman and Homsy (1991).

1-7.3 Potential Flows

- *Primary review references* — Hele-Shaw (1898c), Hele-Shaw (1898d), Stokes (1898), Riegels (1938).

Bairstow, Cave et al. (1922); Bairstow, Cave et al. (1923); Hele-Shaw (1898a); Hele-Shaw (1898b); Hele-Shaw and Hay (1900); Reynolds (1898).

1-7.4 Multilayer Flows

- *Primary review references* — MacLean (1973), Anturkar, Papanastasiou et al. (1990b), Everage (1973), Everage (1975), Williams (1975).

Apazidis (1985); Lee and White (1974); Lee and White (1975); Schwartz and Michaelides (1988); Shibata and Mei (1986a); Shibata and Mei (1986b); White and Lee (1975); Yu and Sparrow (1967).

1-7.5 Multilayer Stability

- *Primary review references* — Joseph, Renardy et al. (1984), Ripa (1991), Anturkar, Papanastasiou et al. (1990a), Hooper (1989).

Chen and Joseph (1991); Hooper and Boyd (1983); Hu and Joseph (1989); Joseph, Nguyen et al. (1984); Joseph and Preziosi (1987); Loewenherz and Lawrence (1989); Pradhan and Tripathy (1986); Renardy (1989); Strykowski and Niccum (1992); Than, Rosso et al. (1987); Yiantsios and Higgins (1988); Yih (1967).

1-7.6 Multiphase Flows

- *Primary review references* — Gray and Hassanizadeh (1989), Kataoka (1986), Truesdell (1984).

Anderson and Jackson (1967); Bilicki, Dafermos et al. (1987).

1-7.7 Meniscus and Contact Angles

- *Primary review references* — Dussan (1979), Dussan, Ramé et al. (1991), Brochard and de Gennes (1991), Johnson, Kreuter et al. (1986), Li and Slattery (1991), Merchant and Keeller (1992).

Cox (1986); Dodge (1988); Dussan (1976); Elliott and Riddiford (1967); Goodwin and Homsy (1991); Haley and Miksis (1991); Hocking (1977); Hoffman (1975); Jansons (1985); Jerrett and J.R. (1992); Lowndes (1980); Miles (1991); Milinazzo and Shinbrot (1988); Moriarty, Schwartz et al. (1991); Schwartz and Michaelides (1988).

1-7.8 Wetting and Spreading

- *Primary review references* — de Gennes (1985), de Gennes (1991), Brochard-Wyart and de Gennes (1992), Zisman (1964).

El-Shimi and Goddard (1974a); El-Shimi and Goddard (1974b); Kwei, H. et al. (1969); Padday (1969); Schonhorn, H.L. et al. (1966); Van Remoortere and Joos (1991); Yang, Zografi et al. (1988a); Yang, Zografi et al. (1988b); Zettlemoyer (1969).

1-7.9 Surface Characteristics

- *Primary review references* — Hamilton (1972), Lamperski (1991)

Ambwani and Fort (1974); ASTM-D1331 (1989); ASTM-D971 (1982); Christenson (1988); Krause and Kildsig (1972); Ramé-Hart (1992); Sacher (1988); Somasundaran and Danitz (1974).

1-7.10 Bubbles and Drops

- *Primary review references* — Koh and Leal (1990), Saffman and Tanveer (1989).

Baker and Moore (1989); Burgess and Foster (1990); Burgess and Tanveer (1991); Maxworthy (1991); Meiburg (1989).

1-7.11 Coating, Mold Filling and Polymeric Flows

- *Primary review references* — Ruschak (1985), Mavridis, Hrymak et al. (1986a), Huh and Scriven (1971).

Behrens, Crochet et al. (1987); Coyle, Blake et al. (1987); Kamal, Goyal et al. (1988); Manas-Zloczower, Blake et al. (1987); Mavridis, Hrymak et al. (1986b); Mavridis, Hrymak et al. (1987); Mavridis, Hrymak et al. (1988); Michael (1981); Novy, Davis et al. (1989); Pranckh and Scriven (1989); Rose (1961); Schmidt (1978).

1-7.12 Moving Meshes and Finite Element Analysis

- *Primary review references* — Lynch and Sidén (1988), Sullivan and Lynch (1987b), Cuvelier and Schulkes (1990), Zabaras and Ruan (1989b); Zabaras and Ruan (1989c).

Cuvelier and Driessen (1986); Derby and Brown (1986); Ho (1989); Sullivan and Lynch (1987a); Zabaras and Ruan (1989a); Zabaras and Richmond (1990).

1-7.13 Parallel Processing and Nonlinear Algorithms

- *Primary review references* — Junior (1989), Mathur (1989), Carey and Jiang (1984), Fellipa (1988), Hayes (1989); Hayes and Devloo (1984), Tezduyar, Liou et al. (1988), Nour-Omid, Parlett et al. (1987).

Tezduyar and Liou (1987); Suarez, Oñate et al. (1984); Strang (1980); Sørensen and Reffstrup (1986); Salinas, Nguyen et al. (1974); Plesha (1984); Nour-Omid (1984); Nakazawa (1984); Muller and Hughes (1984); Marques (1986); Kamat, Watson et al. (1984); Kamat, VandenBrink et al. (1985); Kamat and Watson (1984); Huynh and Wong (1984); Hughes and Ferencz (1987); Hughes, Raefsky et

al. (1984); Hughes, Pister et al. (1978); Herting (1984); Haisler and Stricklin (1974); Fellipa (1984a); Fellipa (1984b); Fellipa and Park (1978); Carmignani, Cella et al. (1974); Borst (1984); Bjørstad and Hvidsten (1987); Belytschko, Smolinski et al. (1984); Bellman (1973); Argyris, Doltsinis et al. (1985).

1-7.14 General

Belytschko, Engelmann et al. (1989); Sand and Østerby (1979); Adamson (1967); Clift, Grace et al. (1978); Drazin and Reid (1981); Flügge (1962); Lamb (1932); Maeder (1990); Milne-Thomson (1968); Noor (1987); Pearson (1983); Pelcé (1988); Wolfram (1988).

2 The Physics of Convection in Hydraulic Fracturing

2-1 Introduction

The flow of two immiscible liquids of different viscosities, separated by an interface, presents a high degree of non-uniqueness, even for a steady low Reynolds number flow in a simple bounded region. For instance, the study by Joseph, Nguyen et al. (1984) of Couette flow in plane and circular layers, as well as layered Poiseuille flow, disregarding gravity driven forces. To obtain the size of the layers, the viscous dissipation integral was minimized (or the velocities maximized for a given flow rate). It was found that the arrangement of layers in Plane Couette flow has no solution.

In addition to the well-known mechanism of viscous fingering instability (usually associated to the displacement of a more viscous liquid by a less viscous liquid), a mechanism, denominated *encapsulation instability* is identified. Higher viscosity fluids have a tendency to migrate to regions of lower shear rates (encapsulated by a lower viscosity fluid).

Encapsulation has been studied in the literature of Polymeric Flows, Everage (1973); Everage (1975); Lee and White (1974); Lee and White (1975); MacLean (1973); White and Lee (1975); Williams (1975), Multilayer Stability Analysis, Anturkar, Papanastasiou et al. (1990a); Anturkar, Papanastasiou et al. (1990b); Hooper (1989); Joseph, Renardy et al. (1984); Ripa (1991); Than, Rosso et al. (1987), and transport in oil pipelines,Chen and Joseph (1991); Hu and Joseph (1989); Yu and Sparrow (1967). However, the analysis presented herein introduces novel algorithms and interpretation of the phenomena.

Although the tracking of the interface between two immiscible liquids is very difficult to achieve (either by computational or analytical methods), some simplified analysis can provide an insight on the basic mechanisms governing the motion of the liquids, as

well as on the order of magnitude of the velocities associated with the interface motion.

The objectives of this Chapter are to:

I. provide a simplified analysis and model of the downwards motion of a moving fluid body, hereafter denominated *blob*, driven by gravity. The falling *blob* displaces an involving fluid bath, and the fluids are assumed to be immiscible. This study encompasses:

I.A. a characterization of the relative importance of three physical mechanisms, i.e., convection (gravity-driven), settling (gravity-driven) and pumping-pressure-driven flows, in hydraulic fracturing. Convection being the mechanism describing the blob motion, and settling the mechanism describing the relative motion of dispersed particles within the blob;

I.B. a physical characterization of forces and boundary conditions;

I.C. a dependence analysis of the transverse interface morphology, fluid front location and velocity on the governing physical parameters (i.e., viscosities, densities, crack opening distribution, and surface tension).

II. address two instability mechanisms, i.e., fingering and encapsulation, and discuss how these instabilities affect the blob motion.

III. quantify the influence of encapsulation instabilities on the overall convective motion of fluid stages within a fracture.

In the following derivations it is assumed two immiscible fluids contained within a fracture channel, where the displacing fluid *blob* is labeled stage 2 and the displaced fluid *bath* is labeled stage 1. The variables are defined as:

ρ_1 — fluid stage 1 average density

μ_1 — fluid stage 1 average channel (12*) viscosity

ρ_P — proppant density

ϕ_P — proppant volume fraction

D — proppant diameter

ρ_2' — fluid stage 2 density

ρ_2 — fluid stage 2 average density ($\rho_2 = \phi_P \rho_P + (1 - \phi_P)\rho_2$')

μ_2 — fluid stage 2 average channel (12*) viscosity

$V_{convection} \equiv V$ — downwards *blob* velocity

$V_{settling} \equiv V_P$ — downwards velocity of proppant within *blob*

δ — channel aperture (crack opening)

g — gravity acceleration constant

$\rho \equiv \rho_1 + \rho_2$

$\Delta\rho \equiv \rho_2 - \rho_1$

$\mu \equiv \mu_1 + \mu_2$

σ_{12} — *blob* interfacial tension

p — fluid stage 1 pressure field around *blob*

R — *blob* average radius

T — time scale

2-2 Convection versus Settling in Hydraulic Fracturing

From the Stokes' approximation for flow past a solid sphere with very low Reynolds number, the average settling velocity of the proppant ("sphere") within the gel (See **Figure 2-1** on **Page 42**) is $V_{settling} = 2(\rho_P - \rho_2')gD^2/3\mu_2$, while the *blob* velocity can be approximately given by the Darcy's Law, i.e., $V_{convection} = (\rho_2 - \rho_1)g\ \delta^2/\mu_2$ (assuming both ends, at $z = \pm\delta/2$, attached to the walls). For the cases of interest: $\rho_1 < \rho_2' < 1.5\rho_1$, $2\rho_1 < \rho_P < 4\rho_1$ and $10^{-2}\delta < D < 0.2\delta$ (i.e., 20/40 mesh proppant within a 1/4−1.1/4" channel

aperture). Hence, the ratio of velocities is

$$\frac{V_{convection}}{V_{settling}} \approx \left[\frac{crack\ opening}{particle\ diameter}\right]^2 \approx \left[\frac{\delta}{D}\right]^2 \approx 10^2 \Leftrightarrow 10^4 \qquad (2\text{-}1)$$

Even correcting the Stokes approximation for a smaller channel ratio ($D \sim 0.2\delta$), without even considering the role of encapsulation or fluid viscoelasticity, the proppant settling velocity within the *blob* is orders of magnitude slower than the mixture's overall convective velocity. However, curiously, only the settling mechanism is well studied and characterized in hydraulic fracturing (probably because most industry thinking focuses on one-dimensional displacement of stages out along the reservoir).

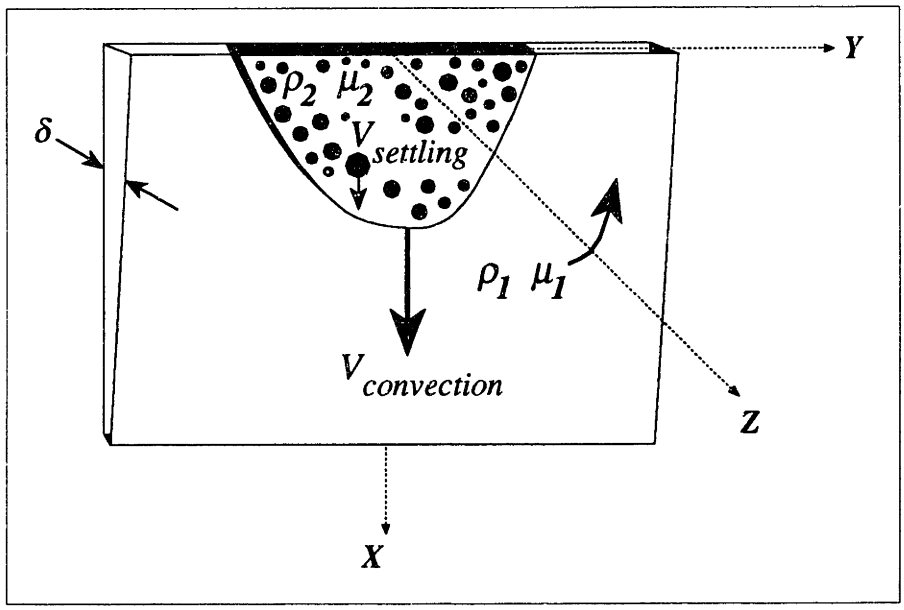

FIGURE 2-1: Relative displacement (settling velocity) of proppants within fluid stage 2 (blob), compared to the blob convective velocity (within fluid stage 1 bath)

Notice that:

- the pumping-pressure-gradient is not accounted in the derivation of Eq. (2-1).
- Settling and convection are driven by the same physical mechanism, i.e., gravity forces.

- The dominant mechanism (convection) is separately compared to the pumping-pressure driven flow in the next Section.

2-3 Convection versus Pumping-Pressure-Driven Flows

For typical hydraulic fracturing field operation conditions, the convective mecha-

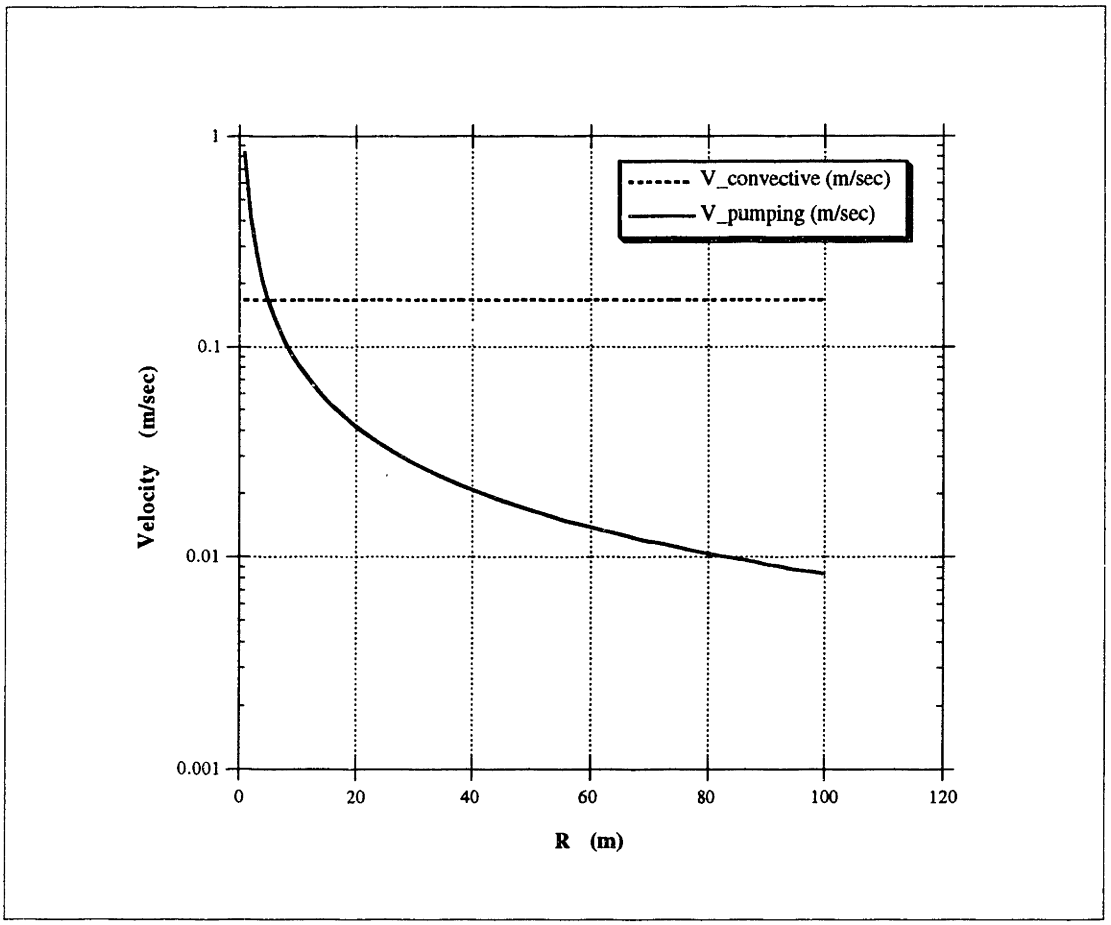

FIGURE 2-2: Convective and pumping-pressure-driven velocities as a function of the fracture length

nism is dominant after approximately a factor of one effective welbore characteristic length (See **Figure 2-2**). An important practical consequence of this finding is the predominance of the downwards motion over the horizontal motion for uncontained fractures.

Notice that:

- crack opening, flow rate, effective welbore radius, density differential and effective viscosity values are, respectively, 1 *cm*, 20 *bbl/min*, 10 *m*, 0.? kg/m^3, 1200 *cp*. The velocity ratio is qualitatively given as $V_{convection}/V_{pumping} \sim (\rho_2 - \rho_1) g R \delta^3 / q \mu_2$, where q is the flow rate.
- result depicted in **Figure 2-2** doesn't assume encapsulation, i.e., displacing fluid is assumed to touch both walls. If encapsulation occurs, the convective velocity will greatly exceed the horizontal velocity (pumping-pressure driven).

2-4 Physical Characterization of the Multi-Stage Fluids Motion

A model is developed to study the injection of a more dense viscous fluid preceded by a less dense fluid, into a narrow Hele-Shaw's type cell. The model provides a physical characterization of forces and boundary conditions on the movement of a well-defined shape, which is called a *blob*. The following simplifications are assumed (see sketch in **Figure 2-3**):

1) the two fluid stages are immiscible;

2) the channel (crack) opening dependence is limited to either constant, $\delta(x,y,t) = \delta_o$, or wedged, $\delta(x,y,t) = \delta(x)$. General crack opening dependence on y, and t can be easily incorporated;

3) the *blob* formed by the injection of the second fluid stage has either a circular or elliptical shape, in the in-plane directions (x and y), and it is delimited by the fracture walls ($z = \pm \delta(x,y,t)/2$), in the transverse direction, in the absence of encapsulation. General shapes can also be incorporated, but experimental observation has demonstrated that circular and elliptical shapes are well suited for a wide range of fluids;

4) if encapsulation occurs, then the *blob* will be delimited in the transverse direc-

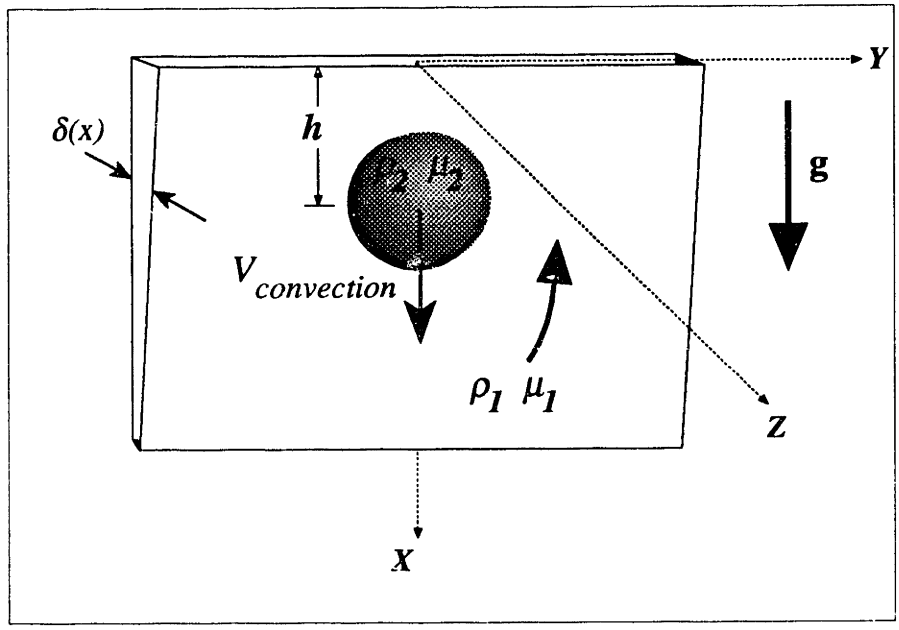

FIGURE 2-3: Blob of heavier fluid (2) displacing fluid bath (1) at a height *h*. Height (*h*) based on center of gravity of the blob

tion by fluid layers of the less viscous fluid.

Although the viscosity of the *blob* is higher than the viscosity of the displaced fluid for the cases under scrutiny, the model can handle the reverse case (fingering will then be the predominant instability mechanism, and the *blob* assume a non-symmetrical shape).

The heavier *blob* will sink against the following counteracting forces (See **Figure 2-4** on **Page 46**):

- shear stresses at the walls (no encapsulation); or shear stresses at the interfaces with the lighter fluid in the transverse direction (if encapsulated). This contribution is integrated on $\partial\Omega_z$;
- buoyancy;
- shear stresses to displace the lighter fluid. This contribution is integrated along $\partial\Omega_{xy}$;
- surface/interfacial tension. Although the quantitative contribution of surface

tension can be shown negligible for the cases of interest, its incorporation in the model is done via the wetting conditions at the wall, i.e., if encapsulation occurs the interfacial tension between the two fluids is used, otherwise estimated values (from experiments described in **Chapter 4**) for the moving contact angle (meniscus) and surface adhesion properties are used.

For convenience, the blob is assumed to behave like a "solid" (maintaining its shape) with respect to in-plane deformation, due to gravity and buoyancy, and to behave like a fluid with respect to shear in the transverse plane, i.e., the "solid" and fluid behavior are associated to energy dissipation modes based, respectively, on the velocity of the blob and gradients of velocity within the blob. Shape instabilities are addressed separately—fingering in **Appendix H**, and encapsulation in **Section 2-6**.

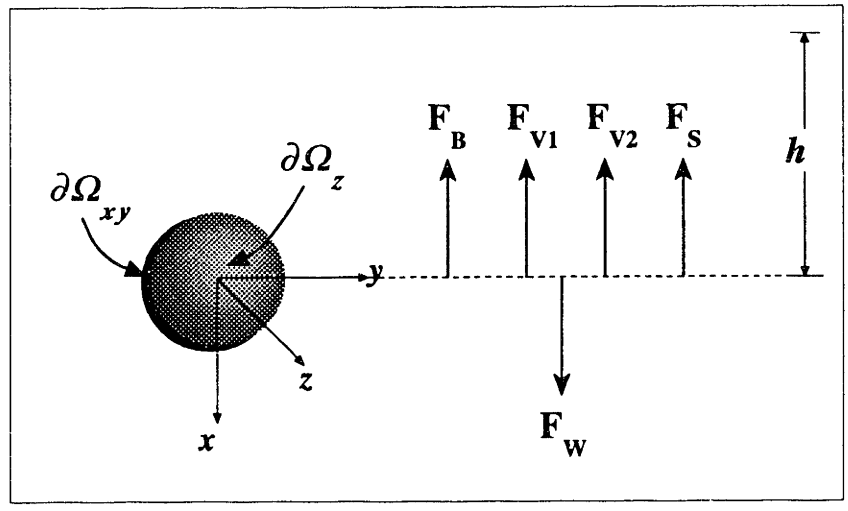

FIGURE 2-4: Balance of forces for moving blob

2-5 Modeling the In-Plane Motion

In practice (for instance, in using TARG-DECH—vide **Chapter 4**) the formation of a heavy well-defined shape blob can be achieved by injecting a higher viscosity and higher density fluid (stage 2) within a bath of lower viscosity and lower density fluid (stage 1). Factors contributing to unstable motion can be listed (in order of importance) as:

1) *surface affinity/wettability* — although surface/interfacial tension measurements are useful for characterization of fingering, TARG-DECH results have demonstrated that surface affinity is the determining physical parameter characterizing fluid motion within a narrow channel. Unfortunately, there is **not** an obvious way to quantize the values of surface affinity for a given set of fluids and channel walls, e.g., contact angle measurements are misleading (a more detailed analysis of wettability issues is presented in **Chapter 4**). For instance, the same injected fluid *blob* presents very different patterns of motion by changing the fluid bath (although two distinct fluids used for the bath have similar values of viscosity and density). Low surface affinity of the injected fluid (stage 2) to the walls (for a given fluid stage bath) seems to be the leading cause of encapsulation instabilities.

2) *viscosity and density contrast* — large contrasts of viscosity ratio, $\mu_R = (\mu_2 - \mu_1)/(\mu_1 + \mu_2)$, and/or density ratio, $\rho_R = (\rho_2 - \rho_1)/(\rho_1 + \rho_2)$, can trigger either fingering or encapsulation instabilities. In the present work it is assumed that both $\rho_R > 0$ and $\mu_R > 0$.

3) *surface/interfacial tension* — seems to control, solely, the morphology and shape of the *blob*, e.g., low surface/interfacial tension can lead to fingering. Surface tension can be almost neglected as a parameter when modeling encapsulation instabilities. Fingering instabilities can be shown, Homsy (1987), to be relevant for negative or small ratio of viscosities, i.e., $(\mu_2 - \mu_1)/(\mu_1 + \mu_2) \approx 0$ or $(\mu_2 - \mu_1)/(\mu_1 + \mu_2) < 0$, but of secondary relevance for most cases of interest, i.e., $(\mu_2 - \mu_1)/(\mu_1 + \mu_2) \approx 1$.

The model introduced in this section has the following features/limitations:

- it can predict the effects of crack opening variations and the presence of a finite channel "wall" (the crack tip perimeter at the bottom of the fracture), represented by a series of doublets;
- it cannot predict the onset of instabilities. A subsidiary set of calculations based on energy dissipation arguments can be performed to predict the onset

of instabilities, however its accuracy is dependent on parameters that are seldom available in practice, e.g., surface contamination, variations of the surface asperity ratio. For instance, assuming the values of the interfacial tension polar and non-polar components known, the surface free energy could be estimated. A criteria could be developed—the decrease in energy due to shedding the higher viscosity fluid from the wall balanced against the free surface energy. The applicability of this criteria is very limited, unless the full dynamics of the meniscus movement can be modeled;

- ❒ once encapsulation happens, a set of algorithms (vide **Section 2-6** on **Page 54**) has been devised to find the thickness of the fluid layers in the transverse direction. These algorithms minimize the viscous dissipation energy (subsequently maximizing the flow gain velocity), and provide the means to find the key variable of interest, i.e. the *blob* downwards velocity.

In this Section a physical analysis of the process is addressed. Also, some results are discussed (comparisons between this model and experimental results is presented in **Chapter 5**). Details of the derivation are presented in **APPENDIX B** on **Page 157**.

2-5.1 The Hele-Shaw & Stokes Potential Flow Field Paradox

A curious diversion is presented. While searching for the original work of Hele-Shaw, I found interesting personal correspondences among H.S. Hele-Shaw, O. Reynolds and G.G. Stokes.

When Hele-Shaw introduced his cell to provide a visualization of streamlines, Hele-Shaw (1898a); Hele-Shaw (1898c), he gained an immediate opponent: Reynolds. Reynolds claimed that Hele-Shaw's experiment was plagiarizing his ideas and, moreover, it was useless, since it only dealt with very slow flows, Reynolds (1898). However, Reynolds didn't predict he would face a formidable foe: G.G. Stokes.

Stokes was interested in confirm some of his theoretical predictions, i.e., the potential flow theory. Hele-Shaw's experiment provided him with a unique capability, except that his predictions were (physically) valid for flows in which inertial effects dominated

viscous effects. Few weeks after Hele-Shaw's initial article, Stokes presented a simple, and physically sound, proof that his theories could be scrutinized by means of the Hele-Shaw's cell, Stokes (1898) and Hele-Shaw's accompanying article Hele-Shaw (1898d).

The idea behind Stokes proof was: in the limit of a highly-viscous motion, the flow field can be shown to be irrotational (also know as the Viscous-Irrotational Potential Flow Paradox). Hele-Shaw's reply to Reynolds, Hele-Shaw (1898b), made that point very clear.

Later, corrections to Hele-Shaw's derivations were presented—see Bairstow, Cave et al. (1922); Bairstow, Cave et al. (1923). In particular, there is an interesting critical work by Riegels (1938) that seems to be unknown in the current literature on Hele-Shaw flow and fingering analysis (it extends some of the limits of applicability of the "slow flow" approximation to Reynolds numbers of order 1 using an Onseen's type asymptotic expansion).

Recently, Hele-Shaw type flows have received a renewed research interest, in areas ranging from fingering to chaotic/fractal behavior, Ben-Amar, Hakim et al. (1991); Brener, Levine et al. (1991); Burgess and Tanveer (1991); Hu and Joseph (1990); Lacey, Howison et al. (1990); Meiburg (1989); Saffman and Tanveer (1989), and multilayer stability analysis, Anturkar, Papanastasiou et al. (1990a); Chen and Joseph (1991); Hooper (1989); Hu and Joseph (1989); Ripa (1991).

With respect to the present work, in **APPENDIX B** on **Page 157**, an analysis of the validity of Hele-Shaw's approximation for wedge shaped cells (as well as, the usual parallel walls cell) is presented. It is shown that under the very low Reynolds number assumption, an additional condition has to be satisfied:

- the tapering (wedge) angle must be small, i.e., the magnitude of the crack opening variation along any direction should be negligible when compared to the crack opening times the in-plane velocity field gradient.

2-5.2 A Semi-Analytical Algorithm for In-Plane Motion

The set of solutions derived in **APPENDIX B** on **Page 157**—unbounded/bounded container walls & parallel/wedged plates—are utilized here as coefficients for a semi-analytical algorithm. This algorithm models both the dynamic (excluding the nonlinear convective components) and steady-state in-plane movement of the *blob*.

Equation (B-28) is solved using a modified fourth order Runge-Kutta procedure. If inertia effects become negligible the eigenvalues will present a behavior characteristic of stiff ODE problems and limit the time step size. To avoid this problem, results from the parallel plate solution are used as a lower bound for the time step size as follows:

- for $t_{ParMax} >> (1 + \rho_1)/(n_2 + \mu_1 n_1)$ inertia effects are neglected and the reduced 1st. order ODE problem is solved;
- for $t_{ParMax} \approx (1 + \rho_1)/(n_2 + \mu_1 n_1)$ the full 2nd. order problem is solved.

where the r.h.s. is t_{dyn}, and t_{ParMax} is how long the center of the *blob* would take to reach $(1 - R_2)$—values in nondimensional form—(See **Section B-3.1** on **Page 162**). Other useful terms are: U_{ParMax}, the "terminal" velocity of the blob; Re_{ParMax}, Reynolds number based on the "terminal velocity of the blob; t_{WedMax} is how long the center of the *blob* would take to reach $(1 - R_2)$ for wedged plates; h_{WedMax} the effective distance travelled by the *blob* (accounting for the dilation rate) for wedged plates.

Eigenvalues for the parallel plates problem are: $E_1 = 0$ and $E_2 = -(n_2 + \mu_1 n_1)/(1 + \rho_1)$. For time steps $\Delta t > 5/|E_2|$ the solutions are approximated by the 1st. order reduced system. Otherwise, the full 2nd. order problem is solved.

A priori t_{WedMax} is unknown. However consistent results should be obtained for values of $h < h_{WedMax}$, and t_{ParMax} can be used, initially, as a lower bound for t_{WedMax}.

The doublet power series solution introduced in **Appendix B** converges very fast when $R_{20}/(1 - h - R_{20})$ is small with respect to the unit, i.e., the *blob* is relatively far from the end-boundary. An adaptive integration procedure is utilized to add more terms to the power series as the end-boundary effects dominate. For instance in **Figure 2-5** the effect

of the end-boundary is preponderant for the wedged plates.

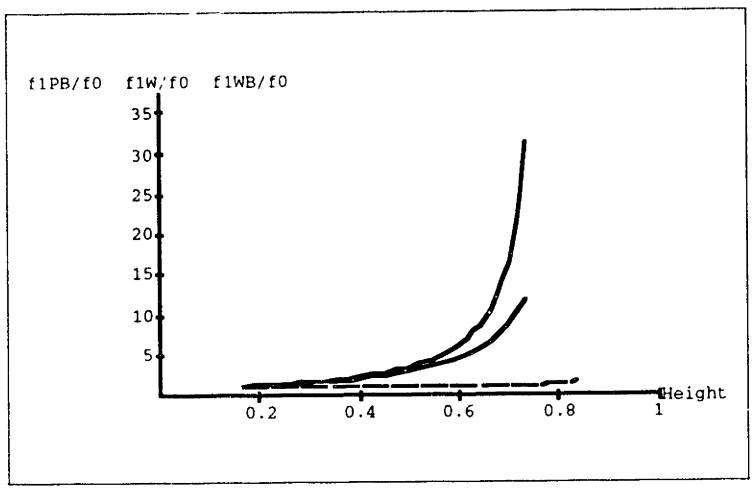

FIGURE 2-5: Squeeze shape function as a function of dimensionless height (NG = 0.0533 and TAU = 0.4). The lower curve is for parallel plates and bounded cell, the mid-curve for wedged plates and unbounded cell, and the steeper curve for wedged plates and bounded cell. Squeeze shape coefficient values are scaled by the parallel plates and unbounded cell coefficient

In **Figure 2-6** end-boundary effects are excluded. The shear shape coefficient is compared against the squeeze shape coefficient for the wedged case (taking a set of values of the modified Darcy-Raleigh number and time scale). The dilation rate is shown in Fig-

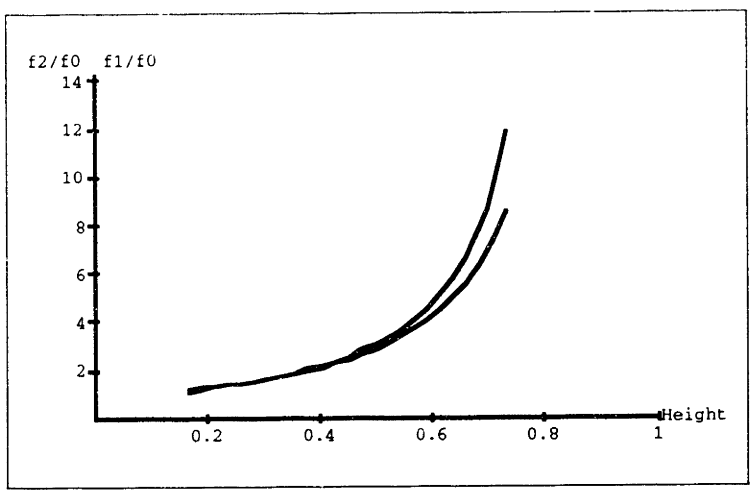

FIGURE 2-6: Shear vs. squeeze shape functions for unbounded cell with wedged plates, as a function of dimensionless height (NG = 0.0533 and TAU = 0.4). The lower curve is the shear shape function. Values are scaled by the parallel plates and unbounded cell coefficient

ure **2-11.**

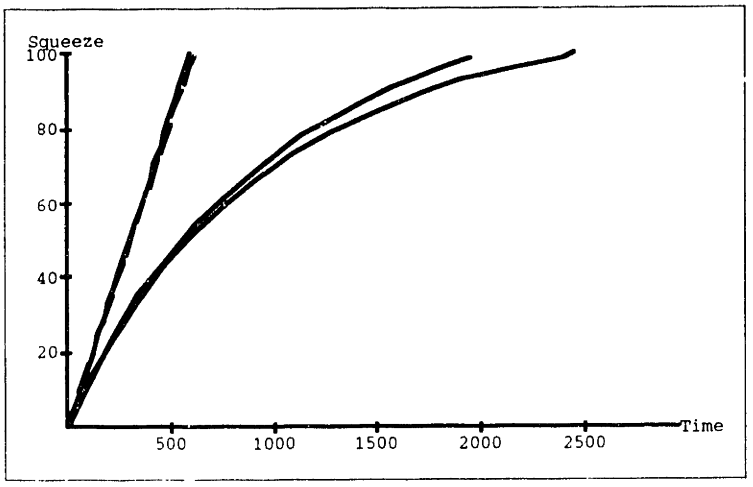

FIGURE 2-7: Squeeze rate as a function of time (NG = 0.0533 and TAU = 0.4). From left to right the curves represent: parallel plates & unbounded cell; parallel plates & bounded cell; wedged plates & unbounded cell; wedged plates & bounded cell. Compare against the following figure

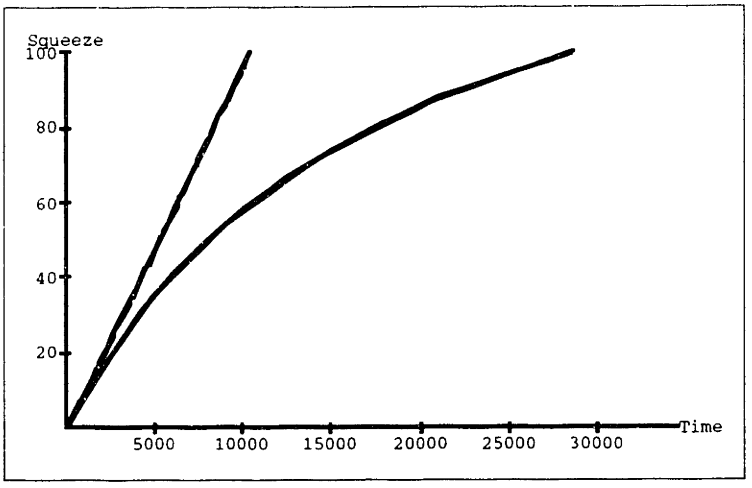

FIGURE 2-8: Squeeze rate as a function of time (NG = 0.00312 and TAU = 0.0126). From left to right the curves represent: parallel plates & unbounded cell; parallel plates & bounded cell; wedged plates & unbounded cell; wedged plates & bounded cell. Difference between bounded and unbounded cells almost indistinguishable—low Darcy-Raleigh number

The squeeze rate shown in **Figures 2-7** and **2-8** is a measure of the percentage of fluid stage 1 "column" to be displaced as a function of time. For lower Darcy-Raleigh numbers (i.e., highly viscous) the end-boundary effects are reduced.

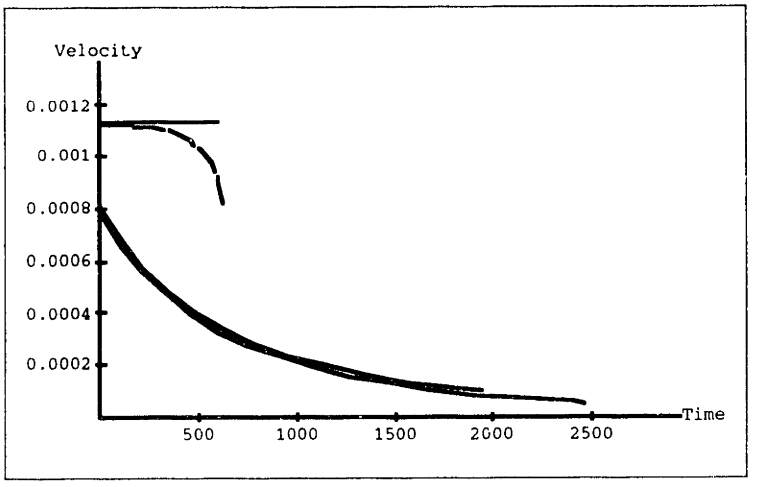

FIGURE 2-9: Velocity as a function of time (NG = 0.0533 and TAU = 0.4). From top to bottom the curves represent: parallel plates & unbounded cell; parallel plates & bounded cell; wedged plates & unbounded cell; wedged plates & bounded cell. Compare against the following figure

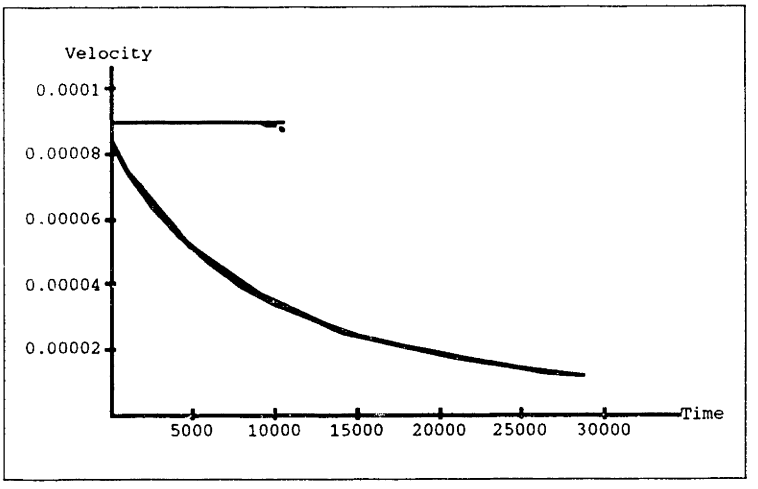

FIGURE 2-10: Velocity as a function of time (NG = 0.00312 and TAU = 0.0126). From top to bottom the curves represent: parallel plates & unbounded cell; parallel plates & bounded cell; wedged plates & unbounded cell; wedged plates & bounded cell. Difference between bounded and unbounded cells almost indistinguishable—low Darcy-Raleigh number

Velocity (in m/sec) dependence with time (in seconds) is shown in **Figures 2-9** and **2-10**. Notice the importance of end-boundary effects in **Figure 2-9**.

The result of various simulations is presented in **Figure 2-12**. The upper bound on Reynolds number is given as 0.33 for parallel plates and the rightmost point. The time

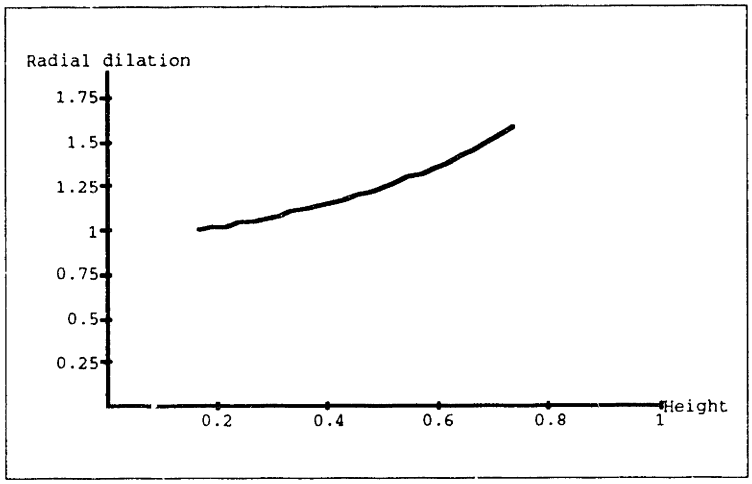

FIGURE 2-11: Dilation rate (wedge) as a function of dimensionless height (NG = 0.0533 and TAU = 0.4)

ratio is a comparison of the time it takes the *blob* to reach the end-boundary for wedged plates and bounded media, versus parallel plates and unbounded media (for the parallel plates the end-boundary is just a reference point). The dilation ratio expresses the functional dependence of the *blob* radius on the wedge shape and time the *blob* takes to reach the end-boundary.

Again for **Figure 2-12** the two rightmost points were obtained through a dynamic analysis (they didn't satisfy the eigenvalue criteria given at the beginning of this section), the remaining points through a steady-state analysis.

2-6 An Analytical Algorithm for the Transverse Motion

The viscous dissipation criteria and a recursive relationship for the n-stage flow problem are derived in **Appendix C**. Two cases of interest are presented:

1) bi-layer

2) symmetrical tri-layer

The formulation, introduced in **Section C-4** on **Page 186**, is applied to fluids of interest. Measured values of viscosity and effective flow rate are used as input.

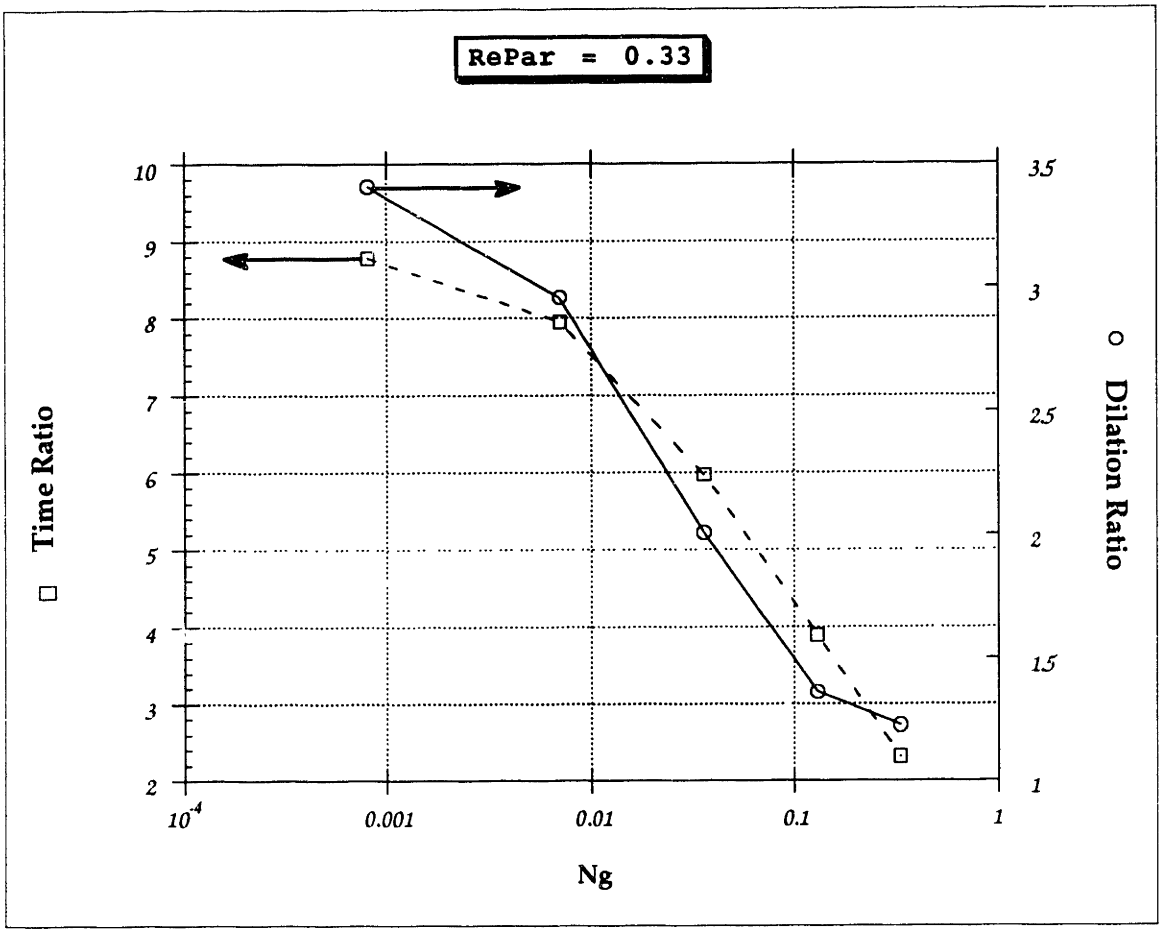

FIGURE 2-12: Time and dilation ratios —wedged crack opening and bounded fracture bottom versus constant crack opening and unbounded fracture bottom— for *blob* to reach the bottom of the fracture. *RePar* (Reynolds number based on parallel cell –conservative upper bound– crack opening) and *Ng* (Modified Darcy's-Raleigh number –also known as Archimedes number) are dimensionless numbers characterizing the relative importance of viscous, inertia, and gravity forces.

The transversal velocity profile is shown as a function of various encapsulation flow ratios in **Figures 2-13** through **2-16**. On TARG-DECH-2 experiments, Mineral Oil was utilized as the displaced fluid (*bath*) and the following as the displacing fluids: Glycerol, Hershey's and Karo—their chemical composition is discussed in **Chapter 4**. The following analysis incorporates the physical characteristics of these fluids. Out of the three displacing fluids, results pictured here are for Hershey's and Karo.

In **Figures 2-13** and **2-14** a bi-layer analysis is presented. Notice that the steeper

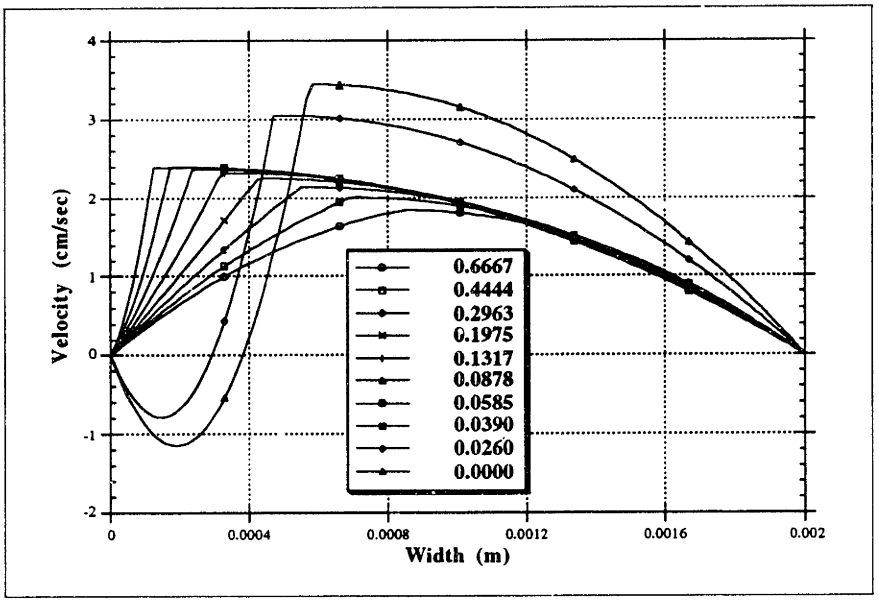

FIGURE 2-13: Velocity distribution (transversal) for bi-layer analysis—using properties of Karo (higher viscosity) and Mineral Oil. Crack opening is 2mm. Table of numbers represent encapsulation flow ratio q_1/q_2 values, and its influence on the layer (thickness) ratio

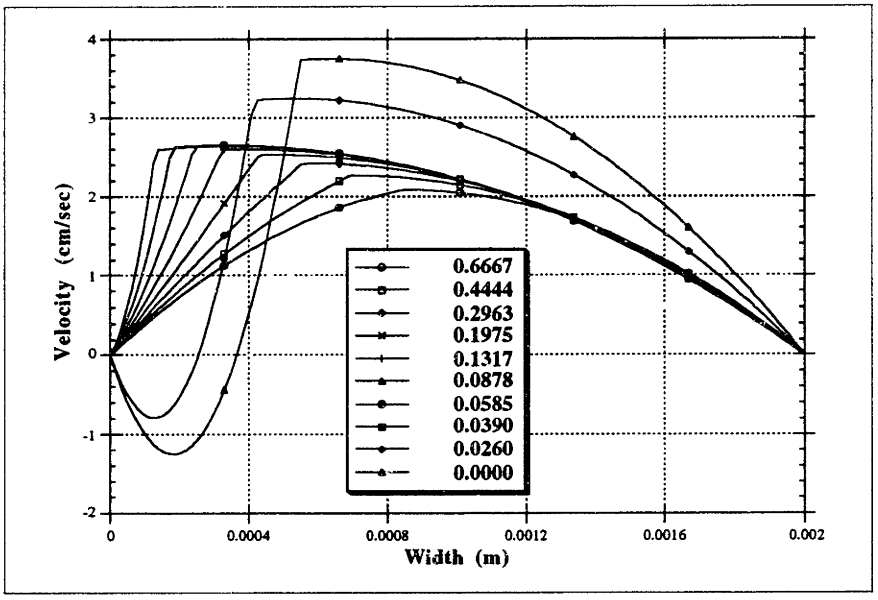

FIGURE 2-14: Velocity distribution (transversal) for bi-layer analysis—using properties of Hershey's (higher viscosity) and Mineral Oil. Crack opening is 2mm. Table of numbers represent encapsulation flow ratio q_1/q_2 values, and its influence on the layer (thickness) ratio

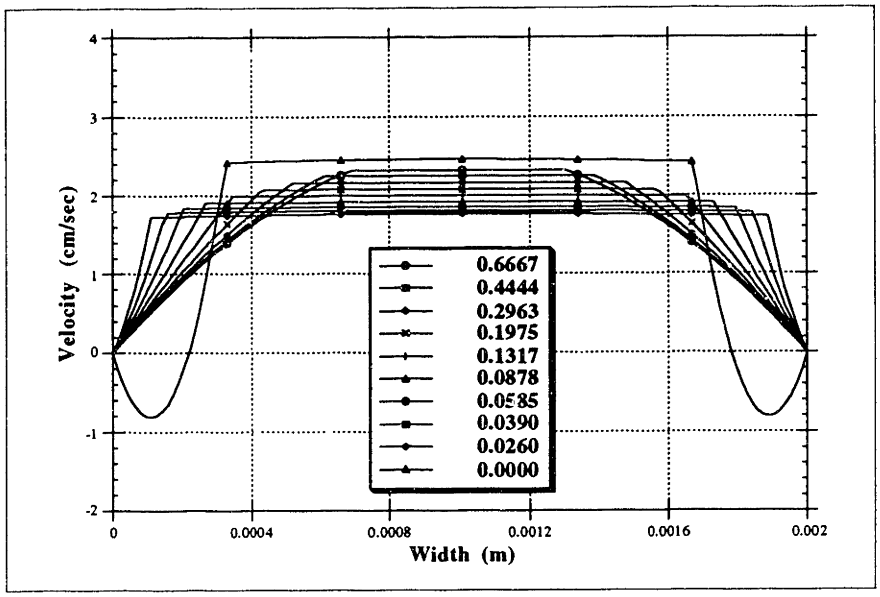

FIGURE 2-15: Velocity distribution (transversal) for symmetrical tri-layer analysis—using properties of Karo (higher viscosity) and Mineral Oil. Crack opening is 2mm. Table of numbers represent encapsulation flow ratio q_1/q_2 values, and its influence on the layer (thickness) ratio

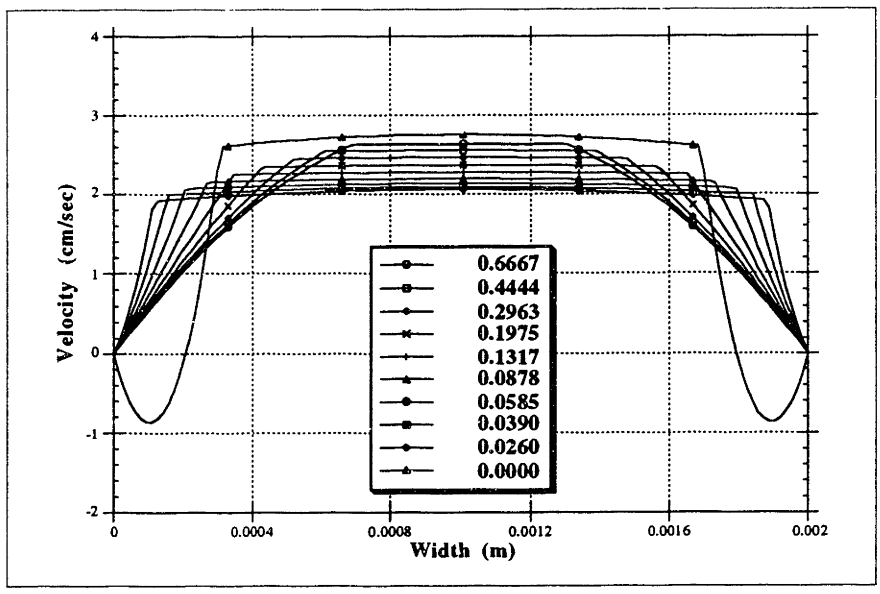

FIGURE 2-16: Velocity distribution (transversal) for symmetrical tri-layer analysis—using properties of Hershey's (higher viscosity) and Mineral Oil. Crack opening is 2mm. Table of numbers represent encapsulation flow ratio q_1/q_2 values, and its influence on the layer (thickness) ratio

velocity gradient occurs on the left side (Mineral Oil). The overall configuration should minimize energy by reducing shear dissipation for the higher viscosity fluid. Also, more fluctuation (for a given encapsulation flow ratio) is seen in **Figure 2-14**, due to a lower viscosity contrast (Hershey's vs. Mineral Oil). An important characteristic in both cases is the back-flow to match a low (or zero) integrated volume flow rate for the Mineral Oil. In addtion, notice that the layer ratio, δ_2/δ—representing the transversal space occupied by fluid stage 2 relative to the crack opening (2mm in this case)—is maximum for an encapsulation flow ratio value of approximately 0.0390.

Results for the symmetrical tri-layer analysis are presented in **Figures 2-15** and **2-16**. The tendency for back-flow is reduced in this case, and the layer ratio is maximum for an encapsulation flow ratio value of approximately 0.0260. Notice the tendency for a plug-flow type behavior (more pronounced in **Figure 2-15**).

Per se the velocity profiles, shown in the previous figures, do not provide a criteria to pick an encapsulated flow configuration. As described in **Appendix C** the criteria utilized to select the encapsulated flow configuration is based on maximizing the flow gain ratio, i.e.,

- given possible encapsulation scenarios that already minimize total shear dissipation, it is assumed that the two fluid stages will assume a configuration that will deliver the maximum flow rate of the heavier and more viscous fluid *blob*.

Figures 2-17 through **2-20** show the effect of varying the flow rate ratio on the: flow gain ratio; effective viscosity; and, layer (thickness) ratio. This effect is analyzed for a given viscosity ratio and overall configuration (e.g., bi-layer or symmetrical tri-layer).

Notice that: **Figures 2-13** through **2-16** are presented in terms of the encapsulation flow ratio, **Figures 2-17** through **2-21** are presented in terms of the flow rate ratio. The flow rate ratio definition imposes a dependence on the overall configuration (e.g., bi-layer different than tri-layer), while the encapsulation flow ratio definition is configuration independent. The use of this artifact to represent the different flow configurations is easily pictured in **Figure 2-21**—the 10 points used to generate each curve have a very different spread for the bi-layer when compared to the symmetrical tri-layer.

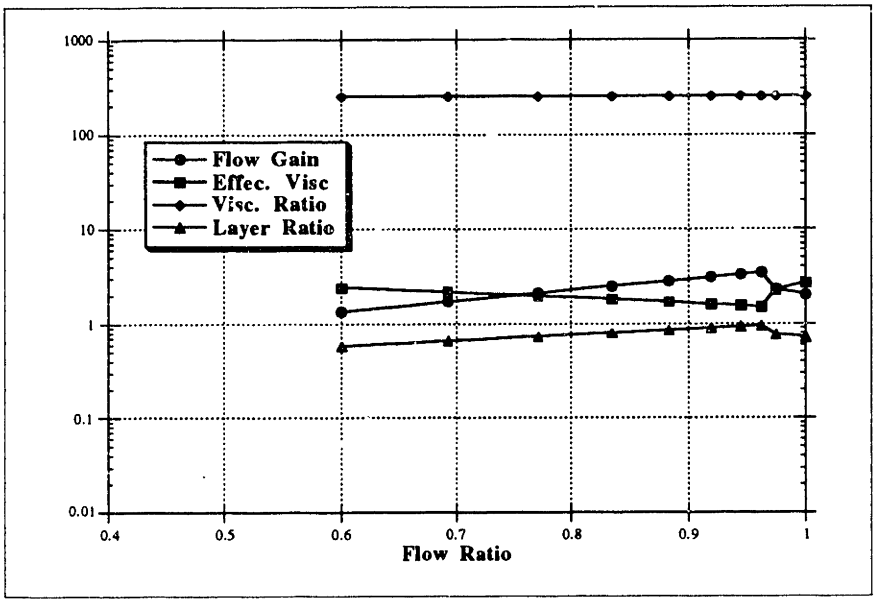

FIGURE 2-17: Flow gain ratio, effective viscosity, viscosity ratio (single number) and layer ratio as a function of the flow rate ratio—$q_2/(q_1 + q_2)$. Bi-layer analysis using properties of Karo (higher viscosity) and Mineral Oil. Crack opening is 2mm

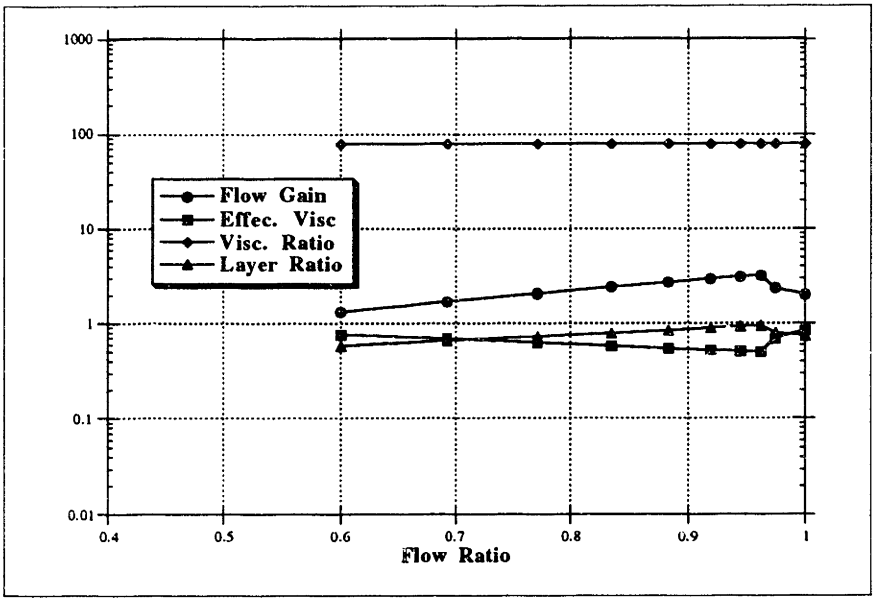

FIGURE 2-18: Flow gain ratio, effective viscosity, viscosity ratio (single number) and layer ratio as a function of the flow rate ratio—$q_2/(q_1 + q_2)$. Bi-layer analysis using properties of Hershey's (higher viscosity) and Mineral Oil. Crack opening is 2mm

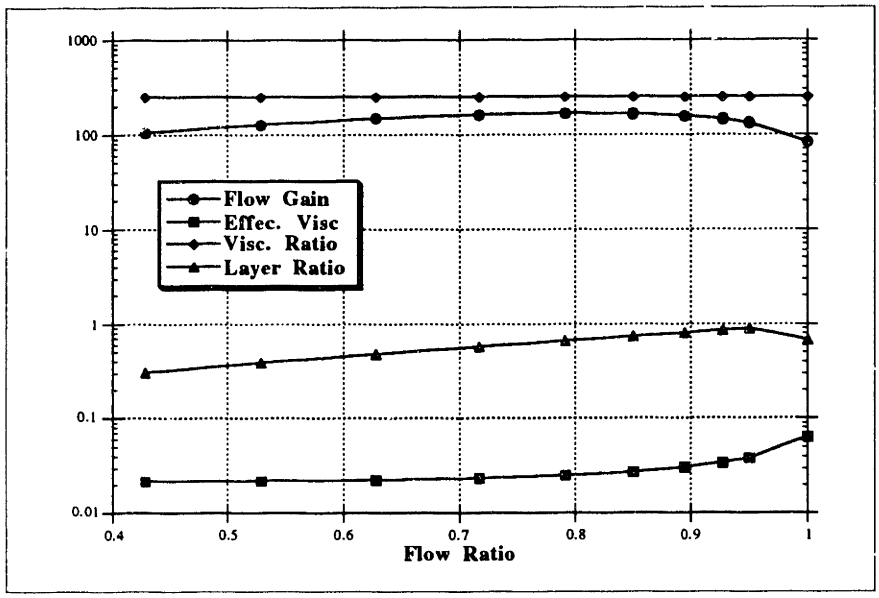

FIGURE 2-19: Flow gain ratio, effective viscosity, viscosity ratio (single number) and layer ratio as a function of the flow rate ratio—$q_2/(2q_1 + q_2)$. Symmetrical tri-layer analysis using properties of Karo (higher viscosity) and Mineral Oil. Crack opening is 2mm

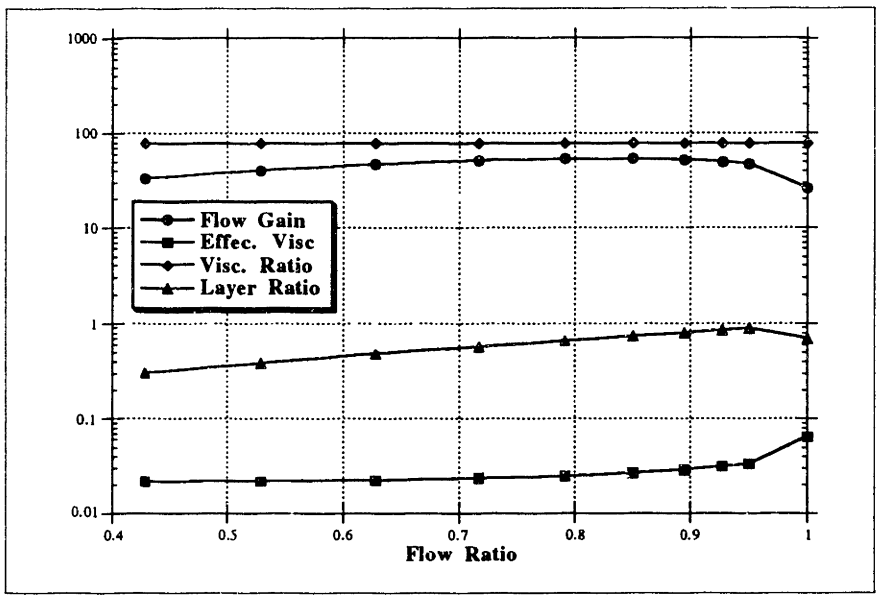

FIGURE 2-20: Flow gain ratio, effective viscosity, viscosity ratio (single number) and layer ratio as a function of the flow rate ratio—$q_2/(2q_1 + q_2)$. Symmetrical tri-layer analysis using properties of Hershey's (higher viscosity) and Mineral Oil. Crack opening is 2mm

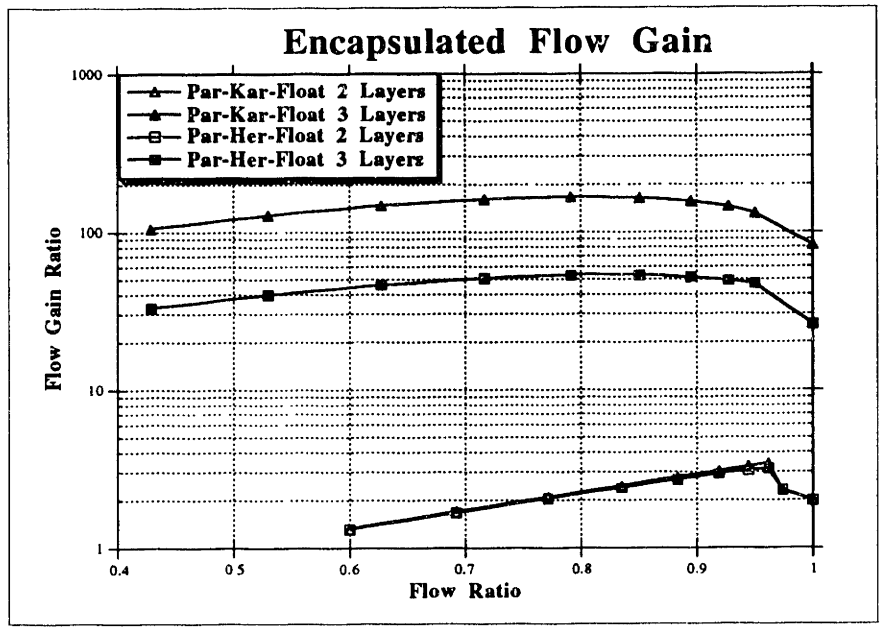

FIGURE 2-21: Flow gain ratio versus flow rate ratio. Comparison for: Karo in Mineral Oil—bi-layer and symmetrical tri-layer; Hershey's in Mineral Oil—bi-layer and symmetrical tri-layer

Analyzing **Figure 2-21**

- the symmetrical tri-layer configuration offers a higher flow gain ratio when compared to the bi-layer (roughly 2 orders of magnitude!);
- the flow gain ratio for the bi-layer is roughly a factor of 3 over an attached configuration flow rate, and roughly a factor of 40–170 for the symmetrical tri-layer;
- the flow rate ratio associated to the maximum value of flow gain ratio for the bi-layer configuration is approximately 0.96 for both 2-stage scenarios;
- the flow rate ratio associated to the maximum value of flow gain ratio for the symmetrical tri-layer configuration is, approximately, 0.85 for the Hershey's/ Mineral Oil set, and 0.81 for the Karo/Mineral Oil set.

Analyzing the layer (thickness) ratio in **Figures 2-17** through **2-20**, it's obvious that an attached blob would not occur (even for $q_l = 0$). This point shows a clear short-

come of the theory derived here.

Refering to item *3)* in **Section C-1** on **Page 183**, the transition process from attachment to encapsulation is not addressed in this work. Consequently, the analyst (making use of this theory) has to decide if encapsulation is present and, if practical conditions will enhance the detachment of the *blob* from the walls. This decision process is by no means easy and, very often, misleading—a typical example is discussed below.

Surface characteristics, fluid-solid wettability and surface roughness play a key role on determining the attachment of a *blob* to the walls (while displacing another fluid stage). For instance, experiments described in **Chapter 4** have demonstrated that a rougher surface enhances the adhesion of a *blob* to the walls. If this fact is extrapolated to field conditions in hydraulic fracturing, it seems obvious that the expected fracture inner walls (rock) roughness would enhance adhesion of the fluids and gels to the walls. However, such inference is misleading. Most of the fracture surfaces created underground are very smooth, due to the quasi-static characteristic of the hydraulic fracturing operation.

3 PARFES — PARallel Finite Element Solvers

3-1 Introduction

PARFES (acronym for PARallel Finite Element Solvers) performs detailed tracking of multiple fluid interfaces motion within a fracture.

PARFES differs from standard finite element method implementations in the following aspects: *i)* data structure—it accommodates parallelism, avoiding the conventional build up of connectivity arrays, or assembling the stiffness matrix, Junior (1989); *ii)* solver—an iterative solver is used, exploiting matrix sparsity and nonlinearity; and, *iii)* symbolic mathematics—the coefficients of "stiffness" are automatically generated by a program written in the symbolic programming language Mathematica.

PARFES is composed of three modules:

- PARFES1 — used for tracking the interface motion and distortion between the multiple fluid stages, is based on an Euler-Lagrangian approach, i.e., nodes at interfaces in contact with solid regions, such as the fracture walls, are assumed to be at rest, while nodes located within fluid fronts are free to move, based on the coupling of flow field variables with the elastic stress field. A finite element algorithm with a local data structure is employed, utilizing an elliptical conjugate-gradient-type iterative solver. Matrices are sparse and not assembled
- PARFES2 — this modified nonlinear Newton-Raphson algorithm incorporates the important physics governing the multiple fluids flow motion. The nodal movement and the fluid flow velocity fields are coupled with the pressure and crack opening distribution fields. Although the algorithm's data structure follows the same ideas implemented in PARFES1, its results depend on the 3-D elastic field and fracture criterion coupling performed by R3DH—

a general fracture simulator developed in a separate project, Cleary, Barr et al. (1988); Cleary, Kavvadas et al. (1983). R3DH is used to synchronize the global variations in crack opening distribution with the predicted pressure flow field given by PARFES2. The coupling of the two algorithms would represent a serious computational bottleneck (due to the physics of the problem), if calculations were performed for both algorithms in very refined meshes. However, a better use of the computational resources is obtained by immersing the very refined meshes needed in PARFES2 with somewhat coarse discretizations done in R3DH (the global data structure surface integral scheme employed in R3DH, although computationally intensive, doesn't require refined meshes, except near the crack tip perimeter)

- PARFESAX — contains all the intrinsic physical modeling capabilities of PARFES2 combined with the mesh motion of PARFES1, but it is limited to track the movement of multiple fluid stages for axisymmetrical cases. In spite of this simplifying symmetry, the accurate solution of cases of interest is also computationally intensive. By comparing the results of this code with the few available analytical solutions of one fluid stage problem, a great amount of physical insight has been gained.

There are two versions of PARFES1. The first version was initially designed to exploit conventional vector supercomputers (e.g., CRAY Y-MP). The algorithm was optimized to run at close-to-peak performance. The second version of PARFES1 was designed for Massively Parallel Processors (e.g., Connection Machine 2)—it handles larger meshes.

3-2 Parallelization Issues

Implementation of a Finite Element Method for parallel computers requires an analysis of the following issues (see Junior 1989):

1) Local/global connectivity for the physical and computational mesh and its embedment in the machine topology—see **Figures 3-1** and **3-2**;

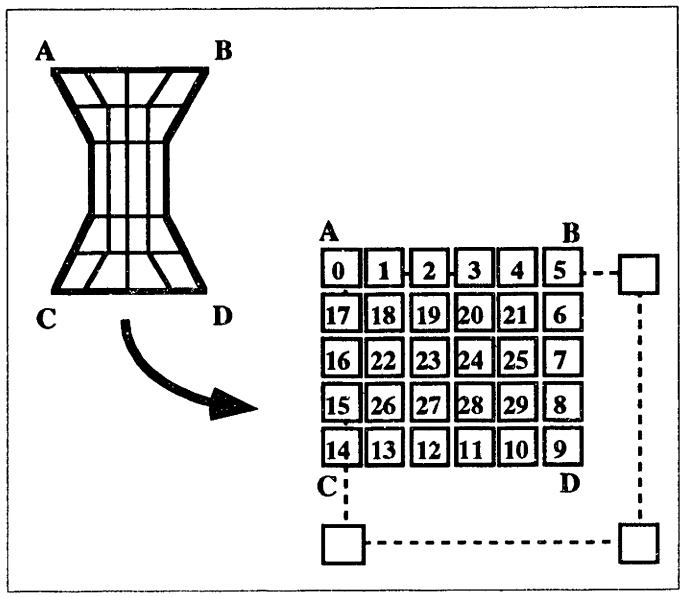

FIGURE 3-1: Physical mesh topology embedded in the machine topology – convex geometry

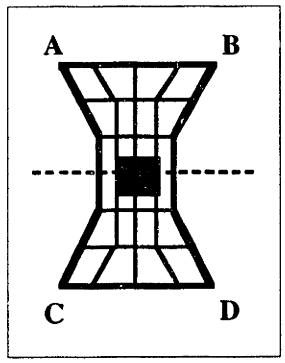

FIGURE 3-2: Possible partition of non-convex geometry for immersion in the machine topology

2) Development of a splitting strategy of shared nodes (used for mesh wrapping)—see **Figure 3-3**

3) Packing nodes, elements and degrees of freedom as a function of the processors distribution and support functions—see **Figures 3-4** and **3-5**.

The implementation discussed here utilizes virtual processor addressing and direct nodal mapping. Nodes are not split, except for end-of-the-boundary shifts to allow the mesh to wrap around itself. A bi-linear isoparametric base is used.

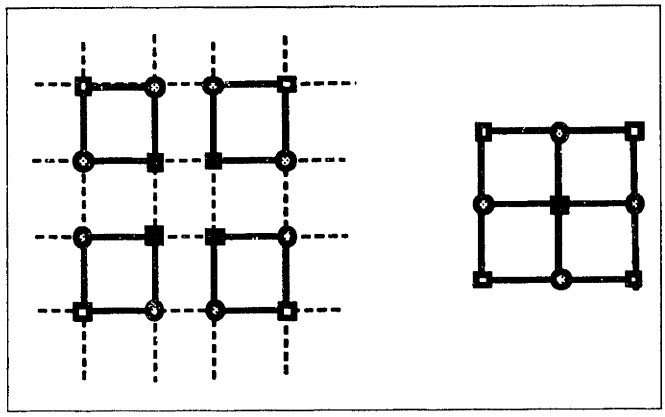

FIGURE 3-3: Node split among neighbor elements

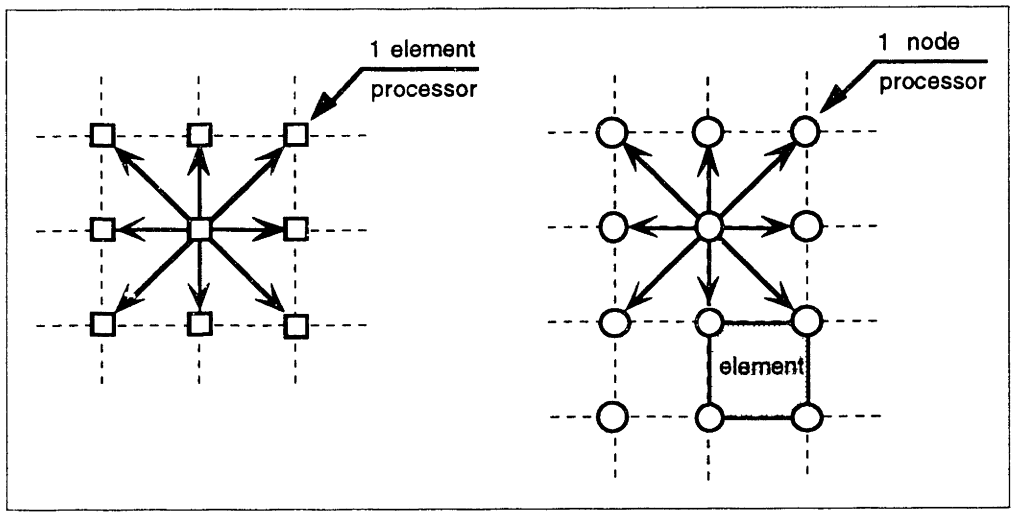

FIGURE 3-4: Communi cation cost: 1/1 node and element packing using a bi-linear isoparametric element

3-3 Error, Convergence and Performance Analysis

The tendency of higher viscosity fluids to migrate to regions of lower shear rates may dramatically alter the wetting conditions at the fracture walls (vide sketch in **Figure 3-6**). This (transverse) migration mechanism, previously termed encapsulation, may substantially affect the average velocity of the heavier proppant-laden fluid(s) and, consequently, the placement of proppant particles within the fracture cavity. Although fingering (in-plane instability—modelled by PARFES1), can modify the morphology of the fluid stages' interfaces, encapsulation instabilities are more important in hydraulic fracturing. For instance, experiments conducted for different fluids, vide **Chapter 4**, have demon-

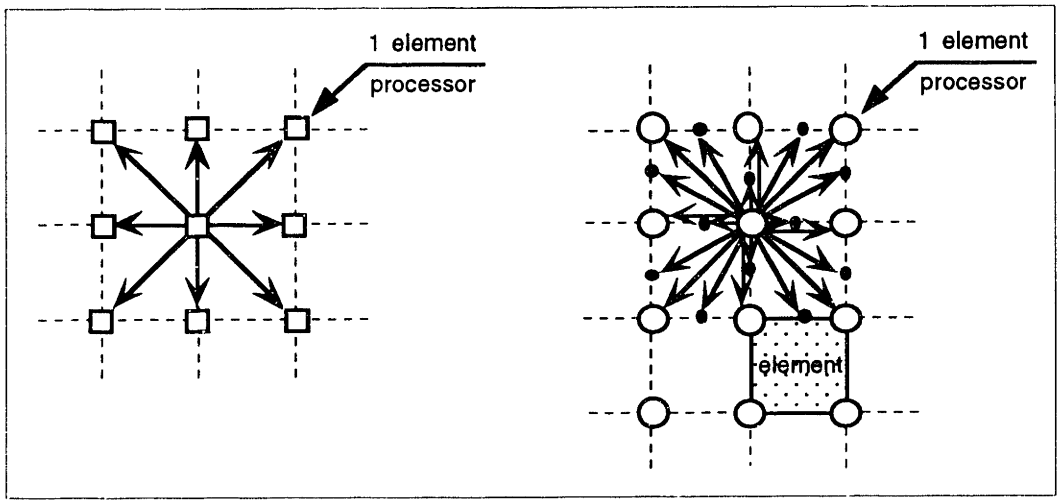

FIGURE 3-5: Communi cation cost: 1/1 node and element packing using a bi-quadratic isoparametric element

strated a spread of about two orders of magnitude on the downwards *blob* velocity.

The downwards motion of multiple, immiscible, fluid stages is far more complex than the 2-stage problem, specially when modelling in-plane distortion. Excluding fluid losses through the fracture walls, the various stages compete against each other when filling the fracture, i.e., the lighter fluid when displaced upwards is also constrained to move within the fracture boundaries.

The tracking of one interface motion was verified against derived analytical solutions using PARFESAX. An error analysis for various physical variables of interest, is shown in **Figures 3-7** through **3-10**.

Multiple interface tracking was verified in two ways: *i)* imposing exactly the same boundary conditions and fluid characteristics of the 1-fluid stage analytical solution to the various fluid stages—**Figures 3-11** through **3-24** show an error analysis for 1, 2 and 5 fluid stages; *ii)* doing a convergence analysis in the general case (no analytical solution available), vide **Figures 3-25** through **3-29** (except **Figure 3-27**).

With respect to the suitability of the algorithm(s) to parallelization, optimization results for PARFES1, using the NCSA's CRAY Y-MP, show a good parallel scale-up when the number of mesh points is increased, see **Figures 3-30, 3-31** and **3-32**. Also, perfor-

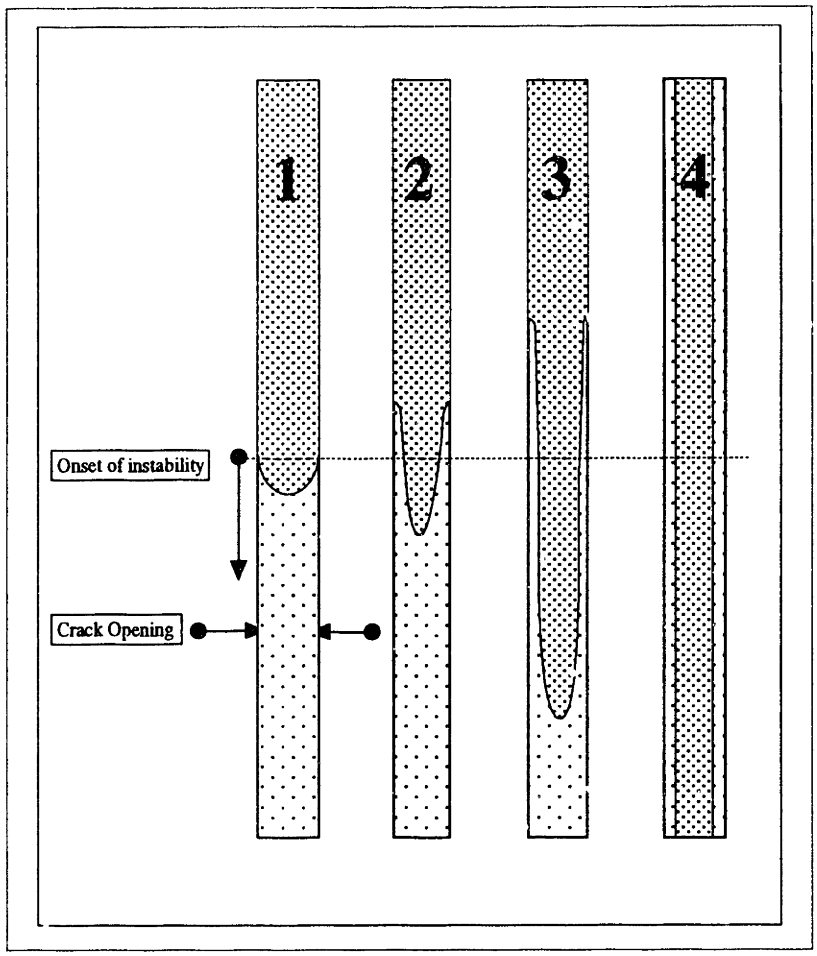

FIGURE 3-6: Onset of encapsulation instability

mance is good for larger meshes (215 MFlops out of a 330 MFlops theoretical peak performance)—See **Figure 3-33** on **Page 84**. The fine grained implementation, using the Connection Machine-2 (at various locations), confirmed the expectations, e.g., large problems run with almost 98 percent processes utilization.

For more details refer to **Appendices D** and **E**. Additional results presented in **Appendices G, H** and **I**.

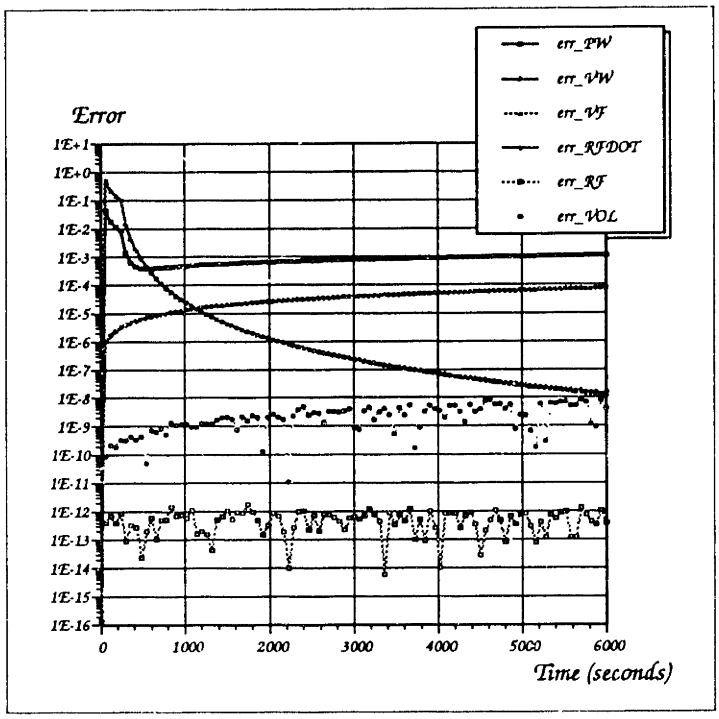

FIGURE 3-7: PARFESAX results for 100 mesh points and 101 time steps. Numerical error (comparison against analytical results) for: pressure at the wellbore; velocities at the wellbore; velocities at the fluid front; mesh velocities at the fluid front; fluid front position; and, total volume conservation

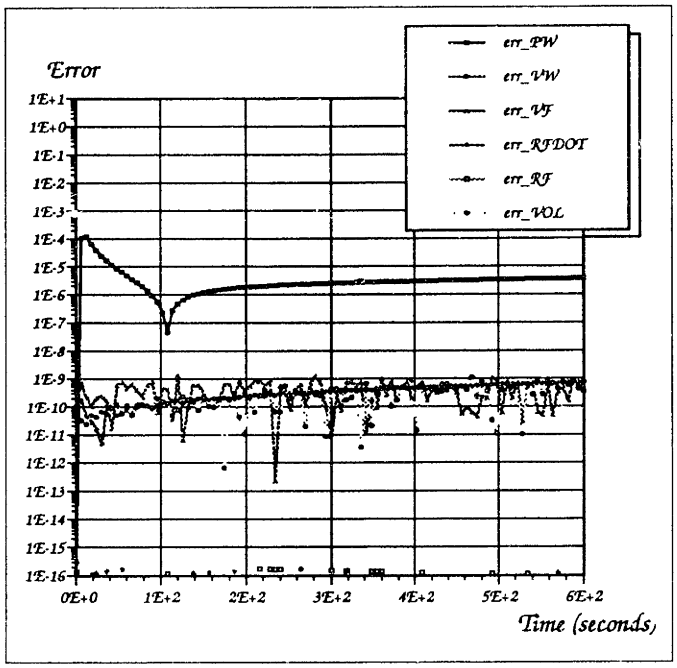

FIGURE 3-8: PARFESAX results for 1000 mesh points and 101 time steps. Numerical error (comparison against analytical results) for: pressure at the wellbore; velocities at the wellbore; velocities at the fluid front; mesh velocities at the fluid front; fluid front position; and, total volume conservation

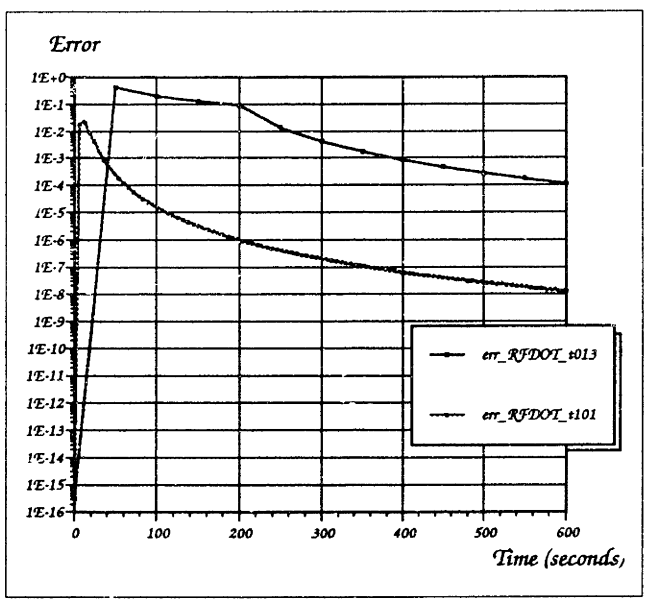

FIGURE 3-9: PARFESAX results for 13 and 101 time steps (1000 mesh points). Numerical error (comparison against analytical results) for: mesh velocities at the fluid front

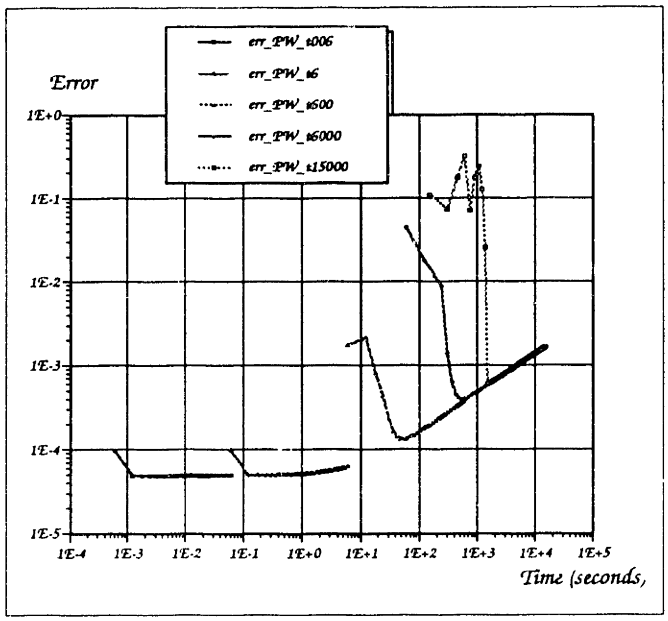

FIGURE 3-10: PARFESAX results, using 1000 mesh points and 101 time steps, for different values of total running time (0.06 sec, 6 sec, 600 sec, 6,000 sec, 15,000 sec). Numerical error (comparison against analytical results) for pressure at the wellbore

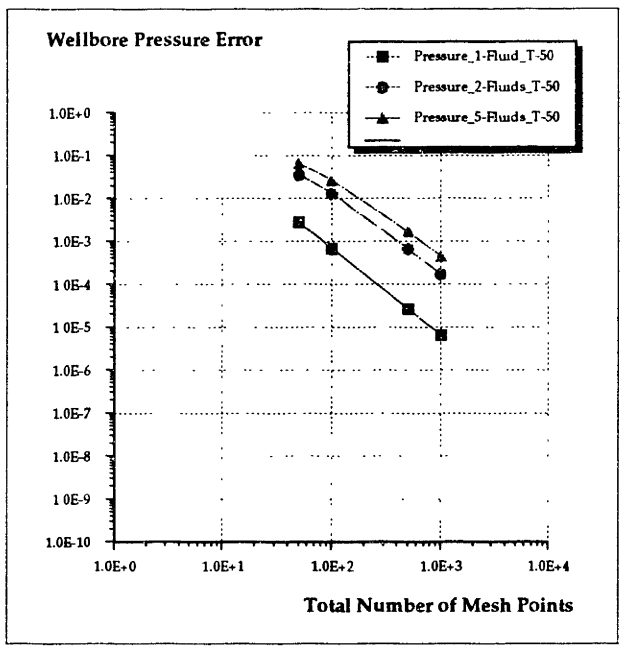

FIGURE 3-11: PARFESAX error analysis for the final predicted wellbore pressure versus the total number of mesh points. Same boundary conditions and fluid characteristics of the 1-fluid stage imposed on both the 2-stage and 5-stage problems. Result for 50 time steps

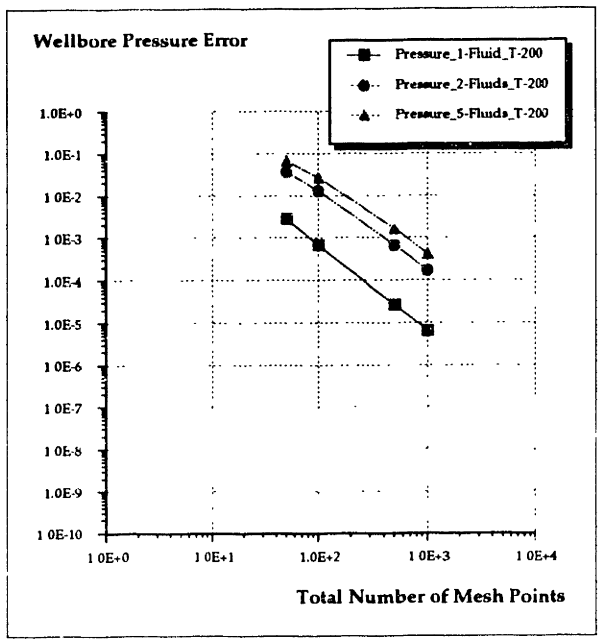

FIGURE 3-12: PARFESAX error analysis for the final predicted wellbore pressure versus the total number of mesh points. Same boundary conditions and fluid characteristics of the 1-fluid stage imposed on both the 2-stage and 5-stage problems. Result for 200 time steps (notice that the error is weakly dependent on the number of time steps

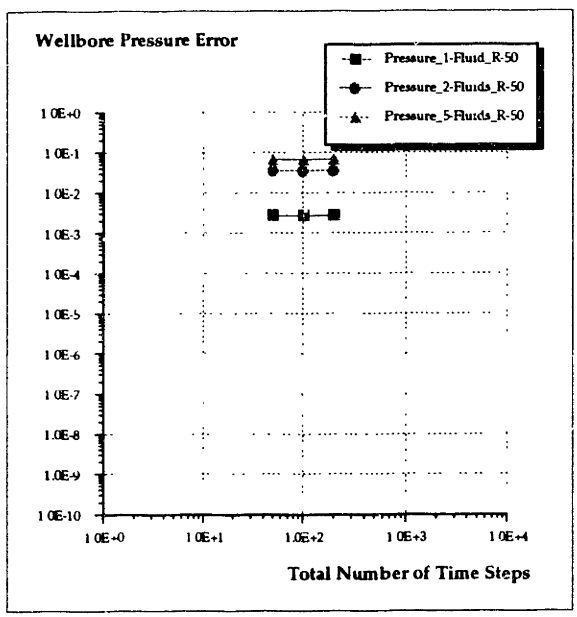

FIGURE 3-13: PARFESAX error analysis for the final predicted wellbore pressure versus the total number of time steps. Same boundary conditions and fluid characteristics of the 1-fluid stage imposed on both the 2-stage and 5-stage problems. Result for 50 mesh points

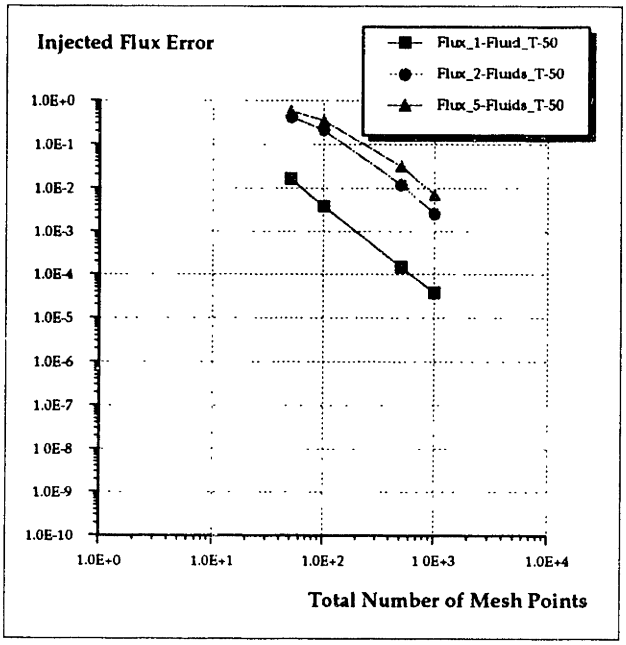

FIGURE 3-14: PARFESAX error analysis for injected flux versus the total number of mesh points. Same boundary conditions and fluid characteristics of the 1-fluid stage imposed on both the 2-stage and 5-stage problems. Result for 50 time steps

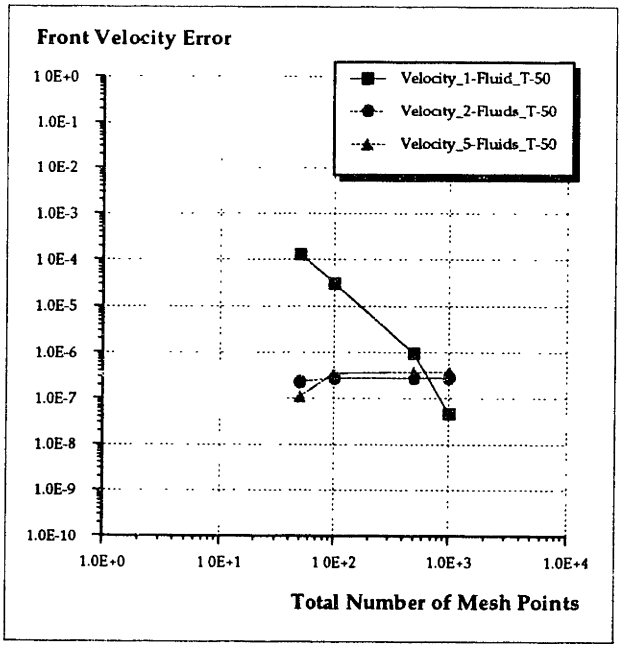

FIGURE 3-15: PARFESAX error analysis for fluid front versus the total number of mesh points. Same boundary conditions and fluid characteristics of the 1-fluid stage imposed on both the 2-stage and 5-stage problems. Result for 50 time steps

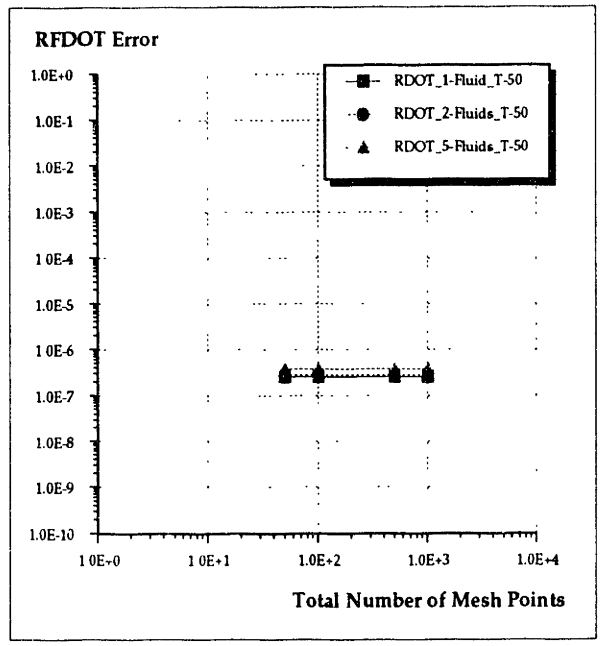

FIGURE 3-16: PARFESAX error analysis for nodal front velocity versus the total number of mesh points. Same boundary conditions and fluid characteristics of the 1-fluid stage imposed on both the 2-stage and 5-stage problems. Result for 50 time steps

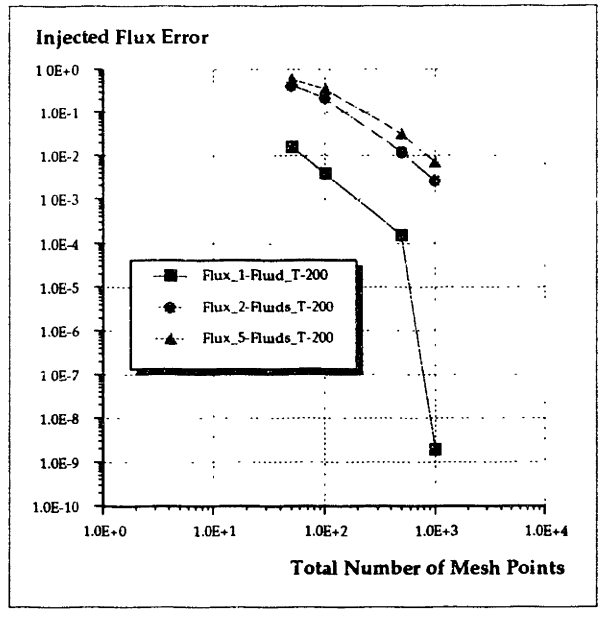

FIGURE 3-17: PARFESAX error analysis for injected flux versus the total number of mesh points. Same boundary conditions and fluid characteristics of the 1-fluid stage imposed on both the 2-stage and 5-stage problems. Result for 200 time steps

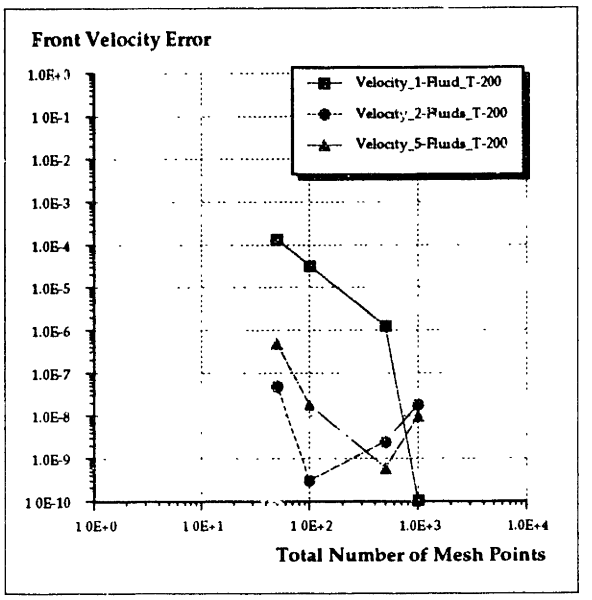

FIGURE 3-18: PARFESAX error analysis for fluid front velocity versus the total number of mesh points. Same boundary conditions and fluid characteristics of the 1-fluid stage imposed on both the 2-stage and 5-stage problems. Result for 200 time steps

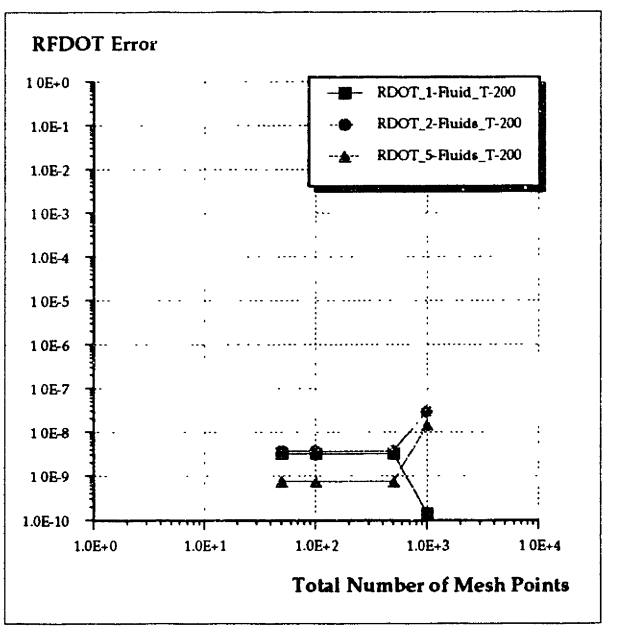

FIGURE 3-19: PARFESAX error analysis for nodal front velocity versus the total number of mesh points. Same boundary conditions and fluid characteristics of the 1-fluid stage imposed on both the 2-stage and 5-stage problems. Result for 200 time steps

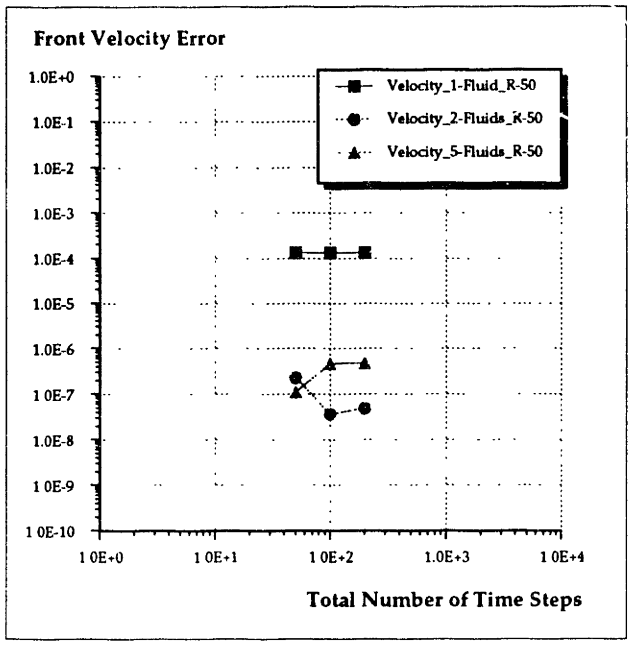

FIGURE 3-20: PARFESAX error analysis for fluid front velocity versus the total number of time steps. Same boundary conditions and fluid characteristics of the 1-fluid stage imposed on both the 2-stage and 5-stage problems. Result for 50 mesh points

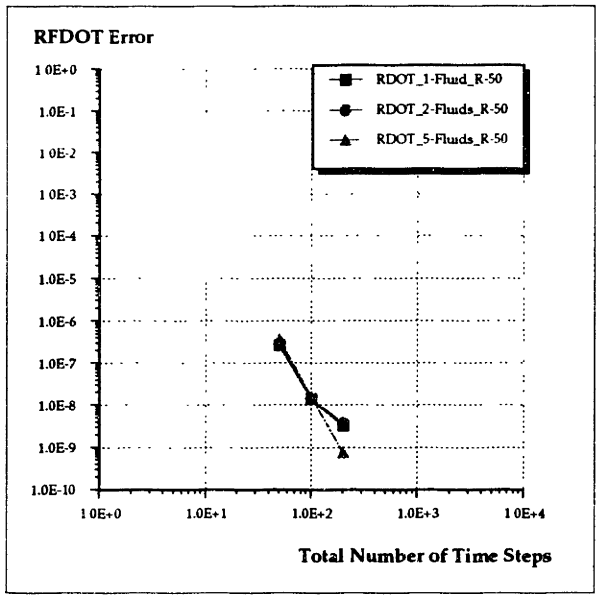

FIGURE 3-21: PARFESAX error analysis for nodal front velocity versus the total number of time steps. Same boundary conditions and fluid characteristics of the 1-fluid stage imposed on both the 2-stage and 5-stage problems. Result for 50 mesh points

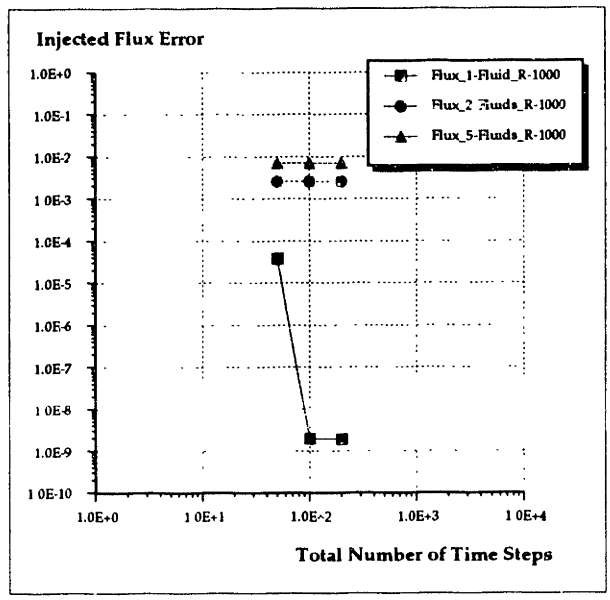

FIGURE 3-22: PARFESAX error analysis for injected flux versus the total number of time steps. Same boundary conditions and fluid characteristics of the 1-fluid stage imposed on both the 2-stage and 5-stage problems. Result for 1000 mesh points

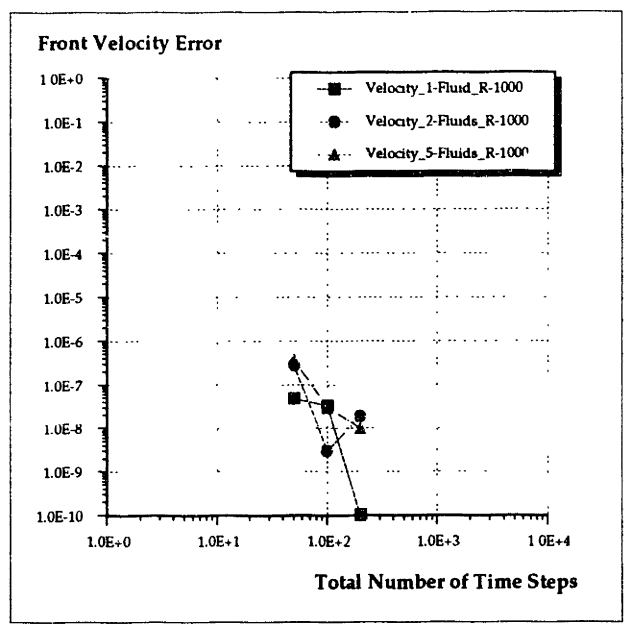

FIGURE 3-23: PARFESAX error analysis for fluid front velocity versus the total number of time steps. Same boundary conditions and fluid characteristics of the 1-fluid stage imposed on both the 2-stage and 5-stage problems. Result for 1000 mesh points

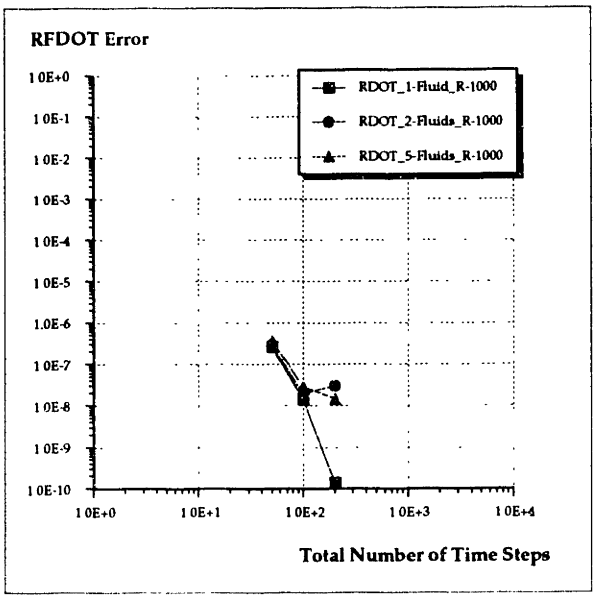

FIGURE 3-24: PARFESAX error analysis for nodal front velocity versus the total number of time steps. Same boundary conditions and fluid characteristics of the 1-fluid stage imposed on both the 2-stage and 5-stage problems. Result for 1000 mesh points

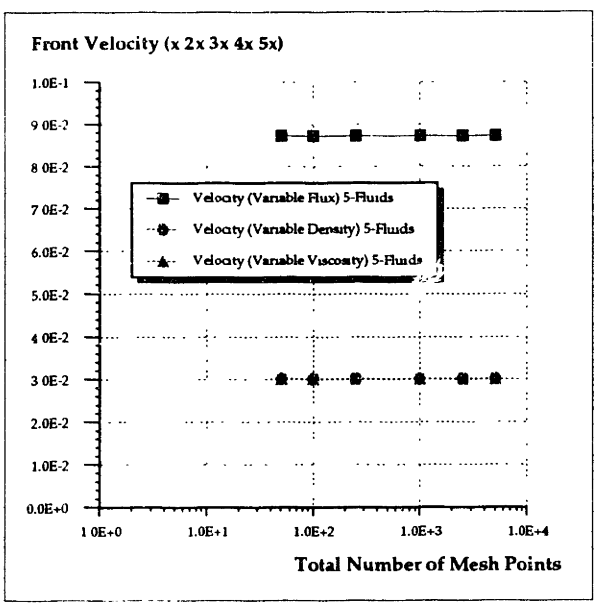

FIGURE 3-25: Convergence analysis for fluid front velocity versus the total number of mesh points tracking 5 fluid stages. The injected flux/density/viscosity are increased as x 2x 3x 4x 5x, for each stage (x is the flux/density/viscosity for the first fluid stage)

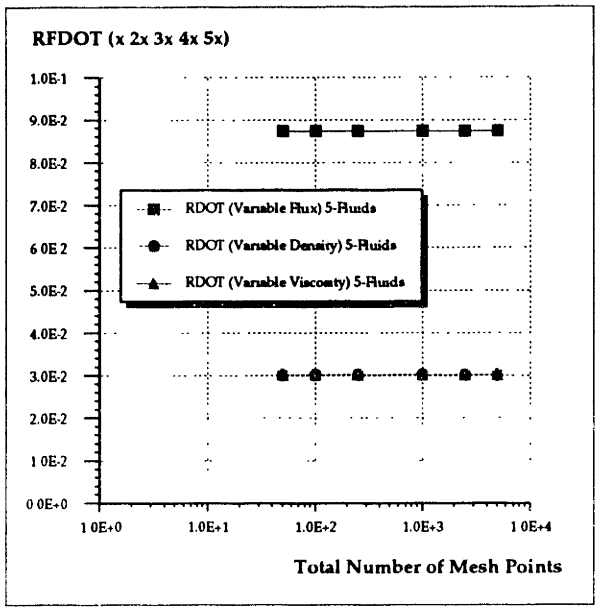

FIGURE 3-26: Convergence analysis for nodal front velocity versus the total number of mesh points tracking 5 fluid stages. The injected flux/density/viscosity are increased as x 2x 3x 4x 5x, for each stage (x is the flux/density/viscosity for the first fluid stage)

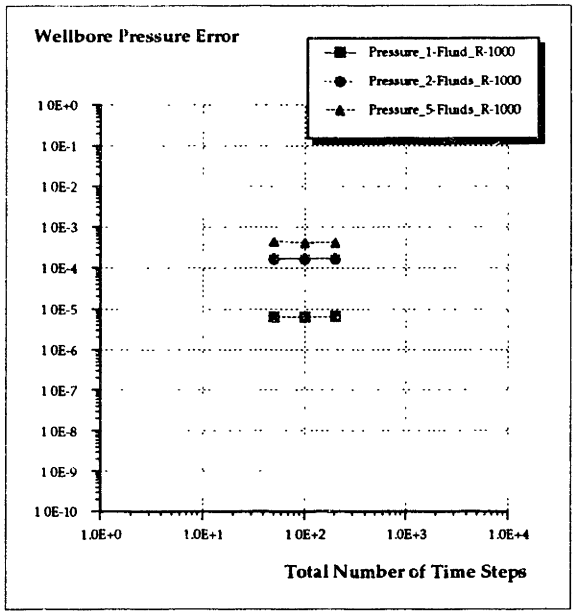

FIGURE 3-27: PARFESAX error analysis for the final predicted wellbore pressure versus the total number of time steps. Same boundary conditions and fluid characteristics of the 1-fluid stage imposed on both the 2-stage and 5-stage problems. Result for 1000 mesh points

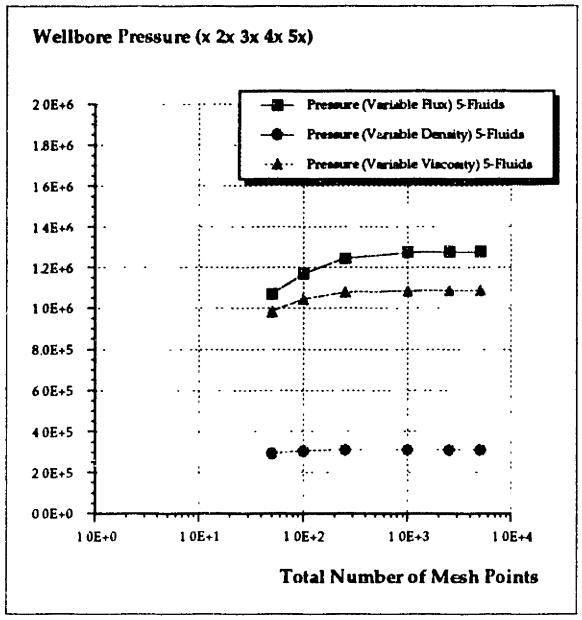

FIGURE 3-28: Convergence analysis for the final predicted wellbore pressure versus the total number of mesh points tracking 5 fluid stages. The injected flux/density/viscosity are increased as x 2x 3x 4x 5x, for each stage (x is the flux/density/viscosity for the first fluid stage)

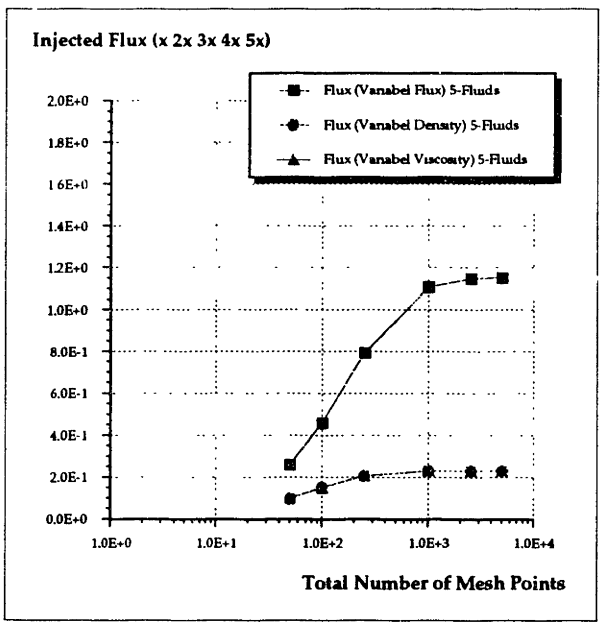

FIGURE 3-29: Convergence analysis for the final injected flux versus the total number of mesh points tracking 5 fluid stages. The injected flux/density/viscosity are increased as x 2x 3x 4x 5x, for each stage (x is the flux/density/viscosity for the first fluid stage)

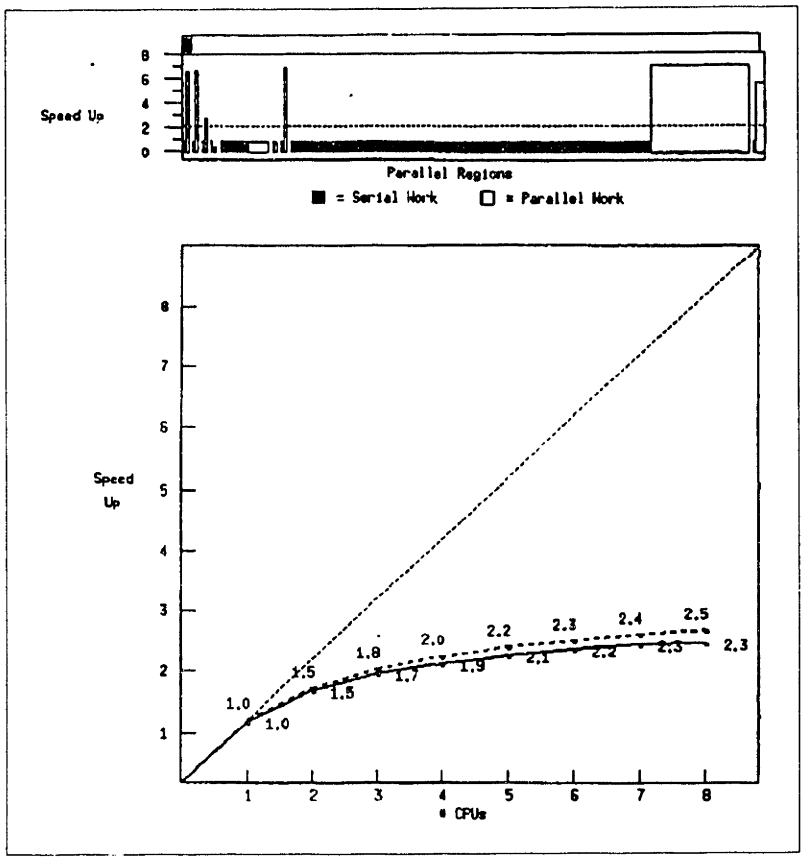

FIGURE 3-30: PARFES1 optimization results for a 100x100 mesh, using the NCSA's CRAY Y-MP. Compare parallel scale-up when number of mesh points is increased (vide Figure 23)

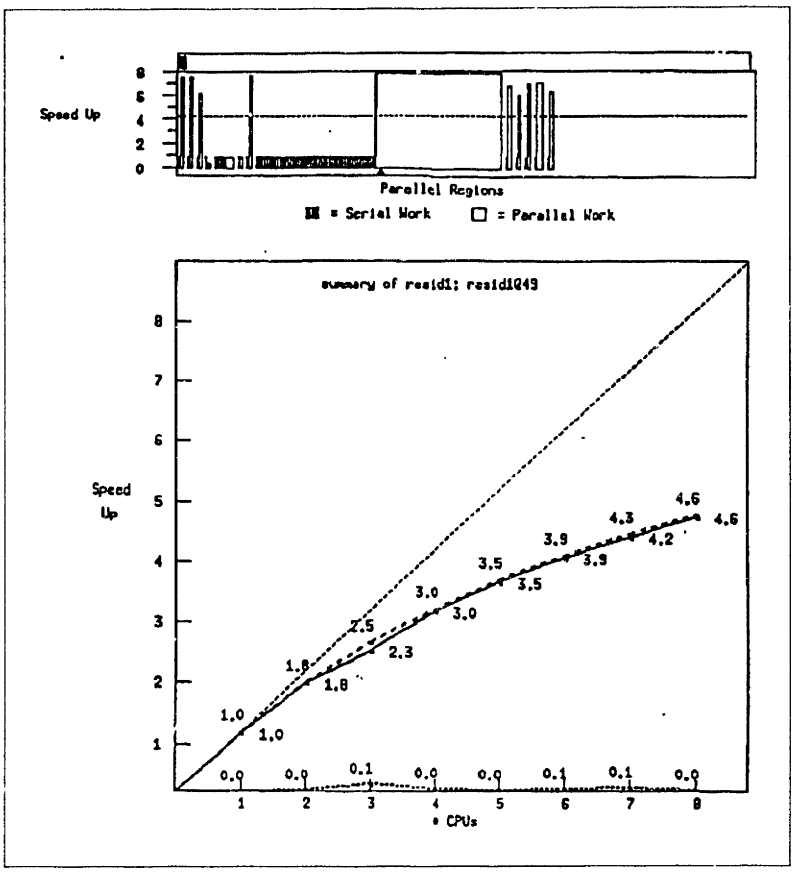

FIGURE 3-31: PARFES1 optimization results for a 150x150 mesh, using the NCSA's CRAY Y-M

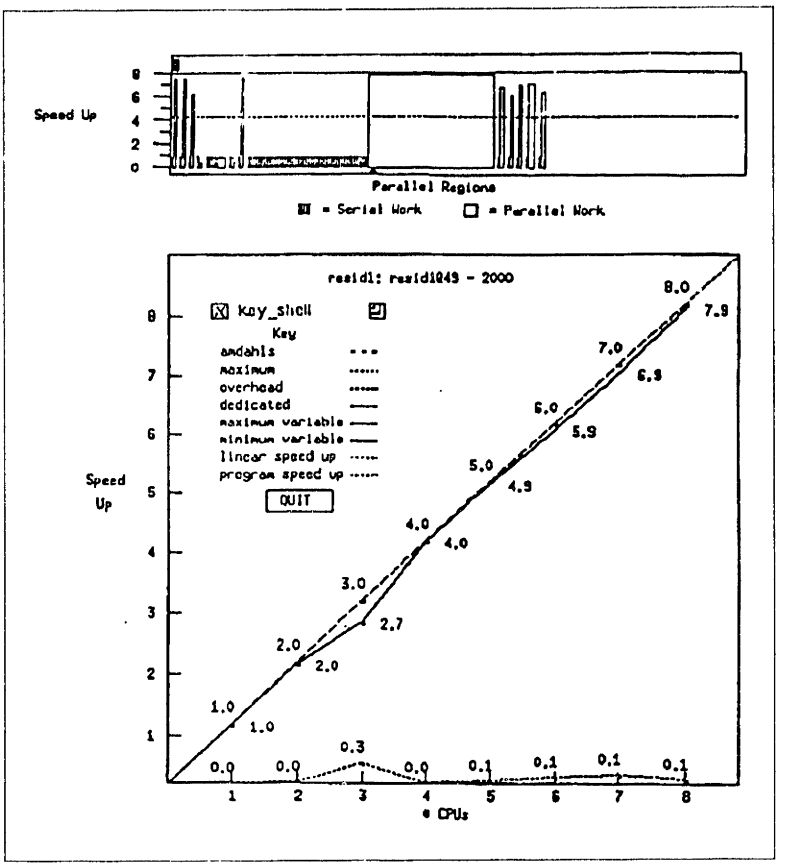

FIGURE 3-32: PARFES1 optimization results for a 150x150 mesh, using the NCSA's CRAY Y-MP. Result for most computationally intensive subroutine. Program presents a good parallel scale-up (even in its coarse grained implementation) when number of mesh points is increase

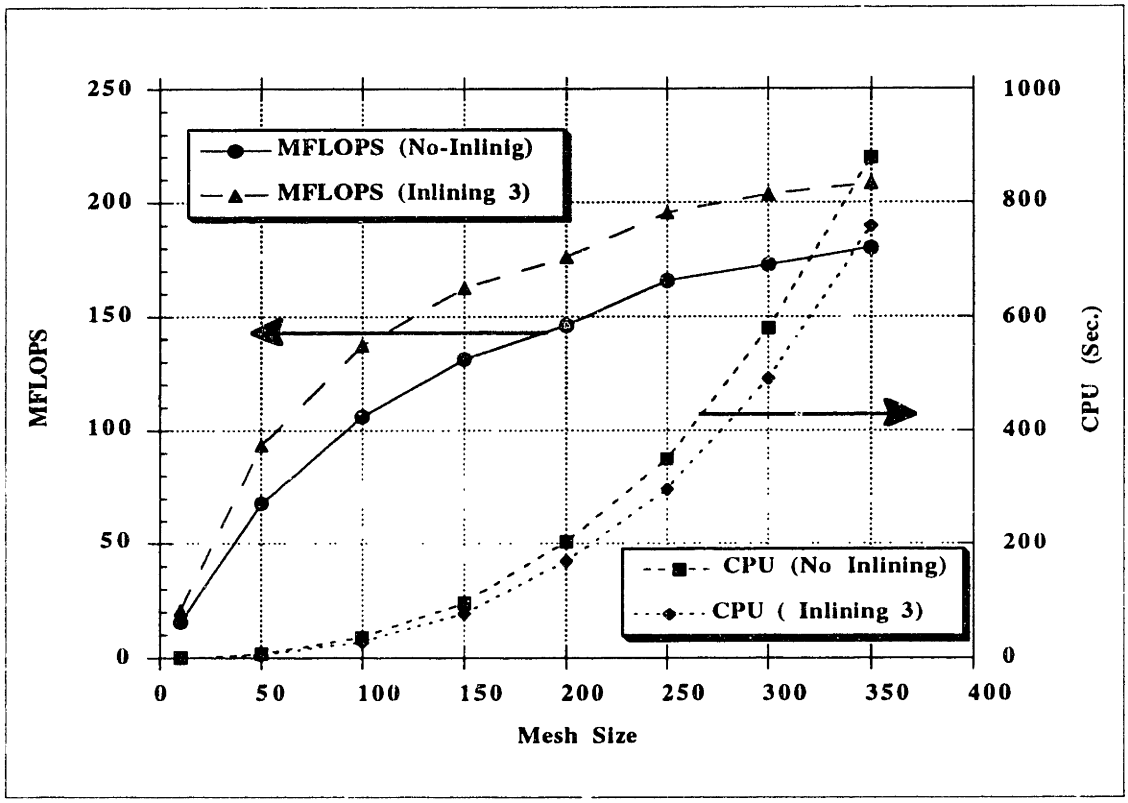

FIGURE 3-33: Performance results for vectorized version of PARFES1 as a function of the mesh size. Number of degrees of freedom is $2m^2$, where m is the mesh size

4 TARG-DECH — Gravity-Driven Convective Hydraulics

4-1 Introduction

Two apparatus named TARG-DECH1 and TARG-DECH2—acronym for Test Apparatus for Response of Gravity-Driven Effects in Convective Hydraulics—were designed and constructed to study various flow regimes at low Reynolds' numbers. Such flows are induced by variations of density between different fluid stages (immiscible phases) contained within a cavity. A variety of instability mechanisms (such as fingering and encapsulation instabilities) and, sometimes, chaotic behavior can be observed.

In their study of fingering instabilities, using a Hele-Shaw cell, Bensimon, Kadanoff et al. (1986) pointed out that: *i)* the prediction of the motion of the interface separating two fluids is still an unsolved problem, despite the apparent simplicity of the low Reynolds' number flow regimes; *ii)* a chaotic behavior ("turbulence") is often observed in the limit of small surface tension.

Hele-Shaw cells were initially designed to permit potential flow visualization, Hele-Shaw (1898a); Hele-Shaw (1898b); Hele-Shaw (1898c); Hele-Shaw (1898d); Hele-Shaw and Hay (1900); Reynolds (1898); Stokes (1898). More recently they became an excellent tool to study the growth and development of fingering instabilities, Bensimon, Kadanoff et al. (1986); Homsy (1987); Park, Gorell et al. (1984); Paterson (1981); Saffman (1986); Taylor and Saffman (1958). On the other hand, the TARG-DECH was developed to canvass a different class of instability phenomena—named *encapsulation instability* —that leads to transversal viscosity stratification, i.e., in-plane flow of immiscible fluid layers stratified across the gap width.

The encapsulation instability is the tendency of lower viscosity fluids to encapsulate a higher viscosity fluid—detaching the higher viscosity fluid from the walls and considerably reducing its apparent viscosity. The encapsulation instability phenomena has

been previously addressed in the following areas: multilayered flows, White and Lee (1975); Yih (1967); Yu and Sparrow (1967), polymer flows, Everage (1973); Everage (1975); Lee and White (1974); Lee and White (1975); MacLean (1973); Williams (1975), and lubrication, Coyne and Elrod (1970). Also, in the initial studies of fingering, Chuoke, Meurs et al. (1958); Saffman and Taylor (1958); Taylor and Saffman (1958), addressed the possibility of a displaced fluid to form a layer between the walls and the displacing fluid. Nevertheless, the thickness of the fluid layers and its formation from a stable configuration were not pursued.

Recently Weinstein, Dussan et al. (1990), taking advantage of developments in moving contact line modeling over the last decade, tackled the formation of multiple fluid layers as a moving boundary-value fingering problem. Though, their analysis had to be restricted to the limit of small capillary numbers (directly proportional to the average interface velocity and displaced fluid viscosity, and inversely proportional to the interfacial tension).

There is a clear distinction between fingering and encapsulation—in-plane versus transversal instability. Yet Saffman (1986), in a literature review of fingering, classified possible boundary conditions in the transversal direction as; *i)* idealized, *ii)* realistic static; and *iii)* realistic dynamic. Saffman's realistic dynamic boundary condition corresponds to a *reversed* encapsulation instability.

Curiously, the fingering literature addresses only an effect opposite to the encapsulation instability, i.e., a less viscous fluid (the displacing fluid) being encapsulated by a more viscous fluid (the displaced fluid). The incorporation of the reversed encapsulation instability phenomena into the study of fingering proves to be a difficult task, and only simplified analysis exists that assimilate the size of the fluid layers as a parameter.

4-2 Design of the TARG-DECH

The physical situation of interest is the displacement of a lower viscosity and lower density fluid(s) by a higher viscosity and higher density fluid(s). Since in hydraulic fracturing the movement of different fluid stages, driven by density variations within the

fracture cavity, is of paramount importance, the TARG-DECH was developed to study:

- how fast the fluid layers carrying proppant move within a cavity
- how thick they are.

Also, to verify experimentally the viscous energy dissipation criteria and corresponding algorithms from **Chapter 2** (predicting the thickness of each fluid layer and the speed at which they move).

Although studies on the stability of multi-layer flows are available, Ripa (1991); Yih (1967), there is no agreement on the criteria used to establish the conditions for the onset of the encapsulation instability, as well as its properties (e.g., thickness of each layer). Consequently, the TARG-DECH provides direct experimental evidence on the accuracy and suitability of part of the theoretical and numerical developments presented in Chapters 3.

The design of the TARG-DECH relied on preliminary calculations that estimated the magnitude of the forces affecting the fluid flow —surface tension, friction (viscous dissipation), gravity and buoyance— obtained with the simulator described in Chapter 2. Ultimately, the apparatus' physical dimensions should provide an adequate time range to record the data, and take pictures of the fluid stages motion. Also, to permit the formation of a well defined blob, the injection rate of each fluid stage should be fast relative to the downwards flow field velocity.

Henceforth, the fluid stage initially filling up the TARG-DECH cell is denominated the *primary* fluid-stage. The first fluid-stage blob injected is denominated the *secondary* fluid-stage, the second fluid-stage blob injected is the *tertiary* fluid-stage, and so on.

Two apparatus were built:

1) TARG-DECH1 – first apparatus built. Used to understand the qualitative behavior of multiple fluid stages motion within the cell. TARG-DECH1 provided an invaluable insight on the existence of the encapsulation mechanism

and the importance of wetting conditions.

2) TARG-DECH2 – all quantitative results presented in this Chapter (Figures **4-6** through **4-56**) were obtained from TARG-DECH2.

4-3 TARG-DECH1

TARG-DECH1 consists of two square parallel plates, with varying spacing between them, measuring 43.18 cm each, and made out of Plexiglass (PMMA) for flow visualization. It is similar to a vertical Hele-Shaw cell (transversal gap width much smaller than in-plane width or height), with a back plate radial source to simulate a wellbore (See **Figure 4-1** on **Page 89**). The back plate is 2.54 cm thick with a groove, measuring 1.27 cm wide by 1.91 cm deep, and cut 5.08 cm from the outside perimeter (See **Figure 4-2** on **Page 90**). The front plate is 1.27 cm thick with a protruding spacer that fits snugly within the back plate groove, permitting a variation of the transversal gap width with respect to the front plate. An O-ring seal (running along the spacer outer surface), and a Foamex gasket (affixed to the base of the groove and reinforced with silicone sealant) obstruct fluids from leaking outside the cell. Two configurations of interest can be simulated; a vertical parallel cavity, and a vertical wedged cavity.

Spacing between the two plates is controlled by a system of screws, clamps and metal spacers. The transversal gap width can be made either constant or wedged, along the in-plane coordinates, by changing the top and bottom spacers. The apparatus is held together by a set of four bolts, and aluminum reinforcements are used to prevent warping of the plates due to unequal tension applied to the bolts. The front plate aluminum reinforcing frame (See **Figure 4-3** on **Page 92**) is hinged to an horizontal bottom wood platform, which supports the whole apparatus. The back plate is supported by a heavy metal block and an aluminum frame, both bolted to the same platform. To avoid large deformations, a secondary set of small spacers is located at convenient positions between the two plates. Measured variations of spacing—using an indicator table—are less than 10% of the separation gap.

The following set of gap spacers—all with a machining tolerance of less than ±

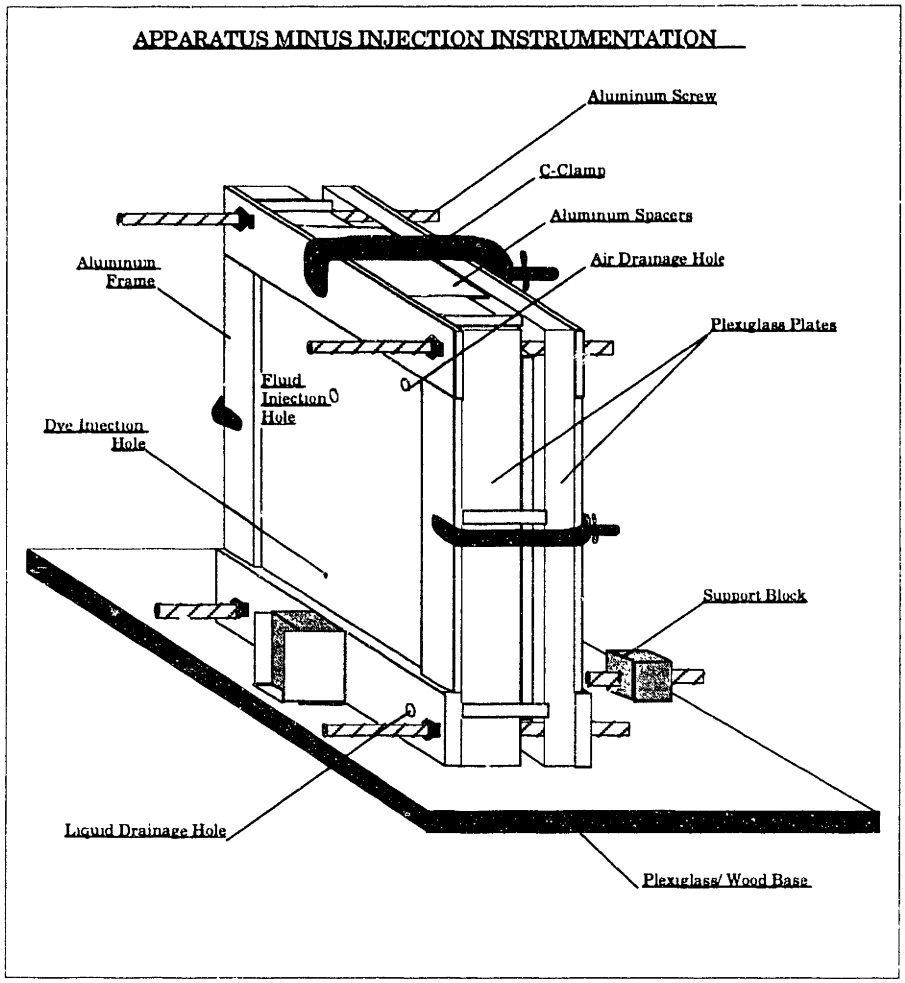

FIGURE 4-1: Sketch of the assembled TARG-DECH1

0.08 mm—were built: 25.4 + 1.02 mm, 25.4 + 2.03 mm and 25.4 + 10.16 mm. For each spacer: the first number (1") represents the back plate groove top-to-bottom distance; and the second number is the gap space between the two plates.

A set of four holes, of different sizes, were drilled in the backplate. A central hole 0.85 cm in diameter, is connected to a cross-connector. Two Swagelock bidirectional valves and one unidirectional valve are linked to the connector allowing the injection of 5 different fluid stages, in addition to the primary fluid stage (See **Figure 4-4** on **Page 94**). A hole on the upper right corner is used for air drainage during the primary fluid-stage filling, and a hole on the lower right corner is used for drainage after the exper-

iment is completed. Both holes are obstructed during the experiment. A fourth very narrow central hole, located 22.86 cm down from the injection hole, is used for injection of dyes or coloring agents, which permits visualization of the streamlines around the falling blobs. Usually a mixture of the primary fluid stage and dyes at a temperature higher than the temperature of the fluids used in the experiment, is employed. This mixture tends to flow to the top of the cell, encountering the falling blobs on its way upwards, and creating an approximate streamline path around the blobs.

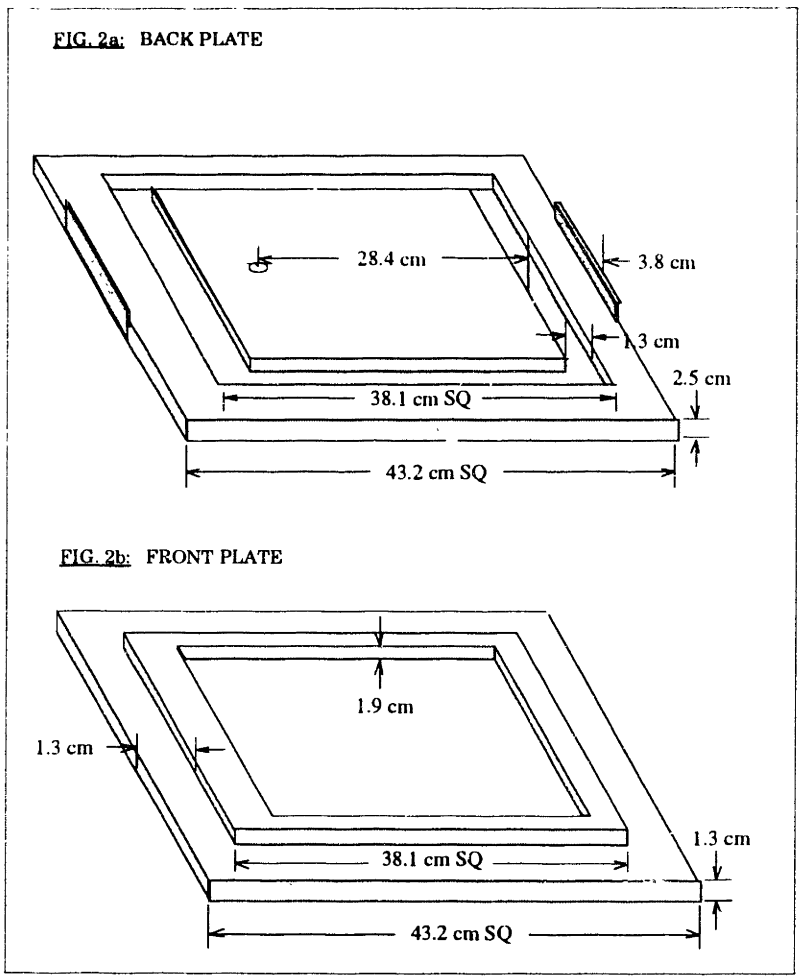

FIGURE 4-2: TARG-DECH1 back (a) and front (b) plates

One of the concerns during the design phase was on how easily would the apparatus be cleaned after each experiment. An easy setup for assembling, disassembling and

cleaning would considerably reduce the turnaround time. The assembling and disassembling turns out to be relatively fast (3-5 minutes each), however the cleaning takes much longer — between 20-25 minutes.

In hydraulic fracture the mix of proppant particles to the injected fluids/gels is necessary in order to maintain the crack opened after the fracturing treatment. The ideal proppant would be a reasonably sized particle (of order one millimeter in diameter, e.g., 20/40 mesh size), extremely resistant, very cheap and with specific weight close to the unity. Unfortunately, the above combination is very difficult to achieve.

The most used proppant particles are: sand for shallow reservoirs; resin coated sand or Clay/Silica/Alumina for intermediate depths; and Alumina/Bauxite for deeper reservoirs. Also, Zirconia and Silicon Carbide are used for special purposes. Sand has the advantage of being cheap and its specific weight is of order 2.7, although not very resistant. The intermediate compounds are more resistant against crushing, but present a higher specific weight — between 3.0 and 3.2. Pure Alumina has a specific weight of 3.98, and the Alumina/Bauxite mix is about 3.7.

The solely purpose of mixing particles to the fluid stages while running experiments with the TARG-DECH1 is to increase the specific gravity of the mixture (ergo controlling the driving force). Although the particles (mixed to fluid and/or gels) used in the TARG-DECH1 will be loosely referred as "proppants", a series of observations ought to be made:

- *convective velocity vs. settling velocity* – In hydraulic fracturing treatments typical average crack opening sizes are in the range of 1 to 10 cm, and proppant sizes of order 1 mm. Except for unusual situations, such as very tight crack openings or the use of large proppant particles, the convective motion is the dominant physical mechanism, responsible for proppant transport within the fracture. So, the "proppant" movement within the fluid/gels—proppant settling—in the TARG-DECH1 is disregarded. Since the TARG-DECH1 minimum gap size is 1 mm, the diameter of the "proppants" used should be scaled down. A variety of small diameter particles have been used—80 μm

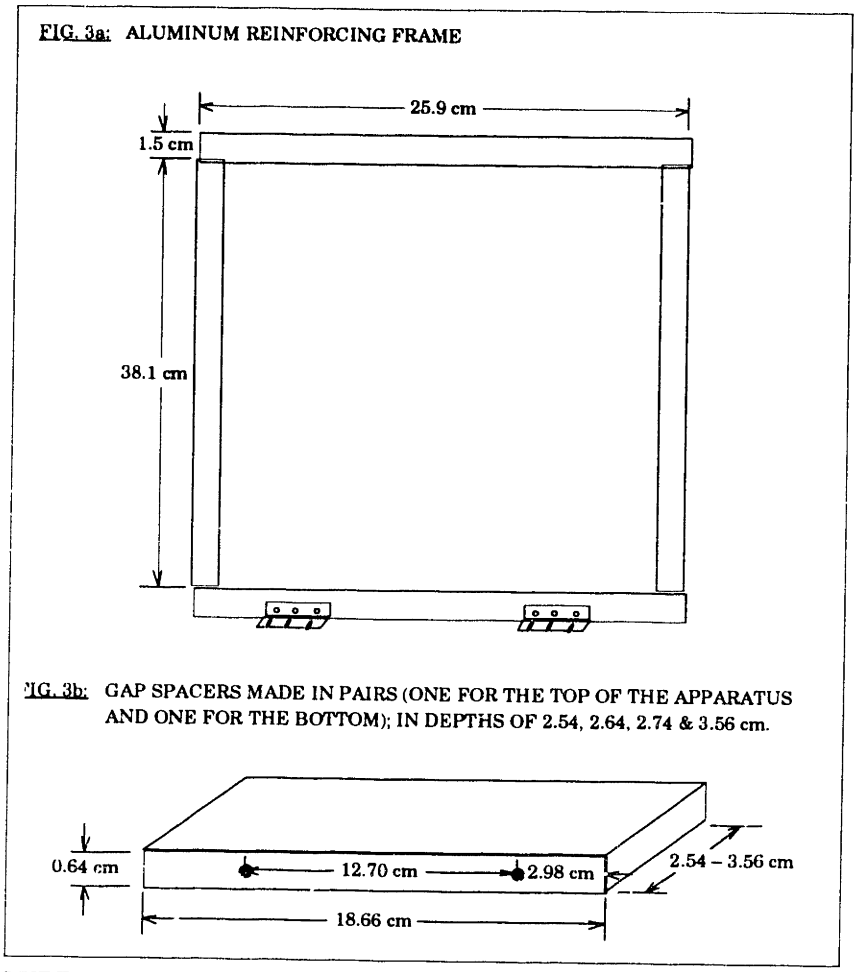

FIGURE 4-3: TARG-DECH1 aluminum reinforcing frame (a) and gap spacers (b)

Silicon Carbide, 15 μm Zirconia, 5 μm Tungsten and 10 μm Alumina. Hereafter, for the TARG-DECH1 experiments, the word proppant means particles sizes of at most 100 μm.

- *dispersion* – The above referred particles don't dissolve in water without the use of dispersants, however they disperse very well in Silicone fluids and Ethanol based Cellulose gels. This is a plus for running the experiment, since we can use water as the primary fluid and variations of the Silicone fluids and Celluiose gels to contain the proppants.

- *injection velocity vs. convective velocity* – To permit the formation of well-

defined blob shapes, the injection velocity should be always higher than the convective average velocity field. This is particularly important in the TARG-DECH1 since it also relies on visual data acquisition (pictures) to track down the movement of the fluid blobs. Based on the TARG-DECH physical dimensions and used gap sizes, the projected injection rate velocity should be faster than 0.07 m/s, and the estimated average convective velocity should not exceed 0.01 m/s. The use of proppants usually increases the apparent viscosity of the fluid blobs, and, in turn, allows a better control of the downwards fluid movement.

- *non-abrasive particles and non-corrosive liquids* – One of the drawbacks of using PMMA as the cell container is its susceptibility to abrasion (by large mesh particles) and corrosion (by acetones and most of the petroleum based chemicals). Hence, the use of particles with diameters 100 μm or less is a necessity. As a matter of fact, those fine particles behave like a polisher when in contact with the cell surfaces.

- *cleaning* – Although finer proppant particles are easier to disperse and needed to operate the TARG-DECH1, they impose a small handicap; cleaning of the injection lines and injection instrumentation is cumbersome.

In summary, the TARG-DECH1's design goals are the following: *i)* use of a gravity driven —as opposed to pressure driven— fluid motion; *ii)* ability to track the various fluid-fronts and interfaces; *iii)* provide a quantitative measurement of multiple fluid stages motion and dispersion within a narrow channel; *iv)* offer a qualitative understand of the parameters affecting the fluid motion, i.e., when, why and how encapsulation will occur; and, in case an encapsulation instability develops, *v)* provide a quantitative measure on how fast the fluid blob will move, due to the detachment of the heavier and more viscous fluid from the cell walls.

4-4 Operation of the TARG-DECH1

Three physical properties measurements, described below, are required for the operation of the TARG-DECH1

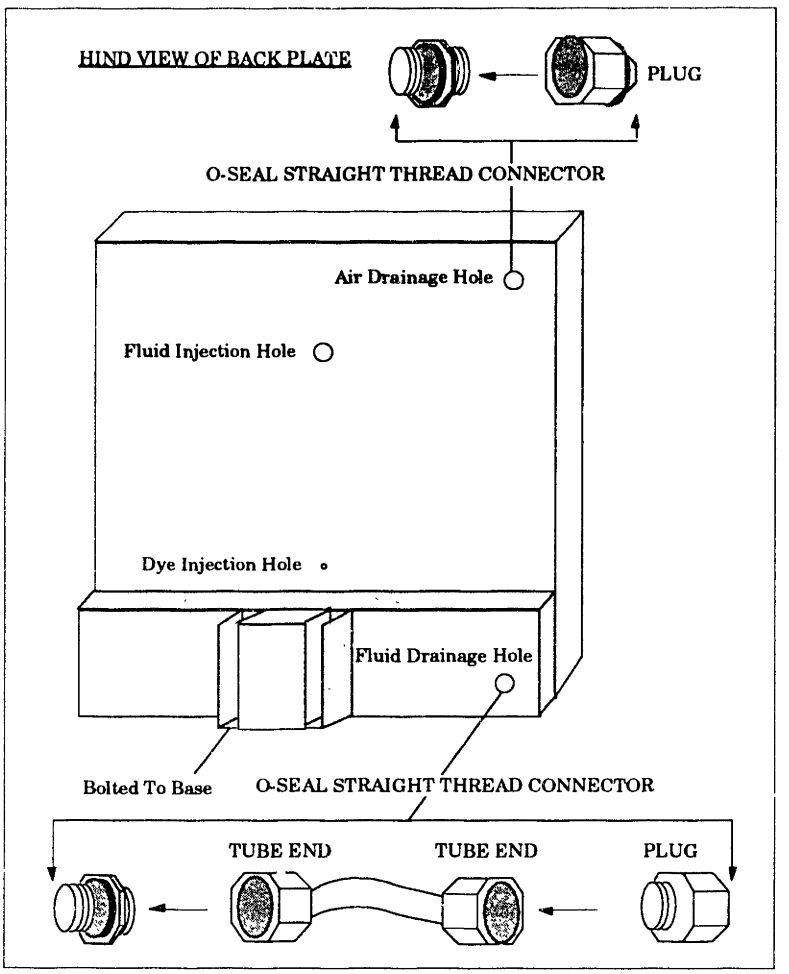

FIGURE 4-4: TARG-DECH1 back plate (supported) and fluid injection gear

- *density* – Using distilled water and Dow 200 Silicone a container was calibrated to measure the density of fluids and mixtures. An accurate scale, with readings of 1/10000 of a gram, is used to weigh the container and its contents. In average an accuracy of at least 0.5% is expected. The two main causes for inaccuracies are; variations in room temperature, and the dependence on visual acuity to read the fluid/mixture volume level from the container.

- *surface tension* – Initially the Wilhelmy slide method. Adamson (1967), was employed. This method consists on; balancing a very thin lamina (for instance a microscope glass cover) by means of a lever based scale, introduc-

ing the lamina inside of the fluid/mixture, and adding weights to the other side of the scale until the lamina withdraws from the fluid/mixture. Using distilled water for calibration, the error range was 3–10%. Since a rudimentary scale (built in-house) was used, it was difficult to control the accretion of weights to the balancing side of the lever. Moreover, the Wilhelmy method does not provide any information about surface tension measurements of multi-fluids interfaces. Another method—the Drop method—was adopted. The Drop method consists in introducing a probe (such as a pipet with known inner and outer diameter) holding a fluid A, within a pre-weighed container filled with a fluid B. Then, a counted number of drops of fluid A are injected into the fluid B container, and the container's final weight is measured. Utilizing a chart that corrects for variations of drop shapes as a function of the probe drop wetted diameter and the drop volume (and accounting for the specific weight of both fluids), the fluids A/B interfacial surface tension is obtained. Using distilled water and Dow 200 Silicone fluids for calibration, the achieved error range for the Drop method was 2–4%.

- *viscosity* – A set of two Cannon-Fenske 1600-8000 cSt viscometers were calibrated using the ASTM S2000-Cannon standard in the range of 20 to 40°C. Since the S2000 standard is strongly dependant on temperature variations (1/100°C), a variety of special procedures had to be employed during calibration, e.g., room controlled temperature and a "constant" temperature bath. Also, a small Mathematica™ algorithm was written to find the best fit to the values of viscosity as a function of temperature in the range of 20 to 40°C (the S2000 standard is provided with viscosity values only at 20, 25, 37.78, 40, 98.89 and 100°C). **Figure 4-5**, shows the resulting equation and its coefficients. To obtain the above results a modification of the ASTM D341-74 charts, assuming kinematic viscosities above 3.0 cSt, was employed. A procedure described in ASTM D445-88 was then used to obtain the calibration constants for each viscometer — 6.26 and 7.99 cSt/sec. The resulting calibration constants were estimated to within 0.3%.

One drawback of the method employed for measuring the kinematic viscosity is

the inaccuracy introduced when utilizing opaque liquids — the method is only accurate for clear liquids with kinematic viscosities in the viscometer original range. However, tests made with various opaque fluids and mixtures indicate that a 2–3% error can be achieved.

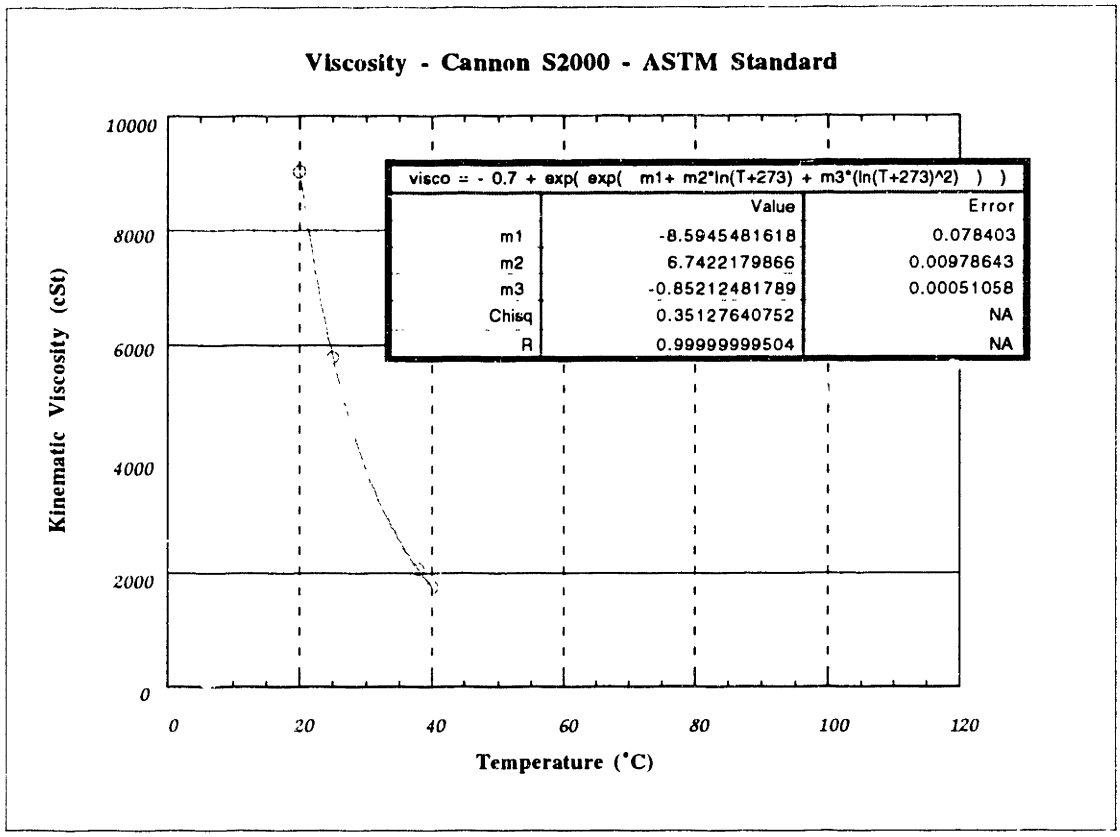

FIGURE 4-5: Viscosity versus temperature for ASTM Cannon S2000 viscometer standard. Coefficients and best fit equation included

The procedure to operate the TARG-DECH1 (parts are described in **Figure 4-1**) is the following:

1) The top aluminum spacer (B) and the upper reinforcement frame (A) are put together. Subsequently, the bottom aluminum gap spacer (B) is inserted inside a cavity under the back plate. The bottom spacer rests against a vertical aluminum reinforcement plate that supports the whole apparatus. The spacer selection will define the test to be run, i.e., the cavity will be wedged if spacers

of different size are used for top and bottom slots. The cell channel can be wedged either with increasing or decreasing downwards slopes. Though, only constant channel and decreasing downwards wedged gaps were tested. Then, the other aluminum reinforcements (C and F), and the smaller gap spacers (E) are simultaneously clamped (G). Finally the bolts (D) and the front large screw (H) are tightened.

2) Before final assembling, a paper marked with a total of 11 horizontal equally spaced lines (2.54 cm apart), is taped to the posterior surface of the back plate. The paper grid layout provides a set of markers used for pictures, i.e., each picture is taken when the leading edge of the falling blob(s) is about to cross one of the horizontal lines. Also, a chronometer, taped against the front plate, is used to register the elapsed time since the beginning of the experiment. Hence, in the resulting pictures, the velocity and the shape of the blob(s) can be obtained as a function of time.

3) Pictures taken from different experiments can be digitized and compared, since a fixed frame sets the distance and height of the camera with respect to the apparatus.

4) After the apparatus is assembled, the cell is filled with the primary fluid through the central injection hole. A permanent pressurized reservoir stores the primary fluid, and the injection rate is controlled by a pressure gauge. The secondary (tertiary, etc.) fluid(s) is injected with a syringe. In order to insure repeatability, the dead volume within the injection gear is subtracted from the total volume of fluid to be injected.

5) Once the experiment is finalized, the cell is emptied by attaching a pressure line to the top air-drainage valve and opening the bottom fluid-drainage valve. Disassembling takes less than 5 minutes, but to clean the injection lines and the inside walls it takes about 25 minutes.

4-5 TARG-DECH2

TARG-DECH2 is an improved design version of TARG-DECH1, with two major modifications:

1) Higher energy surfaces for the inner walls—glass instead of plexiglass. Also, able to vary the wall roughness, i.e., two different plates used, float glass and frosted float glass (approximately 1/120" asperity);

2) Top part of the cell is open—allowing much easier handling and maintenance.

Figure 4-6 shows TARG-DECH2. The design is even simpler than TARG-DECH1. Except for wetting, surface and interfacial tension measurements utilizing a goniometer, all the remaining Figures demonstrate results from TARG-DECH2.

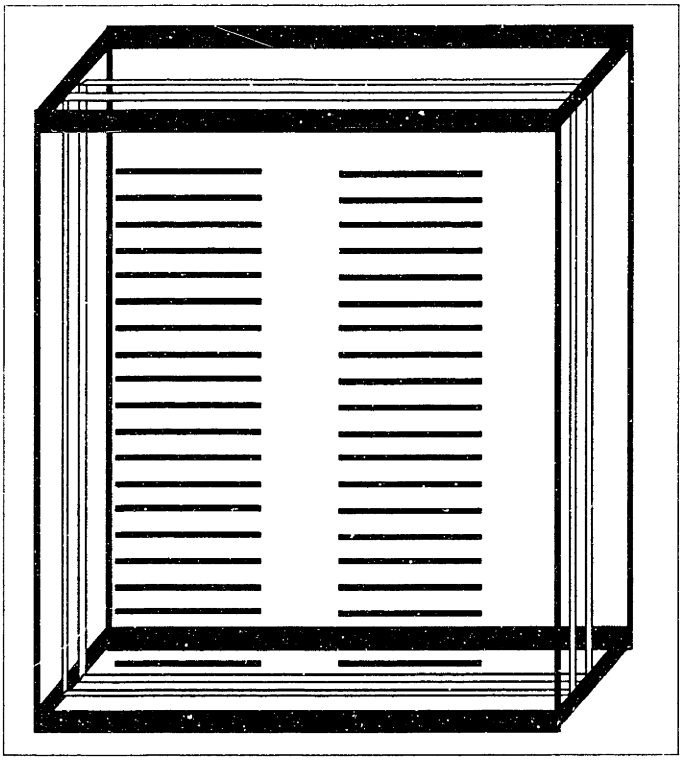

FIGURE 4-6: TARG-DECH2 container

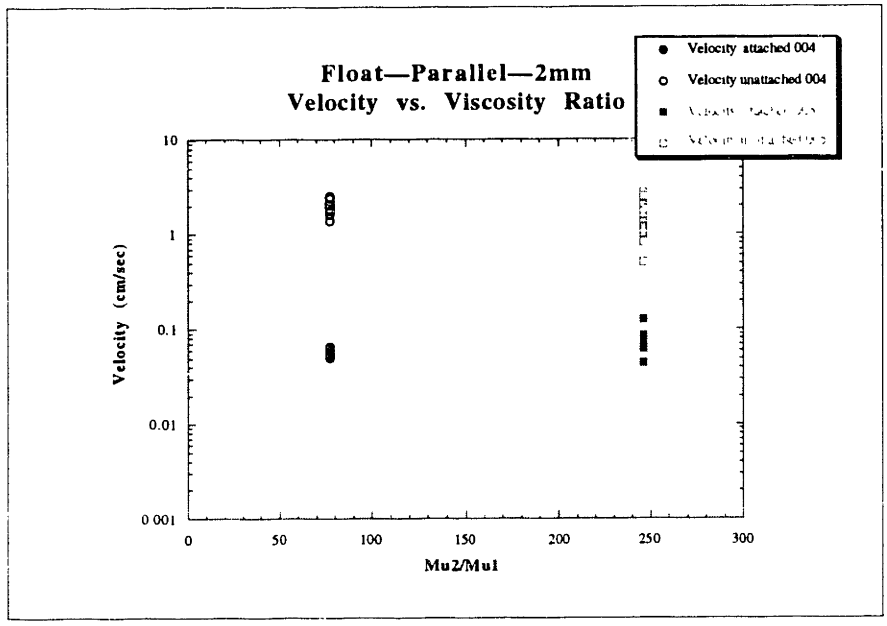

FIGURE 4-7: Experimental values of velocity vs. viscosity ratio—float glass/parallel plates/2mm

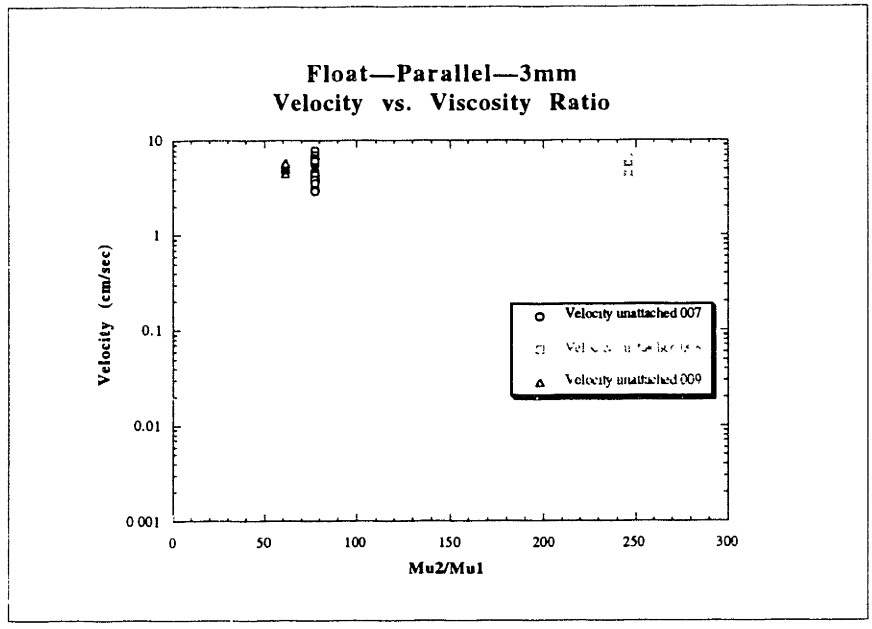

FIGURE 4-8: Experimental values of velocity vs. viscosity ratio—float glass/parallel plates/3mm

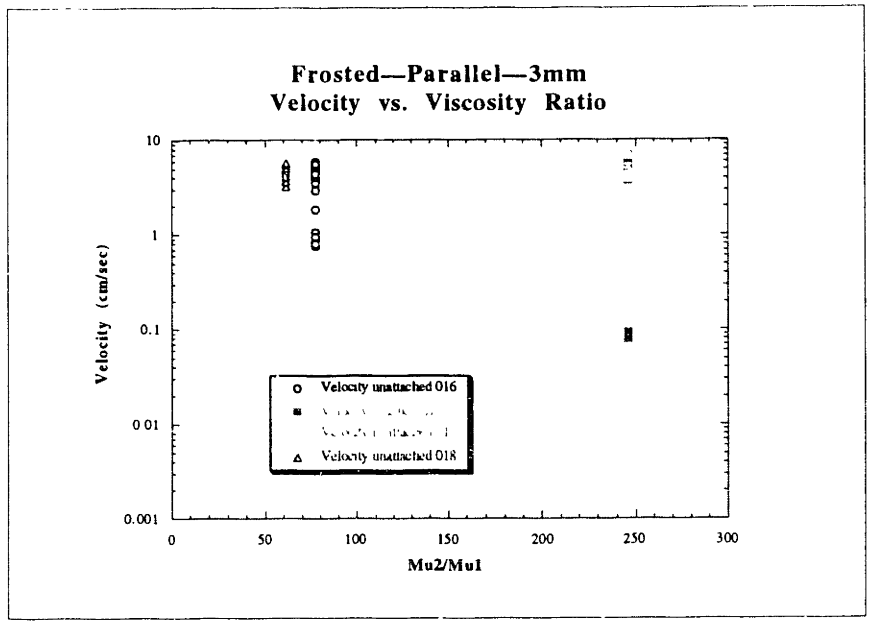

FIGURE 4-9: Experimental values of velocity vs. viscosity ratio—frosted glass/parallel plates/3mm

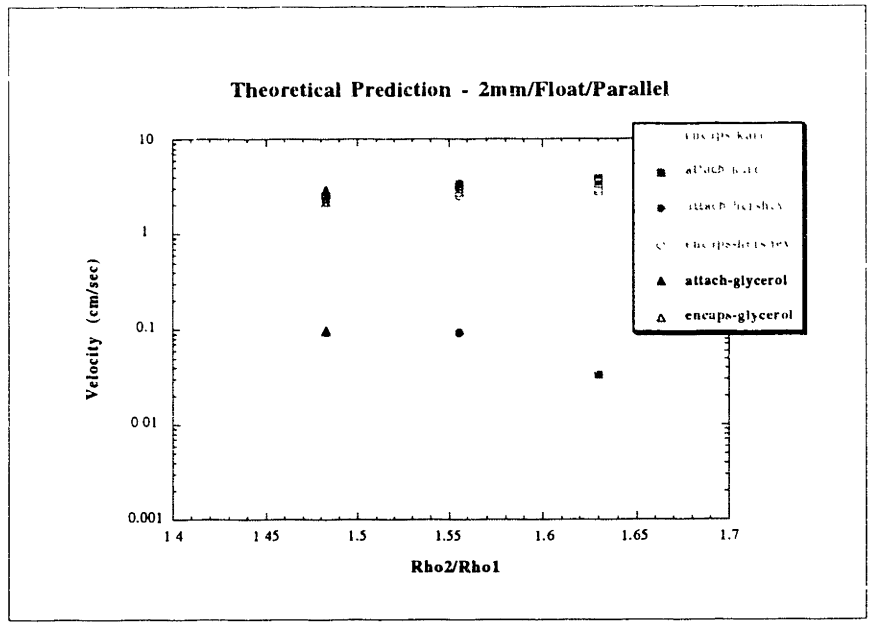

FIGURE 4-10: Theoretical values of velocity vs. density ratio—float glass/parallel plates/2mm

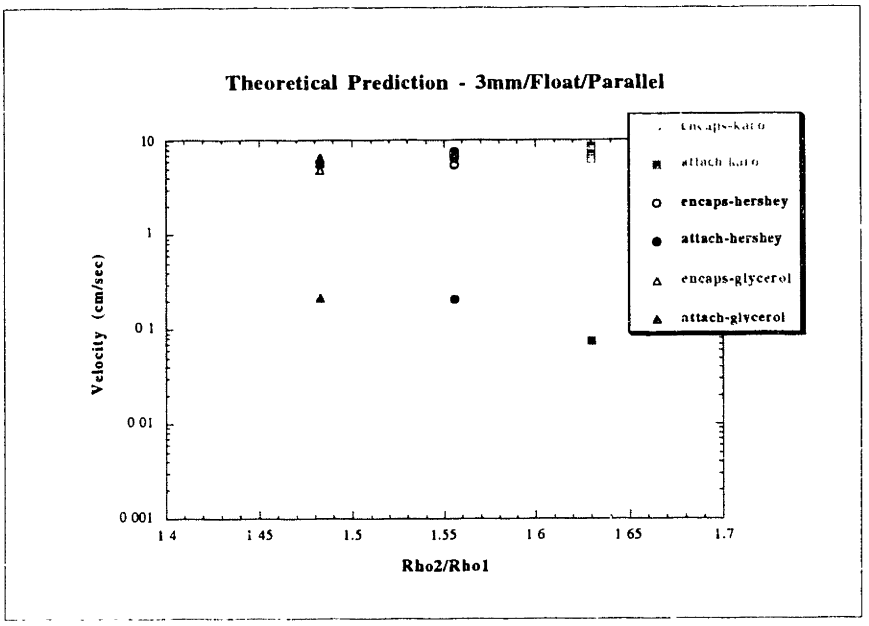

FIGURE 4-11: Theoretical values of velocity vs. viscosity ratio—float glass/parallel plates/3mm

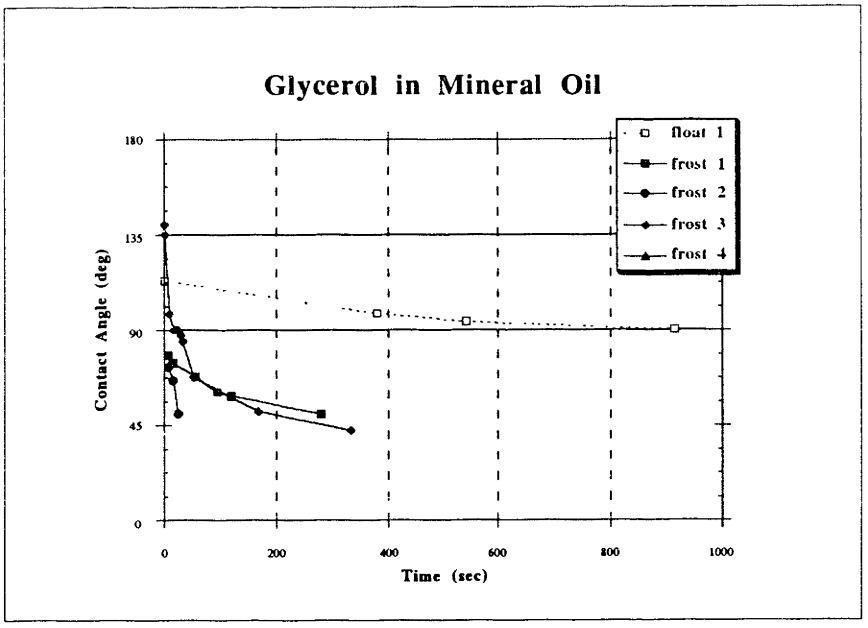

FIGURE 4-12: Glycerol in Mineral Oil contact angle spread—float vs. frosted glass

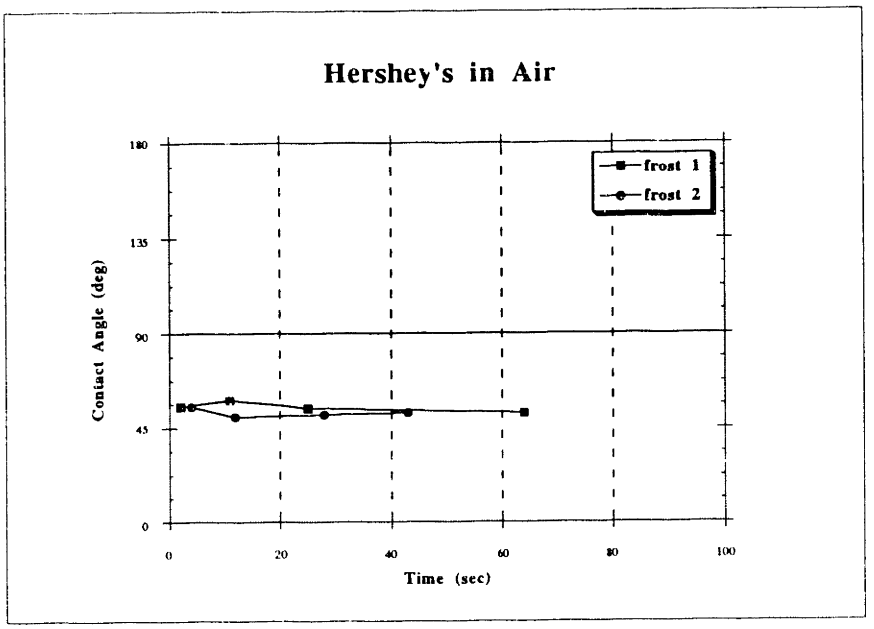

FIGURE 4-13: Hershey's in Air contact angle spread—frosted glass

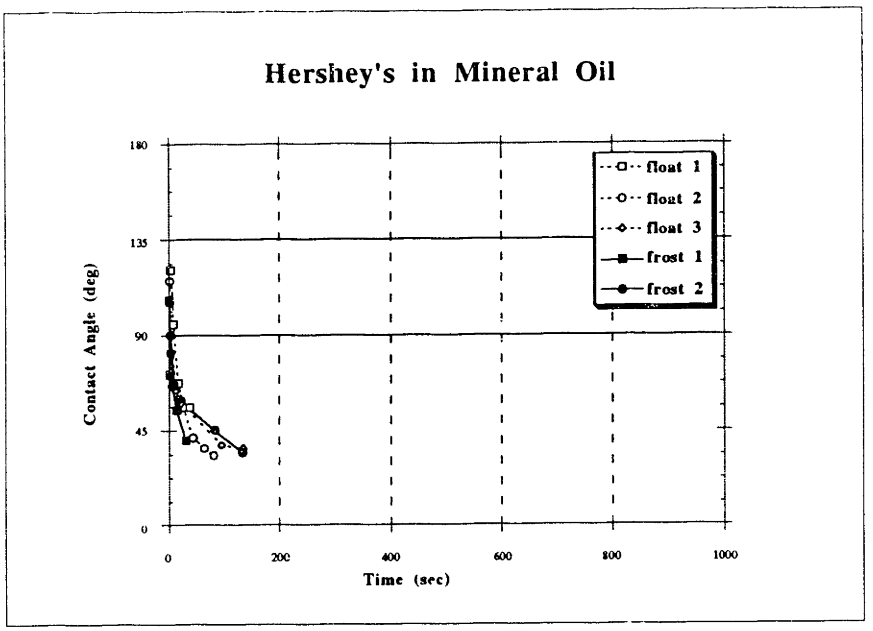

FIGURE 4-14: Hershey's in Mineral Oil contact angle spread—float vs. frosted glass

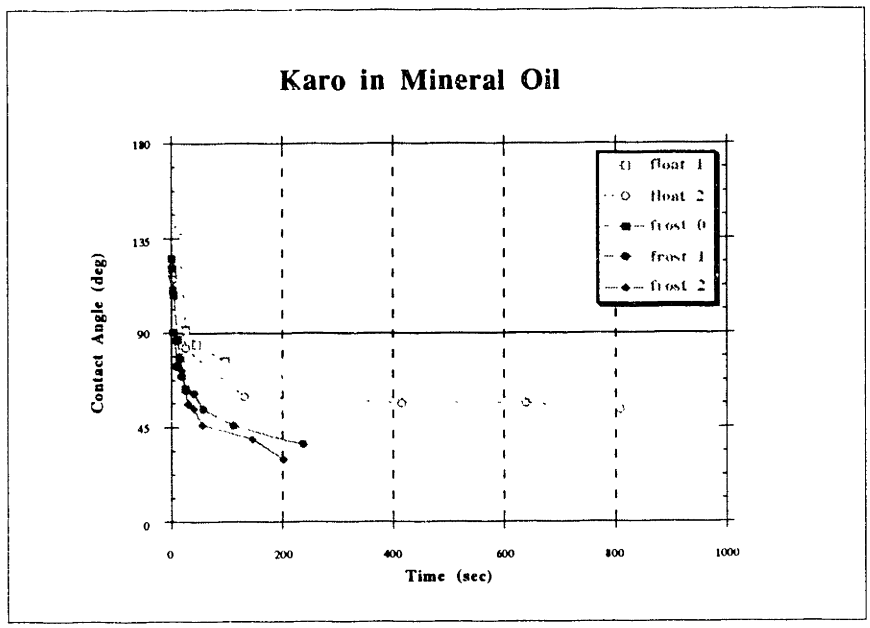

FIGURE 4-15: Karo in Mineral Oil contact angle spread—float vs. frosted glass

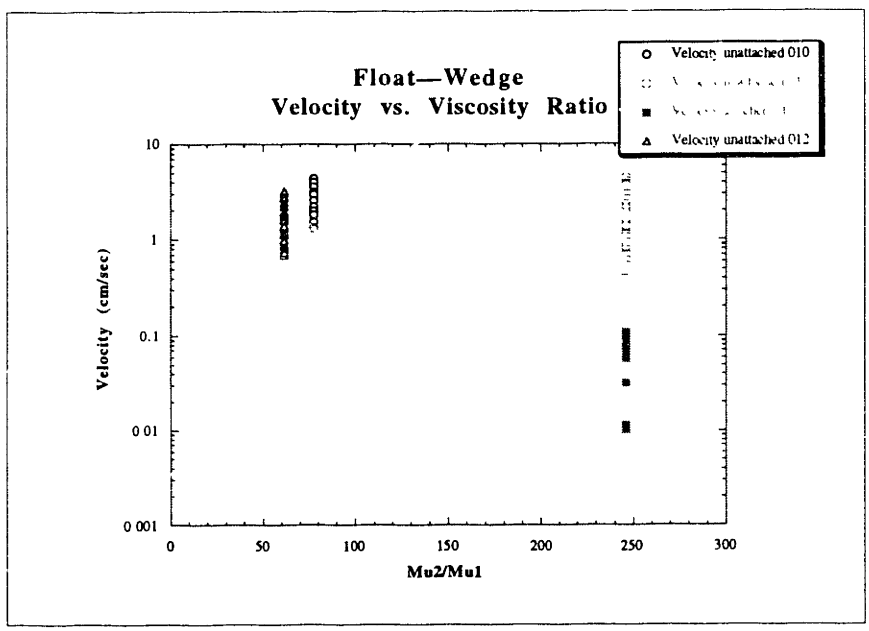

FIGURE 4-16: Experimental values of velocity vs. viscosity ratio—frosted glass/wedged plates

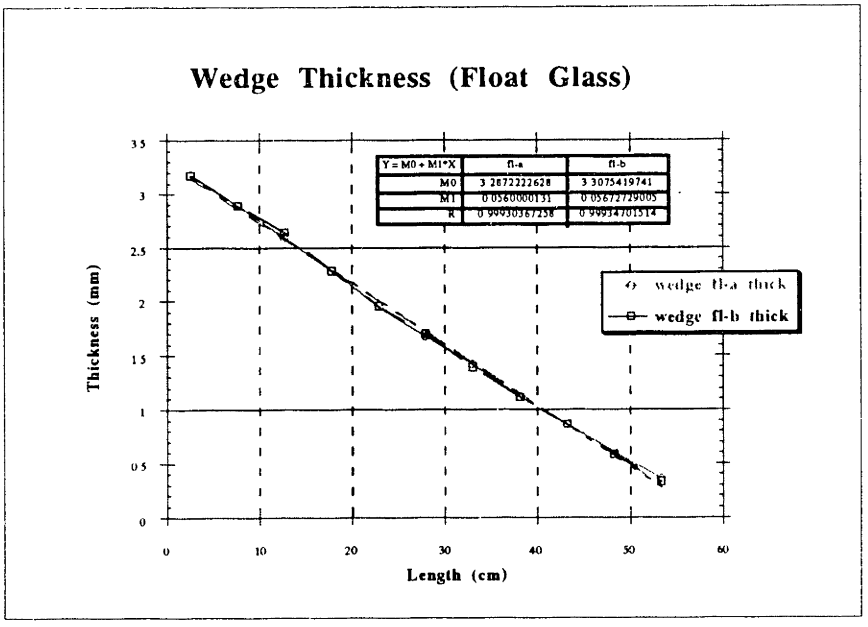

FIGURE 4-17: Measured wedge variation for float glass—prior to test

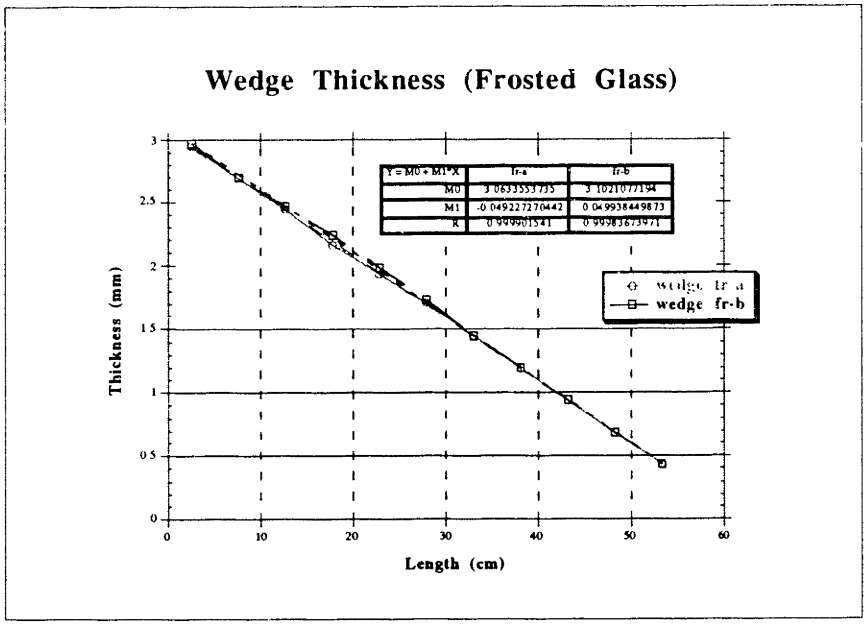

FIGURE 4-18: Measured wedge variation for frosted glass—prior to test

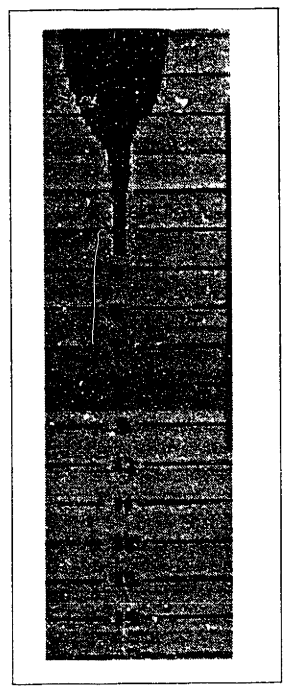

FIGURE 4-19: Sequence of blob movement—Hershey's in Mineral Oil, 2 mm gap. Attached blob

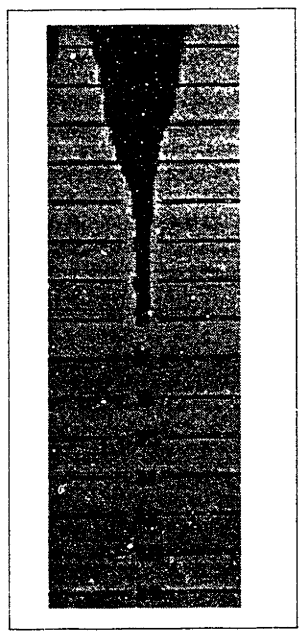

FIGURE 4-20: Sequence of blob movement—Hershey's in Mineral Oil, 2mm gap

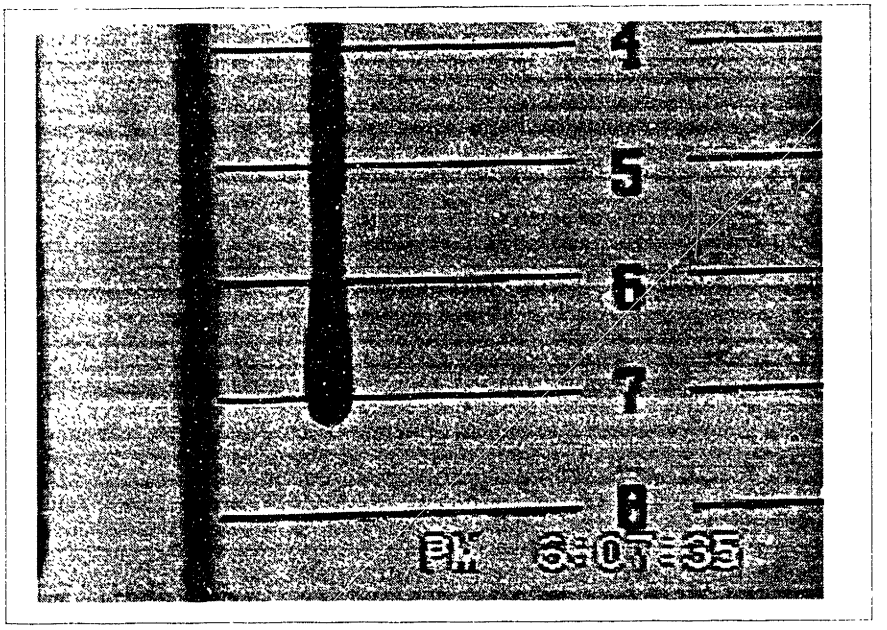

FIGURE 4-21: Sequence of blob movement—Karo in Mineral Oil. Wedged plates

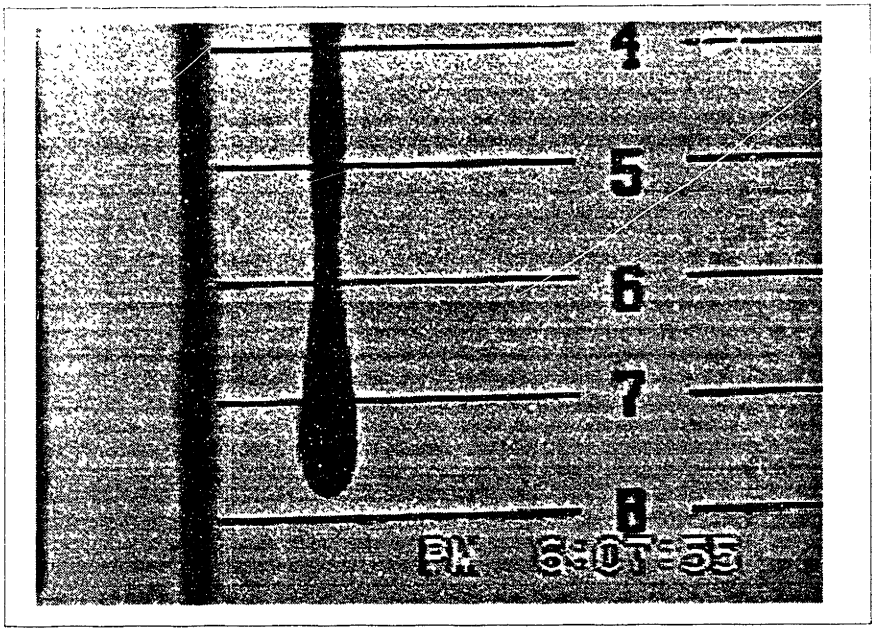

FIGURE 4-22: Sequence of blob movement—Karo in Mineral Oil. Wedged plates

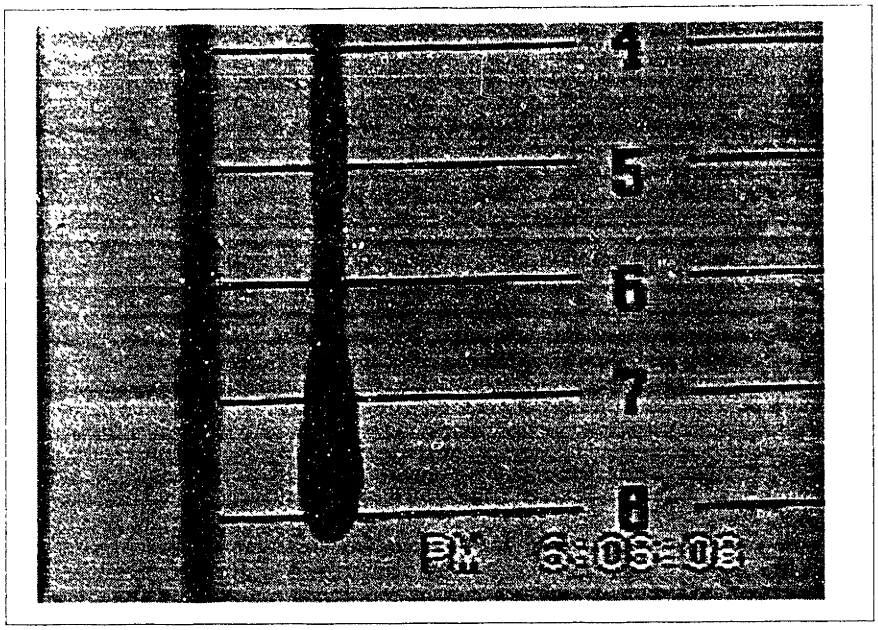

FIGURE 4-23: Sequence of blob movement—Karo in Mineral Oil. Wedged plates

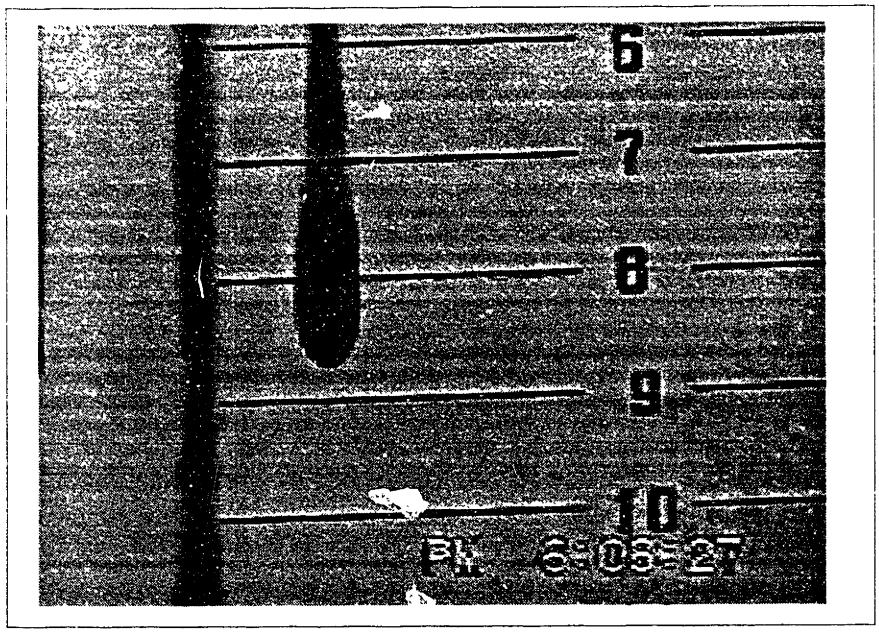

FIGURE 4-24: Sequence of blob movement—Karo in Mineral Oil. Wedged plates

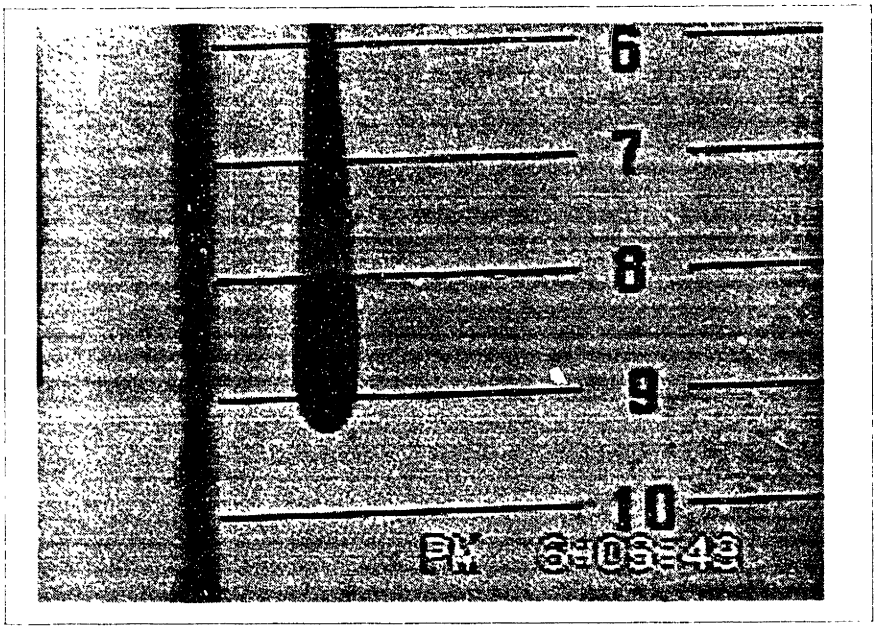

FIGURE 4-25: Sequence of blob movement—Karo in Mineral Oil. Wedged plates

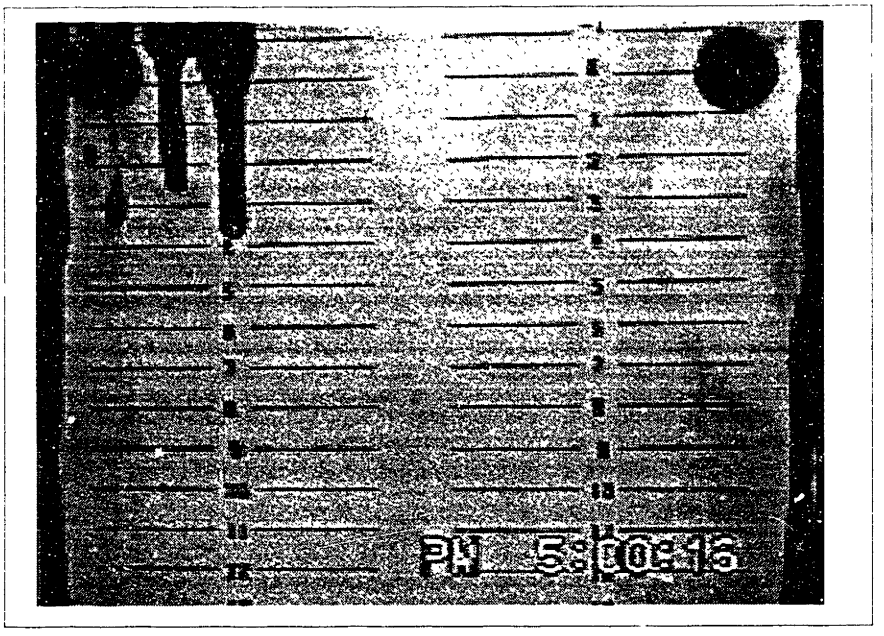

FIGURE 4-26: Sequence of blob movement—Hershey's in Mineral Oil, 2 mm gap. Frosted Plates

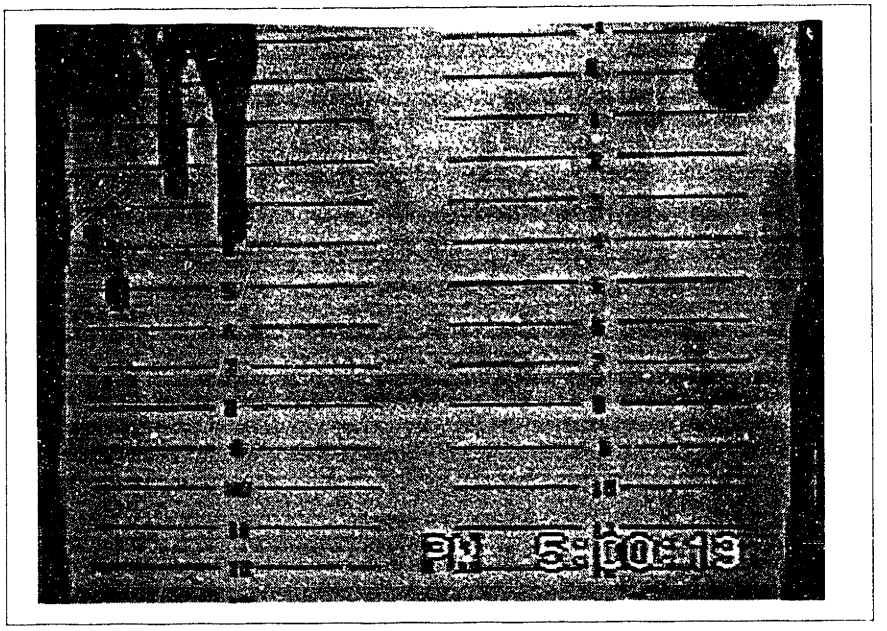

FIGURE 4-27: Sequence of blob movement—Hershey's in Mineral Oil, 2 mm gap. Frosted Plates

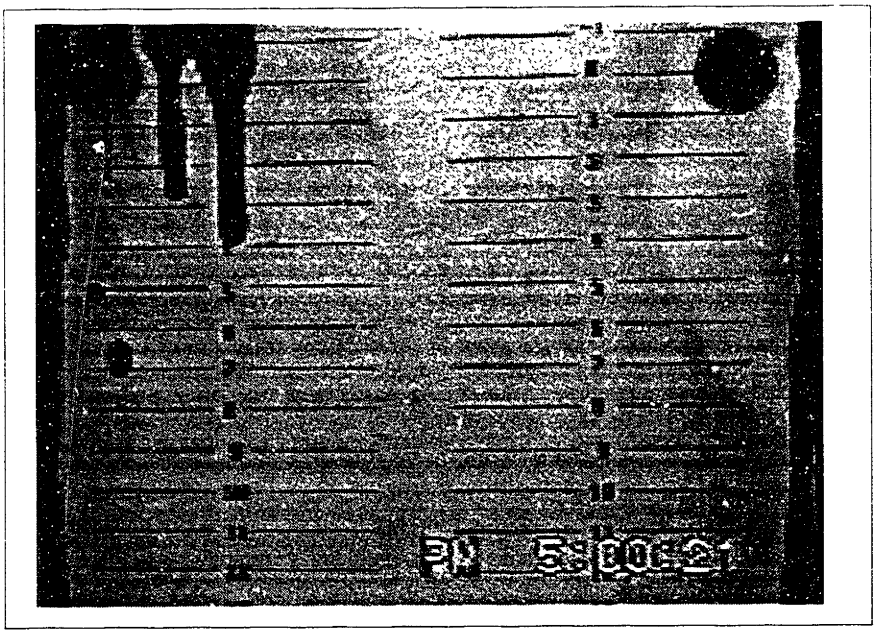

FIGURE 4-28: Sequence of blob movement—Hershey's in Mineral Oil, 2 mm gap. Frosted Plates

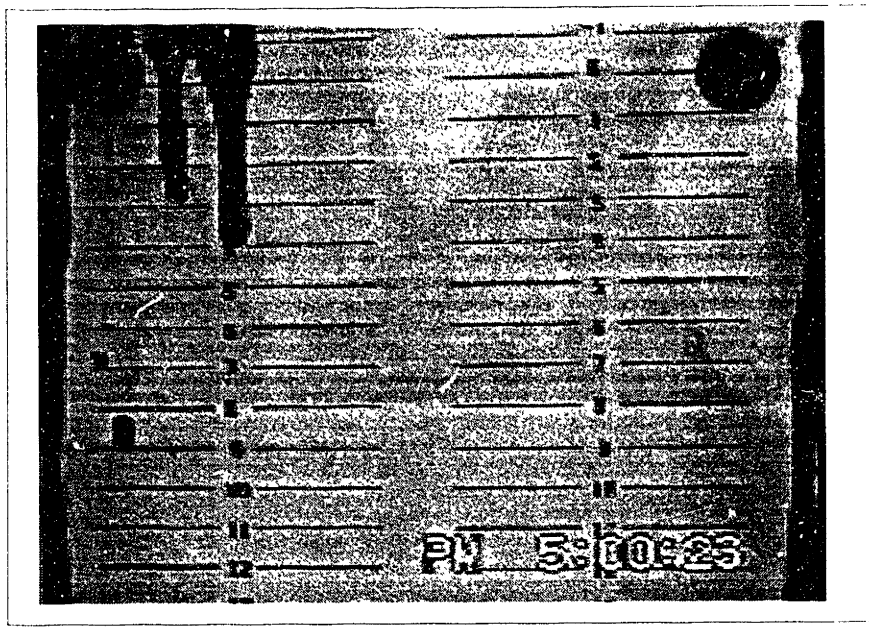

FIGURE 4-29: Sequence of blob movement—Hershey's in Mineral Oil, 2 mm gap. Frosted Plates

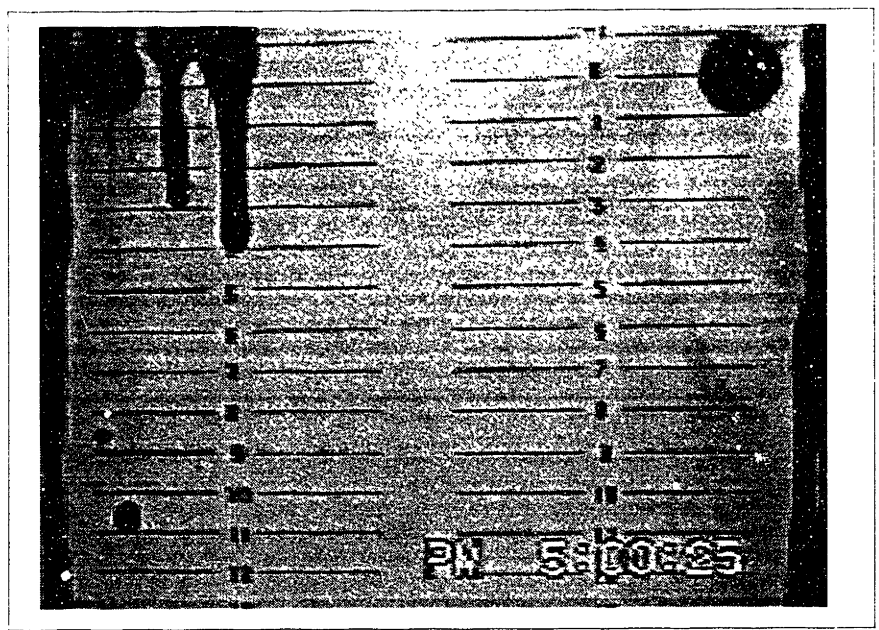

FIGURE 4-30: Sequence of blob movement—Hershey's in Mineral Oil, 2 mm gap. Frosted Plates

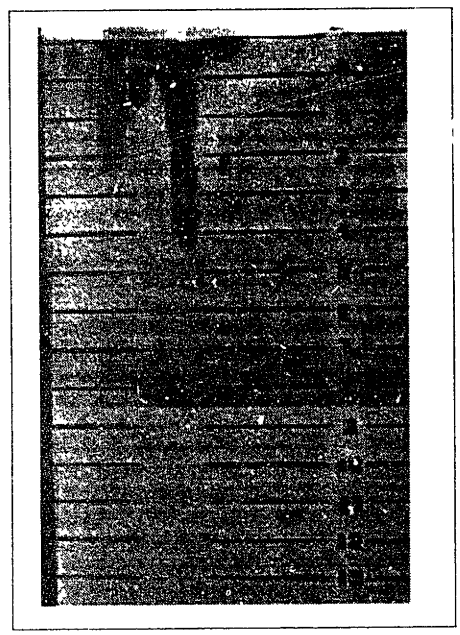

FIGURE 4-31: Sequence of blob movement—Karo in Mineral Oil, 2 mm gap. Frosted Plates

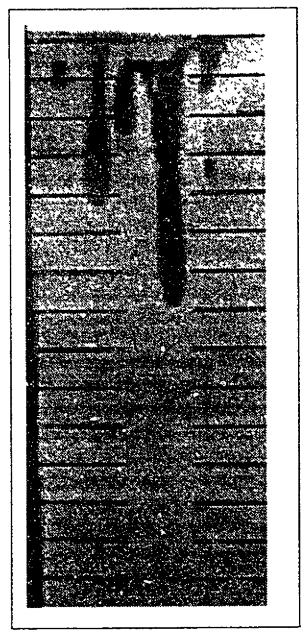

FIGURE 4-32: Sequence of blob movement—Karo in Mineral Oil, 2 mm gap. Frosted Plates

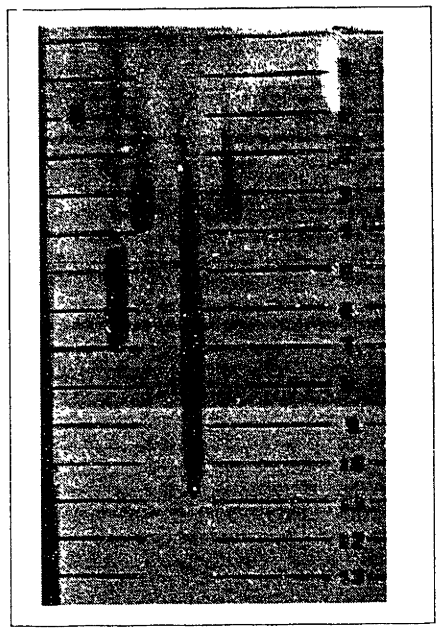

FIGURE 4-33: Sequence of blob movement—Karo in Mineral Oil, 2 mm gap. Frosted Plates. Notice prolated shape

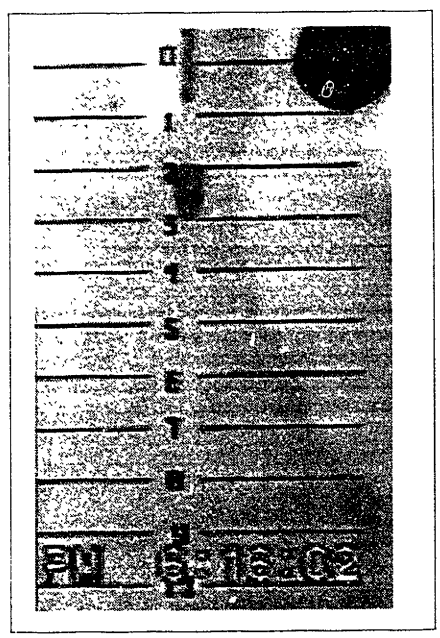

FIGURE 4-34: Sequence of blob movement—Glycerol in Mineral Oil, 2 mm gap. Frosted plates

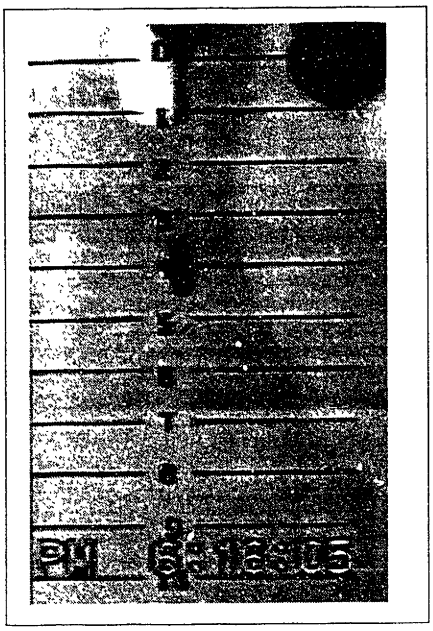

FIGURE 4-35: Sequence of blob movement—Glycerol in Mineral Oil, 2 mm gap. Frosted plates

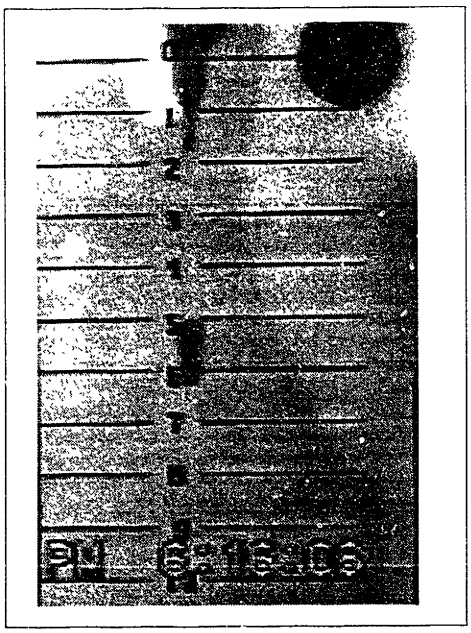

FIGURE 4-36: Sequence of blob movement—Glycerol in Mineral Oil, 2 mm gap. Frosted plates

FIGURE 4-37: Sequence of blob movement—Glycerol in Mineral Oil, 2 mm gap. Frosted plates

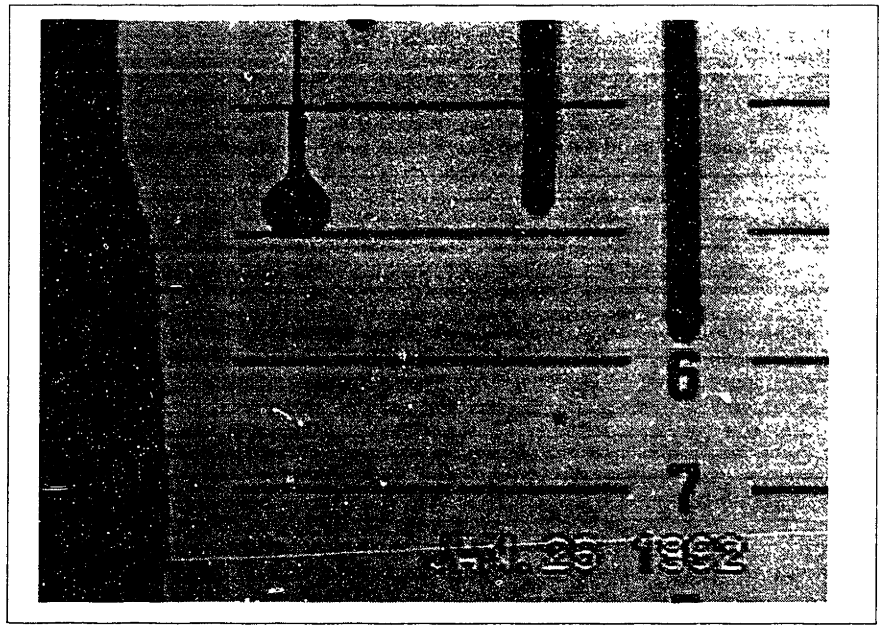

FIGURE 4-38: Sequence of blob movement—Hershey's in Mineral Oil, 3 mm parallel plates. Frosted glass

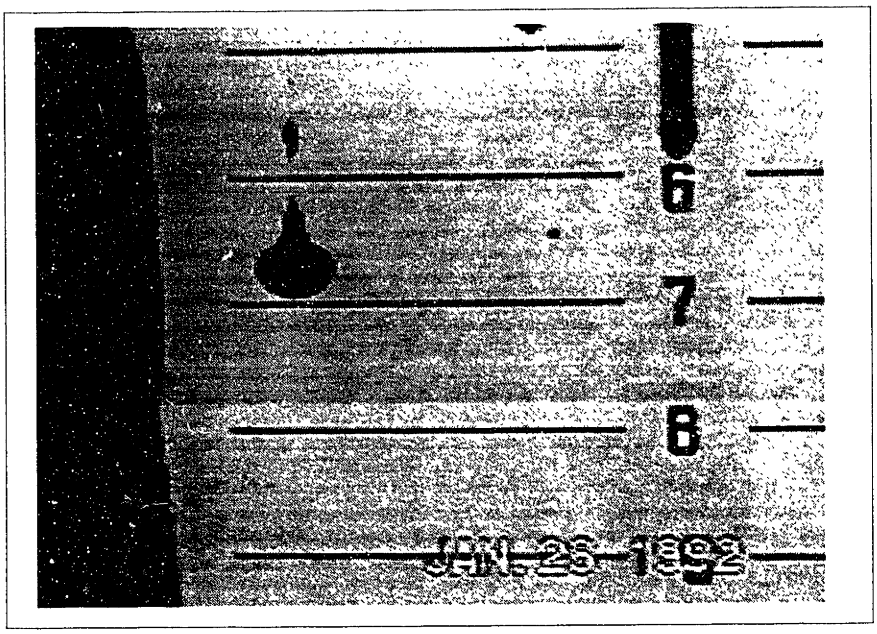

FIGURE 4-39: Sequence of blob movement—Hershey's in Mineral Oil, 3 mm parallel plates. Frosted glass

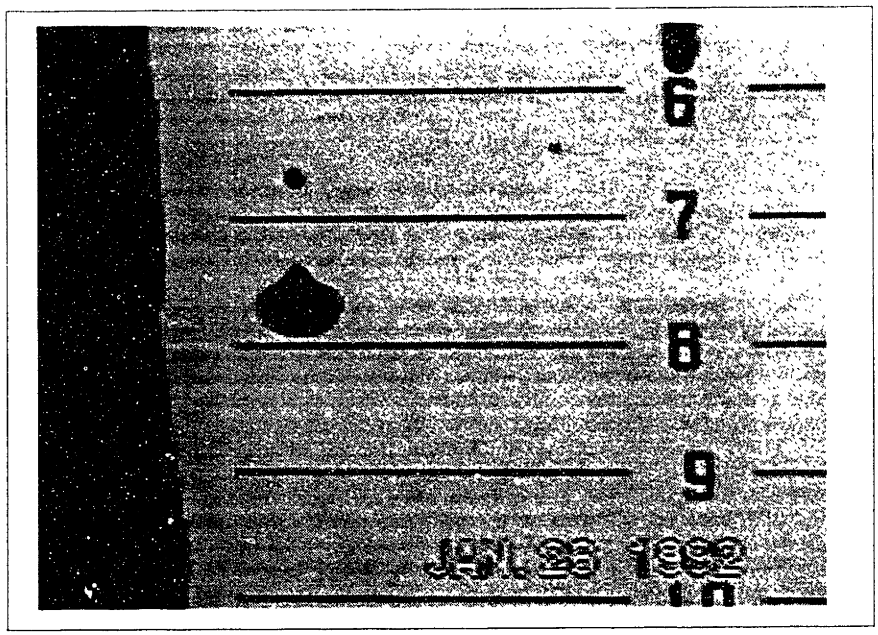

FIGURE 4-40: Sequence of blob movement—Hershey's in Mineral Oil, 3 mm parallel plates. Frosted glass

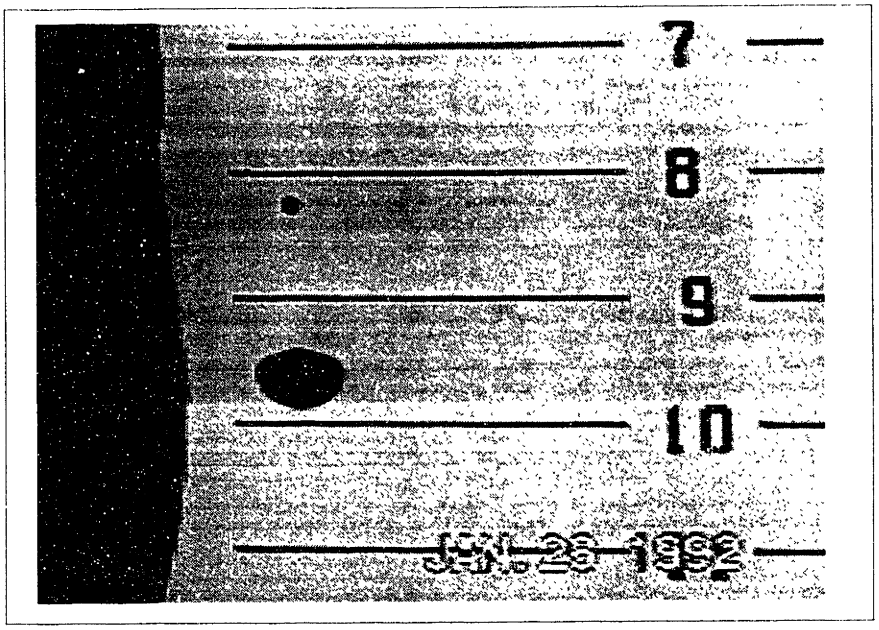

FIGURE 4-41: Sequence of blob movement—Hershey's in Mineral Oil, 3 mm parallel plates. Frosted glass

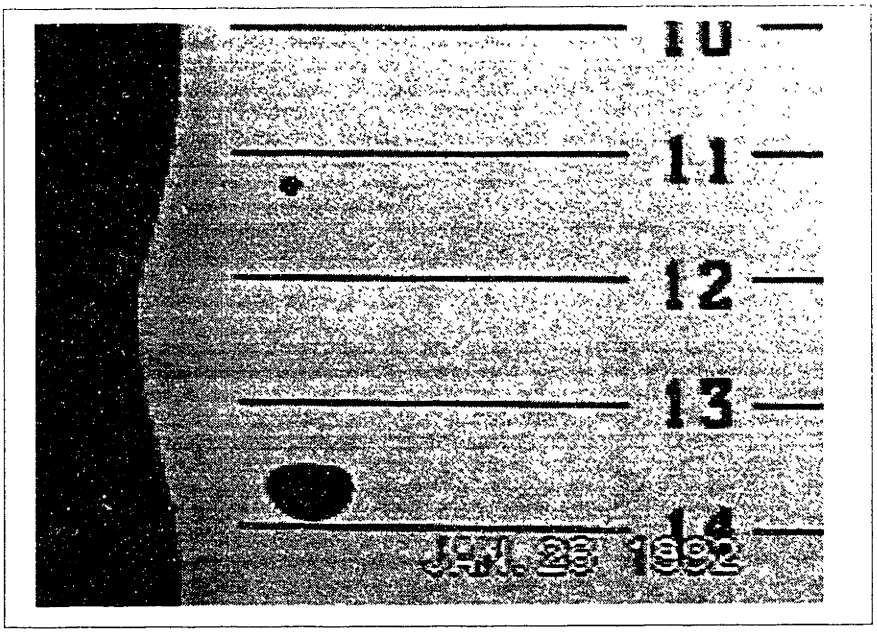

FIGURE 4-42: Sequence of blob movement—Hershey's in Mineral Oil, 3 mm parallel plates. Frosted glass

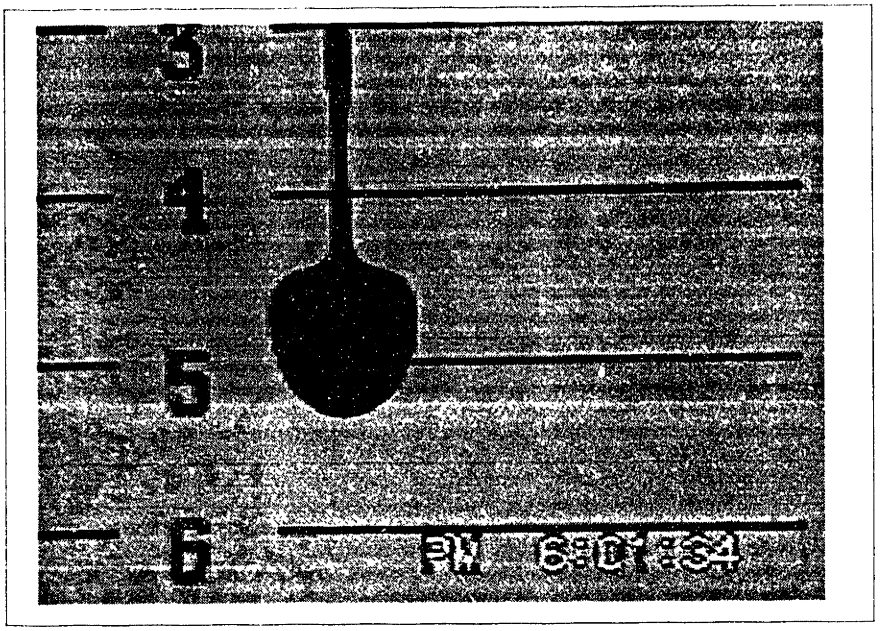

FIGURE 4-43: Sequence of blob movement—Hershey's in Mineral Oil, wedged plates. Frosted glass

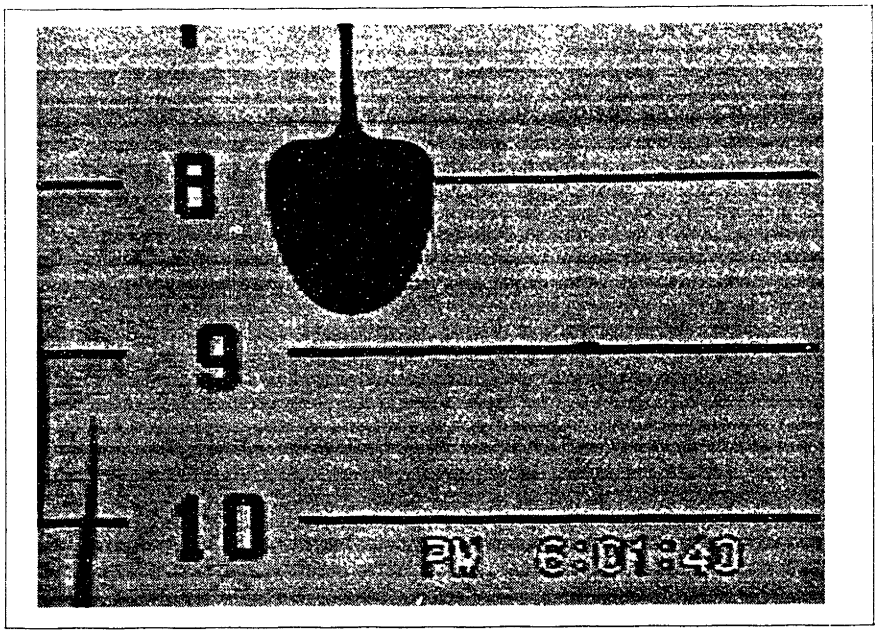

FIGURE 4-44: Sequence of blob movement—Hershey's in Mineral Oil, wedged plates. Frosted glass

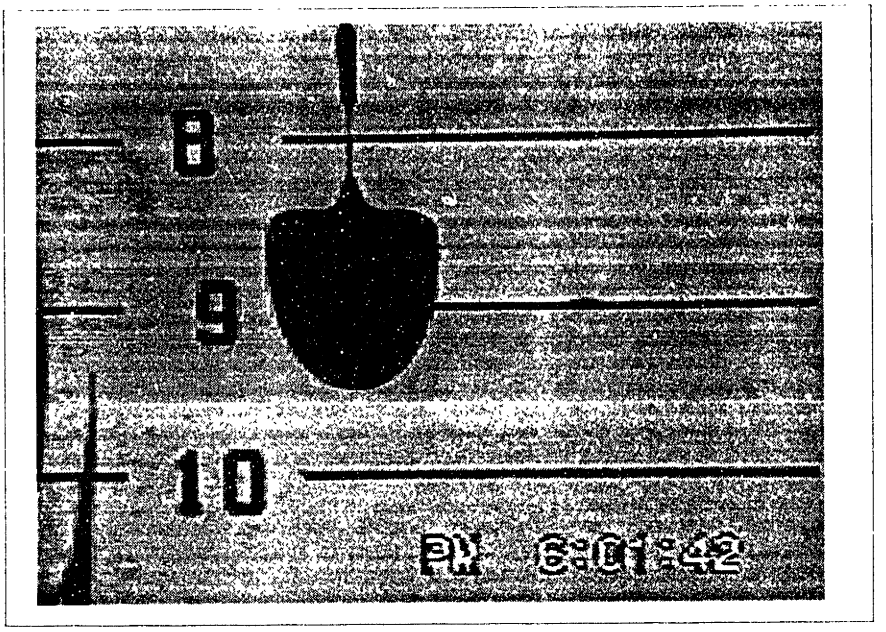

FIGURE 4-45: Sequence of blob movement—Hershey's in Mineral Oil, wedged plates. Frosted glass

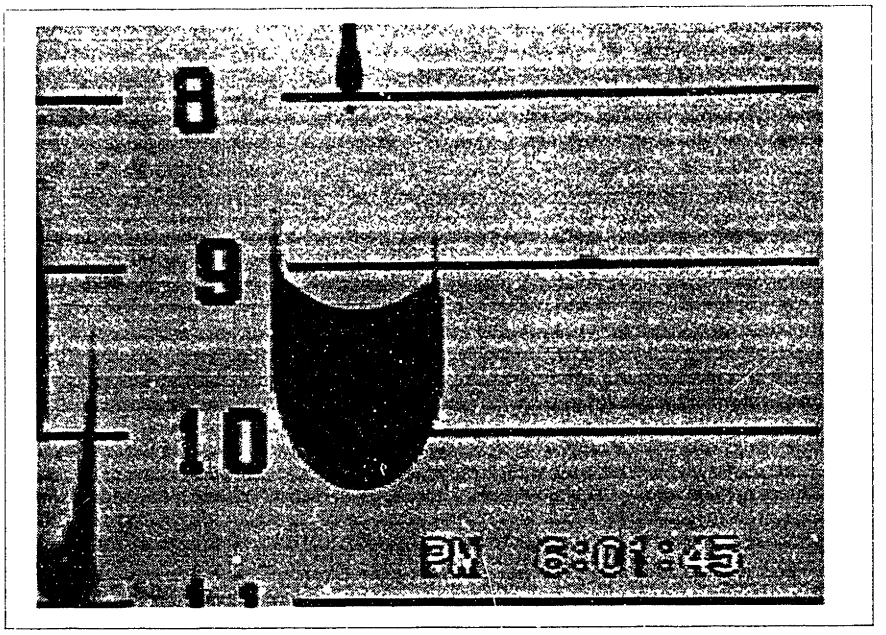

FIGURE 4-46: Sequence of blob movement—Hershey's in Mineral Oil, wedged plates. Frosted glass

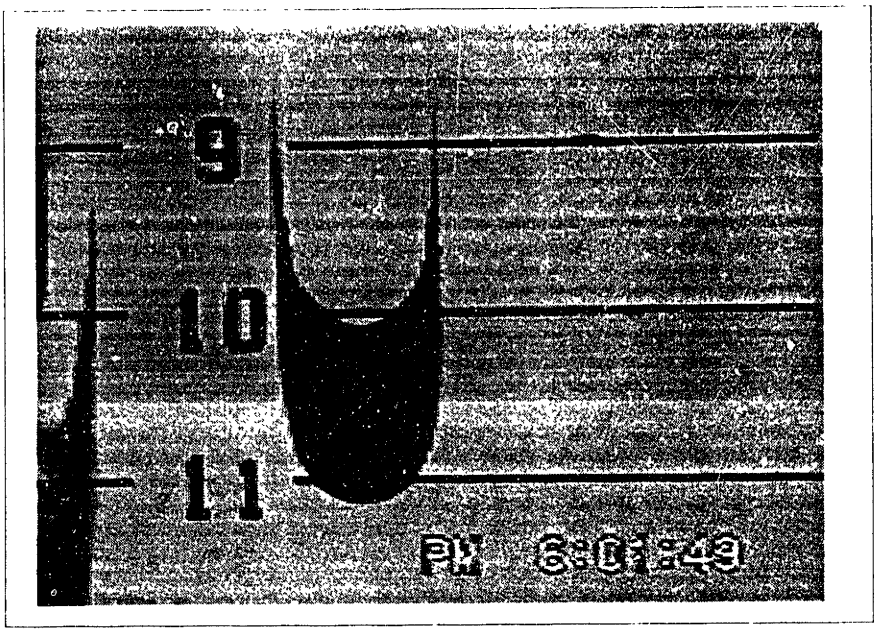

FIGURE 4-47: Sequence of blob movement—Hershey's in Mineral Oil, wedged plates. Frosted glass

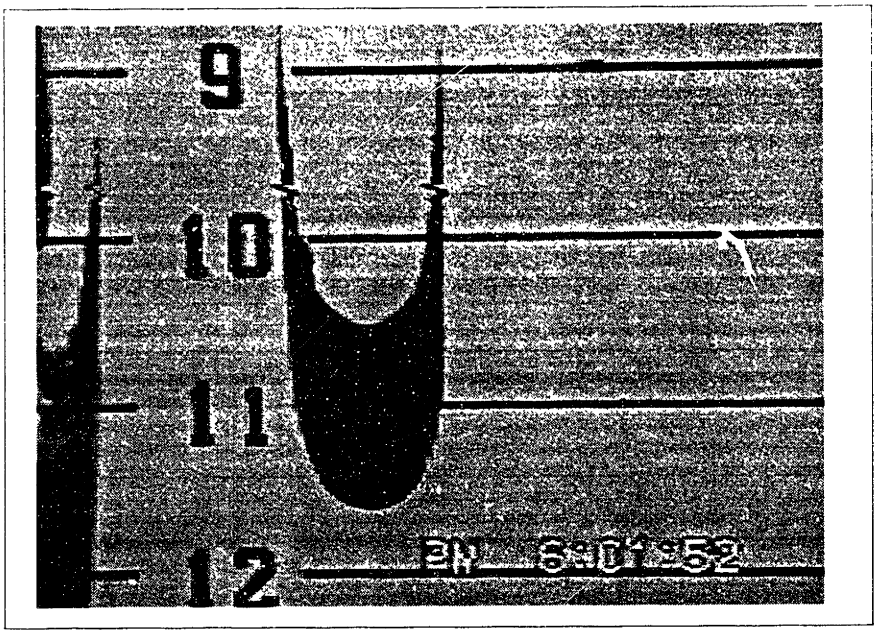

FIGURE 4-48: Sequence of blob movement—Hershey's in Mineral Oil, wedged plates. Frosted glass

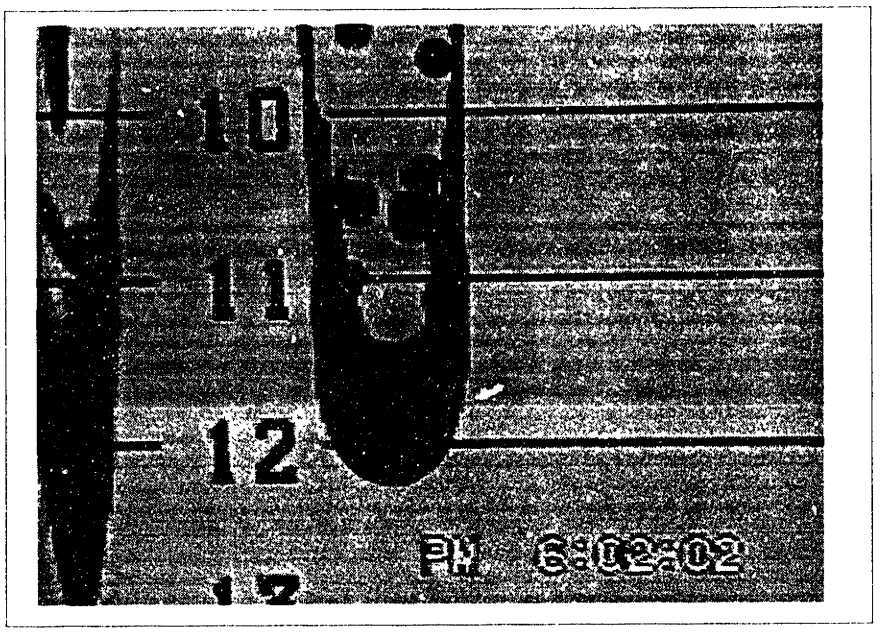

FIGURE 4-49: Sequence of blob movement—Hershey's in Mineral Oil, wedged plates. Frosted glass

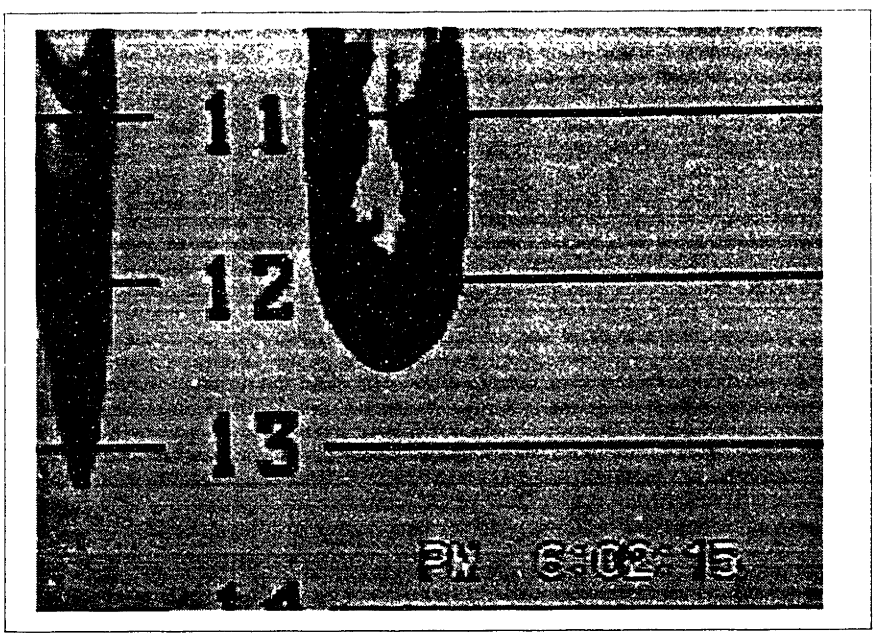

FIGURE 4-50: Sequence of blob movement—Hershey's in Mineral Oil, wedged plates. Frosted glass

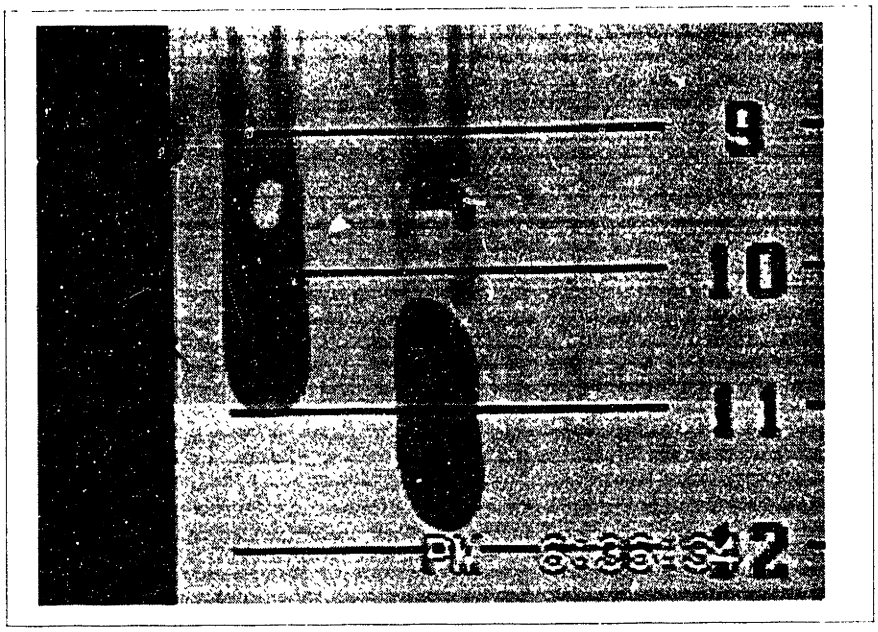

FIGURE 4-51: Sequence of blob movement—Karo in Mineral Oil, wedged plates. Frosted glass

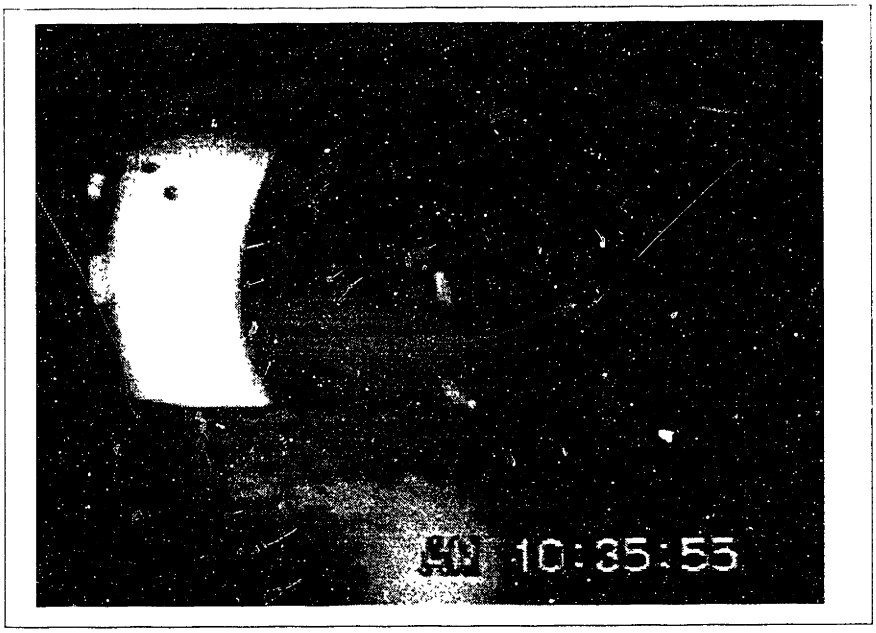

FIGURE 4-52: Glycerol displacing Mineral Oil over float glass

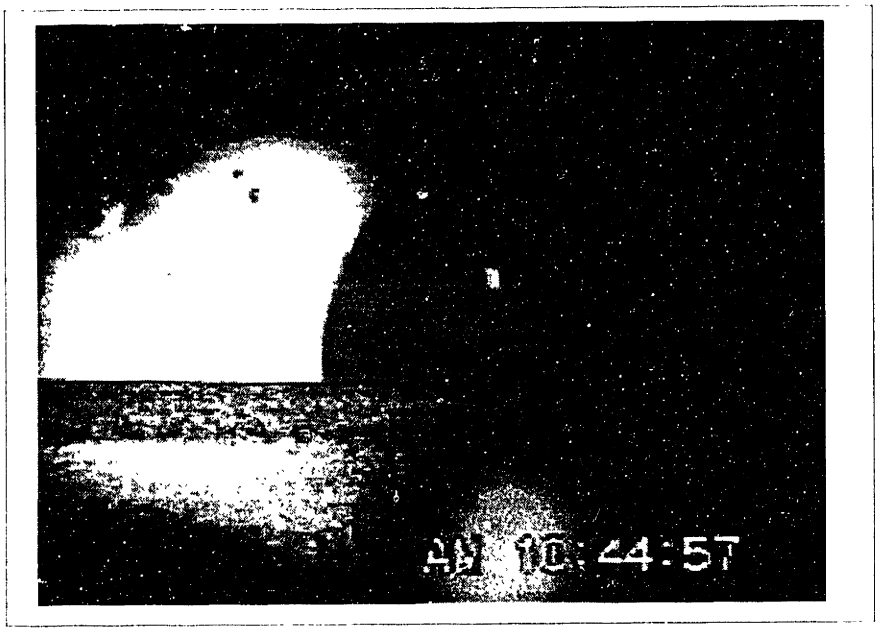

FIGURE 4-53: Glycerol displacing Mineral Oil over float glass

FIGURE 4-54: Glycerol displacing Mineral Oil over float glass

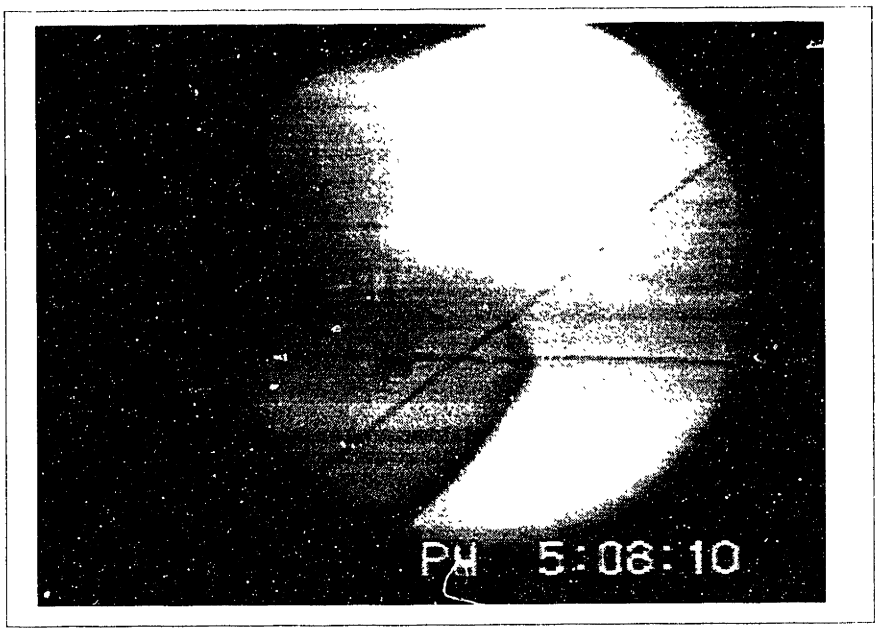

FIGURE 4-55: Glycerol displacing Mineral Oil over float glass

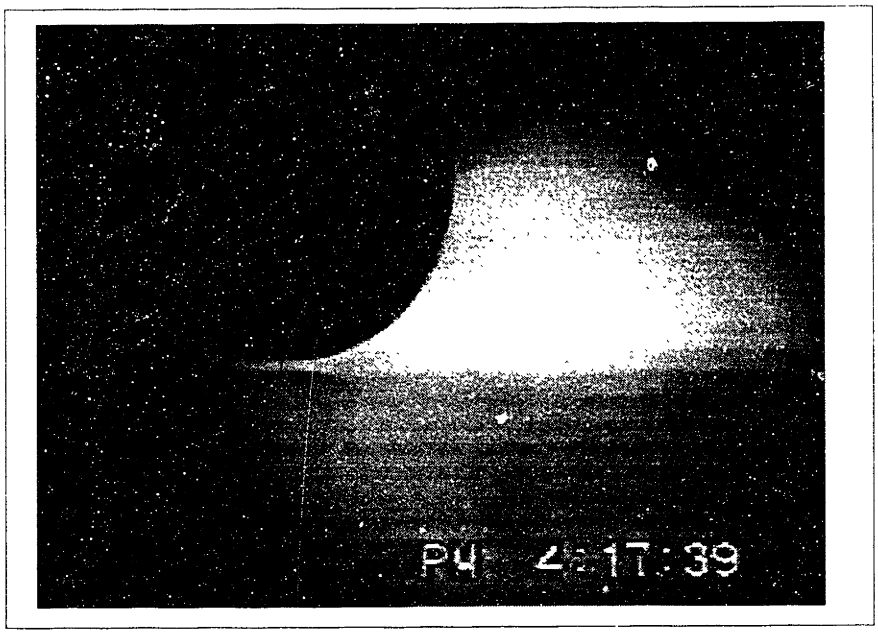

FIGURE 4-56: Hershey's displacing Mineral Oil over float glass

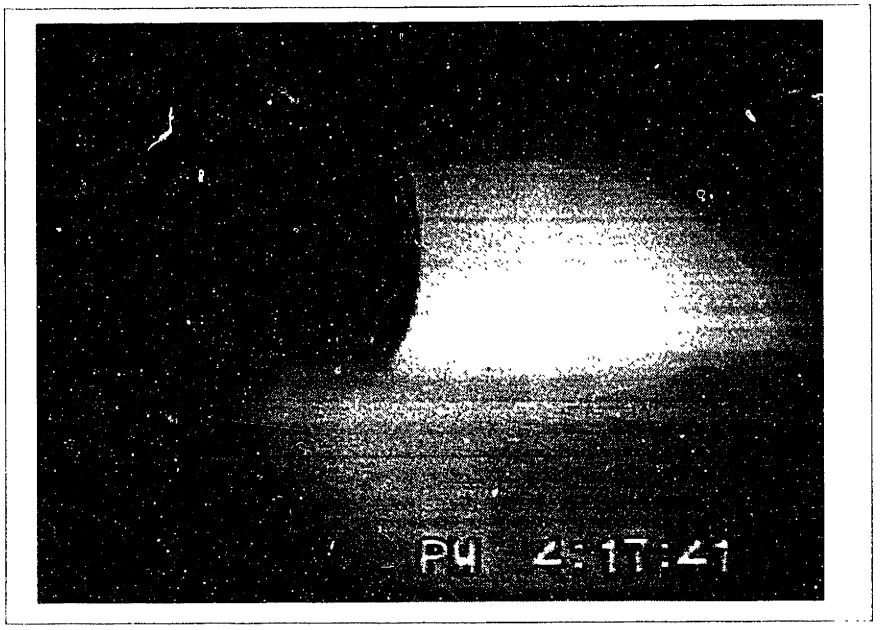

FIGURE 4-57: Hershey's displacing Mineral Oil over float glass

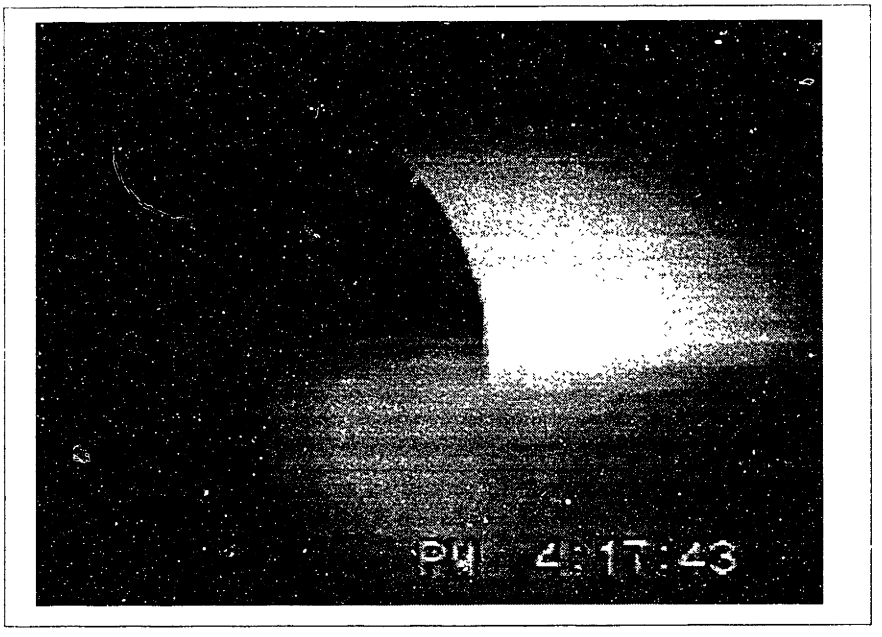

FIGURE 4-58: Hershey's displacing Mineral Oil over float glass

FIGURE 4-59: Hershey's displacing Mineral Oil over float glass

FIGURE 4-60: Karo displacing Mineral Oil over float glass

FIGURE 4-61: Glycerol in air over frosted glass

FIGURE 4-62: Glycerol displacing Mineral Oil over frosted glass

FIGURE 4-63: Glycerol displacing Mineral Oil over frosted glass

FIGURE 4-64: Glycerol displacing Mineral Oil over frosted glass

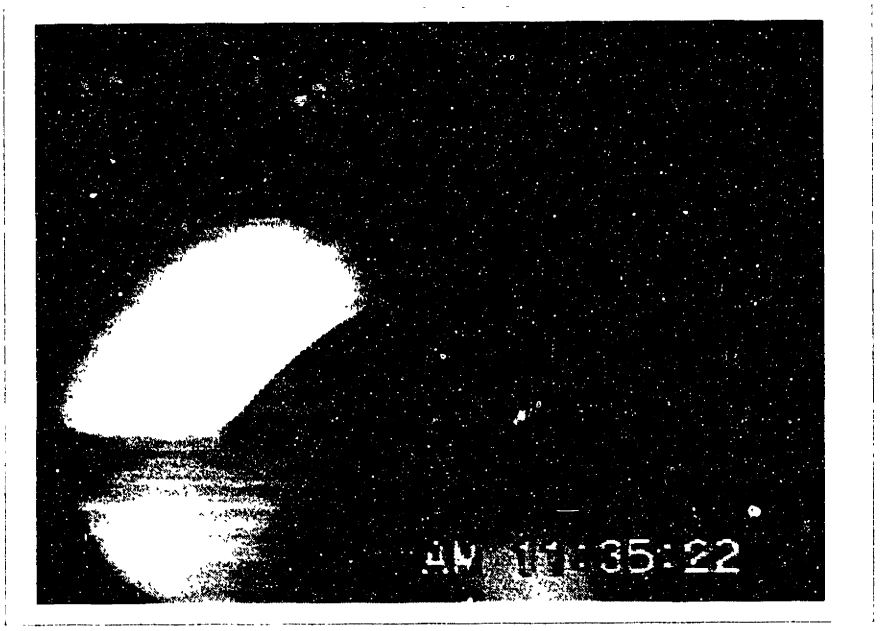

FIGURE 4-65: Glycerol displacing Mineral Oil over frosted glass

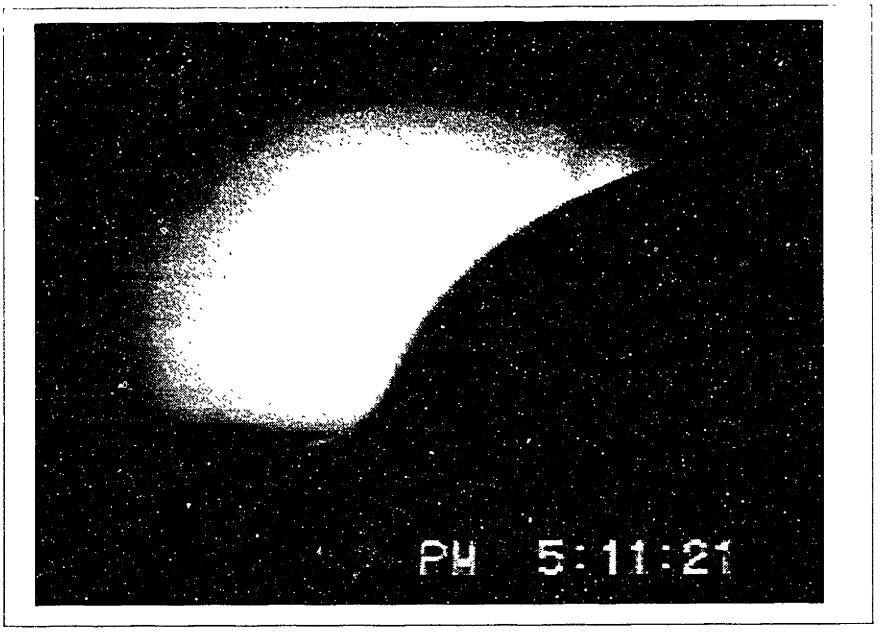

FIGURE 4-66: Karo displacing Mineral Oil over frosted glass. Notice a precursor film

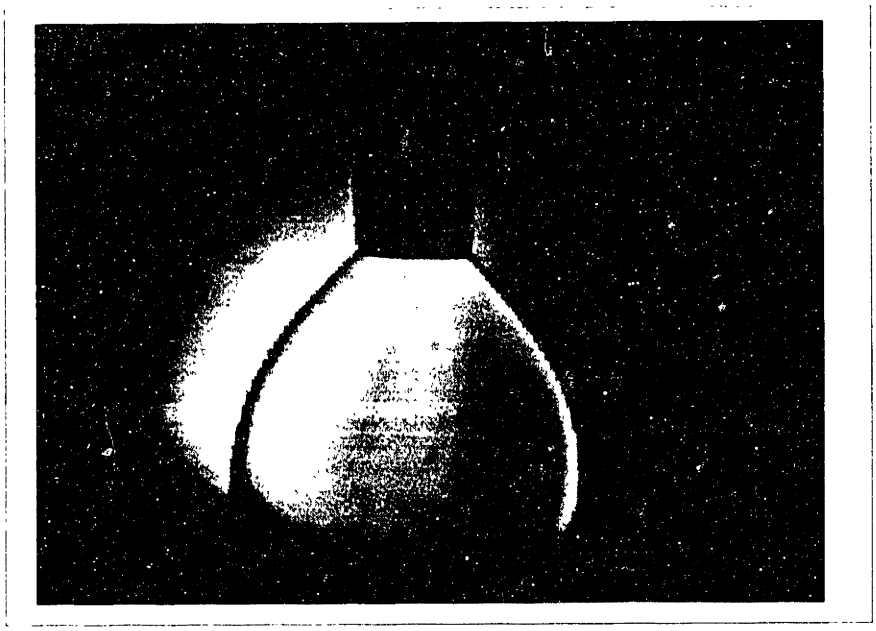

FIGURE 4-67: Interfacial tension measurements utilizing a goniometer. Glycerol in Mineral Oil

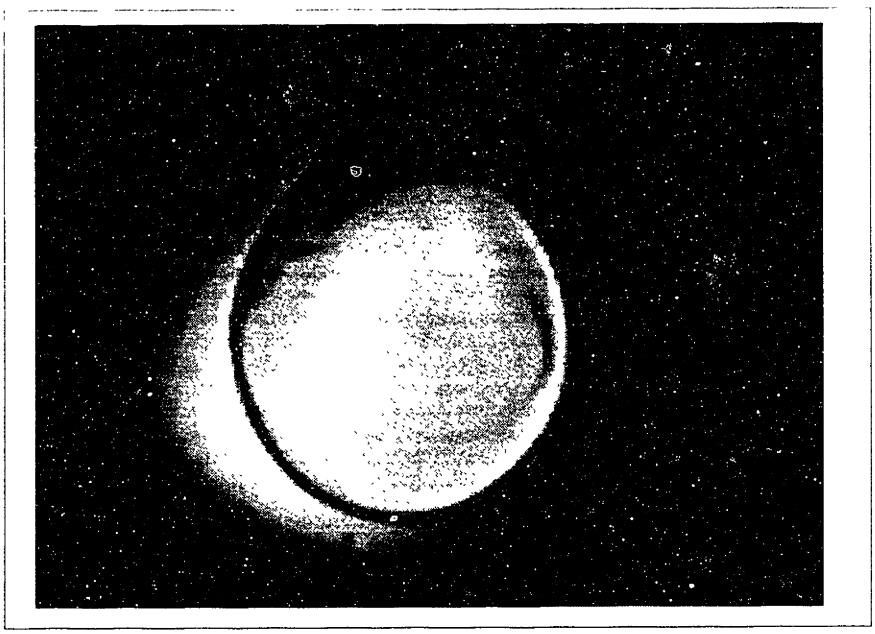

FIGURE 4-68: Interfacial tension measurements utilizing a goniometer. Glycerol in Mineral Oil

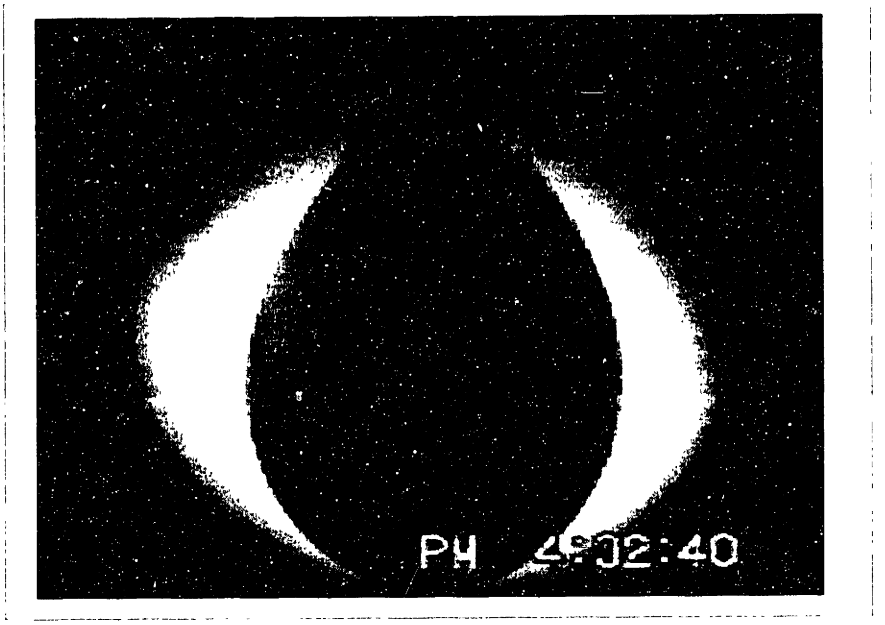

FIGURE 4-69: Interfacial tension measurements utilizing a goniometer. Hershey's in Mineral Oil

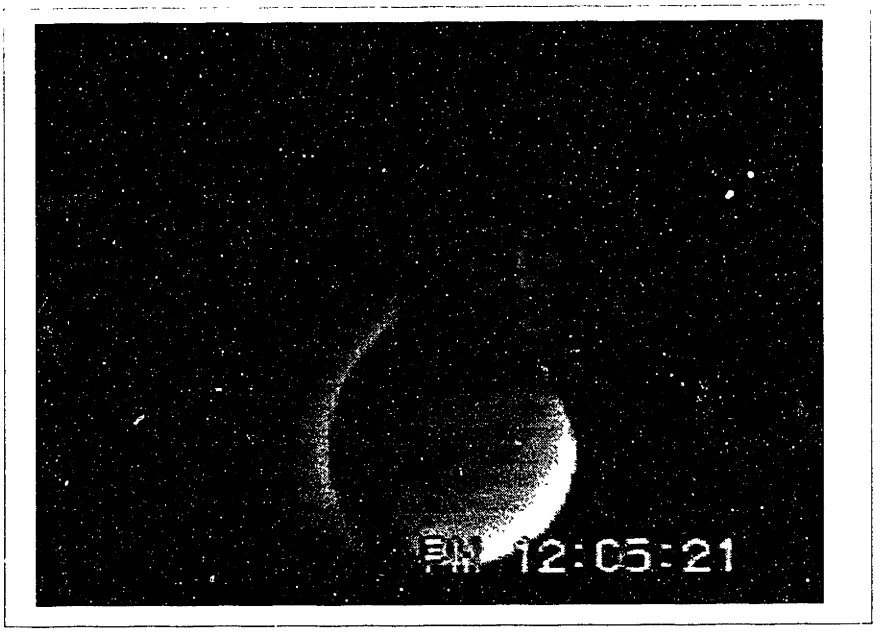

FIGURE 4-70: Interfacial tension measurements utilizing a goniometer. Karo in Mineral Oil

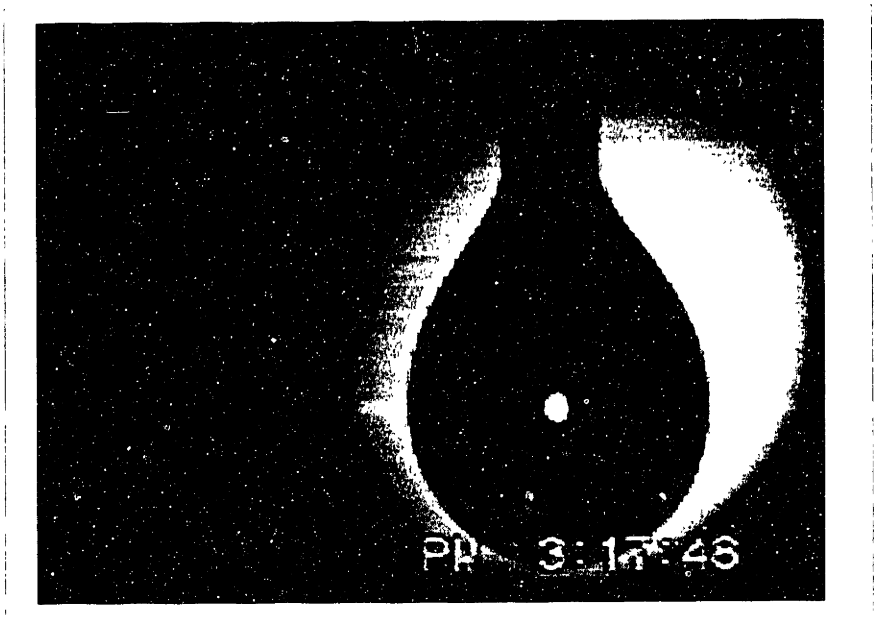

FIGURE 4-71: Surface tension measurements utilizing a goniometer. Glycerol in air

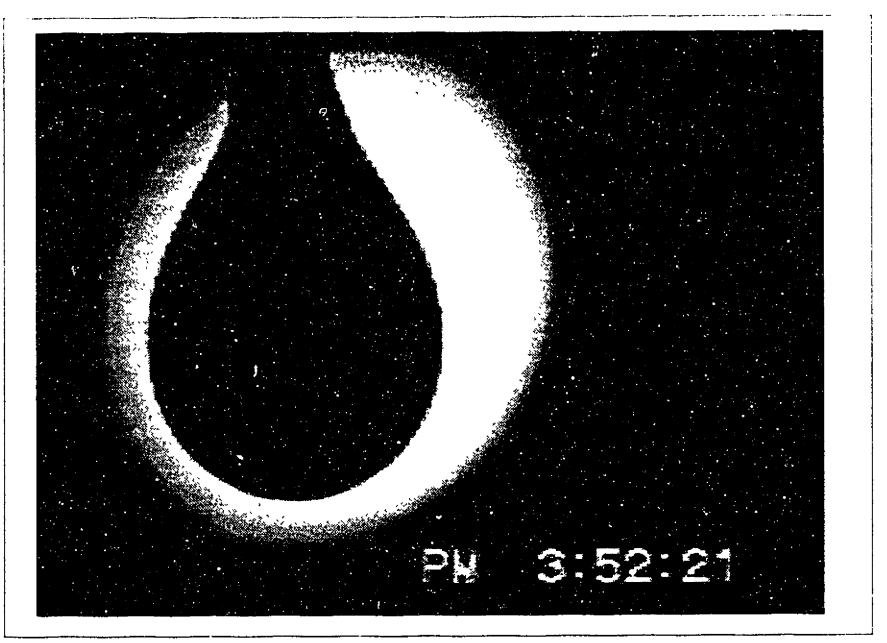

FIGURE 4-72: Surface tension measurements utilizing a goniometer. Hershey's in air

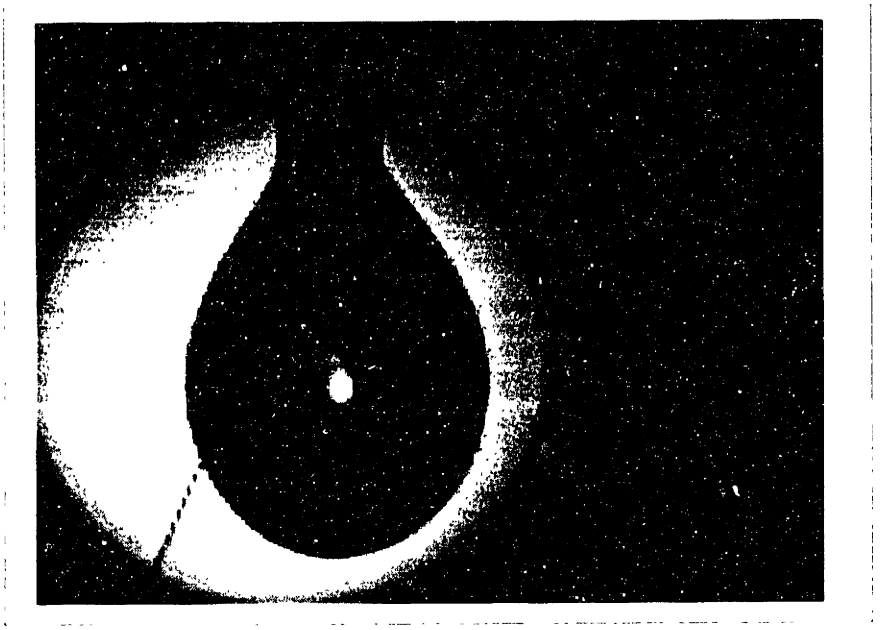

FIGURE 4-73: Surface tension measurements utilizing a goniometer. Karo in air. Notice formation of gel

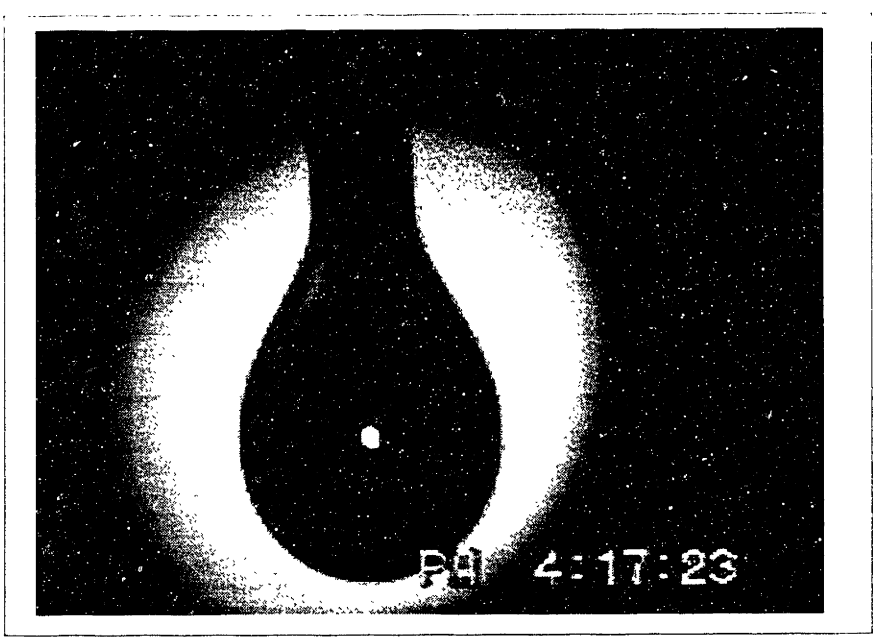

FIGURE 4-74: Surface tension measurements utilizing a goniometer. Mineral Oil in air

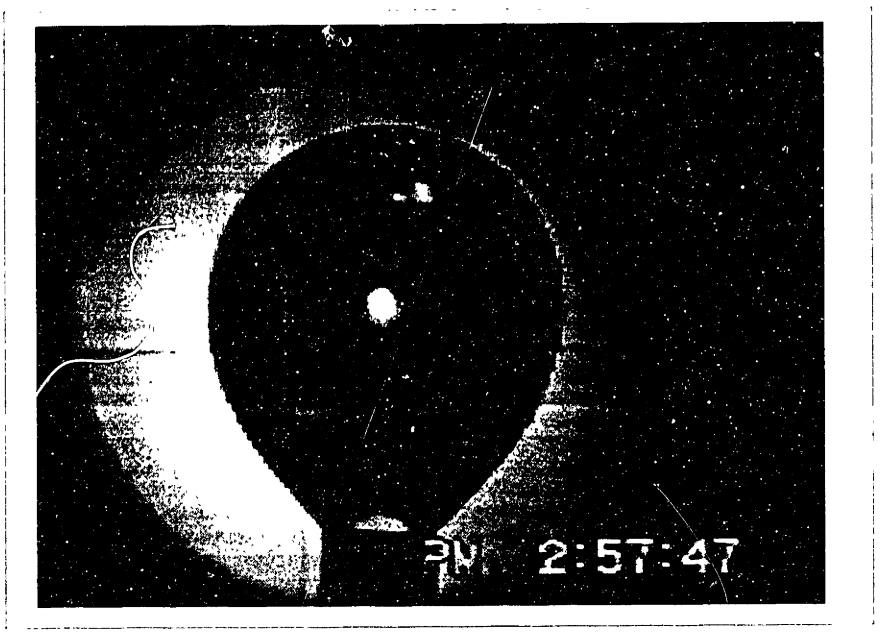

FIGURE 4-75: Surface tension calibration utilizing a goniometer. Distilled water in air

5 Conclusions and Future Work

The main contributions of the present work are the following:

1) Demonstrate that gravity driven convection is the dominant flow mechanism in poorly contained hydraulic fractures.

2) Demonstrate that encapsulation instabilities can dramatically accelerate the movement of proppant laden fluid towards the bottom of the fracture.

3) Introduce a novel set of highly-parallel algorithms (PARFES) to handle the movement of immiscible fluid stages within a cavity.

4) Build an inexpensive and simple (repeatability was the design goal) experimental apparatus (TARG-DECH) to verify the models developed herein.

The mathematical simulators currently used by industry do not incorporate the convective mechanisms referred above. Current designs for propped fracture dimensions are typically entirely unrealistic. For example, shorter fracture dimensions may often be a more cost-effective alternative to unattainable (and more expensive) massive fracture jobs commonly employed.

In order to quantify this important issue more fully, PARFES needs to be integrated in codes like R3DH to provide a complete simulation of the hydraulic fracture process. The results of such simulations can then be downloaded to more practical field oriented systems, Barr and Cleary (1992); Cleary (1988); Cleary, Wright et al. (1991), for routine use on commercial jobs.

APPENDIX A

Basic Equations for Multiple Fluid Phases and Stages

A-1 Introduction

The movement of an arbitrary number of fluid phases can be described through an extension of a single fluid mass and momentum conservation equations, disregarding temperature and further general properties variation (e.g., electromagnetic, etc.). If N fluid phases are present within a certain volume, their respective volume fraction is represented by ${}^{i}v$ (i^{th} fluid phase indicated by the upper prescript i) such that

$$\sum_{i=1}^{N} {}^{i}v = 1$$

The region of interest Ω (see **Figure A-1**), circumscribed by $\partial\,\Omega$, contains each phase i (the i^{th} phase occupies a volume ${}^{i}\Omega$within boundary $\partial\,{}^{i}\Omega$)

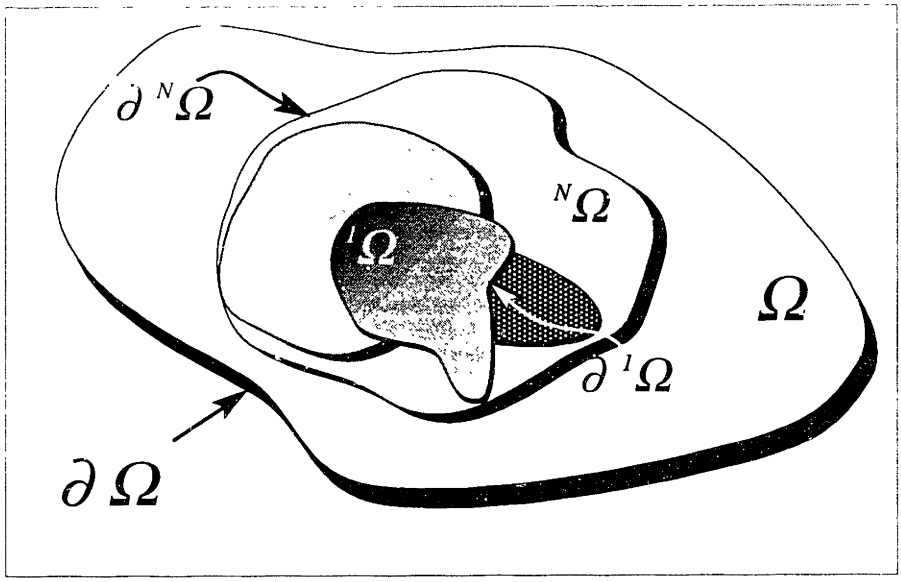

FIGURE A-1: N fluid phases within region Ω and delimited by $\partial\,\Omega$ (i^{th} phase occupying volume ${}^{i}\Omega$ within boundary $\partial\,{}^{i}\Omega$)

The balance of mass for each phase is

$$ {}^{i}\rho_{,t} + ({}^{i}\rho\ {}^{i}u_k)_{,k} = {}^{i}s \tag{A-1} $$

where: the comma denotes partial differentiation; the subindex k double summation on the spatial variables (k =1, 2 and 3); the prescript i, which is not a double summation index, the i^{th} fluid stage; ${}^{i}u_k$ the velocity components of each phase; ${}^{i}\rho$ the density of each phase; ${}^{i}s$ the mass source per unit of volume.

Equation (A-1) is expressed for an orthogonal system of coordinates. Mass conservation should be satisfied for each phase i, as well as for the summation over all phases in Ω

$$ \rho_{,t} + (\rho\, u_k)_{,k} = 0 \tag{A-2} $$

where u_k, the volume fraction averaged velocity, is given by

$$ u_k = \frac{\sum_{i=1}^{N} {}^{i}v\ {}^{i}u_k}{\sum_{i=1}^{N} {}^{i}v} \tag{A-3} $$

the sum of the source terms over all phases is assumed to be zero (no external sources), and ρ is the volume fraction averaged density, analogous to Eq. (A-3) above. Further, the momentum conservation (volume fraction averaged) in Ω is

$$ (\rho\, u_k)_{,t} + (\rho\, u_m\, u_k)_{,m} = T_{mk,m} + \sum_{i=1}^{N} {}^{i}b_k + S_k\, a \tag{A-4} $$

${}^{i}b_k$ are the body force components acting on the i^{th} phase; S_k are the interfacial force components per unit of interfacial area; a is the interfacial area per unit of volume; and, ${}^{i}T_{mk}$ (T_{mk} being the sum over all phases) is given for Newtonian fluids as

$$ {}^{i}T_{mk} = -\,{}^{i}p\,\delta_{mk} - \frac{2}{3}\,{}^{i}\mu\,{}^{i}u_{l,l}\,\delta_{mk} + {}^{i}\mu\,({}^{i}u_{k,m} + {}^{i}u_{m,k}) \tag{A-5} $$

where: δ_{mk} is 1 if $k=m$, and 0 otherwise; ${}^{i}p$ is the i^{th} phase hydrostatic pressure; and, ${}^{i}\mu$ is the

i^{th} phase viscosity.

Although the above set of equations, combined to appropriate boundary conditions, forms the current analysis general framework, few remarks should be made:

- The interface between phases has measure zero in three-dimensions, attempts to average mass conservation and/or momentum at the interface leads to a singularity if we use the notion of Lebesgue integration. To overcome this restriction, limits are taken in the sense of the distributions, weighted by appropriate functions (e.g., Dirac δ-function). For instance in Kataoka (1986) the space or time averaged values of the local instant void fraction (either 0 or 1) corresponds to the volume fraction (any value in [0,1]).

- The tracking of the interface movement poses a challenging mathematical problem, even under very simplifying assumptions. For instance Pelcé (1988) provides an overview of current research on the dynamics of interface motion in various fields (Bubbles Movement, Flame Propagation, Fingering and Crystal Growth). In the context of this thesis numerical algorithms are devised to track the movement of multistage flow fields within a narrow channel of variable height. To control the movement of each stage, even for motions that are clearly physically stable, is difficult.

- In the literature various approaches to tackle the multiphase problem are available. The basic model, the homogeneous mixture model —vide Anderson and Jackson (1967), assumes completely mixed phases moving with the same velocity. The drift flux model, which can be viewed as an extension of the homogeneous mixture model, allows different speeds among phases. For finely dispersed suspensions a rational thermodynamics based approach by Truesdell (1984) is applicable. Local instant formulations—Kataoka (1986)—and averaged theorems for interface transport—Gray and Hassanizadeh (1989)—provide a theoretical formulation to handle the interfaces. However, several difficulties, as pointed by Bilicki, Dafermos et al. (1987), arise, even in the simplest cases, when the interface motion is to be tracked.

In what follows phases are assumed to be contained within a narrow channel, i.e., $\Delta << L$, where Δ represents the characteristic height of the channel (along the z direction) and L both the characteristic length (along x) and width (along y) scales. The in-plane directions are x and y; the transverse direction is z. Mass and momentum will be averaged along the transverse direction, positing symmetry with respect to the plane $z = 0$. Depicted in **Figure A-2** is the channel height (crack opening for the hydraulic fracture problem), $\delta \equiv \delta(x,y,t)$, a function of the coordinates x and y, and the time t.

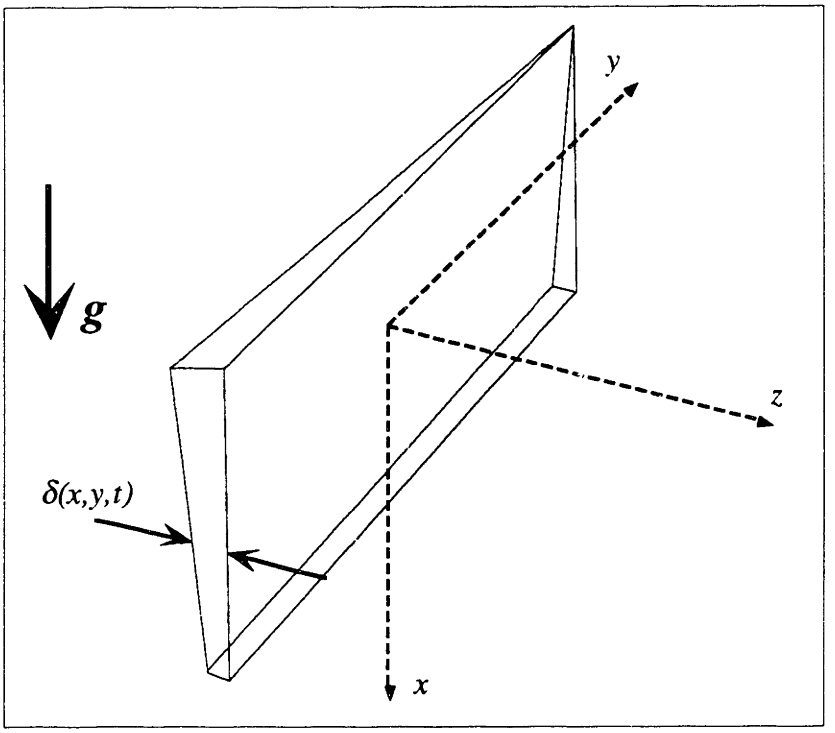

FIGURE A-2: Sketch of vertical channel geometry

A-2 Mass Conservation

To obtain the mass balance of the i^{th} phase (using a Cartesian set of coordinates), presuppose that its density is independent of z, and sources of mass (e.g., chemical reactions) are absent. The volume element is $\delta \Delta x \Delta y$, the in-plane components of velocity are ${}^{i}u_x$ and ${}^{i}u_y$, and the average fluid leakage velocity (through both walls at $z=\pm\delta/2$) is ${}^{i}V_{loss}$. Therefore, the time and coordinate components of the mass fraction can be

expressed as

$$\begin{aligned} {}^{i}m_{t} &= {}^{i}\rho\ {}^{i}\nu\ \delta\ \Delta x\ \Delta y \\ {}^{i}m_{x} &= {}^{i}\rho\ \overline{({}^{i}\nu\ {}^{i}u_{x})}\ \delta\ \Delta y\ \Delta t \\ {}^{i}m_{y} &= {}^{i}\rho\ \overline{({}^{i}\nu\ {}^{i}u_{y})}\ \delta\ \Delta x\ \Delta t \\ {}^{i}m_{\delta/2} &= {}^{i}\rho\ {}^{i}\nu\ {}^{i}V_{loss}\ \Delta x\ \Delta y\ \Delta t \end{aligned} \tag{A-6}$$

where the averaged velocities are

$$\begin{aligned} \xi &\leftarrow \frac{2z}{\delta} \\ \overline{({}^{i}\nu\ {}^{i}u_{y})} &= \int_{0}^{1} {}^{i}\nu\ {}^{i}u_{y}\, d\xi \\ \overline{({}^{i}\nu\ {}^{i}u_{x})} &= \int_{0}^{1} {}^{i}\nu\ {}^{i}u_{x}\, d\xi \end{aligned} \tag{A-7}$$

Notice that: the upper prescript i is <u>not</u> a double summation index; velocities are averaged according to their respective volume fractions.

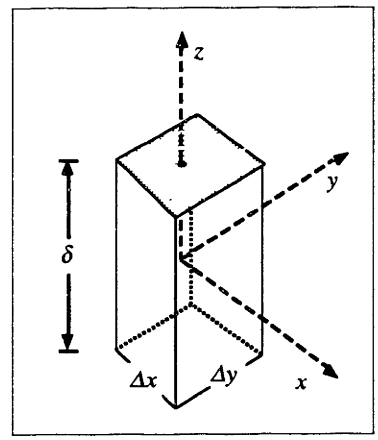

FIGURE A-3: Sketch of z-averaged control volume

The mass flux through the control volume in **Figure A-3** is balanced below

$$({}^{i}m_{t+\Delta t} - {}^{i}m_{t}) + ({}^{i}m_{x+\Delta x} - {}^{i}m_{x}) + ({}^{i}m_{y+\Delta y} - {}^{i}m_{y}) + 2\,{}^{i}m_{\delta/2} = 0 \tag{A-8}$$

In terms of a generic subindex α, the first order expansion of $m_{\alpha+\Delta\alpha}$ is

$$ {}^{i}m_{\alpha+\Delta\alpha} = {}^{i}m_{\alpha} + \frac{\partial\, {}^{i}m_{\alpha}}{\partial\alpha}\Delta\alpha + O(\Delta\alpha^2) \qquad \text{(A-9)} $$

Taking the limit of $\Delta\alpha \rightarrow 0$ and substituting Eqs.(A-7), (A-6), and (A-9) in (A-8) leads to the averaged i^{th} phase mass balance

$$ \frac{\partial}{\partial t}\left({}^{i}\rho\, {}^{i}v\, \delta\right) + \frac{\partial}{\partial x}\left({}^{i}\rho\,\overline{({}^{i}v\, {}^{i}u_x)}\,\delta\right) + \frac{\partial}{\partial y}\left({}^{i}\rho\,\overline{({}^{i}v\, {}^{i}u_y)}\,\delta\right) + 2\, {}^{i}\rho\, {}^{i}v\, {}^{i}V_{loss} = 0 \qquad \text{(A-10)} $$

The above equation can be interpreted in the distribution sense. For instance at the interface between two phases (vide **Figure A-4** below), the boundary condition jump can be

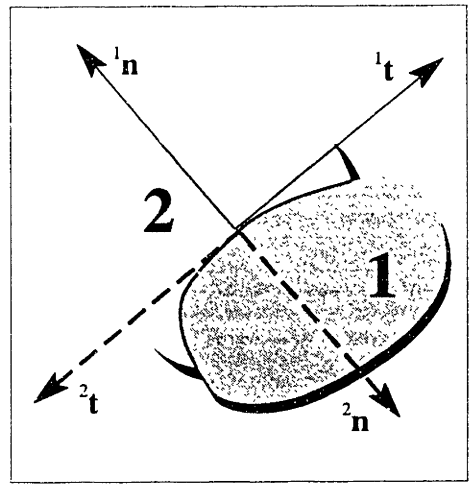

FIGURE A-4: Normal and tangential components of a two-phase interface, where for the i^{th} phase ${}^{i}\mathbf{n} = ({}^{i}n_1, {}^{i}n_2, {}^{i}n_3)$ and ${}^{i}\mathbf{t} = ({}^{i}t_1, {}^{i}t_2, {}^{i}t_3)$

obtained by integrating Eq. (A-10) weighted by a Dirac δ-function. The resulting mass balance is

$$ {}^{1}\rho\left({}^{1}u_k - U_k^{interface}\right){}^{1}n_k + {}^{2}\rho\left({}^{2}u_k - U_k^{interface}\right){}^{2}n_k = 0 \qquad \text{(A-11)} $$

such that: $U_k^{interface}$ are the absolute interfacial velocity components; ${}^{1}u_k$ (or ${}^{2}u_k$) are the limit of phase 1 (or phase 2) velocity components at the interface; ${}^{1}n_k$ and ${}^{1}t_k$ are the unit normal and unit tangential components describing the interface from phase 1 (${}^{2}n_k = -{}^{1}n_k$ and ${}^{2}t_k = -$

$^{l}t_k$). Equation (A-11) is only valid for a two fluid interface. For an intersection line between more than two phases (e.g., tricuspids etc.), a more elaborate extension of the above equation (except for the z-averaging introduced in this Appendix) can be found in Gray and Hassanizadeh (1989).

If the fluid phases are immiscible, control volumes can be conveniently introduced to track their movement. Hereafter, an immiscible macroscopic phase with in-plane dimensions of the order of the characteristic length scale L will be denominated stage.

For instance, in **Figure A-5** each control volume with in-plane characteristic length scale L is delimited by at least one immiscible fluid phase interface and the channel height.

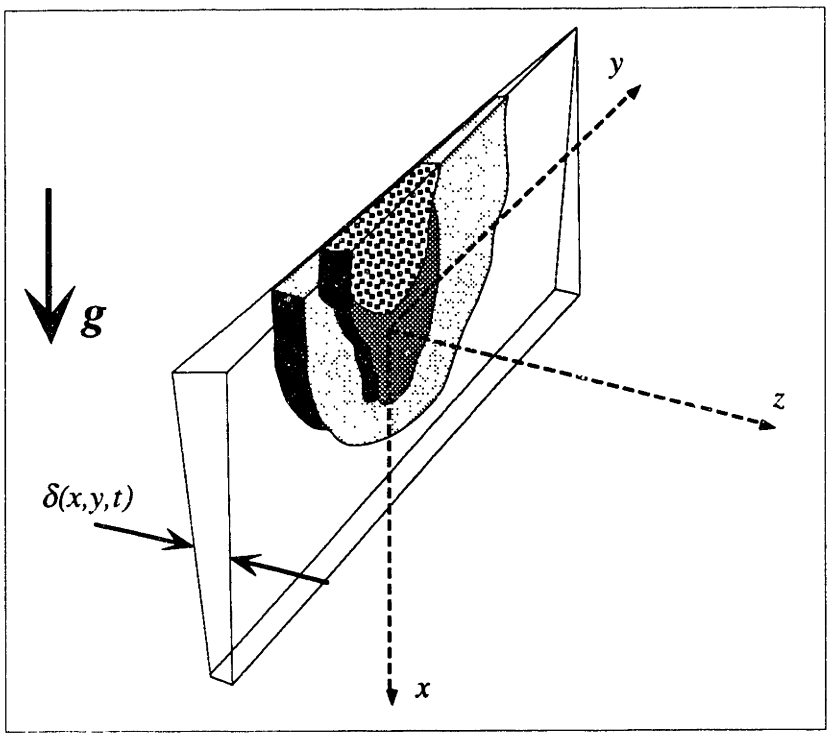

FIGURE A-5: Downward movement of three immiscible fluid stages contained within a channel of variable height $\delta(x,y,t)$

Equation (A-10) can be simplified for the multistage fluid motion as follows

$$\frac{\partial}{\partial t}\left({}^{i}\rho\,\delta\right) + \frac{\partial}{\partial x}\left({}^{i}\rho\,{}^{i}\overline{u}_x\,\delta\right) + \frac{\partial}{\partial y}\left({}^{i}\rho\,{}^{i}\overline{u}_y\,\delta\right) + 2\,{}^{i}\rho\,{}^{i}V_{loss} = 0 \tag{A-12}$$

Using the notation introduced in Eq. (A-1), equation (A-12), with the index k=3 already expanded (${}^{i}u_z|_{z=\delta/2} = {}^{i}V_{loss} + \frac{1}{2}\delta_{,t}|_{z=\delta/2}$), can be expressed as

$$\left({}^{i}\rho\,\delta\right)_{,t} + \left({}^{i}\rho\,{}^{i}\overline{u}_k\,\delta\right)_{,k} + 2\,{}^{i}\rho\,{}^{i}V_{loss} = 0 \tag{A-13}$$

In the absence of mass exchange between the two stages, Eq. (A-11) is simplified

$${}^{1}u_k\,{}^{1}n_k = U_k^{interface}\,{}^{1}n_k = -\,{}^{2}u_k\,{}^{2}n_k \tag{A-14}$$

and interpreted as a kinematic boundary condition between two fluid stages, i.e., continuity of normal components of velocity. On the other hand, continuity of tangential components of velocity may be imposed as a kinematic boundary condition, if we assume the "no-slip" boundary condition at the interface

$${}^{1}u_k\,{}^{1}t_k = -\,{}^{2}u_k\,{}^{2}t_k \tag{A-15}$$

A counterexample would be the interface between two fluids with a very large difference in viscosity (e.g., oil/air): tangential components of velocities may be assumed to be discontinuous (as a kinematic boundary condition), but continuity of normal velocities cannot be violated.

Performing an order of magnitude analysis on Eq. (A-12), gives

$$\begin{aligned}
\frac{\partial}{\partial t}\left({}^{i}\rho\,\delta\right) &\sim \frac{\rho\,\Delta}{T} \\
\frac{\partial}{\partial x}\left({}^{i}\rho\,{}^{i}\overline{u}_x\,\delta\right) &\sim \frac{\rho\,\Delta\,V}{L} \\
\frac{\partial}{\partial y}\left({}^{i}\rho\,{}^{i}\overline{u}_y\,\delta\right) &\sim \frac{\rho\,\Delta\,V}{L} \\
2\,{}^{i}\rho\,{}^{i}V_{loss} &\sim \rho\,V_{loss}
\end{aligned} \tag{A-16}$$

where ρ, Δ and T are, respectively, the characteristic density, crack opening and time

scales. V is the in-plane characteristic velocity (both x and y) and V_{loss} the characteristic fluid leakage (z). Consequently, the characteristic velocities are scaled as

$$V \sim \frac{L}{T} \tag{A-17}$$

$$V_{loss} \sim V\frac{\Delta}{L} \tag{A-18}$$

A-3 Momentum Conservation

The balance of momentum for the multiphase flow is not as straightforward as the mass conservation presented in the previous section. An interfacial, unknown, force S_k was introduced in Eq. (A-4) to account for interactions between multiple fluid stages. In the macroscopic scale, at a given point of an in interface with normal components n_k and with mean surface curvature κ, S_k can be associated to the surface tension σ as follows

$$S_k = \sigma \kappa n_k \tag{A-19}$$

Although the addition of the interfacial force to the momentum equation provides a formulation that, theoretically, accounts for all the relevant forces, experimentally it poses a challenge: Is it possible to measure the interfacial forces? In general, the answer is no.

At the interface between two phases (See **Figure A-4** on **Page 142**) Eq. (A-4) reduces to

$$\sum_{i=1}^{2} \left({}^{i}\rho \; {}^{i}u_m \left({}^{i}u_m - U_m^{interface} \right) {}^{i}n_k - {}^{i}T_{km} \; {}^{i}n_m \right) + S_k = 0 \tag{A-20}$$

The above jump condition follows the same interpretation given to Eq. (A-11). In addition, at the interface, notice the following: the interfacial force per unit of interfacial area, S_k, may be viewed as a source term; and, the normal stresses, as well as the hydro-

static pressure, may be discontinuous. The discontinuity of stresses is an important point to be observed while implementing numerical schemes to track the interface movement. For instance, vide Mavridis, Hrymak et al. (1987), a "double-node" technique should be used for implementations based on the finite element method.

Consider the problem of interest, depicted in **Figure A-2**, and assume the same simplifications introduced in the previous section. Below, the general expression for the momentum balance, Eq. (A-4), is expanded and simplified based on the control volume in **Figure A-3**. To keep the derivation short, only the x direction contributions to the momentum equation are presented.

$$
\begin{aligned}
{}^{i}M_{x\_t} &\equiv \int_{-\delta/2}^{\delta/2} {}^{i}\rho\ {}^{i}v\ {}^{i}u_x\ \Delta x\ \Delta y\ dz \quad = {}^{i}\rho\ \overline{({}^{i}v\ {}^{i}u_x)}\ \delta\ \Delta x\ \Delta y \\
{}^{i}M_{x\_x} &\equiv \int_{-\delta/2}^{\delta/2} {}^{i}\rho\ {}^{i}v\ {}^{i}u_x\ \Delta y\ \Delta t\ {}^{i}u_x\ dz \quad = {}^{i}\rho\ \overline{({}^{i}v\ {}^{i}u_x^2)}\ \delta\ \Delta y\ \Delta t \\
{}^{i}M_{x\_y} &\equiv \int_{-\delta/2}^{\delta/2} {}^{i}\rho\ {}^{i}v\ {}^{i}u_x\ \Delta y\ \Delta t\ {}^{i}u_y\ dz \quad = {}^{i}\rho\ \overline{({}^{i}v\ {}^{i}u_x\ {}^{i}u_y)}\ \delta\ \Delta y\ \Delta t \\
{}^{i}M_{x\_z} &\equiv 2\ {}^{i}\rho\ {}^{i}v\ {}^{i}V_{loss}\ \Delta x\ \Delta y\ {}^{i}u_x\big|_{z=\delta/2} = 0
\end{aligned}
\tag{A-21}
$$

${}^{i}M_{x\_t}$, ${}^{i}M_{x\_x}$, ${}^{i}M_{x\_y}$, ${}^{i}M_{x\_z}$, are, respectively, the instantaneous x momentum, x momentum through the x plane, y plane and z plane. Symmetry in the z direction is assumed, and the "no-slip" boundary condition at the channel walls ($z = \pm\ \delta/2$) leads to ${}^{i}u_x\big|_{z=\delta/2} = 0$. The net forces in the x direction are the following

$$
\begin{aligned}
{}^{i}F_{xx} &= \int_{-\delta/2}^{\delta/2} \frac{\partial\left({}^{i}\nu\ {}^{i}T_{xx}\right)}{\partial x}\,\Delta x\,\Delta y\,dz \\
{}^{i}F_{xy} &= \int_{-\delta/2}^{\delta/2} \frac{\partial\left({}^{i}\nu\ {}^{i}T_{xy}\right)}{\partial y}\,\Delta y\,\Delta x\,dz \\
{}^{i}F_{xz} &= 2\ {}^{i}\nu\ {}^{i}T_{xz}\Big|_{z=\delta/2}\,\Delta x\,\Delta y
\end{aligned}
\tag{A-22}
$$

$$
\begin{aligned}
{}^{i}F_{x}^{body} &= {}^{i}\rho\ {}^{i}\nu\ g_x\ \delta\,\Delta x\,\Delta y \\
{}^{i}F_{x}^{hydrostatic} &= -\frac{\partial\left({}^{i}\nu\ {}^{i}p\right)}{\partial x}\,\delta\,\Delta x\,\Delta y \\
{}^{i}F_{x}^{interfacial} &= \overline{(S_x\,a)}\,\delta\,\Delta x\,\Delta y
\end{aligned}
\tag{A-23}
$$

The net forces in Eq. (A-22) are viscous forces. The hydrostatic pressure contribution to the stress tensor has been decoupled as follows

$$
\begin{aligned}
{}^{i}T_{xx} &= 2\ {}^{i}\mu\frac{\partial\,{}^{i}u_x}{\partial x} - \frac{2}{3}\,{}^{i}\mu\left(\frac{\partial\,{}^{i}u_x}{\partial x} + \frac{\partial\,{}^{i}u_y}{\partial y} + \frac{\partial\,{}^{i}u_z}{\partial z}\right) \\
{}^{i}T_{xy} &= {}^{i}\mu\left(\frac{\partial\,{}^{i}u_x}{\partial y} + \frac{\partial\,{}^{i}u_y}{\partial x}\right) \\
{}^{i}T_{zx} &= {}^{i}\mu\left(\frac{\partial\,{}^{i}u_x}{\partial z} + \frac{\partial\,{}^{i}u_z}{\partial x}\right)
\end{aligned}
\tag{A-24}
$$

In order to balance the x momentum (change of x momentum = sum of net x forces), Eq. (A-24) is inserted into Eq. (A-22) and expanded. The resulting expression

$$
\begin{aligned}
\frac{\partial}{\partial t}\left({}^{i}\rho\overline{\left({}^{i}\nu\ {}^{i}u_x\right)}\delta\right) + \frac{\partial}{\partial x}\left({}^{i}\rho\overline{\left({}^{i}\nu\ {}^{i}u_x^2\right)}\delta\right) + \frac{\partial}{\partial y}\left({}^{i}\rho\overline{\left({}^{i}\nu\ {}^{i}u_y\ {}^{i}u_x\right)}\delta\right) &= -\delta\frac{\partial}{\partial x}\left({}^{i}\nu\ {}^{i}p\right) + \overline{(S_x\,a)}\,\delta + \\
\frac{4}{3}\frac{\partial}{\partial x}\left({}^{i}\mu\ {}^{i}\nu\frac{\partial\left({}^{i}\overline{u}_x\,\delta\right)}{\partial x}\right) - \frac{2}{3}\frac{\partial}{\partial x}\left({}^{i}\mu\ {}^{i}\nu\frac{\partial\left({}^{i}\overline{u}_y\,\delta\right)}{\partial y}\right) - \frac{2}{3}\frac{\partial\left({}^{i}\mu\ {}^{i}\nu\ {}^{i}u_z\big|_{z=\delta/2}\right)}{\partial x} &+ \\
\frac{\partial}{\partial y}\left({}^{i}\mu\ {}^{i}\nu\frac{\partial\left({}^{i}\overline{u}_x\,\delta\right)}{\partial y}\right) + \frac{\partial}{\partial y}\left({}^{i}\mu\ {}^{i}\nu\frac{\partial\left({}^{i}\overline{u}_y\,\delta\right)}{\partial x}\right) &+ \\
2\ {}^{i}\mu\ {}^{i}\nu\left(\frac{\partial\,{}^{i}u_x}{\partial z} + \frac{\partial\,{}^{i}u_z}{\partial x}\right)\Bigg|_{z=\delta/2} + {}^{i}\rho\ {}^{i}\nu\,\delta\,g_x &
\end{aligned}
\tag{A-25}
$$

relies on the subsequent issues:

- due to continuity of stresses (zero at the walls).
$$ {}^{i}T_{xx}\big|_{z=\pm\delta/2} = {}^{i}T_{xy}\big|_{z=\pm\delta/2} = 0 $$

- due to the "no-slip" boundary condition at the walls.
$$ {}^{i}u_x\big|_{z=\pm\delta/2} = {}^{i}u_y\big|_{z=\pm\delta/2} = 0 $$

- by definition ${}^{i}V_{loss}$ is the fluid leakage velocity.
$$ {}^{i}u_z\big|_{z=\pm\delta/2} = {}^{i}V_{loss} + \frac{1}{2}\delta_{,t}\big|_{z=\pm\delta/2} $$

- symmetry with respect to the plane z=0.

For the multistage problem Eq. (A-25) can be reduced to

$$ \begin{aligned} \frac{\partial}{\partial t}\left({}^{i}\rho\,{}^{i}\overline{u}_x\,\delta\right) + \frac{\partial}{\partial x}\left({}^{i}\rho\,\overline{{}^{i}u_x^2}\,\delta\right) + \frac{\partial}{\partial y}\left({}^{i}\rho\,\overline{\left({}^{i}u_x\,{}^{i}u_y\right)}\,\delta\right) = -\delta\frac{\partial\,{}^{i}p}{\partial x} + \\ \frac{4}{3}\frac{\partial}{\partial x}\left({}^{i}\mu\frac{\partial\left({}^{i}\overline{u}_x\,\delta\right)}{\partial x}\right) - \frac{2}{3}\frac{\partial}{\partial x}\left({}^{i}\mu\frac{\partial\left({}^{i}\overline{u}_y\,\delta\right)}{\partial y}\right) - \frac{2}{3}\frac{\partial\left({}^{i}\mu\,{}^{i}u_z\big|_{z=\delta/2}\right)}{\partial x} + \\ \frac{\partial}{\partial y}\left({}^{i}\mu\frac{\partial\left({}^{i}\overline{u}_x\,\delta\right)}{\partial y}\right) + \frac{\partial}{\partial y}\left({}^{i}\mu\frac{\partial\left({}^{i}\overline{u}_y\,\delta\right)}{\partial x}\right) + \\ 2\,{}^{i}\mu\left(\frac{\partial\,{}^{i}u_x}{\partial z} + \frac{\partial\,{}^{i}u_z}{\partial x}\right)\Big|_{z=\delta/2} + {}^{i}\rho\,\delta\,g_x \end{aligned} \qquad \text{(A-26)} $$

An important difference between Eqs. (A-25) and (A-26) is the absence of the interfacial force term. Although surface tension effects are also relevant for the multistage problem, they are incorporated via the boundary conditions, as opposed to the expression for the multiphase problem. Also, notice that the y-momentum can be obtained by switching $x \leftrightarrow y$ everywhere.

An order of magnitude analysis of Eq. (A-26) gives

$$
\begin{array}{llll}
\dfrac{\partial}{\partial t}\left({}^{i}\rho\ {}^{i}\overline{u}_x\ \delta\right) & \sim \dfrac{\rho\,\Delta\,V^2}{L} & \dfrac{2}{3}\dfrac{\partial}{\partial x}\left({}^{i}\mu\dfrac{\partial\left({}^{i}\overline{u}_y\ \delta\right)}{\partial y}\right) & \sim \dfrac{\mu\,\Delta\,V}{L^2} \\
\dfrac{\partial}{\partial x}\left({}^{i}\rho\ \overline{{}^{i}u_x^2}\ \delta\right) & \sim \dfrac{\rho\,\Delta\,V^2}{L} & \dfrac{2}{3}\dfrac{\partial\left({}^{i}\mu\ {}^{i}u_z\big|_{z=\delta/2}\right)}{\partial x} & \sim \dfrac{\mu\,\Delta\,V}{L^2} \\
\dfrac{\partial}{\partial y}\left({}^{i}\rho\ \overline{\left({}^{i}u_x\ {}^{i}u_y\right)}\ \delta\right) & \sim \dfrac{\rho\,\Delta\,V^2}{L} & \dfrac{\partial}{\partial y}\left({}^{i}\mu\dfrac{\partial\left({}^{i}\overline{u}_x\ \delta\right)}{\partial y}\right) & \sim \dfrac{\mu\,\Delta\,V}{L^2} \\
\delta\dfrac{\partial\,{}^{i}p}{\partial x} & \sim O(1) & \dfrac{\partial}{\partial y}\left({}^{i}\mu\dfrac{\partial\left({}^{i}\overline{u}_y\ \delta\right)}{\partial x}\right) & \sim \dfrac{\mu\,\Delta\,V}{L^2} \\
{}^{i}\rho\ \delta\ g_x & \sim O(1) & 2\ {}^{i}\mu\dfrac{\partial\,{}^{i}u_x}{\partial z}\bigg|_{z=\delta/2} & \sim \dfrac{\mu\,V}{\Delta} \\
\dfrac{4}{3}\dfrac{\partial}{\partial x}\left({}^{i}\mu\dfrac{\partial\left({}^{i}\overline{u}_x\ \delta\right)}{\partial x}\right) & \sim \dfrac{\mu\,\Delta\,V}{L^2} & 2\ {}^{i}\mu\dfrac{\partial\,{}^{i}u_z}{\partial x}\bigg|_{z=\delta/2} & \sim \dfrac{\mu\,\Delta\,V}{L^2}
\end{array}
\qquad \text{(A-27)}
$$

where μ is the characteristic viscosity, and the results (and characteristic scales) of the mass conservation order of magnitude analysis, i.e., Eqs. (A-17) and (A-18), have been used. The hydrostatic pressure and the gravity force terms are assumed to govern the scaling (order 1) of the equation.

The key assumption behind most of the simplifications to be done hereafter is

$$\boxed{\frac{\Delta}{L} << 1} \qquad \text{(A-28)}$$

With this assumption in mind several important simplifications to Eqs. (A-25) and (A-26) are possible. By the same token, the z-momentum contributions are negligible when compared to the x and y momenta.

Two nondimensional numbers result from performing a dimensional analysis on Eq. (A-26)—identically for Eqs. (A-25) and (A-4)

$$\boxed{Re^* \equiv \frac{\rho V \Delta}{\mu}\left(\frac{\Delta}{L}\right)} \tag{A-29}$$

$$\boxed{G^* \equiv \frac{\rho g \Delta^2}{\mu V}} \tag{A-30}$$

Re^* is the scaled (by Δ/L) Reynolds number, G^* a modified Darcy-Rayleigh number. They represent, respectively, the ratio of inertia and gravity to viscous forces. In addition, the balance of normal stresses at the interface between two stages leads to

$$\boxed{Ca^* \equiv \frac{\sigma}{\mu V}} \tag{A-31}$$

the inverse Capillary number, where σ is the surface tension, representing the ratio of surface tension to viscous forces—vide Eqs. (A-19) and (A-20).

A-3.1 Darcy's Law and the Hele-Shaw Cell Approximation

Assuming that $Re^* << 1$ and $\Delta/L << 1$, the following simplification from Eq. (A-26) is obtained

$$-\delta\left({}^{1}p\right)_{,k} + 2\,{}^{i}\mu \left.\frac{\partial\,{}^{1}u_k}{\partial x_3}\right|_{x_3=\delta/2} + {}^{1}\rho\,\delta\,g_k = 0 \tag{A-32}$$

or similarly from Eq. (A-25)

$$-\delta\left({}^{i}v\,{}^{1}p\right)_{,k} + 2\,{}^{1}v\,{}^{1}\mu \left.\frac{\partial\,{}^{1}u_k}{\partial x_3}\right|_{x_3=\delta/2} + {}^{i}\rho\,{}^{i}v\,\delta\,g_k = 0 \tag{A-33}$$

with k=1,2. The interfacial force term is set aside and may be introduced through an analysis of the boundary conditions.

Again applying the same conditions assumed in the previous paragraph to Eq. (A-4) leads to

$$- \left({}^{i}v\ {}^{i}p\right)_{,k} + \left({}^{i}v\ {}^{i}\mu\left({}^{i}u_k\right)_{,3}\right)_{,3} + {}^{i}\rho\,{}^{i}v\ g_k = 0 \qquad \text{(A-34)}$$

Notice that Eqs. (A-32) and (A-33) being the z-averaged restrictions of (A-34), the viscous force term appears in a reduced form as a shear stress at the walls ($z=\pm\delta/2$). Observe, also, that ${}^{i}v$, ${}^{i}p$, ${}^{i}\mu$, ${}^{i}\rho$ are assumed not to be a function of x_3 ($x_1\equiv x$, $x_2\equiv y$, $x_3\equiv z$), consequently Eq. (A-34) can be rewritten (with k=1,2) as

$${}^{i}u_{k,33} = \frac{1}{{}^{i}v\ {}^{i}\mu}\left(\left({}^{i}v\ {}^{i}p\right)_{,k} - {}^{i}\rho\,{}^{i}v\ g_k\right) \equiv f_k(x,y,t)$$

Hence the general dependence on z for ${}^{i}u_k$ is

$${}^{i}u_k = f_k(x,y,t)\frac{z^2}{2} + g_k(x,y,t)\,z + h_k(x,y,t)$$

If the i^{th} phase is in contact with the walls, then the above equation reduces to

$${}^{i}u_k = \frac{f_k(x,y,t)\ \delta^2}{8}\left(4\left(\frac{z}{\delta}\right)^2 - 1\right)$$

Averaging ${}^{i}u_k$ in z

$${}^{i}\overline{u}_k = \frac{1}{\delta}\int_{-\delta/2}^{\delta/2} {}^{i}u_k\,dz$$

gives

$$f_k(x,y,t) = -\frac{12\ {}^{i}\overline{u}_k}{\delta^2}$$

Hence the local and averaged velocities are

$${}^{i}u_k = \frac{\delta^2}{8}\left(\left({}^{i}v\ {}^{i}p\right)_{,k} - {}^{i}\rho\,{}^{i}v\ g_k\right)\left(4\left(\frac{z}{\delta}\right)^2 - 1\right)$$

$${}^{i}\overline{u}_k = -\frac{\delta^2}{12\ {}^{i}v\ {}^{i}\mu}\left(\left({}^{i}v\ {}^{i}p\right)_{,k} - {}^{i}\rho\,{}^{i}v\ g_k\right)$$

In the absence of spatial variations of the volume fraction

$$ {}^{i}\bar{u}_k = -\frac{\delta^2}{12\,{}^{i}\mu}\left({}^{i}p_{,k} - {}^{i}\rho\, g_k\right) \qquad \text{(A-35)} $$

Equation (A-35) is widely used in the literature of porous media, and known as Darcy's Law—vide Homsy (1987), as well as in the study of Fingering instabilities, known as Hele-Shaw cell approximation—vide Saffman (1986); Taylor and Saffman (1958); Weinstein, Dussan et al. (1990).

A-3.2 Surface Tension and Curvature

The interpretation for the interfacial force as an expression involving surface tension and curvature has variations in the literature—vide Ho (1989); Homsy (1987); Mavridis, Hrymak et al. (1987). Below, through a short derivation based on chapter 4.5.1 of the book by Pearson (1983), the distinction between different curvatures of a surface is presented.

Assume a 2-D surface S in an Euclidean 3-D space, such that any point $\mathbf{x}$, $\mathbf{x} = (x_1, x_2, x_3)$, in the surface is expressed as $\mathbf{x} = \mathbf{x}(\xi^1,\xi^2)$, ξ^1 and ξ^2 being the contravariant components of the surface coordinates. An arbitrary vector emanating from the surface at a point $\mathbf{x}$ can be expressed by a triad of base vectors $(\varepsilon_1,\varepsilon_2,N)$, such that

$$ \varepsilon_\alpha = \frac{\partial \mathbf{x}}{\partial \xi^\alpha} \qquad\qquad \alpha = 1,2 $$

and N being the unit normal vector to the surface S at $\mathbf{x}$ (vide **Figure A-6**).

An infinite number of planes contain N at $\mathbf{x}$ and intersect the surface S forming a plane curve C in S. Assume s and θ to measure arc length and inclination along C, and $\mathbf{t}(s)$ to be the unit tangent vector to C at $\mathbf{x}$. Then the curvature κ' and its reciprocal, R, the radius of curvature of C at $\mathbf{x}$ are defined as

$$ \kappa' = \frac{d\theta}{ds} = \frac{1}{R} = -\mathbf{N}\cdot\frac{d\mathbf{t}}{ds} = \frac{\partial \mathbf{N}}{\partial \xi^\alpha}\cdot\frac{\partial \mathbf{x}}{\partial \xi^\beta}\, t^\alpha\, t^\beta $$

The curvature tensor (symmetrical)

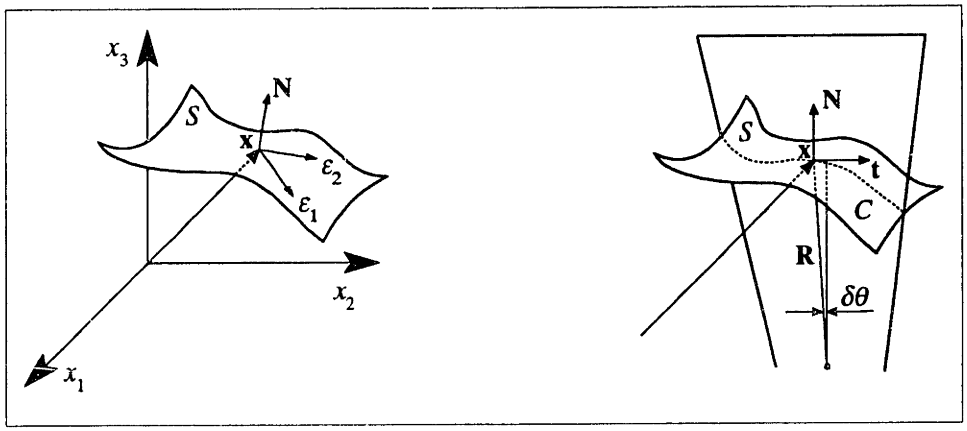

FIGURE A-6: 2-D surface with base vector (ε_1,ε_2,N) at **x**; intersection of plane containing normal N to surface S forming path C

$$b_{\alpha\beta} \equiv \frac{\partial \mathbf{N}}{\partial \xi^{\alpha}} \cdot \frac{\partial \mathbf{x}}{\partial \xi^{\beta}}$$

here expressed in terms of its covariant components, can be used to describe the surface curvature at **x**. On the other hand, by extremalizing the curvature tensor with respect to the surface coordinates ξ^{α} the resulting two roots κ_1 and κ_2, named the principal curvatures, are obtained. The principal directions ξ_1^{α} and ξ_2^{α}, associated to the principal curvatures, form an orthogonal base. Along the principal directions the mixed components of the symmetrical curvature tensor are

$$b_1^1 = \kappa_1 = \frac{1}{R_1}$$

$$b_2^2 = \kappa_2 = \frac{1}{R_2}$$

R_1 and R_2 are the principal radii of curvature. Finally, the mean curvature, an invariant of the curvature tensor, is

$$\frac{1}{2} b_{\alpha}^{\alpha} = \frac{1}{2}\left(\frac{1}{R_1} + \frac{1}{R_2} \right)$$

The curvature κ introduced in Eq. (A-19) is the mean curvature, i.e.

$$\kappa = \left(\frac{1}{R_1} + \frac{1}{R_2} \right) \tag{A-36}$$

A-4 Boundary Conditions

The imposition of boundary conditions (BC's) seems to be the Achilles heel of formulations dealing with the movement of multiple fluid stages within narrow walls, i.e., Hele-Shaw's cell. For instance, browsing through the literature of viscous fingering since its inception, approximately 30 years ago—vide Chuoke, Meurs et al. (1958); Saffman and Taylor (1958); Taylor and Saffman (1958), one can find that slight variations of mathematically imposed BC's dramatically changes the predicted fingering growth behavior. As pointed out by Saffman (1986) "...Bad physics produces bad mathematics...".

The behavior of the interface between multiple fluid stages, as well as the fluid/solid transversal interface (i.e., the channel walls) for the problem under scrutiny, can be adequately represented by BC's similar to the ones used in viscous fingering—vide Homsy (1987), stratified multiphase flows—vide Mavridis, Hrymak et al. (1987), and moving boundary problems—vide Ho (1989). In addition, extra sets of BC's are necessary in order to represent the presence of a source (at the welbore) and the fluid front (contained by the crack tip).

Typically the source BC is either a specified flow rate or specified pressure as a function of time. On the other hand the fluid-front BC is very intricate since the fluid front position and the velocity field are intrinsically dependent on the mechanics of the propagating fracture. A balance of the stress intensity factor, balancing loads over the non-penetrated zone ("vacuum" region between the fluid front and the crack tip) against loads over the remaining of the fracture (region between source and fluid front), is the underlying physically governing phenomena. This balance introduces a global dependence between BC's at the fluid front and the stress/crack-opening fields everywhere.

Per se the study of the BC's at the fluid front as a function of the crack tip growth, is a problem yet to be fully addressed. Some attempts have been made in the past to couple the fluid flow and fracture propagation—vide Abé, Mura et al. (1976); Bui and Parnes (1982); Grif-

fiths, Nilson et al. (1986); Lam (1985); Nilson (1981); Nilson (1986); Nilson and Griffiths (1982); Nilson, Proffer et al. (1985), however the assumptions imposed in those models either neglect relevant physics or oversimplify its interrelationship. Recent studies conducted by Barr (1991) produced encouraging results in the axisymmetrical limit, which can be extended, without loss of generality, to non-symmetrical geometries as long as the characteristic length of the non-penetrated zone scales as Δ.

APPENDIX B

A Semi-Analytical Algorithm for In-Plane Motion

B-1 Modeling the In-Plane Motion

This appendix models the effect of external in-plane flow field on the motion of an idealized *blob* (described in **Section 2-4** on **Page 44**). The very low Reynolds number approximation, derived in **Section A-3**, is assumed.

Two important boundary effects on the *blob* motion are introduced: crack width variation (wedged plates) and finite crack perimeter (bounded container walls). Also, constant crack opening (parallel plates) and unbounded container wall solutions are derived as a reference.

Solutions are obtained for the following scenarios:

1) Unbounded container walls and parallel plates.

2) Unbounded container walls and wedged plates.

3) Bounded container walls and parallel plates.

4) Bounded container walls and wedged plates.

In what follows bath fluid properties are represented by the subindex *1*, and *blob* properties by the subindex *2*.

B-2 The Viscous-Irrotational Paradox

Assuming the usual approximation for the scaled Reynolds number ($Re^* << 1$), the velocity field can be derived (vide **Section A-3.1** on **Page 150**) as

$$\begin{aligned} v_x &= \frac{3}{2} u_x(x,y)\left(1 - 4\left(\frac{z}{\delta}\right)^2\right) \\ v_y &= \frac{3}{2} u_y(x,y)\left(1 - 4\left(\frac{z}{\delta}\right)^2\right) \\ v_z &= 0 \end{aligned} \tag{B-1}$$

where u_x and u_y are the area-averaged velocities (the overbar is dropped).

Cross-differentiating Eq. **(A-35)** on **Page 152** results on

$$\begin{aligned} \frac{\partial^2 p}{\partial y \partial x} &= -12\,\mu_1\, u_x \frac{\partial \delta^{-2}}{\partial y} - \frac{12\,\mu_1}{\delta^2}\frac{\partial u_x}{\partial y} \\ \frac{\partial^2 p}{\partial x \partial y} &= -12\,\mu_1\, u_y \frac{\partial \delta^{-2}}{\partial x} - \frac{12\,\mu_1}{\delta^2}\frac{\partial u_y}{\partial x} \end{aligned} \tag{B-2}$$

Hence, if we assume both

$$\left|\frac{\partial \delta}{\partial x}\right| << \left|\delta \frac{\partial u_x}{\partial y}\right| \tag{B-3}$$

and

$$\left|\frac{\partial \delta}{\partial y}\right| << \left|\delta \frac{\partial u_y}{\partial x}\right| \tag{B-4}$$

then

$$0 = \frac{\partial^2 p}{\partial y \partial x} - \frac{\partial^2 p}{\partial x \partial y} \cong \frac{12\,\mu_1}{\delta^2}\left(\frac{\partial u_y}{\partial x} - \frac{\partial u_x}{\partial y}\right) \tag{B-5}$$

The important consequence of the above equation is

$$\frac{\partial u_y}{\partial x} - \frac{\partial u_x}{\partial y} \cong 0 \tag{B-6}$$

which represents an in-plane **irrotational** flow field. The stringent assumption here is to take both $|\partial\delta/\partial x|$ and $|\partial\delta/\partial y|$ very small or zero, i.e., very small slope or constant crack opening.

B-3 In-plane External Flow Field

In this section the external potential flow field for fluid stage *1* is derived. It is assumed that Eq. (B-6) holds and $Re^* << 1$.

Without loss of generality the moving blob is assumed to:

1) have an in-plane (*x-y* plane) circular shape;

2) be transversely delimited by the crack opening.

Experiments discussed in **Chapter 4** have demonstrated that the first assumption is morphological in nature and does not substantially affect the downwards velocity of the *blob*. On the other hand, the second assumption has to be dropped when addressing encapsulation effects (vide **Appendix C**). The solution obtained for the circular shaped *blob* can also be mapped into other shapes by transformations in the complex plane, e.g., Joukowsky transformation between circular and elliptical shapes.

The scalar potential field for a cylinder of cross-section radius R_2 moving with average velocity U (See **Figure B-1** on **Page 160**) within media originally at rest is

$$\Psi = \frac{U R_2^2}{r} \sin\theta \tag{B-7}$$

where u_x and u_y, the in-plane flow field velocities, are related to the scalar and complex potential fields as follows

$$u_x = \frac{\partial \Psi}{\partial y} \qquad u_y = -\frac{\partial \Psi}{\partial x} \tag{B-8}$$

$$\frac{dw}{dz} = u_x - i\,u_y \qquad w = \phi + i\,\Psi \tag{B-9}$$

Notice that:

- the sign given for the r.h.s. in Eq. (B-7) varies in the literature—for instance, it is the opposite to the one given by Milne-Thomson (1968). The sign has to match the definition of the velocities as expressed in Eq. (B-9).

- the movement of the cylinder is simulated by a doublet of strength

$$\mu = U R^2 \tag{B-10}$$

- doublet strength and flow average velocity can be related as

$$U = \left|\frac{dw}{dz}\right| = \frac{\mu^2}{(z\,\bar{z})^2} = \frac{\mu^2}{R^4} \tag{B-11}$$

- the complex potential for this motion, assuming a doublet located at z_0 and rotated by an angle α with respect to the x-axis, is given as

$$w = -\mu \frac{e^{i\alpha}}{z - z_0} \tag{B-12}$$

- for the derivations that will follow the coordinate system was placed at the center of the *blob* and α set parallel to the x-axis (i.e., $z_0 = 0$ and $\alpha = 0$).

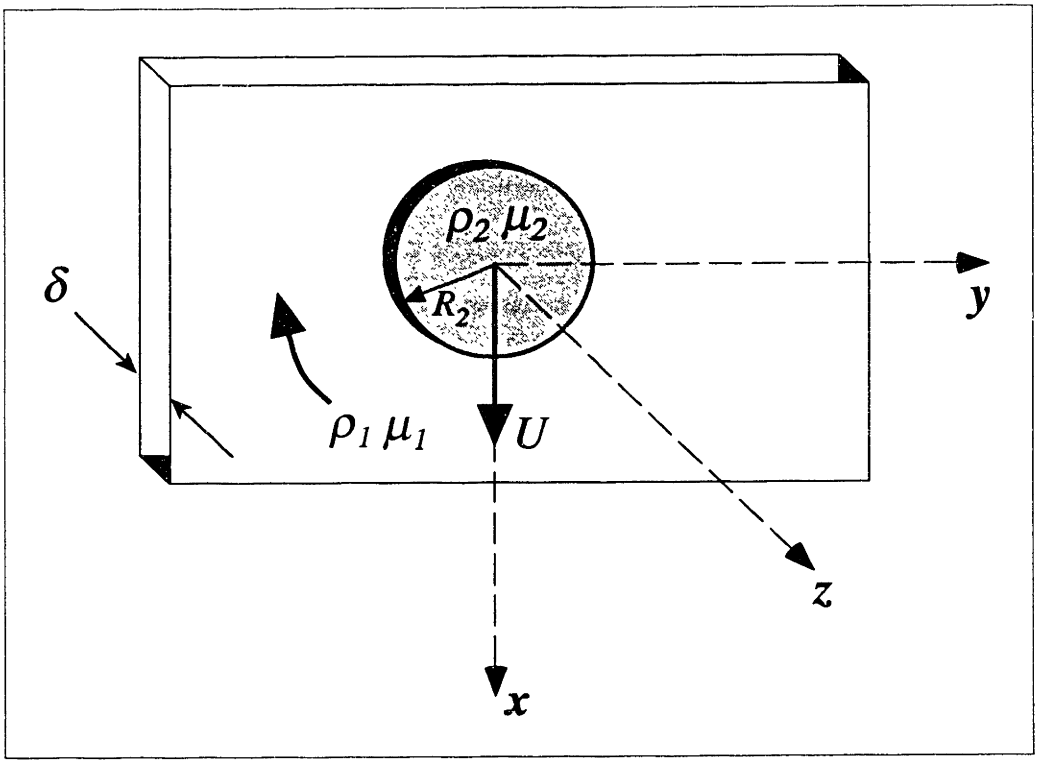

FIGURE B-1: Sketch of in-plane *blob* motion and external flow field

The resulting velocity field is given as

$$u(x,y) = -\frac{U R_2^2 \left(-x^2+y^2\right)}{\left(x^2+y^2\right)^2}\underset{\sim}{i_x} + \frac{2\,U R_2^2\, x\, y}{\left(x^2+y^2\right)^2}\underset{\sim}{i_y}$$

$$u_x = -\frac{U R_2^2 \left(-x^2+y^2\right)}{\left(x^2+y^2\right)^2} \qquad \text{(B-13)}$$

$$u_y = \frac{2\,U R_2^2\, x\, y}{\left(x^2+y^2\right)^2}$$

Assuming the irrotational flow condition, i.e., Eq. (B-6), and substituting the above equation into Eq. **(A-35)** on **Page 152** leads to

$$\frac{\partial p}{\partial x} = +\frac{12\,\mu_1}{\delta^2}\frac{U R_2^2 \left(-x^2+y^2\right)}{\left(x^2+y^2\right)^2} + \rho_1 g_x$$

$$\frac{\partial p}{\partial y} = -\frac{24\,\mu_1}{\delta^2}\frac{U R_2^2\, x\, y}{\left(x^2+y^2\right)^2} + \rho_1 g_y \qquad \text{(B-14)}$$

To obtain the pressure field, δ is assumed to be a function of x and y, however the variation of δ with x and y is disregarded, i.e., assuming the very small slope condition expressed by Eq. (B-3) and Eq. (B-4). Then, the result of integrating the above equation is

$$p(x,y) = \frac{12\,\mu_1\, U}{\delta^2}\frac{R_2^2\, x}{\left(x^2+y^2\right)^2} + \rho_1\left(g_x\, x + g_y\, y\right) + constant \qquad \text{(B-15)}$$

Excluding the gravity contribution (to be addressed separately), the equation can be expressed in polar coordinates as

$$p = \frac{n_1\,\mu_1}{\delta^2}\frac{dh}{dt}\frac{R_2^2\cos\theta}{r}\underset{\sim}{i_r} \qquad where \quad U \equiv \frac{dh}{dt} \qquad \text{(B-16)}$$

h is the change in height of the blob with respect to its initial reference position, and n_1 the viscosity flow channel coefficient for fluid stage *1*, i.e., $n_1 = 12$.

The force exerted on the moving *blob* due to the squeezing of fluid stage *1* is given as

$$F_{V_1} = 2\int_0^{\pi}\left(\frac{n_1\,\mu_1}{\delta^2}\frac{dh}{dt}\frac{R_2^2\cos\theta}{R_2}\right)\frac{\cos\theta}{\delta^2}\frac{dA}{\delta R_2\,d\theta} \tag{B-17}$$

where $R_2 = R_2(h\,(t))$ and $\delta = \delta(R_2(h\,(t)), h\,(t), \theta, t)$

Equation (B-17) can be expressed in terms of a squeeze shape coefficient f_1 as follows

$$\begin{aligned} F_{V_1} &= n_1\,\mu_1\frac{dh}{dt}f_1(h(t),t) \\ f_1(h(t),t) &= 2\,R_2^2\int_0^{\pi}\frac{\cos^2\theta}{\delta}\,d\theta \end{aligned} \tag{B-18}$$

The force exerted on the moving blob due to the shear against both walls ($z=\pm\delta/2$) is

$$\begin{aligned} F_{V_2} &= n_2\,\mu_2\,\frac{dh}{dt}\,f_2(h(t),t) \\ f_2(h(t),t) &= 2\int_0^{R_2}\int_0^{\pi}\frac{1}{\delta}\,r\,dr\,d\theta \end{aligned} \tag{B-19}$$

where: f_2 is denominated the shear shape coefficient; $n_2 = 12$ is the viscosity flow channel coefficient for fluid stage 2; and the force F_{V2} results from the integration of

$$|\,\tau_{xz}\,| = \mu_2\frac{\partial v_x}{\partial z}\bigg|_{z=\pm\frac{\delta}{2}} = \frac{6\,\mu_2}{\delta}\frac{dh}{dt} \tag{B-20}$$

For both f_1 and f_2, the integration of δ with respect to r and θ (or x and y) is relevant. In contrast, to obtain Eq. (B-15) local variations of δ with respect to r and θ are neglected when compared to the far field potential dependence.

B-3.1 Balance of Forces

Disregarding surface tension and surface effects, an integrated balance of forces for the *blob* (see **Figure B-2** below) can be expressed as follows

$$(M_2 + M_1)\frac{d^2h}{dt^2} = F_W - (F_B + F_{V_1} + F_{V_2})$$

$$(\rho_2 + \rho_1)\int_\Omega d\forall\, \frac{d^2h}{dt^2} = \rho_2 g \int_\Omega d\forall - \rho_1 g \int_\Omega d\forall - \int_{\partial\Omega_{xy}} p\, dA - \int_{\partial\Omega_z} 2\tau\, dA \qquad \text{(B-21)}$$

where: Ω represents the volume of the *blob*; $\partial\Omega_{xy}$ the surface of the *blob* in contact with fluid *1*; $\partial\Omega_z$ the surface of the *blob* in contact with the walls (assuming no encapsulation); F_W the weight of the blob; F_B the buoyancy; F_{V1} the viscous force on the *blob* due to fluid stage *1*; F_{V2} the viscous force on the *blob* due to the interaction with the walls; M_2 the mass of the blob; M_1 the virtual mass (associated with the kinetic energy to displace stage *1*); h the height of the center of the *blob* with respect to an initial position $h = h_0$. The volume of

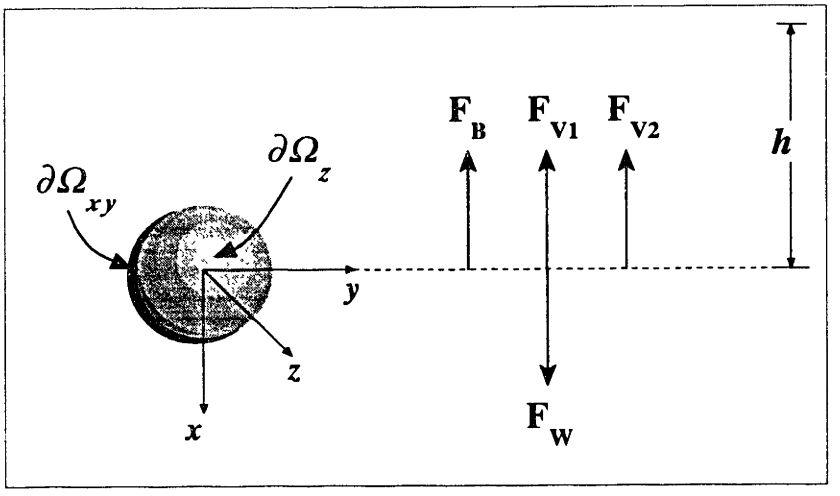

FIGURE B-2: Balance of forces for moving blob—disregarding surface tension and surface effects

the *blob* and scaled Reynolds number are given as

$$\int_\Omega d\forall = \forall_0 \qquad \text{(B-22)}$$

$$Re^* \equiv \frac{\rho_1 \frac{dh}{dt} R_2}{\mu_1}\left(\frac{\delta_0}{R_2}\right)^2 \qquad \text{(B-23)}$$

The scaled Reynolds number is based on the external flow (stage *1*) around the *blob*, a crack opening upper bound δ_0, and velocity (of order dh/dt).

Nondimensionalization of Eq. (B-21) is expressed as follows

$$\begin{aligned} \rho_1 &\leftarrow \frac{\rho_1}{\rho} & \rho_2 &\leftarrow \frac{\rho_2}{\rho} \\ \mu_1 &\leftarrow \frac{\mu_1}{\mu} & \mu_2 &\leftarrow \frac{\mu_2}{\mu} \\ \delta &\leftarrow \frac{\delta}{\delta_0} & R_2 &\leftarrow \frac{R_2}{L} \\ r &\leftarrow \frac{r}{L} & h &\leftarrow \frac{h}{L} \\ g &\leftarrow \frac{g}{G} & t &\leftarrow \frac{t}{\tau} \end{aligned} \tag{B-24}$$

$$\int_{\partial\Omega_z} \frac{dA}{\delta} \leftarrow \frac{\int_{\partial\Omega_z} \frac{dA}{\delta}}{\left(\frac{L^2}{\delta_0}\right)} \qquad \int_{\partial\Omega_{xy}} \frac{dA}{\delta} \leftarrow \frac{\int_{\partial\Omega_{xy}} \frac{dA}{\delta}}{\left(\frac{L^2}{\delta_0}\right)} \qquad \int_{\Omega} d\forall \leftarrow \frac{\int_{\Omega} d\forall}{L^2\,\delta_0} \tag{B-25}$$

$$\left[\frac{\rho\,\delta_0^2}{\mu\,\tau}\right](\rho_1 + \rho_2)\,\forall_0 \frac{d^2h}{dt^2} = \left[\frac{\rho\,G\,L\,\tau}{\mu}\left(\frac{\delta_0}{L}\right)^2\right](\rho_2 - \rho_1)\,g\,\forall_0 - (n_2\,\mu_2\,f_2 + n_1\,\mu_1\,f_1)\frac{dh}{dt} \tag{B-26}$$

A time scale and nondimensional number are obtained, i.e.,

$$\begin{aligned} \frac{\rho\,\delta_0^2}{\mu\,\tau} \equiv 1 \;\Rightarrow\; \tau &\equiv \frac{\rho\,\delta_0^2}{\mu} \\ G\,L^3\left(\frac{\rho}{\mu}\right)^2\left(\frac{\delta_0}{L}\right)^4 &\equiv N_G \end{aligned} \tag{B-27}$$

τ the time scale associated with the flow's unsteady inertia, and N_G a modified Darcy-Raleigh number (ratio of gravity to viscous forces). Equation (B-26) can be rewritten as

$$(\rho_1 + \rho_2)\,\forall_0 \frac{d^2h}{dt^2} - N_G\,(\rho_2 - \rho_1)\,g\,\forall_0 + (n_2\,\mu_2\,f_2(h) + n_1\,\mu_1\,f_1(h))\frac{dh}{dt} = 0 \tag{B-28}$$

This Ordinary Differential Equation incorporates: viscous effects spatial dependence by means of the two coefficients, f_1 and f_2; gravity-driven effects; and dynamic effects. To solve for h two initial conditions, $h(0)$ and $dh(0)/dt$, and the dependence of R_2 on h and t are needed.

B-4 Unbounded Cell and Parallel Plates

Assuming a constant crack opening and no boundaries (vide **Figure B-3**) on the x

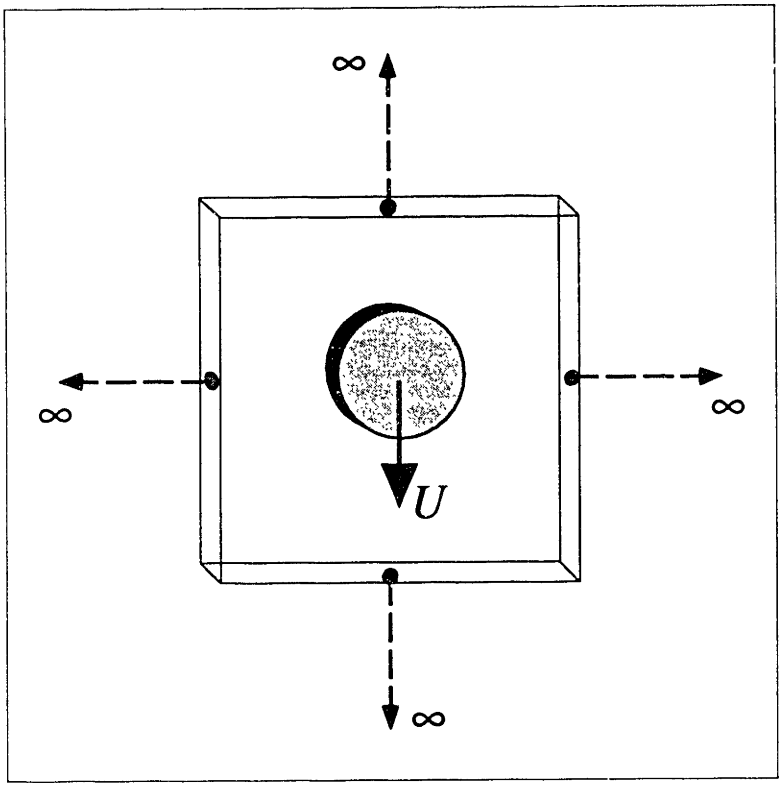

FIGURE B-3: Sketch of unbounded container with constant crack opening. Blob moving with downwards velocity $U = dh/dt$

and y planes, Eq. (B-28) reduces to

$$(1 + \rho_1)\frac{d^2h}{dt^2} - N_G(1 - \rho_1) + 12(1 + \rho_1)\frac{dh}{dt} = 0 \tag{B-29}$$

where the nondimensionalization constants, ρ and μ, were arbitrarily chosen as

$$\rho = \rho_2$$
$$\mu = \mu_2 \tag{B-30}$$

The solution for Eq. (B-29) can be obtained in closed-form and it's rather simple,

i.e.

$$h(t) = \frac{N_G\,(1 - \rho_1)\,t}{12\,(1 + \mu_1)} - \frac{N_G\,(1 - \rho_1^2)}{(12\,(1 + \mu_1))^2}\left(1 - e^{-\frac{12\,(1 + \mu_1)\,t}{(1 + \rho_1)}}\right) \tag{B-31}$$

the velocity, steady-state velocity and scaled Reynolds number are derived from above

$$U = \frac{dh}{dt} = \frac{N_G(1 - \rho_1)}{12\,(1 + \mu_1)}\left(1 - e^{-\frac{12(1 + \mu_1)\,t}{(1 + \rho_1)}}\right)$$

$$U_\infty = \frac{N_G\,(1 - \rho_1)}{12\,(1 + \mu_1)}\,\frac{L}{\tau} \tag{B-32}$$

$$Re^* \equiv \frac{\rho_1\,\bar{V}_\infty\,R_2}{\mu_1}\left(\frac{\delta_0}{R_2}\right)^2$$

Dynamical effects will prevail for time scales such that $t < t_{dyn}$, where

$$t_{dyn} \equiv \frac{(1 + \rho_1)}{12\,(1 + \mu_1)} \tag{B-33}$$

These solutions are used as a reference (compare against bounded and/or wedged solutions).

B-5 Unbounded Cell and Wedged Plates

The difficult for this case is the evaluation of the squeeze and shear shape functions, respectively, $f_1(h(t),t)$ and $f_2(h(t),t)$. In order to evaluate the shape functions it's first necessary to find the dilation rate, i.e., R_2 as a function of h.

The dilation rate of a *blob* within the wedge can be modeled as long as the crack opening is a known function of the in-plane variables (sketch shown in **Figure B-4**). Volume conservation is used to track the *blob* dilation rate (no leaks through the container walls).

Assuming a wedge shape independent of Y and symmetric with respect to X (vide

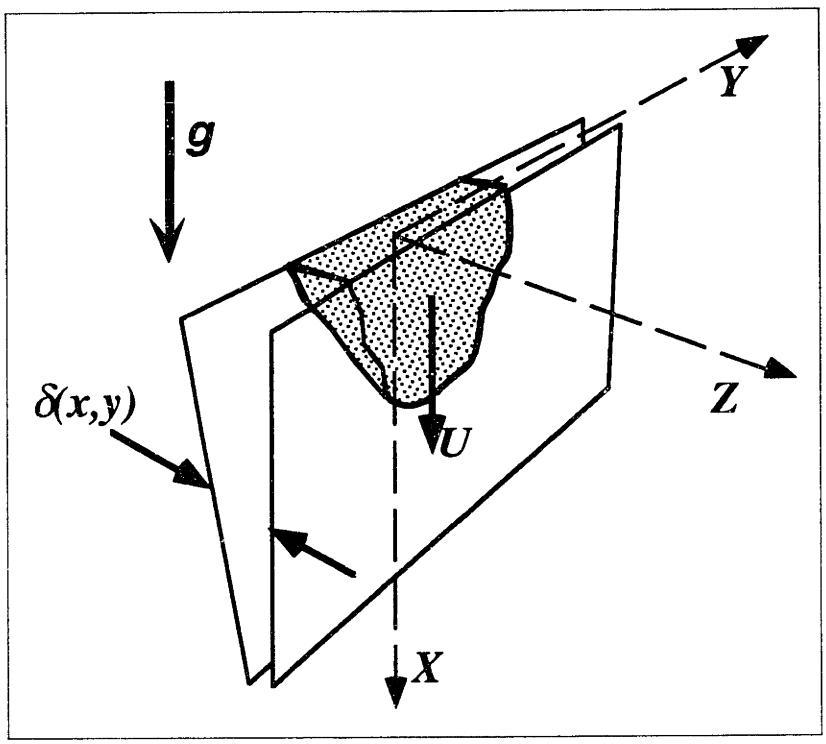

FIGURE B-4: Sketch of unbounded container with variable crack opening

Figure B-5), and a *blob* with initial radius R_{20}, the following volume dependences are obtained:

1) volume dependence for $h = 0$

$$\begin{aligned} \forall_0 &= 2\int_0^{\pi}\int_0^{R_2}\left(1-(1-\delta_m)\left|h+r\cos\theta\right|\right)r\,dr\,d\theta \\ &= \pi R_2^2\cdot 1-2(1-\delta_m)\left[\int_0^{\frac{\pi}{2}}\int_0^{R_2} r\cos\theta\, r\,dr\,d\theta+\int_{\frac{\pi}{2}}^{\pi}\int_0^{R_2}-r\cos\theta\, r\,dr\,d\theta\right] \\ &= \pi R_{20}^2-\frac{4}{3}(1-\delta_m)R_{20}^3 \end{aligned} \tag{B-34}$$

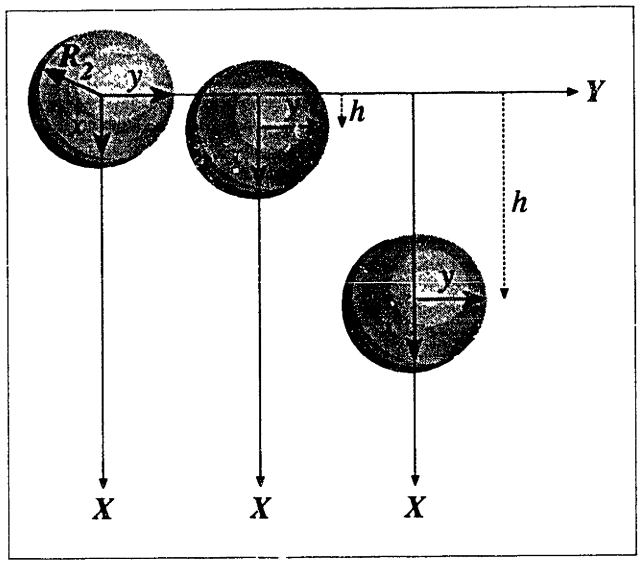

FIGURE B-5: Three possible height (h) positions of a *blob* (initial radius R_2) with respect to wedge center

2) volume dependence for $h < R_2$

$$\forall_0 = \pi R_2^2 \cdot 1 - 2(1 - \delta_m)\left[\int_0^{\frac{\pi}{2}}\int_0^{R_2}(h + r\cos\theta)\, r\, dr d\theta + \int_0^{\sqrt{R_2^2-h^2}}\int_{-h}^{0}(h+x)\, dxdy + \int_{\sqrt{R_2^2-h^2}}^{R_2}\int_{-\sqrt{R_2^2-y^2}}^{0}(h+x)\, dxdy + \int_0^{\sqrt{R_2^2-h^2}}\int_{-\sqrt{R_2^2-y^2}}^{-h}(-h-x)\, dxdy\right] \quad \text{(B-35)}$$

$$\forall_0 = \pi R_2^2 - 2(1-\delta_m)\left[\frac{\pi R_2^2 h}{2} + R_2^2\sqrt{R_2^2-h^2} - \frac{(R_2^2-h^2)^{\frac{3}{2}}}{3} - R_2^2 h \arcsin\left(\frac{\sqrt{R_2^2-h^2}}{R_2}\right)\right] \quad \text{(B-36)}$$

3) volume dependence for $h \geq R_2$

$$\begin{aligned}\forall_0 &= 2\int_0^{\pi}\int_0^{R_2}\left(1 - (1-\delta_m)(h + r\cos\theta)\right) r\, dr d\theta \\ &= \pi R_2^2 (1 - (1-\delta_m) h)\end{aligned} \quad \text{(B-37)}$$

where: δ_0 is the crack opening at $X = 0$; δ_m is the crack opening at $X = L$; δ_0 is the nondimensionalization variable for δ, δ_m (and δ_0); L is the nondimensionalization variable for X, r, R_2, h (and L), i.e.

$$\begin{aligned} \delta_0 &= 1 \qquad \overbrace{x} \\ X &= h + r\cos\theta \\ \delta &= 1 - (1 - \delta_m)|h + r\cos\theta| \end{aligned} \tag{B-38}$$

Experimentally it is easier to start tests with a *blob* positioned at $h \geq R_2$. Hence, only the dilation rate for $h \geq R_2$ will be analyzed.

Expressing Eq. (B-37) in terms of the initial volume (expressed below both in dimensional and nondimensional form) and initial blob position h_0

$$\begin{aligned} &\forall_0 = \pi R_{20}^2 (1 - (1 - \delta_m) h_0) \qquad \delta = 1 - (1 - \delta_m)(h + r\cos\theta) \\ &\forall_0 = \pi R_{20}^2 \left[\delta_0 - \frac{(\delta_0 - \delta_m) h_0}{L}\right] \qquad R_2^2 = \frac{\forall_0}{\pi (1 - (1 - \delta_m) h)} \end{aligned} \tag{B-39}$$

leads to a straightforward dependence of R_2 on h, i.e., inverse square-root. Substituting the above equation in Eq. (B-28) and expanding for the shape functions

$$\begin{aligned} &(1 + \rho_1) \forall_0 \frac{d^2h}{dt^2} - N_G (1 - \rho_1) \forall_0 + \\ &\frac{2 n_1 \mu_1 \forall_0}{\pi (1 - (1 - \delta_m) h)} \left[\int_0^\pi \frac{\cos^2\theta d\theta}{1 - (1 - \delta_m)(h + R_2 \cos\theta)}\right] \frac{dh}{dt} + \\ &2 n_2 \left[\int_0^\pi \int_0^{R_2} \frac{r dr d\theta}{1 - (1 - \delta_m)(h + r\cos\theta)}\right] \frac{dh}{dt} = 0 \end{aligned} \tag{B-40}$$

Recasting Eq. (B-40) in standard form

$$(1 + \rho_1) \forall_0 \frac{d^2h}{dt^2} - N_G (1 - \rho_1) \forall_0 + (n_1 \mu_1 f_1(h(t),t) + n_2 \mu_2 f_2(h(t),t)) \frac{dh}{dt} = 0 \tag{B-41}$$

where the squeeze and shear shape functions are given as

$$f_1 = 2R_2^2 \int_0^{\pi} \frac{\cos^2\theta}{\delta} d\theta = 2R_2^2 \int_0^{\pi} \frac{\cos^2\theta}{a + b\cos\theta} d\theta$$

$$f_2 = 2 \int_0^{R_2} \int_0^{\pi} \frac{1}{\delta} r\, dr d\theta = 2 \int_0^{R_2} \int_0^{\pi} \frac{1}{a + c\, r \cos\theta} r\, dr d\theta \qquad \text{(B-42)}$$

$$a \equiv (1 - (1 - \delta_m)\, h) \qquad |a| > |b|$$
$$b \equiv -(1 - \delta_m)\, R_2 \qquad |a| > |c|$$
$$c \equiv -(1 - \delta_m)$$

Integrating the r.h.s. of Eq. (B-42) for the squeeze shape function leads to

$$\int_0^{\pi} \frac{\cos^2\theta}{a + b\cos\theta} d\theta = \frac{-2 \arctan\left(\frac{(-a+b)}{\sqrt{a^2-b^2}\,(1+\cos\theta)}\right)}{\sqrt{a^2-b^2}}\Bigg|_0^{\pi}$$

$$- \left[\left(\frac{2a}{b^2} + \frac{2}{b}\right)\frac{\theta}{2} - \frac{\theta}{b} - \frac{\sin\theta}{b}\right. \qquad \text{(B-43)}$$

$$\left. + \left(-2 + \frac{2a^2}{b^2}\right) \frac{\arctan\left(\frac{(-a+b)}{\sqrt{a^2-b^2}\,(1+\cos\theta)}\right)}{\sqrt{a^2-b^2}}\right]$$

For $\theta = 0$ the first term on the r.h.s. of Eq. (B-43) is zero. For $\theta = \pi$ the following limit applies

$$\lim_{\theta \to \pi} \left[\frac{\arctan\left(\frac{(-a+b)}{\sqrt{a^2-b^2}\,(1+\cos\theta)}\right)}{\sqrt{a^2-b^2}}\right] = -\frac{1}{2}\frac{\pi}{\sqrt{a^2-b^2}} \qquad \text{(B-44)}$$

Hence, the squeeze shape function is given as

$$f_1 = 2 R_2^2 \pi \frac{a}{b^2}\left(\frac{a - \sqrt{a^2 - b^2}}{\sqrt{a^2 - b^2}}\right)$$

$$\begin{aligned} a &= (1 - (1 - \delta_m) h) \\ b &= -(1 - \delta_m) R_2 \\ R_2^2 &= \frac{\forall_0}{\pi (1 - (1 - \delta_m) h)} \end{aligned} \tag{B-45}$$

$$f_1 = 2 R_2^2 \pi \frac{a}{b^2}\left(\frac{1 - \sqrt{1 - \left(\frac{b}{a}\right)^2}}{\sqrt{1 - \left(\frac{b}{a}\right)^2}}\right)$$

Analogously, the shear shape function is given as

$$\begin{aligned} f_2 &= 2 \int_0^{R_2} \int_0^{\pi} \frac{1}{a + c\, r \cos\theta} r\, dr d\theta \\ &= 2 \int_0^{R_2} \frac{\pi r}{\sqrt{a^2 - c^2 r^2}} dr \\ &= 2\pi \frac{a}{c^2}\left(1 - \sqrt{1 - \left(\frac{R_2^2\, c}{a}\right)^2}\right) \end{aligned} \tag{B-46}$$

$$\begin{aligned} a &= (1 - (1 - \delta_m) h) \\ c &= -(1 - \delta_m) \\ R_2^2 &= \frac{\forall_0}{\pi (1 - (1 - \delta_m) h)} \end{aligned}$$

To test the limit behavior of both functions

- for f_1, taking $\left|\frac{b}{a}\right| << 1$ leads to $f_1 \approx \pi R_2^2$
- for f_2, taking $\left|\frac{R_2\, c}{a}\right| << 1$ leads to $f_2 \approx \pi R_2^2$

B-6 Correction for Boundary Effects

A doublet in an unbounded media can be expressed as

$$\omega_n = -\frac{\Gamma_n e^{i\alpha_n}}{z - z_n} \tag{B-47}$$

where: Γ_n is the doublet strength—same as μ in Eq. (B-12); α_n is the angle of the doublet with the x-axis; $\omega_n = \phi_n + i\psi_n$ is the complex potential; $\frac{d\omega_n}{dz} = u_x - iu_y$ the in-plane velocity field.

A cylinder with cross section radius R moving in an infinite medium with velocity U can be represented by a doublet with strength $\Gamma_0 = UR^2$, see Eq. (B-10). If, in addition to the moving cylinder, there is another doublet with strength Γ_1 outside the cylinder, the boundary condition for $| z - z_0 | = R$ would be violated, unless an additional image (with respect to the cylinder radius) doublet is introduced, e.g.

$$\omega = -\frac{\Gamma_0 e^{i\alpha_0}}{z} - \frac{\Gamma_1 e^{i\alpha_1}}{z - f_{10}} + \frac{R^2}{f_{10}^2}\frac{\Gamma_1 e^{-i\alpha_1}}{(z - f_{20})} \tag{B-48}$$

The equation above expresses the circle theorem—vide Milne-Thomson (1968). The first term represents a cylinder located at $z_0 = 0$, strength Γ_0 and angle α_0 with the x-axis. The second term a doublet at $z_1 = f_{10}$ with strength Γ_1. The last term, an image of the doublet Γ_1, with strength $\Gamma_2 = \frac{R^2}{f_{10}^2}\Gamma_1$ at $z_2 = f_{20}$ ($f_{20} \cdot f_{10} = R^2$).

The introduction of boundaries can be simulated by a variety of sources, sinks and doublets. In particular, the following is the configuration of interest

- at time $t = 0$, assume a cylinder with initial cross-sectional radius $R_2 = R_{20}$, moving with velocity U along the positive direction of the x-axis at position $-s = -(L - h_0)$;
- at $X = 0$ assume an end-boundary;
- the movement of the cylinder is characterized by a doublet of strength Γ_0;
- to simulate the presence of the end-boundary at $X = 0$, an image cylinder is introduced at $z_1 = s$. Its doublet strength is $\Gamma_1 = \Gamma_0$ and the direction $\alpha_0 = \pi$.

The complex potential associated to the two doublets is

$$\begin{aligned} \omega_0 &= -\frac{U R_2^2}{z + s} \\ \omega_1 &= +\frac{U R_2^2}{z - s} \end{aligned} \tag{B-49}$$

The two doublets above correctly account for the presence of the end-boundary at $X = 0$. However, the boundary conditions at $| z + s | = R_2$ and $| z - s | = R_2$ can only be attained if image doublets with respect to the cylinders are introduced, i.e.

$$\begin{aligned} \omega_2 &= -\frac{\Gamma_2}{z + x_2} \\ \omega_3 &= \frac{\Gamma_3}{z - x_3} \\ \Gamma_2 &= \frac{R_2^2}{(2s)^2}\Gamma_0 = \frac{R_2^2}{(2s)^2} U R_2^2 = U R_2^2 \frac{R_2^2}{(2s)^2} \\ \Gamma_3 &= \Gamma_2 \\ x_2 &= x_3 = s - \frac{R_2^2}{2s} \end{aligned} \tag{B-50}$$

The boundary conditions at $| z + s | = R_2$ and $| z - s | = R_2$ are then satisfied, but another set of doublets is needed to correct for the presence of the end-boundary, i.e.

$$\begin{aligned} \omega_4 &= -\frac{\Gamma_4}{z + x_4} \\ \omega_5 &= \frac{\Gamma_5}{z - x_5} \\ \Gamma_4 &= \frac{R_2^2}{(s + x_2)^2}\Gamma_2 = \frac{R_2^2}{(s + x_2)^2}\frac{R_2^2}{(s + x_0)^2}\Gamma_0 = \frac{R_2^4}{\left(2s - \frac{R_2^2}{2s}\right)^2 (2s)^2} U R_2^2 \\ \Gamma_5 &= \Gamma_4 \\ x_4 &= x_5 = s - \frac{R_2^2}{2s - \frac{R_2^2}{2s}} = s - \frac{R_2^2}{s + x_2} = s - \frac{R_2^2}{s + x_3} \end{aligned} \tag{B-51}$$

To compensate for both the cylinders boundaries and the end-boundary an infinite series of (decreasing strength) doublets, as a function of powers of R_2/s, is introduced. Restricting interest to the values of s such $s > R_2$, contributions of the higher order dou-

blets to the series should become negligible as the power exponent grows. A sketch of the doublet series is shown in **Figure B-6** below.

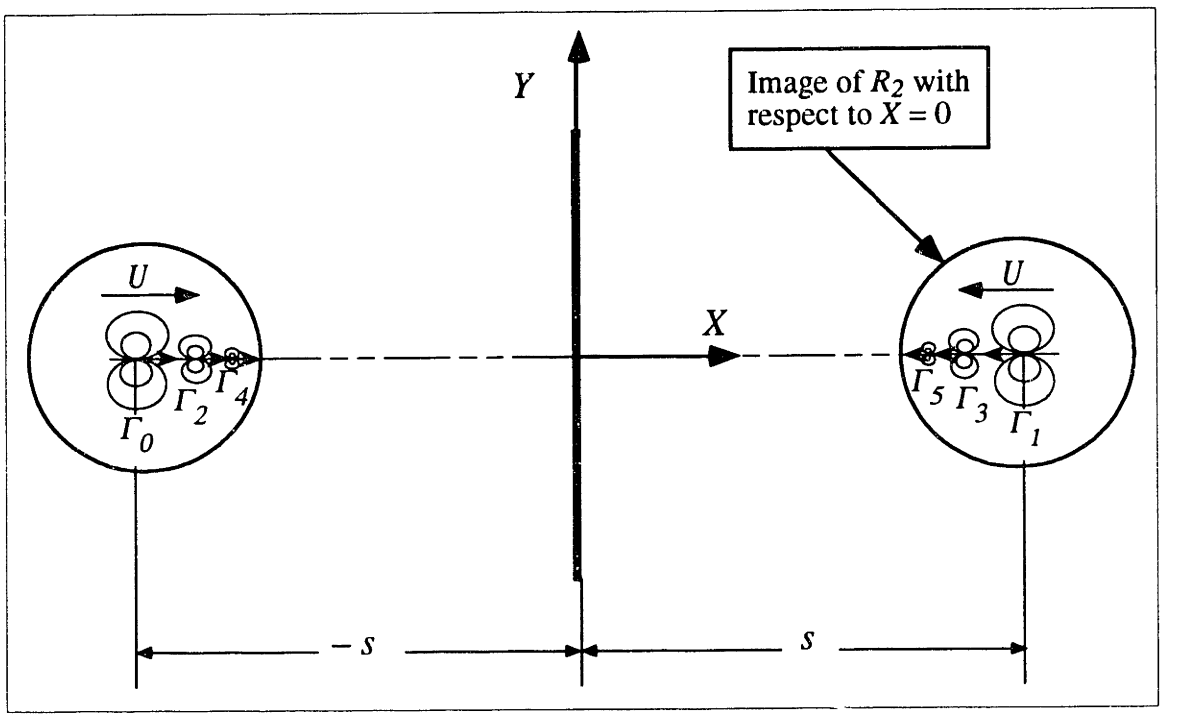

FIGURE B-6: Doublet series simulating the presence of an end-boundary at $X = 0$ and a cylinder moving with velocity U at $x = -s$

The potential ω and the velocity field can be written as

$$\omega = -\sum_{l=0}^{\infty} \frac{\Gamma_{2l}}{z + x_{2l}} + \sum_{l=0}^{\infty} \frac{\Gamma_{2l+1}}{z - x_{2l+1}} \tag{B-52}$$

$$\begin{aligned} \Gamma_0 &= U R_2^2 \\ \Gamma_1 &= U R_2^2 \\ \Gamma_{2l} &= \frac{R_2^2}{(s + x_{2l-2})^2} \Gamma_{2l-2} \\ \Gamma_{2l+1} &= \frac{R_2^2}{(s + x_{2l-1})^2} \Gamma_{2l-1} \\ \Gamma_{2l} &= \Gamma_{2l+1} \end{aligned} \tag{B-53}$$

$$
\begin{aligned}
x_0 &= s \\
x_1 &= s \\
x_{2l} &= s - \frac{R_2^2}{s + x_{2l-2}} \\
x_{2l+1} &= s - \frac{R_2^2}{s + x_{2l-1}} \\
x_{2l} &= x_{2l+1}
\end{aligned}
\tag{B-54}
$$

$$
\begin{aligned}
\frac{d\omega}{dz} &= u_x - i\,u_y \\
&= \sum_{l=0}^{\infty} \left(\frac{\Gamma_{2l}}{(z + x_{2l})^2} - \frac{\Gamma_{2l}}{(z - x_{2l})^2} \right) \\
&= \sum_{l=0}^{\infty} \Gamma_{2l} \left(\frac{(\bar{z} + x_{2l})^2}{(z + x_{2l})^2 (\bar{z} + x_{2l})^2} - \frac{(\bar{z} - x_{2l})^2}{(z - x_{2l})^2 (\bar{z} - x_{2l})^2} \right) \\
&= \sum_{l=0}^{\infty} \Gamma_{2l} \left(\frac{\bar{z}^2 + 2\,x_{2l}\,\bar{z} + x_{2l}^2}{\left(z\,\bar{z} + x_{2l}(z + \bar{z}) + x_{2l}^2\right)^2} - \frac{\bar{z}^2 - 2\,x_{2l}\,\bar{z} + x_{2l}^2}{\left(z\,\bar{z} - x_{2l}(z + \bar{z}) + x_{2l}^2\right)^2} \right) \\
&= \sum_{l=0}^{\infty} \Gamma_{2l} \left(\frac{(x^2 - y^2) - i\,2\,x\,y + 2\,x_{2l}(x - iy) + x_{2l}^2}{\left(x^2 + y^2 + 2\,x_{2l}\,x + x_{2l}^2\right)^2} \right. \\
&\qquad \left. - \frac{(x^2 - y^2) - i\,2\,x\,y - 2\,x_{2l}(x - iy) + x_{2l}^2}{\left(x^2 + y^2 - 2\,x_{2l}\,x + x_{2l}^2\right)^2} \right) \\
&= \sum_{l=0}^{\infty} \Gamma_{2l} \left(\left[\frac{(x + x_{2l})^2 - y^2}{\left((x + x_{2l})^2 + y^2\right)^2} - \frac{(x - x_{2l})^2 - y^2}{\left((x - x_{2l})^2 + y^2\right)^2} \right] \right. \\
&\qquad \left. - i \left[\frac{2\,y\,(x + x_{2l})}{\left((x + x_{2l})^2 + y^2\right)^2} - \frac{2\,y\,(x - x_{2l})}{\left((x - x_{2l})^2 + y^2\right)^2} \right] \right)
\end{aligned}
\tag{B-55}
$$

$$
\begin{aligned}
u_x &= \sum_{l=0}^{\infty} \Gamma_{2l} \left[\frac{(x + x_{2l})^2 - y^2}{\left((x + x_{2l})^2 + y^2\right)^2} - \frac{(x - x_{2l})^2 - y^2}{\left((x - x_{2l})^2 + y^2\right)^2} \right] \\
u_y &= \sum_{l=0}^{\infty} \Gamma_{2l} \left[\frac{2\,y\,(x + x_{2l})}{\left((x + x_{2l})^2 + y^2\right)^2} - \frac{2\,y\,(x - x_{2l})}{\left((x - x_{2l})^2 + y^2\right)^2} \right]
\end{aligned}
\tag{B-56}
$$

The hydrostatic pressure term is obtained by integrating the following

$$
\begin{aligned}
\frac{\partial p}{\partial x} &= -\frac{12\,\mu_1}{\delta^2}\,u_x \\
\frac{\partial p}{\partial y} &= -\frac{12\,\mu_1}{\delta^2}\,u_y
\end{aligned}
\tag{B-57}
$$

i.e.

$$p = -\frac{12\mu_1}{\delta^2}\sum_{l=0}^{\infty}\Gamma_{2l}\left(\frac{x - x_{2l}}{(x - x_{2l})^2 + y^2} - \frac{x + x_{2l}}{(x + x_{2l})^2 + y^2}\right) \tag{B-58}$$

To facilitate the integration of p (needed for the squeeze shape function), Eq. (B-58) is recasted in terms of a polar system of coordinates, centered at $z = -s$

$$p = -\frac{12\mu_1}{\delta^2}\sum_{l=0}^{\infty}\Gamma_{2l}\left(\frac{-s - x_{2l} + R_2\cos\theta}{(-s - x_{2l} + R_2\cos\theta)^2 + R_2^2\sin^2\theta} - \frac{-s + x_{2l} + R_2\cos\theta}{(-s + x_{2l} + R_2\cos\theta)^2 + R_2^2\sin^2\theta}\right) \tag{B-59}$$

Thence, integrating p to obtain the contribution of the squeeze shape function leads to

$$F_{V_1} = 2n_1\mu_1 R_2\sum_{l=0}^{\infty}\Gamma_{2l}\left\{-\int_0^{\pi}\frac{1}{\delta}\frac{(-s - x_{2l} + R_2\cos\theta)\cos\theta}{(-s - x_{2l} + R_2\cos\theta)^2 + R_2^2\sin^2\theta}d\theta + \int_0^{\pi}\frac{1}{\delta}\frac{(-s + x_{2l} + R_2\cos\theta)\cos\theta}{(-s + x_{2l} + R_2\cos\theta)^2 + R_2^2\sin^2\theta}d\theta\right\} \tag{B-60}$$

These integrals can be rewritten as

$$-\int_0^{\pi}\frac{1}{\delta}\frac{R_2}{R_2^2}\frac{\left(\frac{-s - x_{2l}}{R_2} + \cos\theta\right)\cos\theta}{\left(\frac{-s - x_{2l}}{R_2} + \cos\theta\right)^2 + \sin^2\theta}d\theta + \int_0^{\pi}\frac{1}{\delta}\frac{R_2}{R_2^2}\frac{\left(\frac{-s + x_{2l}}{R_2} + \cos\theta\right)\cos\theta}{\left(\frac{-s + x_{2l}}{R_2} + \cos\theta\right)^2 + \sin^2\theta}d\theta$$

$$= -\frac{1}{R_2}\int_0^{\pi}\frac{1}{\delta}\frac{a\cos\theta\,d\theta}{(a^2+1) + 2a\cos\theta} - \frac{1}{R_2}\int_0^{\pi}\frac{1}{\delta}\frac{\cos^2\theta\,d\theta}{(a^2+1) + 2a\cos\theta} \tag{B-61}$$

$$+\frac{1}{R_2}\int_0^{\pi}\frac{1}{\delta}\frac{b\cos\theta\,d\theta}{(b^2+1) + 2b\cos\theta} + \frac{1}{R_2}\int_0^{\pi}\frac{1}{\delta}\frac{\cos^2\theta\,d\theta}{(b^2+1) + 2b\cos\theta}$$

where

$$a = -\frac{(s + x_{2l})}{R_2}$$
$$b = -\frac{(s - x_{2l})}{R_2} \tag{B-62}$$

Reexpressing Eq. (B-60)

$$F_{V_1} = 2 n_1 \mu_1 \sum_{l=0}^{\infty} \Gamma_{2l} \left\{ - \int_0^{\pi} \frac{1}{\delta} \frac{a \cos\theta \, d\theta}{(a^2 + 1) + 2a \cos\theta} - \int_0^{\pi} \frac{1}{\delta} \frac{\cos^2\theta \, d\theta}{(a^2 + 1) + 2a \cos\theta} \right.$$
$$\left. + \int_0^{\pi} \frac{1}{\delta} \frac{b \cos\theta \, d\theta}{(b^2 + 1) + 2b \cos\theta} + \int_0^{\pi} \frac{1}{\delta} \frac{\cos^2\theta \, d\theta}{(b^2 + 1) + 2b \cos\theta} \right\} \tag{B-63}$$

B-7 Bounded Cell and Parallel Plates

Assuming the nondimensional value of $\delta = 1$ for parallel plates, the viscous force

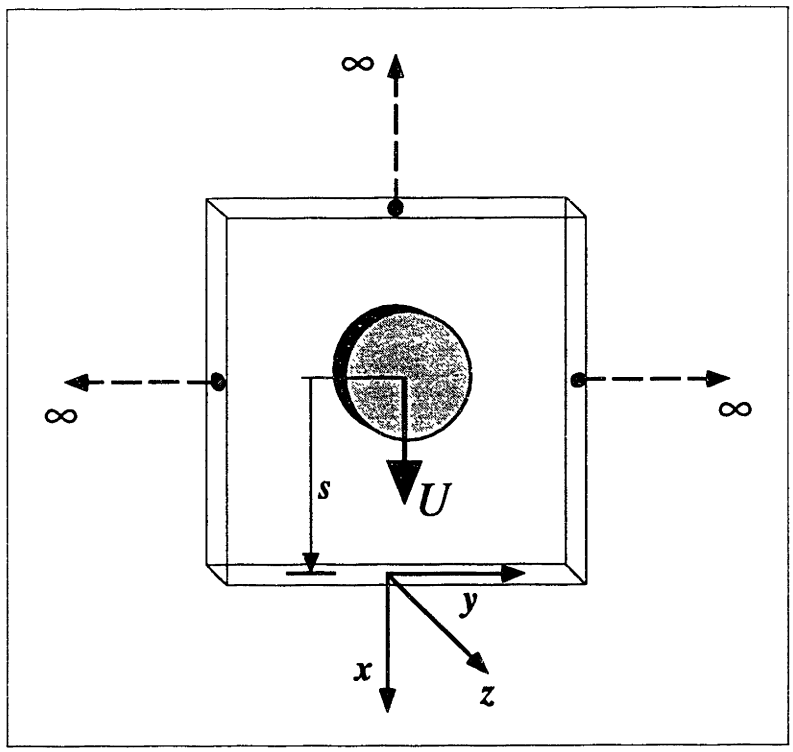

FIGURE B-7: Sketch of bounded cell (at $X = 0$) with parallel plates

contribution due to the squeezing of fluid stage *1* (in the presence of an end-boundary located at $X = 0$) is

$$\begin{aligned} F_{V_1} &= n_1 \mu_1 \frac{dh}{dt} f_1(h) \\ f_1(h) &= \pi R_2^2 \sum_{l=0}^{\infty} \overline{\Gamma_{2l}} \left(\frac{R_2^2}{(1-h+x_{2l})^2} + 1 \right) \end{aligned} \tag{B-64}$$

where

$$\begin{aligned} \overline{\Gamma_0} &\equiv 1 \\ \overline{\Gamma_{2l}} &\equiv \frac{\Gamma_{2l}}{U R_2^2} \\ \overline{\Gamma_{2l}} &= \frac{R_2^2}{(1-h+x_{2l-2})^2} \Gamma_{2l-2} \\ x_0 &= 1-h \\ x_{2l} &= (1-h) - \frac{R_2^2}{(1-h+x_{2l-2})} \end{aligned} \tag{B-65}$$

$$\underbrace{|a| > 1}$$

$$\int_0^{\pi} \frac{a\cos\theta \, d\theta}{(a^2+1) + 2a\cos\theta} = -\frac{\pi}{a^2-1} \tag{B-66}$$

$$\int_0^{\pi} \frac{\cos^2\theta \, d\theta}{(a^2+1) + 2a\cos\theta} = \frac{\pi}{2} \frac{a^2+1}{a^2(a^2-1)}$$

$$\underbrace{|b| < 1 \quad b \neq 0} \qquad \underbrace{b = 0}$$

$$\int_0^{\pi} \frac{b\cos\theta \, d\theta}{(b^2+1) + 2b\cos\theta} = -\frac{\pi b^2}{1-b^2} \qquad 0 \tag{B-67}$$

$$\int_0^{\pi} \frac{\cos^2\theta \, d\theta}{(b^2+1) + 2b\cos\theta} = \frac{\pi}{2} \frac{1+b^2}{1-b^2} \qquad \frac{\pi}{2}$$

i.e., the shape functions are given as

$$
\begin{aligned}
n_1 &= n_2 = 12 \\
\forall_0 &= \pi R_2^2 \cdot 1 \\
f_2 &= \pi R_2^2 \\
f_1(h) &= \pi R_2^2 \bar{f}_1(h) \\
\bar{f}_1(h) &= \sum_{l=0}^{\infty} \Gamma_{2l} \left(\frac{R_2^2}{((1-h) + x_{2l})^2} + 1 \right)
\end{aligned}
\tag{B-68}
$$

B-8 Bounded Cell and Wedged Plates

Again, assuming the nondimensional crack opening variation as

$$
\begin{aligned}
\delta &= 1 - (1 - \delta_m)(h + r\cos\theta) \\
h &= 1 - s \\
r &= R_2
\end{aligned}
\tag{B-69}
$$

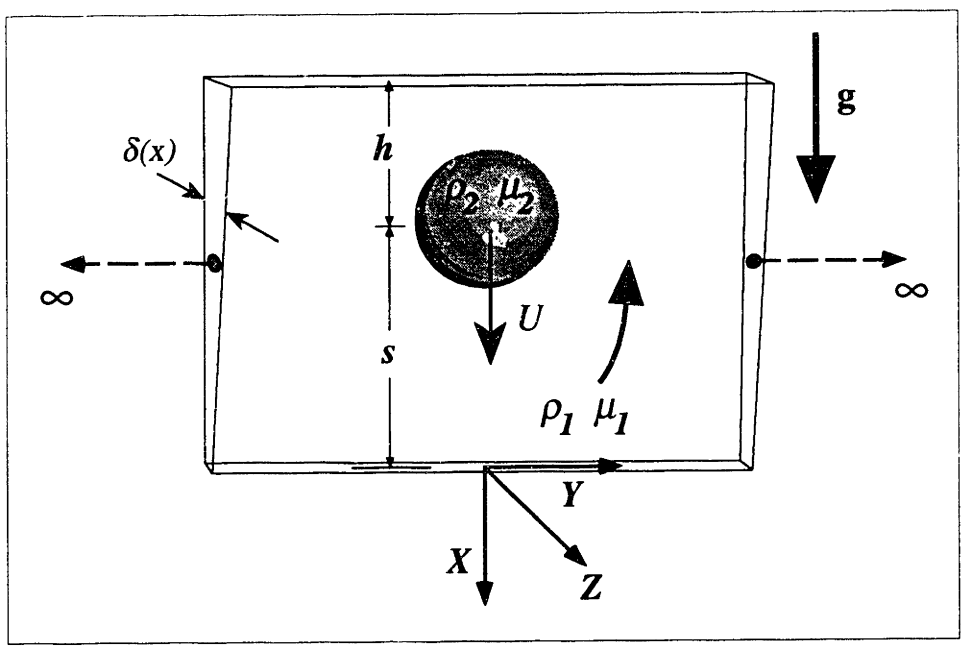

FIGURE B-8: Sketch of bounded cell (at $X = 0$) with wedged plates

or in terms of two extra coefficients, c and d

$$\begin{aligned} \delta &= c + d\cos\theta \\ c &= 1 - (1 - \delta_m)\, h \\ d &= -(1 - \delta_m)\, R_2 \end{aligned} \tag{B-70}$$

where

$$\begin{aligned} c &\neq \frac{(1 + a^2)d}{2a} \\ a &= -\frac{(s + x_{21})}{R_2} \\ b &= -\frac{(s - x_{21})}{R_2} \end{aligned} \tag{B-71}$$

For $|a| > 1$

$$\begin{aligned} \int_0^{\pi} \frac{1}{\delta} \frac{a\cos\theta\, d\theta}{\left((a^2+1) + 2a\cos\theta\right)} &= \frac{\pi a}{(1+a^2)d - 2ac}\left(\frac{a^2+1}{a^2-1} - \frac{c}{\sqrt{c^2-d^2}}\right) \\ \int_0^{\pi} \frac{1}{\delta} \frac{\cos^2\theta\, d\theta}{\left((a^2+1) + 2a\cos\theta\right)} &= \frac{\pi}{2ad} + \frac{\pi}{(1+a^2)d - 2ac}\left(-\frac{(a^2+1)^2}{2(a^2-1)a} + \frac{c^2}{d\sqrt{c^2-d^2}}\right) \end{aligned} \tag{B-72}$$

For $0 \leq |b| < 1$

$$\begin{aligned} \int_0^{\pi} \frac{1}{\delta} \frac{b\cos\theta\, d\theta}{\left((b^2+1) + 2b\cos\theta\right)} &= \frac{\pi b}{(1+b^2)d - 2bc}\left(\frac{1+b^2}{1-b^2} - \frac{c}{\sqrt{c^2-d^2}}\right) \\ &= 0 \quad ; \quad b = 0 \\ \int_0^{\pi} \frac{1}{\delta} \frac{\cos^2\theta\, d\theta}{\left((b^2+1) + 2b\cos\theta\right)} &= \frac{\pi}{2bd} + \frac{\pi}{(1+b^2)d - 2bc}\left(\frac{c^2}{d\sqrt{c^2-d^2}} - \frac{(1+b^2)^2}{2(1-b^2)b}\right) \\ &= \frac{\pi c}{d^2}\left(\frac{c}{\sqrt{c^2-d^2}} - 1\right) \quad ; \quad b = 0 \end{aligned} \tag{B-73}$$

Then, assume

$$\begin{aligned} b &\neq 0 \\ c &\neq \frac{(1+a^2)d}{2a} \\ |c| &> |d| \\ c &\neq \frac{(1+b^2)d}{2b} \end{aligned} \tag{B-74}$$

leads to

$$F_{V_1} = \pi n_1 \mu_1 \sum_{l=0}^{\infty} \Gamma_{2l} \left\{ \left(\frac{1}{bd} - \frac{1}{ad}\right) - \frac{a^2+1}{a\left((1+a^2)d-2ac\right)} - \frac{b^2+1}{b\left((1+b^2)d-2bc\right)} + \frac{2c(ad-c)}{d\sqrt{c^2-d^2}\left((1+a^2)d-2ac\right)} - \frac{2c(bd-c)}{d\sqrt{c^2-d^2}\left((1+b^2)d-2bc\right)} \right\} \tag{B-75}$$

otherwise assuming

$$\begin{aligned} b &= 0 \\ c &\neq \frac{(1+a^2)d}{2a} \\ |c| &> |d| \end{aligned} \tag{B-76}$$

leads to

$$F_{V_1} = \pi n_1 \mu_1 \sum_{l=0}^{\infty} \Gamma_{2l} \left\{ -\frac{1}{ad} - \frac{a^2+1}{a\left((1+a^2)d-2ac\right)} + \frac{2c(ad-c)}{d\sqrt{c^2-d^2}\left((1+a^2)d-2ac\right)} + \frac{2c}{d^2}\left(-1+\frac{c}{\sqrt{c^2-d^2}}\right) \right\} \tag{B-77}$$

APPENDIX C

An Analytical Algorithm for Encapsulated Multilayer Analysis

C-1 Modeling Encapsulated Flows

The previous Appendix presented an analysis of the in-plane *blob* motion. In contrast, this Appendix will focus on characterizing the transversal *blob* motion. There are four cases of interest:

1) *Blob* fully attached to both walls;

2) *Blob* attached to one wall only;

3) *Blob* in transition to detachment from the walls;

4) *Blob* detached from both walls.

Item *1)* was already studied in **Appendix B**. Item *3)* will not be addressed in this work—albeit its importance very little progress has been made to date to characterize and quantify the various parameters influencing the transition process. Items *2)* and *4)* are addressed here.

C-2 Matching Velocities, Flow Rates and Shear Boundary Conditions

Assuming a multiple n-layer flow field within a narrow channel, and for each layer i, with thickness d_i, an independent set of coordinates z_i —vide Figure **C-1**. The velocity flow field for each layer is

$$u_i(z_i) = a_i z_i^2 + b_i z_i + c_i \quad ; \qquad 1 \le i \le n \tag{C-1}$$

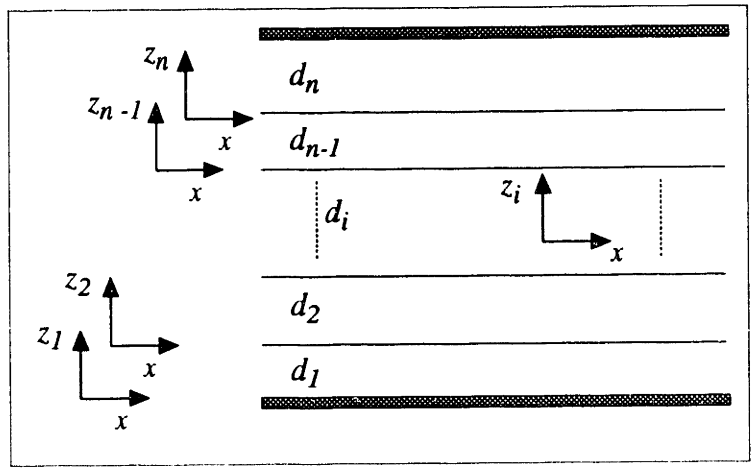

FIGURE C-1: Multiple fluid stages flow. Each layer i characterized by system of coordinates (x,y,z_i) and thickness d_i

Boundary conditions (BCs) can be expressed as follows:

I. Velocity boundary conditions at both walls

$$\begin{aligned} u_1 (z_1 = 0) &= 0 \\ u_n (z_n = d_n) &= 0 \end{aligned} \tag{C-2}$$

II. Velocity boundary conditions for each fluid interface

$$u_i (z_i = 0) = u_{i-1} (z_{i-1} = d_{i-1}) \quad ; \qquad 2 \le i \le n \tag{C-3}$$

III. Shear boundary conditions for each fluid interface

$$\mu_i \frac{\partial u_i}{\partial z_i} (z_i = 0) = \mu_{i-1} \frac{\partial u_{i-1}}{\partial z_{i-1}} (z_{i-1} = d_{i-1}) \quad ; \qquad 2 \le i \le n \tag{C-4}$$

In addition, mass conservation leads to

$$\int_0^{d_i} u_i \, dz_i = q_i \quad ; \qquad 1 \le i \le n \tag{C-5}$$

where q_i is the **volume flow rate per unit of channel length** for stage i.

Substituting BCs *I*, *II*, and *III* in Eq. (C-1) leads to the following recursive rela-

tions

$$\begin{aligned} c_1 &= 0 \\ b_i &= \sum_{k=2}^{i} \left[2 \frac{\mu_{k-1}}{\mu_i} a_{k-1} d_{k-1} \right] + \frac{\mu_1}{\mu_i} b_1 \quad ; \quad 2 \le i \le n \\ c_i &= \sum_{k=2}^{i} \left[a_{k-1} d_{k-1}^2 + b_{k-1} d_{k-1} \right] \quad ; \quad 2 \le i \le n \end{aligned} \tag{C-6}$$

and integrating Eq. (C-5)

$$q_i = \frac{1}{3} a_i d_i^3 + \frac{1}{2} b_i d_i^2 + c_i d_i \quad ; \quad 1 \le i \le n \tag{C-7}$$

The previous two set of equations can be recasted as a matrix problem like

$$\mathbf{M}\,\mathbf{a} = \mathbf{q} \tag{C-8}$$

where: $\mathbf{q}$ is the array $(q_1, q_2, ..., q_n)$, $\mathbf{a}$ is the array $(a_1, a_2, ..., a_n)$, and M is the matrix of polynomial coefficients in Eq. (C-7) collected in terms of $\mathbf{a}$. To form the matrix M, the coefficient b_1 is expressed as a function of the remaining coefficients b_i $(2 \le i \le n)$ and c_i $(1 \le i \le n)$.

C-3 The Energy Balance

The energy equation—vide Dussan (1979) and Joseph, Nguyen et al. (1984)—governing the flow of immiscible incompressible fluids can be expressed as

$$\begin{aligned} &\frac{d}{dt} \int_V \left[\frac{1}{2} \rho \, |u|^2 + \rho \, g \, z \right] dV + \frac{d}{dt} \oint_S \sigma \, dS = \\ &\int_S \frac{d\sigma}{dt} dS + \oint_{\partial S} \sigma \, \tau \cdot \mathbf{U} dl + \int_{\partial V} \mathbf{u} \cdot (\mathbf{T} \cdot \mathbf{n}) d(\partial V) + \int_V \text{trace}(\mathbf{TD}) dV \end{aligned} \tag{C-9}$$

The terms on the l.h.s. express, respectively, variations on kinetic energy, potential energy, and surface energy. Whereas, the terms on the r.h.s., surface tension path dependence, contact line dissipation, traction boundary dissipation, and stress volumetric dissipation. Assuming the simplifications described in **Appendix A**, only the last two terms on the

r.h.s. are of interest, and they can be simplified as follows

$$\sum_{i=1}^{n} \mu_i \int_0^{d} \left[\frac{\partial u_i}{\partial z_i}\right]^2 dz_i = -2\frac{dp}{dx}\sum_{i=1}^{n} q_i \tag{C-10}$$

The surface affinity effects are neglected in the derivation. As demonstrated in the experiments presented, surface affinity and wetting conditions play a key role in the development of encapsulation instabilities. However, the goal is to characterize the final thickness and flow rate of encapsulated layers, not their development. Very little progress has been made to date to characterize and quantify the transition process.

C-4 Minimizing Energy Dissipation and Maximizing Encapsulated Flow

The formulation derived in **Sections C-2** and **C-3**, is applied to the following cases of interest:

- symmetrical tri-layer (two equal outer layers of fluid 1, one inner layer of fluid 2) with known fluid properties, i.e., densities (ρ_1, ρ_2, ρ_1) and viscosities (μ_1, μ_2, μ_1); unknown layer thicknesses (δ_1, δ_2, δ_1); unknown volume (per unit of length) flow rates (q_1, q_2, q_1)—the total volume flow rate ($2\,q_1 + q_2$) is known.
- bi-layer (one layer of fluid 1, one layer of fluid 2) with known fluid properties, i.e., densities (ρ_1, ρ_2) and viscosities (μ_1, μ_2); unknown layer thicknesses (δ_1, δ_2); unknown volume (per unit of length) flow rates (q_1, q_2)—the total volume flow rate ($q_1 + q_2$) is known.

For instance the velocity field for the tri-layer ($2\delta_1 = \delta - \delta_2$) can be expressed as follows

$$a_1 = 12(-4\delta_2^{\,2}\mu_1 q_1 - 12\delta\delta_2\mu_2 q_1 + 12\delta_2^{\,2}\mu_2 q_1 + 3\delta^2\mu_2 q_2 - 6\delta\delta_2\mu_2 q_2 + 3\delta_2^{\,2}\mu_2 q_2)/ ((\delta - \delta_2)^3\delta_2(4\delta_2\mu_1 + 3\delta\mu_2 - 3\delta_2\mu_2)) \tag{C-11}$$

$$a_2 = 24\mu_1(3\delta_2 q_1 - \delta q_2 + \delta_2 q_2)/((\delta - \delta_2)\delta_2^{\,2}(4\delta_2\mu_1 + 3\delta\mu_2 - 3\delta_2\mu_2)) \tag{C-12}$$

$$a_3 = 12(-4\delta_2^{\,2}\mu_1 q_1 - 12\delta\delta_2\mu_2 q_1 + 12\delta_2^{\,2}\mu_2 q_1 + 3\delta^2\mu_2 q_2 - 6\delta\delta_2\mu_2 q_2 + 3\delta_2^{\,2}\mu_2 q_2)/ ((\delta - \delta_2)^3\delta_2(4\delta_2\mu_1 + 3\delta\mu_2 - 3\delta_2\mu_2)) \quad \text{(C-13)}$$

$$b_1 = -12(-4\delta_2^{\,2}\mu_1 q_1 - 6\delta\delta_2\mu_2 q_1 + 6\delta_2^{\,2}\mu_2 q_1 + \delta^2\mu_2 q_2 - 2\delta\delta_2\mu_2 q_2 + \delta_2^{\,2}\mu_2 q_2)/ ((\delta - \delta_2)^2\delta_2(4\delta_2\mu_1 + 3\delta\mu_2 - 3\delta_2\mu_2)) \quad \text{(C-14)}$$

$$b_2 = 24\mu_1(3\delta_2 q_1 - \delta q_2 + \delta_2 q_2)/(\delta_2(-\delta + \delta_2)(4\delta_2\mu_1 + 3\delta\mu_2 - 3\delta_2\mu_2)) \quad \text{(C-15)}$$

$$b_3 = 24\mu_2(3\delta_2 q_1 - \delta q_2 + \delta_2 q_2)/((\delta - \delta_2)\delta_2(4\delta_2\mu_1 + 3\delta\mu_2 - 3\delta_2\mu_2)) \quad \text{(C-16)}$$

$$c_1 = 0 \quad \text{(C-17)}$$

$$c_2 = 3(4\delta_2^{\,2}\mu_1 q_1 + \delta^2\mu_2 q_2 - 2\delta\delta_2\mu_2 q_2 + \delta_2^{\,2}\mu_2 q_2)/((\delta - \delta_2)\delta_2(4\delta_2\mu_1 + 3\delta\mu_2 - 3\delta_2\mu_2)) \quad \text{(C-18)}$$

$$c_3 = 3(4\delta_2^{\,2}\mu_1 q_1 + \delta^2\mu_2 q_2 - 2\delta\delta_2\mu_2 q_2 + \delta_2^{\,2}\mu_2 q_2)/((\delta - \delta_2)\delta_2(4\delta_2\mu_1 + 3\delta\mu_2 - 3\delta_2\mu_2)) \quad \text{(C-19)}$$

and the total energy as

$$part11 = 24(-4\delta_2^{\,2}\mu_1 q_1 - 12\delta\delta_2\mu_2 q_1 + 12\delta_2^{\,2}\mu_2 q_1 + 3\delta^2\mu_2 q_2 - 6\delta\delta_2\mu_2 q_2 + 3\delta_2^{\,2}\mu_2 q_2)^2/ ((\delta - \delta_2)^3\delta_2^{\,2}(4\delta_2\mu_1 + 3\delta\mu_2 - 3\delta_2\mu_2)^2) \quad \text{(C-20)}$$

$$part12 = 768\mu_1^{\,2}(3\delta_2 q_1 - \delta q_2 + \delta_2 q_2)^2/((\delta - \delta_2)^2\delta_2(4\delta_2\mu_1 + 3\delta\mu_2 - 3\delta_2\mu_2)^2) \quad \text{(C-21)}$$

$$part13 = 24(-4\delta_2^{\,2}\mu_1 q_1 - 12\delta\delta_2\mu_2 q_1 + 12\delta_2^{\,2}\mu_2 q_1 + 3\delta^2\mu_2 q_2 - 6\delta\delta_2\mu_2 q_2 + 3\delta_2^{\,2}\mu_2 q_2)^2/ ((\delta - \delta_2)^3\delta_2^{\,2}(4\delta_2\mu_1 + 3\delta\mu_2 - 3\delta_2\mu_2)^2) \quad \text{(C-22)}$$

$$part21 = -72(-4\delta_2^{\,2}\mu_1 q_1 - 6\delta\delta_2\mu_2 q_1 + 6\delta_2^{\,2}\mu_2 q_1 + \delta^2\mu_2 q_2 - 2\delta\delta_2\mu_2 q_2 + \delta_2^{\,2}\mu_2 q_2) (-4\delta_2^{\,2}\mu_1 q_1 - 12\delta\delta_2\mu_2 q_1 + 12\delta_2^{\,2}\mu_2 q_1 + 3\delta^2\mu_2 q_2 - 6\delta\delta_2\mu_2 q_2 + 3\delta_2^{\,2}\mu_2 q_2)/ ((\delta - \delta_2)^3\delta_2^{\,2}(4\delta_2\mu_1 + 3\delta\mu_2 - 3\delta_2\mu_2)^2) \quad \text{(C-23)}$$

$$part22 = -1152\mu_1^{\,2}(-3\delta_2 q_1 + \delta q_2 - \delta_2 q_2)^2/((\delta - \delta_2)^2\delta_2(4\delta_2\mu_1 + 3\delta\mu_2 - 3\delta_2\mu_2)^2) \quad \text{(C-24)}$$

$$part23 = 144\mu_2(3\delta_2 q_1 - \delta q_2 + \delta_2 q_2)(-4\delta_2^{\,2}\mu_1 q_1 - 12\delta\delta_2\mu_2 q_1 + 12\delta_2^{\,2}\mu_2 q_1 + 3\delta^2\mu_2 q_2 - 6\delta\delta_2\mu_2 q_2 + 3\delta_2^{\,2}\mu_2 q_2)/((\delta - \delta_2)^2\delta_2^{\,2}(4\delta_2\mu_1 + 3\delta\mu_2 - 3\delta_2\mu_2)^2) \quad \text{(C-25)}$$

$$part31 = 72(-4\delta_2^{\,2}\mu_1 q_1 - 6\delta\delta_2\mu_2 q_1 + 6\delta_2^{\,2}\mu_2 q_1 + \delta^2\mu_2 q_2 - 2\delta\delta_2\mu_2 q_2 + \delta_2^{\,2}\mu_2 q_2)^2/ ((\delta - \delta_2)^3\delta_2^{\,2}(4\delta_2\mu_1 + 3\delta\mu_2 - 3\delta_2\mu_2)^2) \quad \text{(C-26)}$$

$$part32 = 576\mu_1^{\,2}(3\delta_2 q_1 - \delta q_2 + \delta_2 q_2)^2/(\delta_2(-\delta + \delta_2)^2(4\delta_2\mu_1 + 3\delta\mu_2 - 3\delta_2\mu_2)^2) \quad \text{(C-27)}$$

$$part33 = 288\mu_2^{\,2}(3\delta_2 q_1 - \delta q_2 + \delta_2 q_2)^2/((\delta - \delta_2)\delta_2^{\,2}(4\delta_2\mu_1 + 3\delta\mu_2 - 3\delta_2\mu_2)^2) \quad \text{(C-28)}$$

$$energy\ 3 = part11 + part12 + part13 + part21 + part22 + part23 + part31 + part32 + part33 \quad \text{(C-29)}$$

To obtain the thickness of the layers, the flow rates are assumed fixed and Eq. (C-29) is solved by a numerical nonlinear minimization procedure, i.e., minimizing the total energy dissipation.

For each set of fixed flow rates, a different flow gain ($q_{2\text{-}encaps}/q_{2\text{-}no\_encaps}$) is obtained. The selected set of flow rates is the one that maximizes the flow gain ratio (and minimizes the total energy dissipation).

The flow gain ratio, flow rate ratio, encapsulation flow ratio, viscosity ratio, layer ratio, and effective viscosity are defined as

$$\frac{q_{2\text{-}encaps}}{q_{2\text{-}no\_encaps}} = \frac{6\, q_2\, \mu_2}{|b_1|\, \delta^2\, \mu_1} \tag{C-30}$$

$$\frac{q_2}{q_2 + 2\, q_1} \tag{C-31}$$

$$\frac{q_1}{q_2} \tag{C-32}$$

$$\frac{\mu_2}{\mu_1} \tag{C-33}$$

$$\frac{\delta_2}{\delta} \tag{C-34}$$

$$\mu_{effective} = \frac{|b_1|\, \delta^2\, \mu_1}{6\, q} \tag{C-35}$$

where b_1 is given, for instance, in Eq. (C-14). The flow rate ratio is dependent on the layer configuration, e.g., for a bi-layer the flow rate ratio is $q_2/(q_1 + q_2)$. The effective viscosity serves as a single lumped value of viscosity (representing the encapsulated multiple-viscosity system).

C-5 Effective Viscosity Derivation—Symmetrical Tri-Layer

Equation (C-35) is derived as follows: assume that the *blob* has encapsulated and moves down with a given positive flow rate q_2 (the primary fluid has a flow rate q_1—positive or negative). Disregarding surface effects, a simplified balance of forces (see **Figure C-2**) leads to

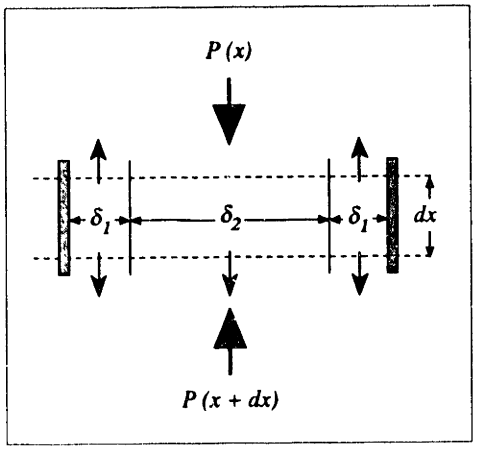

FIGURE C-2: Simplified balance of forces for encapsulated *blob*

$$\rho_2 g \delta_2 dx L + 2 \rho_1 g \delta_1 dx L + P(x) \delta L = P(x + dx) \delta L + 2 \mu_1 dx L \left.\frac{\partial u_1}{\partial z_1}\right|_{z_1 = 0} \tag{C-36}$$

$\delta = \delta_2 + 2\delta_1$, and u_1 is known from the derivations presented in **Section C-4**, i.e.,

$$u_1 = u_1(\delta_1, \delta_2, \mu_1, \mu_2, q_1, q_2) \tag{C-37}$$

such that

$$\left.\frac{\partial u_1}{\partial z_1}\right|_{z_1 = 0} = b_1 \tag{C-38}$$

where

$$b_1 = b_1(\delta_1, \delta_2, \mu_1, \mu_2, q_1, q_2) \tag{C-39}$$

Equation (C-36) reduces to

$$\frac{P(x + dx) - P(x)}{dx} = \rho_2 g \frac{\delta_2}{\delta} + 2\rho_1 g \frac{\delta_1}{\delta} - 2 \frac{\mu_1 b_1}{\delta} \tag{C-40}$$

If the *blob* is attached to the walls (see **Figure C-3**)

$$\rho_2 g \delta dx L + P(x) \delta L = P(x + dx) \delta L + 2 \mu_{effective} dx L \left.\frac{\partial u_{effective}}{\partial z}\right|_{z = 0} \tag{C-41}$$

where

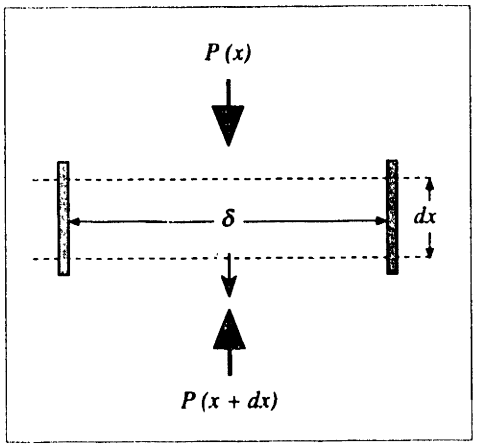

FIGURE C-3: Simplified balance of forces for attached *blob*

$$u_{effective} = -\frac{b}{\delta} z^2 + b\, z \tag{C-42}$$

$$q_{effective} = \frac{b\ \delta^2}{6} \tag{C-43}$$

are the effective velocity and the effective volume flow rate per unit of channel length. The coefficient b in Eq. (C-43) is unknown. Equation (C-41) can be expanded as

$$\frac{P(x + dx) - P(x)}{dx} = \rho_2 g - 2\frac{\mu_{effective}\, b}{\delta} \tag{C-44}$$

Two assumptions are made to obtain the effective viscosity:

1) pressure drop for encapsulated and attached cases are the same—r.h.s. of Eqs. (C-40) and (C-44);

2) the effective volume flow rate per unit of channel length (for the attached case) is equal to the total volume flow rate per unit of channel length (for the encapsulated case), i.e., $q_{effective} \equiv q = q_2 + 2q_1$

The resulting expression is given below

$$\mu_{effective} = \frac{|b_1|\,\mu_1 + (\rho_2 - \rho_1)\, g\, \delta_1}{\frac{6q}{\delta^2}} \tag{C-45}$$

Notice that Eq. (C-45) differs from Eq. (C-35). The additional buoyancy term in Eq. (C-45) can be dropped if the hydrostatic pressure drop is substituted by the overall pressure drop—including gravity effects.

APPENDIX D

PARFES1 Governing Equations — Derivation

D-1 The Mesh Tracking Algorithm

The tracking of the interface motion and distortion between the multiple fluid stages is performed by PARFES1. A finite element algorithm with a local data structure is employed and an elliptical conjugate-gradient-type iterative solver utilized. Matrices are sparse and not assembled.

The mesh movement/stretching assumes a simple elastostatic formulation

$$\begin{aligned} T_{ij,j} &= f_i \quad \text{in } \Omega \\ u_i &= \bar{u}_i \quad \text{in } \partial\Omega_u \\ T_{ij}\, n_j &= \bar{t}_i \quad \text{in } \partial\Omega_t \end{aligned} \tag{D-1}$$

$$\begin{aligned} \partial\Omega_u \cup \partial\Omega_t &= \partial\Omega \\ \partial\Omega_u \cap \partial\Omega_t &= \varnothing \end{aligned} \tag{D-2}$$

$$T_{ij} = \lambda_1 \delta_{ij} u_{l,l} + \lambda_2 (u_{i,j} + u_{j,i}) \tag{D-3}$$

$$\int_\Omega [\lambda_1 \delta_{ij} u_{l,l} + \lambda_2 (u_{i,j} + u_{j,i})] w_{i,j} d\Omega = \int_\Omega f_i w_i d\Omega + \int_{\partial\Omega_t} t_i w_i d(\partial\Omega) \tag{D-4}$$

where

$$\begin{aligned} \lambda_1 &= \frac{E\nu}{(1-\nu^2)} \\ \lambda_2 &= \frac{E}{2(1+\nu)} \end{aligned} \tag{D-5}$$

Assuming that the local approximation for displacements are given as

$$u_i^h = \sum_{n=1}^{N} U_{in}\,\phi_n \tag{D-6}$$

the resulting integral formulation is

$$\int_{\Omega^h}\left[\lambda_1\,\delta_{ij}\,u^h_{l,l} + \lambda_2\left(u^h_{i,j} + u^h_{j,i}\right)\right]w^h_{i,j}\,d\Omega = \int_{\Omega^h} f_i w_i^h\,d\Omega + \int_{\partial\Omega_t^h} t_i w_i^h\,d(\partial\Omega) \tag{D-7}$$

Expanding the above integral gives

$$\begin{aligned}\int_{\Omega^h}\{\,&\left[\lambda_1\left(u^h_{1,1}+u^h_{2,2}\right) + \lambda_2\left(u^h_{1,1}+u^h_{1,1}\right)\right]w^h_{1,1} + \left[\lambda_2\left(u^h_{1,2}+u^h_{2,1}\right)\right]w^h_{1,2} + \\ &\left[\lambda_1\left(u^h_{1,1}+u^h_{2,2}\right) + \lambda_2\left(u^h_{2,2}+u^h_{2,2}\right)\right]w^h_{2,2} + \left[\lambda_2\left(u^h_{2,1}+u^h_{1,2}\right)\right]w^h_{2,1}\,\}\,d\Omega = \\ &\int_{\Omega^h}\left(f_1 w_1^h + f_2 w_2^h\right)d\Omega + \int_{\partial\Omega_t^h}\left(t_1 w_1^h + t_2 w_2^h\right)d(\partial\Omega)\end{aligned} \tag{D-8}$$

To simplify derivations the following notation is used

$$\int_{\Omega^e} ab\,d\Omega \equiv \left\langle a \,\middle|\, b \right\rangle \tag{D-9}$$

Expanding Eq. (D-8) in terms of a Finite Element local basis functions ϕ leads to

$$\begin{aligned}\sum_{n=1}^{N}\{\,&(\lambda_1+2\lambda_2)\left\langle\phi_{n,1}\,\middle|\,\phi_{m,1}\right\rangle U_{1n} + \lambda_2\left\langle\phi_{n,1}\,\middle|\,\phi_{m,1}\right\rangle U_{2n} + \lambda_1\left\langle\phi_{n,2}\,\middle|\,\phi_{m,1}\right\rangle U_{2n} + \lambda_2\left\langle\phi_{n,2}\,\middle|\,\phi_{m,1}\right\rangle U_{1n} + \\ &(\lambda_1+2\lambda_2)\left\langle\phi_{n,2}\,\middle|\,\phi_{m,2}\right\rangle U_{2n} + \lambda_2\left\langle\phi_{n,2}\,\middle|\,\phi_{m,2}\right\rangle U_{1n} + \lambda_1\left\langle\phi_{n,1}\,\middle|\,\phi_{m,2}\right\rangle U_{1n} + \lambda_2\left\langle\phi_{n,1}\,\middle|\,\phi_{m,2}\right\rangle U_{2n}\,\} = \\ &\left\langle f_1+f_2 \,\middle|\, \phi_m\right\rangle + \int_{\partial\Omega_t}(t_1\phi_m + t_2\phi_m)\,d(\partial\Omega)\end{aligned} \tag{D-10}$$

Breaking Eq. (D-10) in terms of its components

$$\begin{bmatrix} G_{11} & G_{12}\end{bmatrix}\begin{bmatrix} U_{1n}\\ U_{2n}\end{bmatrix} = \left\langle f_1 \,\middle|\, \phi_m\right\rangle + \int_{\partial\Omega_t} t_1\phi_m\,d(\partial\Omega) \tag{D-11}$$

$$\begin{aligned} G_{11} &= (\lambda_1+2\lambda_2)\left\langle\phi_{n,1}\,\middle|\,\phi_{m,1}\right\rangle + \lambda_2\left\langle\phi_{n,2}\,\middle|\,\phi_{m,2}\right\rangle \\ G_{12} &= \lambda_1\left\langle\phi_{n,2}\,\middle|\,\phi_{m,1}\right\rangle + \lambda_2\left\langle\phi_{n,1}\,\middle|\,\phi_{m,2}\right\rangle\end{aligned} \tag{D-12}$$

$$\begin{bmatrix} G_{21} & G_{22} \end{bmatrix} \begin{bmatrix} U_{1n} \\ U_{2n} \end{bmatrix} = \left\langle f_2 \mid \phi_m \right\rangle + \int_{\partial\Omega_t} t_2 \phi_m d(\partial\Omega) \tag{D-13}$$

$$\begin{aligned} G_{21} &= \lambda_1 \left\langle \phi_{n,1} \mid \phi_{m,2} \right\rangle + \lambda_2 \left\langle \phi_{n,2} \mid \phi_{m,1} \right\rangle \\ G_{22} &= (\lambda_1 + 2\lambda_2) \left\langle \phi_{n,2} \mid \phi_{m,2} \right\rangle + \lambda_2 \left\langle \phi_{n,1} \mid \phi_{m,1} \right\rangle \end{aligned} \tag{D-14}$$

Simplifying Eq. (D-10) in light of the above leads to

$$(\lambda_1 + 2\lambda_2) = \lambda_3 \tag{D-15}$$

$$\begin{aligned} \left\langle f_1 \mid \phi_m \right\rangle &= F_{1m} \\ \left\langle f_2 \mid \phi_m \right\rangle &= F_{2m} \end{aligned} \tag{D-16}$$

$$\begin{aligned} \int_{\partial\Omega_t} t_1 \phi_m d(\partial\Omega) &= T_{1m} \\ \int_{\partial\Omega_t} t_2 \phi_m d(\partial\Omega) &= T_{2m} \end{aligned} \tag{D-17}$$

$$\begin{aligned} U_{1n} &= U_n \\ U_{2n} &= V_n \end{aligned} \tag{D-18}$$

$$\begin{aligned} \left\langle \phi_{n,1} \mid \phi_{m,1} \right\rangle &= a_{nm} \\ \left\langle \phi_{n,1} \mid \phi_{m,2} \right\rangle &= b_{nm} \\ \left\langle \phi_{n,2} \mid \phi_{m,1} \right\rangle &= c_{nm} \\ \left\langle \phi_{n,2} \mid \phi_{m,2} \right\rangle &= d_{nm} \end{aligned} \tag{D-19}$$

$$\begin{bmatrix} \lambda_3 a_{nm} + \lambda_2 d_{nm} & \lambda_1 c_{nm} + \lambda_2 b_{nm} \\ \lambda_1 b_{nm} + \lambda_2 c_{nm} & \lambda_3 d_{nm} + \lambda_2 a_{nm} \end{bmatrix} \begin{bmatrix} U_n \\ V_n \end{bmatrix} - \begin{bmatrix} F_{1m} + T_{1m} \\ F_{2m} + T_{2m} \end{bmatrix} = \begin{bmatrix} R_{1m} \\ R_{2m} \end{bmatrix} \tag{D-20}$$

Equation (D-20) above, expresses the relationship among displacements, driving forces and the geometry—the term in the r.h.s. is the residual. The goal is to solve Eq. (D-20), satisfying the constraints imposed by the physics of the displacing fluids.

The terms in Eq. (D-20) can be further expanded utilizing an isoparametric Finite

Element formulation, i.e.

$$(x_1, x_2)^e \in \Omega^e \rightarrow (r_1, r_2) \in [-1,1] \times [-1,1] \tag{D-21}$$

$$(\cdot),i \equiv \frac{\partial(\cdot)}{\partial x_1} \equiv J_{il}^{-1}\frac{\partial(\cdot)}{\partial r_l}; \qquad \begin{cases} l = 1,2 \\ r_1 \equiv r \\ r_2 \equiv s \end{cases} \tag{D-22}$$

$$\begin{aligned} J &= \begin{bmatrix} x_{1,r} & x_{2,r} \\ x_{1,s} & x_{2,s} \end{bmatrix} \\ det\, J &= x_{1,r}\, x_{2,s} - x_{2,r}\, x_{1,s} \\ J^{-1} &= \frac{1}{det\, J}\begin{bmatrix} x_{2,s} & -x_{2,r} \\ -x_{1,s} & x_{1,r} \end{bmatrix} \end{aligned} \tag{D-23}$$

$$\begin{aligned} \left\langle \phi_{n,i} \,\middle|\, \phi_{m,j} \right\rangle &= \int_{\Omega^e} \phi_{n,i}\, \phi_{m,j} d\Omega \\ &= \int_{\Omega^e} J_{il}^{-1}\frac{\partial \phi_n}{\partial r_l} J_{jl}^{-1}\frac{\partial \phi_m}{\partial r_l} det\, J\, dr_1\, dr_2 \\ &= \int_{\Omega^e}\left[J_{i1}^{-1}\frac{\partial \phi_n}{\partial r} + J_{i2}^{-1}\frac{\partial \phi_n}{\partial s}\right]\left[J_{j1}^{-1}\frac{\partial \phi_m}{\partial r} + J_{j2}^{-1}\frac{\partial \phi_m}{\partial s}\right] det\, J\, dr\, ds \end{aligned} \tag{D-24}$$

$$\begin{aligned} \left\langle f_i \,\middle|\, \phi_m \right\rangle &= \int_{\Omega^e} f_i \phi_m\, det\, J\, dr ds \\ \int_{\partial\Omega_t} t_i \phi_m d(\partial\Omega) &= \int_{\partial\Omega^e} t_i \phi_m dr_i \end{aligned} \tag{D-25}$$

$$\begin{aligned} a_{nm}^e &= \left\langle \phi_{n,1} \,\middle|\, \phi_{m,1} \right\rangle = \int_{\Omega^e} \frac{1}{det\, J}\left[x_{2,s}\frac{\partial \phi_n}{\partial r} - x_{2,r}\frac{\partial \phi_n}{\partial s}\right]\left[x_{2,s}\frac{\partial \phi_m}{\partial r} - x_{2,r}\frac{\partial \phi_m}{\partial s}\right] dr ds \\ b_{nm}^e &= \left\langle \phi_{n,1} \,\middle|\, \phi_{m,2} \right\rangle = \int_{\Omega^e} \frac{1}{det\, J}\left[x_{2,s}\frac{\partial \phi_n}{\partial r} - x_{2,r}\frac{\partial \phi_n}{\partial s}\right]\left[-x_{1,s}\frac{\partial \phi_m}{\partial r} + x_{1,r}\frac{\partial \phi_m}{\partial s}\right] dr ds \\ c_{nm}^e &= \left\langle \phi_{n,2} \,\middle|\, \phi_{m,1} \right\rangle = \int_{\Omega^e} \frac{1}{det\, J}\left[-x_{1,s}\frac{\partial \phi_n}{\partial r} + x_{1,r}\frac{\partial \phi_n}{\partial s}\right]\left[x_{2,s}\frac{\partial \phi_m}{\partial r} - x_{2,r}\frac{\partial \phi_m}{\partial s}\right] dr ds \\ d_{nm}^e &= \left\langle \phi_{n,2} \,\middle|\, \phi_{m,2} \right\rangle = \int_{\Omega^e} \frac{1}{det\, J}\left[-x_{1,s}\frac{\partial \phi_n}{\partial r} + x_{1,r}\frac{\partial \phi_n}{\partial s}\right]\left[-x_{1,s}\frac{\partial \phi_m}{\partial r} + x_{1,r}\frac{\partial \phi_m}{\partial s}\right] dr ds \end{aligned} \tag{D-26}$$

$$x_i = \sum_{l=1}^{N} x_{il}\phi_l \rightarrow \begin{cases} x_{i,r} = \sum_{l=1}^{N} x_{il}\dfrac{\partial \phi_l}{\partial r} \\ x_{i,s} = \sum_{l=1}^{N} x_{il}\dfrac{\partial \phi_l}{\partial s} \end{cases} \tag{D-27}$$

Finally, the previous system is simplified as follows

$$\begin{bmatrix} \lambda_3 a^e_{nm} + \lambda_2 d^e_{nm} & \lambda_1 c^e_{nm} + \lambda_2 b^e_{nm} \\ \lambda_1 b^e_{nm} + \lambda_2 c^e_{nm} & \lambda_3 d^e_{nm} + \lambda_2 a^e_{nm} \end{bmatrix} \begin{bmatrix} U_n \\ V_n \end{bmatrix} = \begin{bmatrix} R_{1m} \\ R_{2m} \end{bmatrix} \tag{D-28}$$

Notice that the forcing terms, on the l.h.s. of Eq. (D-20), were dropped—assuming that all interactions are governed by displacement constraints.

To formulate and to solve Eq. (D-28) is not difficult, if done in a conventional way, i.e, utilizing direct methods as solvers. Also, various programs, currently available, are able to solve the above system.

However the approach utilized here is different. In order to track the development of fingering patterns and folding, a special implementation of Eq. (D-28) was required. The following are the major characteristics of the implementation developed herein

- coefficients generated in symbolic form (to reduce computational time);
- conjugate-gradient-iterative solver with a local data structure (tuned for a massively parallel implementation);
- nearest neighbor communication optimized to reduce communication overhead (in parallel processing), and reduction on the number of wasted cycles for boundary updates;
- the mesh is able to wrap around itself.

For instance each local contribution (from one of the four local neighbor elements to a node) is given below

$$
\begin{aligned}
&K_{71}^{(-,-)}U^{(-,-)} + K_{72}^{(-,-)}V^{(-,-)} + K_{73}^{(-,-)}U^{(0,-)} + K_{74}^{(-,-)}V^{(0,-)} + K_{75}^{(-,-)}U^{(-,0)} + K_{76}^{(-,-)}V^{(-,0)} + K_{77}^{(-,-)}U^{(0,0)} + K_{78}^{(-,-)}V^{(0,0)} = 0 \\
&K_{51}^{(0,-)}U^{(0,-)} + K_{52}^{(0,-)}V^{(0,-)} + K_{53}^{(0,-)}U^{(+,-)} + K_{54}^{(0,-)}V^{(+,-)} + K_{55}^{(0,-)}U^{(0,0)} + K_{56}^{(0,-)}V^{(0,0)} + K_{57}^{(0,-)}U^{(+,0)} + K_{58}^{(0,-)}V^{(+,0)} = 0 \\
&+K_{31}^{(-,0)}U^{(-,0)} + K_{32}^{(-,0)}V^{(-,0)} + K_{33}^{(-,0)}U^{(0,0)} + K_{34}^{(-,0)}V^{(0,0)} + K_{35}^{(-,0)}U^{(-,+)} + K_{36}^{(-,0)}V^{(-,+)} + K_{37}^{(-,0)}U^{(0,+)} + K_{38}^{(-,0)}V^{(0,+)} = 0 \\
&K_{11}^{(0,0)}U^{(0,0)} + K_{12}^{(0,0)}V^{(0,0)} + K_{13}^{(0,0)}U^{(+,0)} + K_{14}^{(0,0)}V^{(+,0)} + K_{15}^{(0,0)}U^{(0,+)} + K_{16}^{(0,0)}V^{(0,+)} + K_{17}^{(0,0)}U^{(+,+)} + K_{18}^{(0,0)}V^{(+,+)} = 0
\end{aligned}
\tag{D-29}
$$

A special control mechanism was developed to handle updates at the boundaries, as well as to handle end of array shifts—to allow the mesh to wrap around itself.

Two different implementations of the algorithm were developed to run at top speed in different architectures, i.e., a vector machine (e.g. CRAY Y-MP), and a massively parallel processor (e.g. Thinking Machines CM-2).

The resulting implementations were considerably successful: approximately 240 MFlops/processor out of a peak performance of 330 Mflops/processor on the CRAY Y-MP for a 130,000 degrees of freedom problem; 98% utilization of the CM-2 (for a 1,000,000 degrees of freedom problem) roughly in the GFlops range.

The need for this kind of performance (possibly better in the future) is fundamental. To track complex structures the most time consuming computational task is the iteration needed to locate the final mesh configuration.

APPENDIX E

PARFES2 & PARFESAX Governing Equations—Derivation

E-1 Multiple Fluid Stages and Interfaces Modeling

The mass and momentum conservation formulation (assuming an aspect ratio of order $\Delta/L \sim \Delta/H \sim 10^{-5}$), for both PARFES2 and PARFESAX, can be expressed as

$$\int_{{}^{i}\Omega(t)} \left[({}^{i}\rho\, {}^{i}v\, \delta)_{,t} + ({}^{i}\rho\, {}^{i}v\, \delta\, {}^{i}\bar{u}_k)_{,k} + 2\, {}^{i}\rho\, {}^{i}v\, {}^{i}V_{loss} \right] {}^{i}\psi_j \, d^{i}\Omega = 0$$

$$\forall\ {}^{i}\psi_j \in L^2\left[{}^{i}\Omega(t)\right] \tag{E-1}$$

$$\int_{{}^{i}\Omega(t)} \left[{}^{i}\bar{u}_k - \frac{\delta^2}{12\, {}^{i}\mu\, {}^{i}v} \left[-({}^{i}v p)_{,k} + {}^{i}\rho\, {}^{i}v\, g_k \right] \right] {}^{i}\phi_j \, d^{i}\Omega = 0$$

$$\forall\ {}^{i}\phi_j \in H_0^1\left[{}^{i}\Omega(t)\right] \tag{E-2}$$

where for each fluid stage (prescript i): ${}^{i}v$ is the volume fraction; ${}^{i}\rho$ the density; ${}^{i}\mu$ the viscosity; ${}^{i}u_k$ the average (in-plane) velocity component in the direction k; ${}^{i}V_{loss}$ the (transverse) fluid loss velocity (through both fracture walls); g_k the gravity acceleration component in the direction k. The crack opening field δ is coupled to the fluid(s) pressure field p by means of a surface integral scheme, Barr (1991), encompassing the elastic stress field around the fracture walls, and the stress intensity factor in mode I. The finite element basis function ϕ and ψ are assumed to be square integrable in Ω for any instant of time t. The first derivative of ϕ is, also, assumed to be square integrable with support zero at the boundaries.

Assuming the following notation for integration in Ω and its boundaries $\partial\Omega$

$$\begin{aligned} \left\langle a_l \,\middle|\, b_m \right\rangle &\equiv \int_{\Omega} a_l \, b_m \, d\Omega \\ \left[a_l \,\middle|\, n_m \right] &\equiv \int_{\partial\Omega} a_l \, n_m \, d(\partial\Omega) \end{aligned} \tag{E-3}$$

the previous Eqs. (E-1) and (E-2) can be combined as follows

$$\begin{aligned} \frac{d}{dt}\left\langle {}^{i}\rho \; {}^{i}\nu \; \delta \,\middle|\, {}^{i}\psi_j \right\rangle + \left[{}^{i}\rho \; {}^{i}\nu \; \delta \; ({}^{i}u_k - \dot{X}_k) \; {}^{i}\psi_j \,\middle|\, n_k \right] \\ - \left\langle {}^{i}\rho \; {}^{i}\nu \; \delta \; ({}^{i}u_k - \dot{X}_k) \,\middle|\, \frac{\partial {}^{i}\psi_j}{\partial x_k} \right\rangle + \left\langle 2 \, {}^{i}\rho \; {}^{i}\nu \; {}^{i}V_{loss} \,\middle|\, {}^{i}\psi_j \right\rangle = 0 \end{aligned} \tag{E-4}$$

For the highly viscous flow limit case discussed in **Appendix A**, the Navier-Stokes equations reduce to

$${}^{i}u_k = \frac{\delta^2}{12 \; {}^{i}\mu \; {}^{i}\nu} \left(- \frac{\partial ({}^{i}\nu \; {}^{i}p)}{\partial x_k} + {}^{i}\rho \; {}^{i}\nu \; g_k \right) \tag{E-5}$$

Substituting Eq. (E-5) into Eq. (E-4) and assuming

$$\begin{aligned} {}^{i}\rho \; {}^{i}\nu &\rightarrow {}^{i}\overline{\rho} \\ 12 \; {}^{i}\mu \; {}^{i}\nu &\rightarrow {}^{i}\overline{\mu} \\ {}^{i}\psi_j &\rightarrow \Psi \end{aligned} \tag{E-6}$$

leads to

$$\begin{aligned} \frac{d}{dt}\left\langle {}^{i}\overline{\rho} \, \delta \;\middle|\; \Psi \right\rangle - \left[\frac{{}^{i}\overline{\rho}}{{}^{i}\overline{\mu}} \delta^3 \, \Psi \frac{\partial p}{\partial x_k} \;\middle|\; n_k \right] + \left[\frac{{}^{i}\overline{\rho}^2}{{}^{i}\overline{\mu}} \delta^3 \, \Psi \, g_k \;\middle|\; n_k \right] \\ - \left[{}^{i}\overline{\rho} \, \delta \, \Psi \dot{X}_k \;\middle|\; n_k \right] + \left\langle \frac{{}^{i}\overline{\rho}}{{}^{i}\overline{\mu}} \delta^3 \frac{\partial p}{\partial x_k} \;\middle|\; \frac{\partial \Psi}{\partial x_k} \right\rangle - \left\langle \frac{{}^{i}\overline{\rho}^2}{{}^{i}\overline{\mu}} \delta^3 \, g_k \;\middle|\; \frac{\partial \Psi}{\partial x_k} \right\rangle \\ + \left\langle {}^{i}\overline{\rho} \, \delta \, \dot{X}_k \;\middle|\; \frac{\partial \Psi}{\partial x_k} \right\rangle - \left\langle 2 \, {}^{i}\overline{\rho} \, {}^{i}V_{loss} \;\middle|\; \Psi \right\rangle = 0 \end{aligned} \tag{E-7}$$

In addition the elastic behavior of the fracture is characterized by the following equation

$$(P_i - \sigma_c) = f(\overline{E}, \nu) \; D_{ij} \; \delta_j \tag{E-8}$$

Nondimensionalization—analogous to Eqs. (B-24) and (B-25) in **Page 164** of **Appendix B**—of Eqs. (E-5), (E-7) and (E-8) results on the following

$$ {}^{i}u_k = \left(\frac{\bar{\rho}_R\, g\, L_R}{\sigma_c} \left(\frac{\Delta_R}{L_R} \right)^2 \right) \frac{{}^{i}\bar{\rho}}{{}^{i}\bar{\mu}}\, \delta^2\, g_k - \left(\frac{\Delta_R}{L_R} \right)^2 \frac{\delta^2}{{}^{i}\bar{\mu}} \frac{\partial p}{\partial x_k} \tag{E-9} $$

$$ \sigma_i = \frac{\Delta_R f(\bar{E}, \nu)}{\sigma_c} D_{ij}\, \delta_j \tag{E-10} $$

$$ \begin{aligned} &\left\{ \frac{\bar{\rho}_R\, \Delta_R\, L_R^2}{T_R} \right\} \frac{d}{dt} \left\langle {}^{i}\bar{\rho}\, \delta \,\middle|\, \Psi \right\rangle - \left\{ \frac{L_R\, \bar{\rho}_R\, \Delta_R^3\, \sigma_R}{L_R\, \bar{\mu}_R} \right\} \left[\frac{{}^{i}\bar{\rho}}{{}^{i}\bar{\mu}}\, \delta^3\, \Psi \frac{\partial \sigma}{\partial x_k} \,\middle|\, n_k \right] \\ &+ \left\{ \frac{\bar{\rho}_R^2\, \Delta_R^3\, g\, L_R}{\bar{\mu}_R} \right\} \left[\frac{{}^{i}\bar{\rho}^2}{{}^{i}\bar{\mu}}\, \delta^3\, \Psi\, g_k \,\middle|\, n_k \right] + \left\{ \frac{\bar{\rho}_R^2\, \Delta_R^3\, \sigma_R\, L_R^2}{\bar{\mu}_R\, L_R^2} \right\} \left\langle \frac{{}^{i}\bar{\rho}}{{}^{i}\bar{\mu}}\, \delta^3 \frac{\partial \sigma}{\partial x_k} \middle| \frac{\partial \Psi}{\partial x_k} \right\rangle \\ &- \left\{ \frac{\bar{\rho}_R\, \Delta_R\, g\, L_R^2}{T_R} \right\} \left[{}^{i}\bar{\rho}\, \delta\, \Psi \dot{X}_k \,\middle|\, n_k \right] - \left\{ \frac{\bar{\rho}_R^2\, \Delta_R^3\, g\, L_R^2}{\bar{\mu}_R\, L_R} \right\} \left\langle \frac{{}^{i}\bar{\rho}^2}{{}^{i}\bar{\mu}}\, \delta^3\, g_k \middle| \frac{\partial \Psi}{\partial x_k} \right\rangle \\ &+ \left\{ \frac{\bar{\rho}_R\, \Delta_R\, g\, L_R^3}{T_R\, L_R} \right\} \left\langle {}^{i}\bar{\rho}\, \delta\, \dot{X}_k \middle| \frac{\partial \Psi}{\partial x_k} \right\rangle + \left\{ \frac{2\, \bar{\rho}_R\, \Delta_R\, L_R^2}{T_R} \right\} \left\langle {}^{i}\bar{\rho}\, {}^{i}V_{loss} \,\middle|\, \Psi \right\rangle = 0 \end{aligned} \tag{E-11} $$

where the excess pressure variation σ, is assumed to be equal to the hydrostatic pressure variation (spatial variation of the confining stresses can be easily introduced though), i.e.

$$ \frac{\partial p}{\partial x_k} = \frac{\partial (p - \sigma_c)}{\partial x_k} \tag{E-12} $$

The previous equations can be combined as

$$ \begin{aligned} &\frac{d}{dt} \left\langle {}^{i}\bar{\rho}\, \delta \,\middle|\, \Psi \right\rangle - \alpha_S^2 \left[\frac{{}^{i}\bar{\rho}}{{}^{i}\bar{\mu}}\, \delta^3\, \Psi \frac{\partial \sigma}{\partial x_k} \,\middle|\, n_k \right] + \alpha_B\, \alpha_S^2 \left[\frac{{}^{i}\bar{\rho}}{{}^{i}\bar{\mu}}\, \delta^3\, \Psi\, g_k \,\middle|\, n_k \right] \\ &- \left[{}^{i}\bar{\rho}\, \delta\, \Psi \dot{X}_k \,\middle|\, n_k \right] + \alpha_S^2 \left\langle \frac{{}^{i}\bar{\rho}}{{}^{i}\bar{\mu}}\, \delta^3 \frac{\partial \sigma}{\partial x_k} \middle| \frac{\partial \Psi}{\partial x_k} \right\rangle + \left\langle {}^{i}\bar{\rho}\, \delta\, \dot{X}_k \middle| \frac{\partial \Psi}{\partial x_k} \right\rangle \\ &- \alpha_B\, \alpha_S^2 \left\langle \frac{{}^{i}\bar{\rho}}{{}^{i}\bar{\mu}}\, \delta^3\, g_k \middle| \frac{\partial \Psi}{\partial x_k} \right\rangle + 2 \left\langle {}^{i}\bar{\rho}\, {}^{i}V_{loss} \,\middle|\, \Psi \right\rangle = 0 \end{aligned} \tag{E-13} $$

where

$$ \begin{aligned} \alpha_S &= \frac{\Delta_R}{L_R} \\ \alpha_B &= \frac{\rho_R\, g\, L_R}{\sigma_c} \end{aligned} \tag{E-14} $$

are the non-dimensionalization variables; σ the excess pressure field ($\sigma = p - \sigma_c$); σ_c the confining stress field; $\dot{X}_k$ the nodal velocity component in the direction k; Ψ the finite element weight function. The terms in $\dot{X}_k$ arise from passing the time differentiation out of the integral (first term in the l.h.s.) in Eq. (E-1).

For the implementation of PARFES2, two implicit A-stable, Sand and Østerby (1979), linear multistep schemes are used to time integrate. An Adams-Moulton of second order is used for the first time step and a Backward Differentiation, also of second order, for the subsequent time steps. For the axisymmetrical problem (the gravity term is dropped in PARFESAX), after the second time step, implicit adaptive variable order (up to fifth order) Backward Differentiation schemes are used.

Identifying terms for Eq. (E-13) as follows

$$\frac{d\,{}^{i}a}{dt} + f({}^{i}a, t) = 0 \tag{E-15}$$

$$\begin{aligned}
{}^{i}a &= < {}^{i}\bar{\rho}\,\delta \,|\, \psi > \\
f({}^{i}a, t) &= \frac{d}{dt} < {}^{i}\bar{\rho}\,\delta \,|\, \psi > - \alpha_S^2 \left[\frac{{}^{i}\bar{\rho}}{{}^{i}\bar{\mu}} \delta^3 \Psi \frac{\partial \sigma}{\partial x_k} \,|\, n_k \right] + \alpha_B \alpha_S^2 \left[\frac{{}^{i}\bar{\rho}}{{}^{i}\bar{\mu}} \delta^3 \Psi g_k \,|\, n_k \right] \\
&\quad - \left[{}^{i}\bar{\rho}\,\delta\,\Psi \dot{X}_k \,|\, n_k \right] + \alpha_S^2 < \frac{{}^{i}\bar{\rho}}{{}^{i}\bar{\mu}} \delta^3 \frac{\partial \sigma}{\partial x_k} \,|\, \frac{\partial \Psi}{\partial x_k} > + < {}^{i}\bar{\rho}\,\delta\,\dot{X}_k \,|\, \frac{\partial \Psi}{\partial x_k} > \\
&\quad - \alpha_B \alpha_S^2 < \frac{{}^{i}\bar{\rho}}{{}^{i}\bar{\mu}} \delta^3 g_k \,|\, \frac{\partial \Psi}{\partial x_k} > + 2 < {}^{i}\bar{\rho}\,{}^{i}V_{loss} \,|\, \Psi >
\end{aligned} \tag{E-16}$$

allow the following time approximation using linear multistep formula

$$\sum_{j=0}^{k} \alpha_j a_{(n+j)} = \Delta t \sum_{j=0}^{k} \beta_j f_{(n+j)} \tag{E-17}$$

Various methods can be derived from the above equation. Though the interest here will focus in a particular class, i.e., A-stable.

Using BD2 (Backward Differentiation of order 2) to approximate Eq. (E-13) in time gives

$$3\left\langle {}^{i}\bar{\rho}\,\delta \middle|\, \Psi \right\rangle^{n} + 2\,\Delta t f^{n} = 4\left\langle {}^{i}\bar{\rho}\,\delta \middle|\, \Psi \right\rangle^{n-1} - \left\langle {}^{i}\bar{\rho}\,\delta \middle|\, \Psi \right\rangle^{n-2} \tag{E-18}$$

Notice that for the initial time step this formula cannot be applied. Hence, the algorithm of choice for start-up is the AM2 (Adams-Moulton of order 2), i.e.

$$2\left\langle {}^{i}\bar{\rho}\,\delta \middle|\, \Psi \right\rangle^{(n=1)} - \Delta t f^{(n=1)} = 2\left\langle {}^{i}\bar{\rho}\,\delta \middle|\, \Psi \right\rangle^{(n=0)} + \Delta t f^{(n=0)} \tag{E-19}$$

Applying Newton-Raphson to Eqs. (E-18) and (E-19) and taking increments on the crack opening and excess pressure as follows

$$\begin{aligned} \delta &= d + \Delta\delta \\ \sigma &= p + \Delta\sigma \end{aligned} \tag{E-20}$$

leads to

$$\begin{aligned} 3\left\langle {}^{i}\bar{\rho}\,\Delta\delta \middle|\, \Psi \right\rangle^{n} + 2\,\Delta t f^{n}(\delta,\sigma) = \\ - 3\left\langle {}^{i}\bar{\rho}\,d \middle|\, \Psi \right\rangle^{n} + 4\left\langle {}^{i}\bar{\rho}\,\delta \middle|\, \Psi \right\rangle^{n-1} - \left\langle {}^{i}\bar{\rho}\,\delta \middle|\, \Psi \right\rangle^{n-2} \end{aligned} \tag{E-21}$$

$$\begin{aligned} 2\left\langle {}^{i}\bar{\rho}\,\Delta\delta \middle|\, \Psi \right\rangle^{(n=1)} - \Delta t f^{(n=1)}(\delta,\sigma) = \\ - 2\left\langle {}^{i}\bar{\rho}\,d \middle|\, \Psi \right\rangle^{(n=1)} + 2\left\langle {}^{i}\bar{\rho}\,\delta \middle|\, \Psi \right\rangle^{(n=0)} + \Delta t f^{(n=0)} \end{aligned} \tag{E-22}$$

Term-by-term expansion of the f^n function follows

$$\begin{aligned} \left[\frac{{}^{i}\bar{\rho}}{{}^{i}\bar{\mu}} (d+\Delta\delta)^3 \Psi \frac{\partial (p+\Delta\delta)}{\partial x_k} \,\middle|\, n_k \right] = \\ \left[\frac{{}^{i}\bar{\rho}}{{}^{i}\bar{\mu}} d^3 \Psi \frac{\partial p}{\partial x_k} \,\middle|\, n_k \right] + 3\left[\frac{{}^{i}\bar{\rho}}{{}^{i}\bar{\mu}} d^2 \Psi \frac{\partial p}{\partial x_k} \Delta\delta \,\middle|\, n_k \right] \\ + \left[\frac{{}^{i}\bar{\rho}}{{}^{i}\bar{\mu}} d^3 \Psi \frac{\partial \Delta\delta}{\partial x_k} \,\middle|\, n_k \right] + O(\Delta\delta^2, \Delta\delta\,\Delta\sigma) \end{aligned} \tag{E-23}$$

$$\begin{aligned} \left[\frac{{}^{i}\bar{\rho}}{{}^{i}\bar{\mu}} (d+\Delta\delta)^3 \Psi g_k \,\middle|\, n_k \right] = \\ \left[\frac{{}^{i}\bar{\rho}}{{}^{i}\bar{\mu}} d^3 \Psi g_k \,\middle|\, n_k \right] + 3\left[\frac{{}^{i}\bar{\rho}}{{}^{i}\bar{\mu}} d^2 \Delta\delta \Psi g_k \,\middle|\, n_k \right] + O(\Delta\delta^2) \end{aligned} \tag{E-24}$$

$$\left[{}^{i}\bar{\rho}(d+\Delta\delta)\,\Psi \dot{X}_k \,\middle|\, n_k \right] = \left[{}^{i}\bar{\rho}\,\delta\,\Psi \dot{X}_k \,\middle|\, n_k \right] + \left[{}^{i}\bar{\rho}\,\Delta\delta\,\Psi \dot{X}_k \,\middle|\, n_k \right] \tag{E-25}$$

$$< \frac{{}^{i}\bar{\rho}}{{}^{i}\bar{\mu}} (d + \Delta\delta)^3 \frac{\partial (p + \Delta\sigma)}{\partial x_k} \mid \frac{\partial \Psi}{\partial x_k} > \; = \; < \frac{{}^{i}\bar{\rho}}{{}^{i}\bar{\mu}} d^3 \frac{\partial p}{\partial x_k} \mid \frac{\partial \Psi}{\partial x_k} > \; + \; 3 < \frac{{}^{i}\bar{\rho}}{{}^{i}\bar{\mu}} d^2 \frac{\partial p}{\partial x_k} \Delta\delta \mid \frac{\partial \Psi}{\partial x_k} > + < \frac{{}^{i}\bar{\rho}}{{}^{i}\bar{\mu}} d^3 \frac{\partial \Delta\sigma}{\partial x_k} \mid \frac{\partial \Psi}{\partial x_k} > \; + \; O (\Delta\delta^2, \Delta\delta \Delta\sigma) \tag{E-26}$$

$$< \frac{{}^{i}\bar{\rho}}{{}^{i}\bar{\mu}} (d + \Delta\delta)^3 \frac{\partial (p + \Delta\sigma)}{\partial x_k} \mid \frac{\partial \Psi}{\partial x_k} > \; = \; < \frac{{}^{i-2}\bar{\rho}}{{}^{i}\bar{\mu}} d^3 \, g_k \mid \frac{\partial \Psi}{\partial x_k} > \; + \; 3 < \frac{{}^{i-2}\bar{\rho}}{{}^{i}\bar{\mu}} d^2 \, \Delta\delta \, g_k \mid \frac{\partial \Psi}{\partial x_k} > \; + \; O (\Delta\delta^2) \tag{E-27}$$

$$< {}^{i}\bar{\rho} (d + \Delta\delta) \dot{X}_k \mid \frac{\partial \Psi}{\partial x_k} > \; = \; < {}^{i}\bar{\rho} \, d \dot{X}_k \mid \frac{\partial \Psi}{\partial x_k} > + < {}^{i}\bar{\rho} \, \Delta\delta \, \dot{X}_k \mid \frac{\partial \Psi}{\partial x_k} > \tag{E-28}$$

$$2 < {}^{i}\bar{\rho} \, {}^{i}V_{loss} \mid \Psi > \tag{E-29}$$

Again, f^n can be split as

$$f^n (\delta, \sigma) \; = \; f^n_{new} (\Delta\delta, \Delta\delta) \; + \; f^n_{old} (d, p) \tag{E-30}$$

where

$$\begin{aligned} f^n_{new} \; = \; & \alpha_S^2 < \frac{{}^{i}\bar{\rho}}{{}^{i}\bar{\mu}} d^3 \frac{\partial \Delta\sigma}{\partial x^k} \mid \frac{\partial \Psi}{\partial x_k} >^n \; + \; 3 \, \alpha_S^2 < \frac{{}^{i}\bar{\rho}}{{}^{i}\bar{\mu}} d^2 \frac{\partial p}{\partial x_k} \Delta\delta \mid \frac{\partial \Psi}{\partial x_k} >^n \\ & - \; 3 \, \alpha_B \, \alpha_S^2 < \frac{{}^{i-2}\bar{\rho}}{{}^{i}\bar{\mu}} d^2 \, g_k \, \Delta\delta \mid \frac{\partial \Psi}{\partial x_k} >^n \; + < {}^{i}\bar{\rho} \, \dot{X}_k \, \Delta\delta \mid \frac{\partial \Psi}{\partial x_k} >^n \\ & - \; \alpha_S^2 \left[\frac{{}^{i}\bar{\rho}}{{}^{i}\bar{\mu}} d^3 \, \Psi \frac{\partial \Delta\sigma}{\partial x_k} \mid n_k \right]^n \; - \; 3 \, \alpha_S^2 \left[\frac{{}^{i}\bar{\rho}}{{}^{i}\bar{\mu}} d^2 \, \Psi \frac{\partial p}{\partial x_k} \Delta\delta \mid n_k \right]^n \\ & + \; 3 \, \alpha_B \, \alpha_S^2 \left[\frac{{}^{i-2}\bar{\rho}}{{}^{i}\bar{\mu}} d^2 \, \Psi \, g_k \, \Delta\delta \mid n_k \right]^n \; - \left[{}^{i}\bar{\rho} \, \Psi \dot{X}_k \, \Delta\delta \mid n_k \right]^n \end{aligned} \tag{E-31}$$

$$\begin{aligned} f^n_{old} \; = \; & - \; \alpha_S^2 \left[\frac{{}^{i}\bar{\rho}}{{}^{i}\bar{\mu}} d^3 \, \Psi \frac{\partial p}{\partial x_k} \mid n_k \right]^n \; + \; \alpha_B \, \alpha_S^2 \left[\frac{{}^{i-2}\bar{\rho}}{{}^{i}\bar{\mu}} d^3 \, \Psi \, g_k \mid n_k \right]^n \; - \left[{}^{i}\bar{\rho} \, d \, \Psi \dot{X}_k \mid n_k \right]^n \\ & + \; \alpha_S^2 < \frac{{}^{i}\bar{\rho}}{{}^{i}\bar{\mu}} d^3 \frac{\partial p}{\partial x_k} \mid \frac{\partial \Psi}{\partial x_k} >^n \; - \; \alpha_B \, \alpha_S^2 < \frac{{}^{i-2}\bar{\rho}}{{}^{i}\bar{\mu}} d^3 \, g_k \mid \frac{\partial \Psi}{\partial x_k} >^n \\ & + < {}^{i}\bar{\rho} \, d \dot{X}_k \mid \frac{\partial \Psi}{\partial x_k} >^n \; + \; 2 < {}^{i}\bar{\rho} \, {}^{i}V_{loss} \mid \Psi >^n \end{aligned} \tag{E-32}$$

Inserting Eqs. (E-31) and (E-32) in Eq. (E-21) leads to

$$
\begin{aligned}
3 <{}^{i}\bar{\rho}\,\Delta\delta \mid \Psi>^{(n)} + 2\,\Delta t f^{n}_{new} = \\
4 <{}^{i}\bar{\rho}\,\delta \mid \Psi>^{(n-1)} - <{}^{i}\bar{\rho}\,\delta \mid \Psi>^{(n-2)} \\
- 3 <{}^{i}\bar{\rho}\,d \mid \Psi>^{(n)} - 2\,\Delta t f^{n}_{old}
\end{aligned}
\tag{E-33}
$$

Expanding the above equation and applying Newton-Raphson for time steps (superscript n) $n \geq 2$, with $\delta = d + \Delta\delta$ and $\sigma = p + \Delta\sigma$, gives the following incremental equation

$$
\begin{aligned}
3 <{}^{i}\bar{\rho}\,\Delta\delta \mid \Psi>^{n} - 2\,\Delta t\,\alpha_S^2 \left[\frac{{}^{i}\bar{\rho}}{{}^{i}\bar{\mu}} d^3\,\Psi \frac{\partial\,\Delta\sigma}{\partial x_k} \mid n_k \right]^{n} - 6\,\Delta t\,\alpha_S^2 \left[\frac{{}^{i}\bar{\rho}}{{}^{i}\bar{\mu}} d^2\,\Psi \frac{\partial p}{\partial x_k}\,\Delta\delta \mid n_k \right]^{n} \\
+ 2\,\Delta t\,\alpha_S^2 < \frac{{}^{i}\bar{\rho}}{{}^{i}\bar{\mu}} d^3 \frac{\partial\,\Delta\sigma}{\partial x_k} \mid \frac{\partial \Psi}{\partial x_k} >^{n} + 6\,\Delta t\,\alpha_S^2 < \frac{{}^{i}\bar{\rho}}{{}^{i}\bar{\mu}} d^2 \frac{\partial p}{\partial x_k}\,\Delta\delta \mid \frac{\partial \Psi}{\partial x_k} >^{n} \\
+ 6\,\Delta t\,\alpha_B\,\alpha_S^2 \left[\frac{{}^{i}\bar{\rho}^2}{{}^{i}\bar{\mu}} d^2\,\Psi\, g_k\,\Delta\delta \mid n_k \right]^{n} - 2\,\Delta t \left[{}^{i}\bar{\rho}\,\Psi\,\dot{X}_k\,\Delta\delta \mid n_k \right]^{n} \\
- 6\,\Delta t\,\alpha_B\,\alpha_S^2 < \frac{{}^{i}\bar{\rho}^2}{{}^{i}\bar{\mu}} d^2\, g_k \Delta\delta \mid \frac{\partial \Psi}{\partial x_k} >^{n} + 2\,\Delta t < {}^{i}\bar{\rho}\,\dot{X}_k\,\Delta\delta \mid \frac{\partial \Psi}{\partial x_k} >^{n} \\
= 2\,\Delta t\,\alpha_S^2 \left[\frac{{}^{i}\bar{\rho}}{{}^{i}\bar{\mu}} d^3\,\Psi \frac{\partial p}{\partial x_k} \mid n_k \right]^{n} - 2\,\Delta t\,\alpha_B\,\alpha_S^2 \left[\frac{{}^{i}\bar{\rho}^2}{{}^{i}\bar{\mu}} d^3\,\Psi\, g_k \mid n_k \right]^{n} \\
+ 2\,\Delta t\,\alpha_B\,\alpha_S^2 < \frac{{}^{i}\bar{\rho}^2}{{}^{i}\bar{\mu}} d^3\, g_k \mid \frac{\partial \Psi}{\partial x_k} >^{n} - 2\,\Delta t < {}^{i}\bar{\rho}\,d\,\dot{X}_k \mid \frac{\partial\,{}^{i}\bar{\rho}}{\partial x_k} >^{n} \\
+ 2\,\Delta t \left[{}^{i}\bar{\rho}\,d\,\Psi\,\dot{X}_k \mid n_k \right]^{n} - 2\,\Delta t\,\alpha_S^2 < \frac{{}^{i}\bar{\rho}}{{}^{i}\bar{\mu}} d^3 \frac{\partial p}{\partial x_k} \mid \frac{\partial \Psi}{\partial x_k} >^{n} \\
- 4\,\Delta t < {}^{i}\bar{\rho}\;{}^{i}V_{loss} \mid \Psi >^{n} - 3 <{}^{i}\bar{\rho}\,d \mid \Psi >^{n} \\
+ 4 <{}^{i}\bar{\rho}\,\delta \mid \Psi >^{n-1} - <{}^{i}\bar{\rho}\,\delta \mid \Psi >^{n-2}
\end{aligned}
\tag{E-34}
$$

Analogously for Eq. (E-22) leads to

$$
\begin{aligned}
2 <{}^{i}\bar{\rho}\,\Delta\delta \mid \Psi>^{(n=1)} - \Delta t f^{(n=1)}_{new} = \Delta t f^{(n=1)}_{old} - 2 <{}^{i}\bar{\rho}\,d \mid \Psi>^{(n=1)} \\
+ 2 <{}^{i}\bar{\rho}\,d \mid \Psi>^{(n=0)} + \Delta t f^{(n=0)}
\end{aligned}
\tag{E-35}
$$

or in expanded form

$$
\begin{aligned}
2 <{}^{i}\bar{\rho}\,\Delta\delta \mid \Psi>^{1} &+ \Delta t\,\alpha_S^2\left[\frac{{}^{i}\bar{\rho}}{{}^{i}\bar{\mu}} d^3\,\Psi\frac{\partial\,\Delta\sigma}{\partial x_k} \mid n_k\right]^{1} + 3\,\Delta t\,\alpha_S^2\left[\frac{{}^{i}\bar{\rho}}{{}^{i}\bar{\mu}} d^2\,\Psi\frac{\partial p}{\partial x_k}\,\Delta\delta \mid n_k\right]^{1} \\
&- 3\,\Delta t\,\alpha_B\,\alpha_S^2\left[\frac{{}^{i}\bar{\rho}^2}{{}^{i}\bar{\mu}} d^2\,\Psi\,g_k\,\Delta\delta \mid n_k\right]^{1} + \Delta t\left[{}^{i}\bar{\rho}\,\Psi\,\dot{X}_k\,\Delta\delta \mid n_k\right]^{1} \\
&- \Delta t\,\alpha_S^2 <\frac{{}^{i}\bar{\rho}}{{}^{i}\bar{\mu}} d^3\frac{\partial\,\Delta\sigma}{\partial x_k} \mid \frac{\partial\Psi}{\partial x_k}>^{1} - 3\,\Delta t\,\alpha_S^2 <\frac{{}^{i}\bar{\rho}}{{}^{i}\bar{\mu}} d^2\frac{\partial p}{\partial x_k}\,\Delta\delta \mid \frac{\partial\Psi}{\partial x_k}>^{1} \\
&+ 3\,\Delta t\,\alpha_B\,\alpha_S^2 <\frac{{}^{i}\bar{\rho}^2}{{}^{i}\bar{\mu}} d^2\,g_k\,\Delta\delta \mid \frac{\partial\Psi}{\partial x_k}>^{1} - \Delta t <{}^{i}\bar{\rho}\,\dot{X}_k\,\Delta\delta \mid \frac{\partial\Psi}{\partial x_k}>^{1} \\
= -\Delta t\,\alpha_S^2\left[\frac{{}^{i}\bar{\rho}}{{}^{i}\bar{\mu}} d^3\,\Psi\frac{\partial p}{\partial x_k} \mid n_k\right]^{1} &+ \Delta t\,\alpha_B\,\alpha_S^2\left[\frac{{}^{i}\bar{\rho}^2}{{}^{i}\bar{\mu}} d^3\,\Psi\,g_k \mid n_k\right]^{1} \\
&- \Delta t\left[{}^{i}\bar{\rho}\,d\,\Psi\,\dot{X}_k \mid n_k\right]^{1} + \Delta t\,\alpha_S^2 <\frac{{}^{i}\bar{\rho}}{{}^{i}\bar{\mu}} d^3\frac{\partial p}{\partial x_k} \mid \frac{\partial\Psi}{\partial x_k}>^{1} \\
&- \Delta t\,\alpha_B\,\alpha_S^2 <\frac{{}^{i}\bar{\rho}^2}{{}^{i}\bar{\mu}} d^3\,g_k \mid \frac{\partial\Psi}{\partial x_k}>^{1} + \Delta t <{}^{i}\bar{\rho}\,d\,\dot{X}_k \mid \frac{\partial\Psi}{\partial x_k}>^{1} \\
&+ 2\,\Delta t <{}^{i}\bar{\rho}\,{}^{i}V_{loss} \mid \Psi>^{1} - 2 <{}^{i}\bar{\rho}\,d \mid \Psi>^{1} \\
&+ 2 <{}^{i}\bar{\rho}\,\delta \mid \Psi>^{0} - \Delta t\,\alpha_S^2\left[\frac{{}^{i}\bar{\rho}}{{}^{i}\bar{\mu}}\delta^3\,\Psi\frac{\partial\sigma}{\partial x_k} \mid n_k\right]^{0} \\
&+ \Delta t\,\alpha_B\,\alpha_S^2\left[\frac{{}^{i}\bar{\rho}^2}{{}^{i}\bar{\mu}}\delta^3\,\Psi\,g_k \mid n_k\right]^{0} - \Delta t\left[{}^{i}\bar{\rho}\,\delta\,\Psi\,\dot{X}_k \mid n_k\right]^{0} \\
&+ \Delta t\,\alpha_S^2 <\frac{{}^{i}\bar{\rho}}{{}^{i}\bar{\mu}}\delta^3\frac{\partial\sigma}{\partial x^k} \mid \frac{\partial\Psi}{\partial x_k}>^{0} - \Delta t\,\alpha_B\,\alpha_S^2 <\frac{{}^{i}\bar{\rho}^2}{{}^{i}\bar{\mu}}\delta^3\,g_k \mid \frac{\partial\Psi}{\partial x_k}>^{0} \\
&+ \Delta t <{}^{i}\bar{\rho}\,\delta\,\dot{X}_k \mid \frac{\partial\Psi}{\partial x_k}>^{0} + 2\,\Delta t <{}^{i}\bar{\rho}\,{}^{i}V_{loss} \mid \Psi>^{0}
\end{aligned}
\tag{E-36}
$$

Isolating similar terms from Eq. (E-34) and Eq. (E-36) gives

$$
\begin{aligned}
T_1 &= \langle {}^{i}\bar{\rho}\,\Delta\delta \mid \Psi \rangle & T_{10} &= \left[\frac{{}^{i}\bar{\rho}^2}{{}^{i}\bar{\mu}} d^3\,\Psi\, g_k \mid n_k \right] \\
T_2 &= \langle {}^{i}\bar{\rho}\, d \mid \Psi \rangle & T_{11} &= \left\langle \frac{{}^{i}\bar{\rho}^2}{{}^{i}\bar{\mu}} d^2\, g_k\, \Delta\delta \mid \frac{\partial \Psi}{\partial x_k} \right\rangle \\
T_3 &= \left[\frac{{}^{i}\bar{\rho}}{{}^{i}\bar{\mu}} d^3\,\Psi \frac{\partial\, \Delta\sigma}{\partial x_k} \mid n_k \right] & T_{12} &= \left\langle \frac{{}^{i}\bar{\rho}^2}{{}^{i}\bar{\mu}} d^3\, g_k \mid \frac{\partial \Psi'}{\partial x_k} \right\rangle \\
T_4 &= \left[\frac{{}^{i}\bar{\rho}}{{}^{i}\bar{\mu}} d^3\,\Psi \frac{\partial p}{\partial x_k} \mid n_k \right] & T_{13} &= \left[{}^{i}\bar{\rho}\,\Psi\, \dot{X}_k\, \Delta\delta \mid n_k \right] \\
T_5 &= \left\langle \frac{{}^{i}\bar{\rho}}{{}^{i}\bar{\mu}} d^3 \frac{\partial\, \Delta\sigma}{\partial x_k} \mid \frac{\partial \Psi}{\partial x_k} \right\rangle & T_{14} &= \left[{}^{i}\bar{\rho}\, d\,\Psi\, \dot{X}_k \mid n_k \right] \qquad \text{(E-37)} \\
T_6 &= \left\langle \frac{{}^{i}\bar{\rho}}{{}^{i}\bar{\mu}} d^3 \frac{\partial p}{\partial x_k} \mid \frac{\partial \Psi}{\partial x_k} \right\rangle & T_{15} &= \left\langle {}^{i}\bar{\rho}\, \dot{X}_k\, \Delta\delta \mid \frac{\partial \Psi}{\partial x_k} \right\rangle \\
T_7 &= \left[\frac{{}^{i}\bar{\rho}}{{}^{i}\bar{\mu}} d^2\,\Psi \frac{\partial p}{\partial x_k}\, \Delta\delta \mid n_k \right] & T_{16} &= \left\langle {}^{i}\bar{\rho}\, d\, \dot{X}_k \mid \frac{\partial \Psi}{\partial x_k} \right\rangle \\
T_8 &= \left\langle \frac{{}^{i}\bar{\rho}}{{}^{i}\bar{\mu}} d^2 \frac{\partial p}{\partial x_k}\, \Delta\delta \mid \frac{\partial \Psi}{\partial x_k} \right\rangle & T_{17} &= \langle {}^{i}\bar{\rho}\, {}^{i}V_{loss} \mid \Psi \rangle \\
T_9 &= \left[\frac{{}^{i}\bar{\rho}^2}{{}^{i}\bar{\mu}} d^2\,\Psi\, g_k\, \Delta\delta \mid n_k \right]
\end{aligned}
$$

The incremental terms in the Newton-Raphson expansion can be numerically approximated as

$$
\begin{aligned}
\Delta\delta \equiv \Delta\delta^h &= \sum_{n=1}^{N} \Delta\delta_n\, \phi_n \\
\Delta\sigma \equiv \Delta\sigma^h &= \sum_{n=1}^{N} \Delta\sigma_n\, \phi_n
\end{aligned}
\qquad \text{(E-38)}
$$

Finally each one of the terms in Eq. (E-37) can be expanded as follows

$$
\begin{aligned}
\mathrm{T1} &= \left\langle {}^{i}\bar{\rho}\,\Delta\delta \,\middle|\, \psi \right\rangle = \sum_{n} \left\langle {}^{i}\bar{\rho}\,\phi_n \,\middle|\, \phi_m \right\rangle \Delta\delta_n \\
\mathrm{T1}^{e} &= \underbrace{\left[\int_{\Omega^e} {}^{i}\bar{\rho}\,\phi_n\,\phi_m\,(det\,J)\,drds \right]}_{\mathrm{T1}^{e}_{mn}} \Delta\delta_n \\
\mathrm{T2}^{e} &= \underbrace{\left[\int_{\Omega^e} {}^{i}\bar{\rho}\,d\,\phi_m\,(det\,J)\,drds \right]}_{\mathrm{T2}^{e}_{m}} \Delta\delta_n
\end{aligned}
\tag{E-39}
$$

Boundary terms are only accounted, when flux boundary condition is non-zero. Henceforth, a generic non-zero boundary term integrated along the direction t is assumed—where t may represent either r or s, depending on what edge the flux is prescribed

$$
\begin{aligned}
\mathrm{T3} &= \left[\frac{{}^{i}\bar{\rho}}{{}^{i}\bar{\mu}}\, d^3 \frac{\partial(\Delta\sigma)}{\partial x_k}\, \Psi \,\middle|\, n_k \right] = \left[\frac{{}^{i}\bar{\rho}}{{}^{i}\bar{\mu}}\, d^3 \left(\frac{\partial(\Delta\sigma)}{\partial x}\, n_x + \frac{\partial(\Delta\sigma)}{\partial y}\, n_y \right) \Psi \right] \\
&= \left[\int_{\Omega^e} \frac{{}^{i}\bar{\rho}}{{}^{i}\bar{\mu}}\, d^3 \left(\phi_{n,x}\, n_x + \phi_{n,y}\, n_y \right) \phi_m \left[line(det\,J) \right] dl \right] \Delta\sigma_n
\end{aligned}
\tag{E-40}
$$

$$
\mathrm{T3}^{e}_{mn} = \int_{-1}^{1} \frac{{}^{i}\bar{\rho}}{{}^{i}\bar{\mu}}\, d^3 \left(J^{-1}_{xk} \frac{\partial\phi}{\partial r_k}\, n_x(r,s) + J^{-1}_{yk} \frac{\partial\phi}{\partial r_k}\, n_y(r,s) \right) \phi_m \sqrt{\left(\frac{dx}{dl}\right)^2 + \left(\frac{dy}{dl}\right)^2}\, dl
$$

$$
\mathrm{T4}^{e}_{m} = \int_{-1}^{1} \frac{{}^{i}\bar{\rho}}{{}^{i}\bar{\mu}}\, d^3\, J^{-1}_{jk} \frac{\partial p}{\partial r_k}\, n_j\, \phi_m \sqrt{\left(\frac{dx}{dl}\right)^2 + \left(\frac{dy}{dl}\right)^2}\, dl \tag{E-41}
$$

$$
\begin{aligned}
\mathrm{T5} &= \left\langle \frac{{}^{i}\bar{\rho}}{{}^{i}\bar{\mu}} d^3 \left(\frac{\partial\Delta\sigma}{\partial x} \frac{\partial\Psi}{\partial x} + \frac{\partial\Delta\sigma}{\partial y} \frac{\partial\Psi}{\partial y} \right) \right\rangle \\
&= \left[\int_{\Omega^e} \frac{{}^{i}\bar{\rho}}{{}^{i}\bar{\mu}}\, d^3 \left(\phi_{n,x}\, \phi_{m,x} + \phi_{n,y}\, \phi_{m,y} \right) (det\,J)\, drds \right] \Delta\sigma_n
\end{aligned}
\tag{E-42}
$$

$$
\mathrm{T5}^{e}_{mn} = \left[\int_{\Omega^e} \frac{{}^{i}\bar{\rho}}{{}^{i}\bar{\mu}}\, d^3\, J^{-1}_{xk}\, \phi_{n,k}\, J^{-1}_{xl}\, \phi_{m,l}\, (det\,J)\, drds + \int_{\Omega^e} \frac{{}^{i}\bar{\rho}}{{}^{i}\bar{\mu}}\, d^3\, J^{-1}_{yk}\, \phi_{n,k}\, J^{-1}_{yl}\, \phi_{m,l}\, (det\,J)\, drds \right]
$$

$$
\mathrm{T6}^{e}_{m} = \int_{\Omega^e} \frac{{}^{i}\bar{\rho}}{{}^{i}\bar{\mu}}\, d^3\, J^{-1}_{xk} \frac{\partial p}{\partial x_l}\, J^{-1}_{xl}\, \phi_{m,l}\, (det\,J)\, drds + \int_{\Omega^e} \frac{{}^{i}\bar{\rho}}{{}^{i}\bar{\mu}}\, d^3\, J^{-1}_{yk} \frac{\partial p}{\partial x_l}\, J^{-1}_{yl}\, \phi_{m,l}\, (det\,J)\, drds \tag{E-43}
$$

$$T7 = \left[\frac{{}^{i}\bar{\rho}}{{}^{i}\bar{\mu}} d^2 \Psi \left(\frac{\partial p}{\partial x} n_x + \frac{\partial p}{\partial y} n_y \right) \Delta\delta \right]$$

$$T7^{e}_{mn} = \left[\int_{\Omega^e} \frac{{}^{i}\bar{\rho}}{{}^{i}\bar{\mu}} d^2 \left(J^{-1}_{xk} \frac{\partial p}{\partial r_k} n_x + J^{-1}_{yk} \frac{\partial p}{\partial r_k} n_y \right) \phi_m \, \phi_n \, [line(det\, J)] \, dl \right] \quad \text{(E-44)}$$

$$T8 = \left\langle \frac{{}^{i}\bar{\rho}}{{}^{i}\bar{\mu}} d^2 \Delta\delta \left(\frac{\partial p}{\partial x} \frac{\partial \Psi}{\partial x} + \frac{\partial p}{\partial y} \frac{\partial \Psi}{\partial y} \right) \right\rangle$$

$$T8^{e}_{mn} = \left[\int_{\Omega^e} \frac{{}^{i}\bar{\rho}}{{}^{i}\bar{\mu}} d^2 \left(J^{-1}_{xl} \frac{\partial p}{\partial r_l} J^{-1}_{xk} \frac{\partial \phi_m}{\partial r_k} \right) \phi_n (det\, J)\, drds + \int_{\Omega^e} \frac{{}^{i}\bar{\rho}}{{}^{i}\bar{\mu}} d^2 \left(J^{-1}_{yl} \frac{\partial p}{\partial r_l} J^{-1}_{yk} \frac{\partial \phi_m}{\partial r_k} \right) \phi_n (det\, J)\, drds \right] \quad \text{(E-45)}$$

$$T11 = \left\langle \frac{{}^{i}\bar{\rho}^{2}}{{}^{i}\bar{\mu}} d^2 \Delta\delta \left(g_x \frac{\partial \Psi}{\partial x} + g_y \frac{\partial \Psi}{\partial y} \right) \right\rangle$$

$$T11^{e}_{mn} = \left[\int_{\Omega^e} \frac{{}^{i}\bar{\rho}^{2}}{{}^{i}\bar{\mu}} d^2 \phi_n \, g_x(r,s) \, J^{-1}_{xl} \frac{\partial \phi_m}{\partial r_l} (det\, J)\, drds + \int_{\Omega^e} \frac{{}^{i}\bar{\rho}^{2}}{{}^{i}\bar{\mu}} d^2 \phi_n \, g_y(r,s) \, J^{-1}_{yl} \frac{\partial \phi_m}{\partial r_l} (det\, J)\, drds \right] \quad \text{(E-46)}$$

$$T12^{e}_{m} = \left[\int_{\Omega^e} \frac{{}^{i}\bar{\rho}^{2}}{{}^{i}\bar{\mu}} d^3 \, g_x(r,s) \, J^{-1}_{xl} \frac{\partial \phi_m}{\partial r_l} (det\, J)\, drds + \int_{\Omega^e} \frac{{}^{i}\bar{\rho}^{2}}{{}^{i}\bar{\mu}} d^3 \, g_y(r,s) \, J^{-1}_{yl} \frac{\partial \phi_m}{\partial r_l} (det\, J)\, drds \right] \quad \text{(E-47)}$$

$$T15 = \left\langle {}^{i}\bar{\rho} \Delta\delta \left(\dot{X} \frac{\partial \Psi}{\partial x} + \dot{Y} \frac{\partial \Psi}{\partial y} \right) \right\rangle$$

$$T15^{e}_{m} = \left[\int_{\Omega^e} {}^{i}\bar{\rho} \, \phi_n \, \dot{X}(r,s) \, J^{-1}_{xl} \frac{\partial \phi_m}{\partial r_l} (det\, J)\, drds + \int_{\Omega^e} {}^{i}\bar{\rho} \, \phi_n \, \dot{Y}(r,s) \, J^{-1}_{yl} \frac{\partial \phi_m}{\partial r_l} (det\, J)\, drds \right] \quad \text{(E-48)}$$

$$T16 = \left\langle {}^{i}\bar{\rho} d \left(\dot{X} \frac{\partial \Psi}{\partial x} + \dot{Y} \frac{\partial \Psi}{\partial y} \right) \right\rangle$$

$$T16^{e}_{m} = \left[\int_{\Omega^e} {}^{i}\bar{\rho} \, d \, \dot{X}(r,s) \, J^{-1}_{xl} \frac{\partial \phi_m}{\partial r_l} (det\, J)\, drds + \int_{\Omega^e} {}^{i}\bar{\rho} \, d \, \dot{Y}(r,s) \, J^{-1}_{yl} \frac{\partial \phi_m}{\partial r_l} (det\, J)\, drds \right] \quad \text{(E-49)}$$

$$T17 = \left\langle {}^{i}\bar{\rho} \, {}^{i}V_{loss} \,\middle|\, \Psi \right\rangle$$

$$T17^{e}_{m} = \int_{\Omega^e} {}^{i}\bar{\rho} \, {}^{i}V_{loss} \, \phi_m \, (det\, J)\, drds \quad \text{(E-50)}$$

The other boundary terms T9, T10, T13 and T14 are expanded analogously to T3.

Finally rewriting Eqs. (E-34) and (E-36)

$$\begin{aligned} 3\,(\mathrm{T1})^{n}_{ml}\,\Delta\delta_l^{n} + 2\,\Delta t\,\alpha_s^2\,(\mathrm{T5})^{n}_{ml}\,\Delta\sigma_l^{n} + 6\,\Delta t\,\alpha_s^2\,(\mathrm{T8})^{n}_{ml}\,\Delta\delta_l^{n} - 6\,\Delta t\,\alpha_B\,\alpha_s^2\,(\mathrm{T11})^{n}_{ml}\,\Delta\delta_l^{n} \\ + 2\,\Delta t\,(\mathrm{T15})^{n}_{ml}\,\Delta\delta_l^{n} = -2\,\Delta t\,(\mathrm{T18})^{n}_{m} - 2\,\Delta t\,\alpha_s^2\,(\mathrm{T6})^{n}_{m} + 2\,\Delta t\,\alpha_B\,\alpha_s^2\,(\mathrm{T12})^{n}_{m} \\ - 2\,\Delta t\,(\mathrm{T16})^{n}_{m} - 4\,\Delta t\,(\mathrm{T17})^{n}_{m} - 3\,(\mathrm{T2})^{n}_{m} \\ + 4\,(\mathrm{T2})^{n-1}_{m} - (\mathrm{T2})^{n-2}_{m} \end{aligned} \tag{E-51}$$

$$\begin{aligned} 2\,(\mathrm{T1})^{n=1}_{ml}\,\Delta\delta_l^{n=1} - \Delta t\,\alpha_s^2\,(\mathrm{T5})^{n=1}_{ml}\,\Delta\sigma_l^{n=1} - 3\,\Delta t\,\alpha_s^2\,(\mathrm{T8})^{n=1}_{ml}\,\Delta\delta_l^{n=1} \\ + 3\,\Delta t\,\alpha_B\,\alpha_s^2\,(\mathrm{T11})^{n=1}_{ml}\,\Delta\delta_l^{n=1} - \Delta t\,(\mathrm{T15})^{n=1}_{ml}\,\Delta\delta_l^{n=1} = \\ \Delta t\,(\mathrm{T18})^{n=1}_{m} + \Delta t\,\alpha_s^2\,(\mathrm{T6})^{n=1}_{m} - \Delta t\,\alpha_B\,\alpha_s^2\,(\mathrm{T12})^{n=1}_{m} \\ + \Delta t\,(\mathrm{T16})^{n=1}_{m} + 2\,\Delta t\,(\mathrm{T17})^{n=1}_{m} - 2\,(\mathrm{T2})^{n=1}_{m} + 2\,(\mathrm{T2})^{n=0}_{m} + \Delta t\,(\mathrm{T18})^{n=0}_{m} \\ + \Delta t\,\alpha_s^2\,(\mathrm{T6})^{n=0}_{m} - \Delta t\,\alpha_B\,\alpha_s^2\,(\mathrm{T12})^{n=0}_{m} + \Delta t\,(\mathrm{T16})^{n=0}_{m} + 2\,\Delta t\,(\mathrm{T17})^{n=0}_{m} \end{aligned} \tag{E-52}$$

E-2 The Axisymmetrical Simplification

For the axisymmetrical case the integrand in Eq. (E-1) and Eq. (E-5) can be simplified to

$$\frac{\partial({}^{i}\rho\,\delta)}{\partial t} + \frac{1}{r}\frac{\partial\left(r\,{}^{i}\rho\,\delta\,{}^{i}\bar{u}_r\right)}{\partial r} + 2\,{}^{i}\rho\,{}^{i}V_{loss} = 0$$

$${}^{i}\bar{u}_r = -\frac{\delta^2}{12\,{}^{i}\mu}\frac{\partial p}{\partial r} \tag{E-53}$$

Notice that the gravity effects are dropped (non-symmetrical). A word of caution should be said. The absence of gravity effects here have nothing to do with the derivations in **Chapter 2** and **Appendices B** and **C**.

In **Chapter 2** the analysis was aimed at a blob that is capable to maintain (approximately) its shape (circular) under the effect of gravity. The objective there was to characterize the overall flow behavior, specifically encapsulation effects. In **Chapter 3** and **Appendix E** the objective is different:

- accurately track the fluid interfaces (study morphological changes)

The weak variational formulation of Eq. (E-53) is

$$\frac{d}{dt}\left[\int_{{}^{i}R_1(t)}^{{}^{i}R_2(t)} {}^{i}\bar{\rho}\,\delta\,2\pi r\,\phi\,dr\right] + {}^{i}\bar{\rho}\,2\pi r\,\delta\left[{}^{i}u_r - \dot{R}\right]\phi\Big|_{{}^{i}R_1(t)}^{{}^{i}R_2(t)}$$
$$- \int_{{}^{i}R_1(t)}^{{}^{i}R_2(t)} {}^{i}\bar{\rho}\,\delta\,2\pi r\left[{}^{i}u_r - \dot{R}\right]\frac{\partial\phi}{\partial r}dr + \int_{{}^{i}R_1(t)}^{{}^{i}R_2(t)} 2\,{}^{i}\bar{\rho}\,{}^{i}V_{loss}\,2\pi r\,\phi\,dr = 0 \tag{E-54}$$

$${}^{i}\bar{u}_r = -\frac{\delta^2}{{}^{i}\bar{\mu}}\frac{\partial p}{\partial r} \tag{E-55}$$

or combining both equations

$$\frac{d}{dt}\left\langle {}^{i}\bar{\rho}\,\delta\,r \;\middle|\; \phi\right\rangle + \left\langle \frac{{}^{i}\bar{\rho}}{{}^{i}\bar{\mu}}\delta^3 r\frac{\partial p}{\partial r} \;\middle|\; \frac{\partial\phi}{\partial r}\right\rangle + \left\langle {}^{i}\bar{\rho}\,\delta\,r\dot{R} \;\middle|\; \frac{\partial\phi}{\partial r}\right\rangle$$
$$+ \left\langle 2\,{}^{i}\bar{\rho}\,V_{loss}\,r \;\middle|\; \phi\right\rangle + \phi\,{}^{i}\bar{\rho}\left[\frac{Q_r}{2\pi} - r\,\delta\,\dot{R}\right]_{{}^{i}R_1}^{{}^{i}R_2} = 0 \tag{E-56}$$

Nondimensionalizing Eq. (E-56) results on

$$\frac{d}{dt}\left\langle {}^{i}\bar{\rho}\,\delta\,r \;\middle|\; \phi\right\rangle + \alpha_s^2\,\alpha_p\left\langle \frac{{}^{i}\bar{\rho}}{{}^{i}\bar{\mu}}\delta^3 r\frac{\partial\sigma}{\partial r} \;\middle|\; \frac{\partial\phi}{\partial r}\right\rangle + \left\langle {}^{i}\bar{\rho}\,\delta\,r\dot{R} \;\middle|\; \frac{\partial\phi}{\partial r}\right\rangle$$
$$+ 2\left\langle {}^{i}\bar{\rho}\,V_{loss}\,r \;\middle|\; \phi\right\rangle + \phi\,{}^{i}\bar{\rho}\left[\frac{Q_r}{2\pi} - r\,\delta\,\dot{R}\right]_{{}^{i}R_1}^{{}^{i}R_2} = 0 \tag{E-57}$$

where

$$\alpha_s \equiv \frac{\Delta_R}{L_R}\;; \qquad \alpha_p = \frac{T_R\,\sigma_R}{\bar{\mu}_R} \tag{E-58}$$

To facilitate the numerical expansion of Eq. (E-57) the following terms are defined

$$
\begin{aligned}
A1^{(n)} &\equiv \left\langle {}^{i}\bar{\rho}\,\delta\, r \;\middle|\; \phi \right\rangle^{(n)} \\
A2^{(n)} &\equiv \left\langle \frac{{}^{i}\bar{\rho}}{{}^{i}\bar{\mu}}\,\delta^{3}\, r \frac{\partial \sigma}{\partial r} \;\middle|\; \frac{\partial \phi}{\partial r} \right\rangle^{(n)} \\
A3^{(n)} &\equiv \left\langle {}^{i}\bar{\rho}\,\delta\, r\, \dot{R} \;\middle|\; \frac{\partial \phi}{\partial r} \right\rangle^{(n)} \\
A4^{(n)} &\equiv \left\langle {}^{i}\bar{\rho}\, V_{loss}\, r \;\middle|\; \phi \right\rangle^{(n)} \\
A5^{(n)} &\equiv \phi\, {}^{i}\bar{\rho} \left[\frac{Q_r}{2\pi} - r\,\delta\,\dot{R} \right]_{{}^{i}R_1}^{{}^{i}R_2^{(n)}}
\end{aligned}
\tag{E-59}
$$

Repeating the same time integration procedures (described in the previous section), the resulting AM2 and BD2 formulations are

$$
\begin{aligned}
&-2\,A1^{(n=1)} - \Delta t\,\alpha_s^2\,\alpha_p\,A2^{(n=1)} - \Delta t\,A3^{(n=1)} - \Delta t\,2\,A4^{(n=1)} - \Delta t\,A5^{(n=1)} = \\
&\quad -2\,A1^{(n=0)} + \Delta t\,\alpha_s^2\,\alpha_p\,A2^{(n=0)} + \Delta t\,A3^{(n=0)} + \Delta t\,2\,A4^{(n=0)} + \Delta t\,A5^{(n=0)}
\end{aligned}
\tag{E-60}
$$

$$
3\,A1^{(n)} + 2\,\Delta t\,\alpha_s^2\,\alpha_p\,A2^{(n)} + 2\,\Delta t\,A3^{(n)} + 4\,\Delta t\,A4^{(n)} + 2\,\Delta t\,A5^{(n)} = 4\,A1^{(n-1)} - A1^{(n-2)} \tag{E-61}
$$

where

$$
\begin{aligned}
A1_m^{(n)} &\equiv \left\langle {}^{i}\bar{\rho}\,\delta\, r \;\middle|\; \phi_m \right\rangle^{(n)} \\
A2_{ml}^{(n)} &\equiv \left\langle \frac{{}^{i}\bar{\rho}}{{}^{i}\bar{\mu}}\,\delta^{3}\, r \frac{\partial \phi_l}{\partial r} \;\middle|\; \frac{\partial \phi_m}{\partial r} \right\rangle^{(n)} \\
A3_m^{(n)} &\equiv \left\langle {}^{i}\bar{\rho}\,\delta\, r\, \dot{R} \;\middle|\; \frac{\partial \phi_m}{\partial r} \right\rangle^{(n)} \\
A4_m^{(n)} &\equiv \left\langle {}^{i}\bar{\rho}\, V_{loss}\, r \;\middle|\; \phi_m \right\rangle^{(r.)} \\
A5_m^{(n)} &\equiv \phi_m\, {}^{i}\bar{\rho} \left[\frac{Q_r}{2\pi} - r\,\delta\,\dot{R} \right]_{{}^{i}R_1}^{{}^{i}R_2^{(n)}}
\end{aligned}
\tag{E-62}
$$

or collecting the terms in Eqs. (E-60) and (E-61)

$$\left[-\Delta t\ \alpha_s^2\ \alpha_p\ \mathrm{A2}_{ml}^{(n=1)}\right]\sigma_l^{(n=1)} = 2\left(-\mathrm{A1}_m^{(n=0)} + \mathrm{A1}_m^{(n=1)}\right) + \Delta t\ \alpha_s^2\ \alpha_p\ \mathrm{A2}_{ml}^{(n=0)}\ \sigma_l^{(n=0)} + \Delta t\left(\mathrm{A3}_m^{(n=0)} + \mathrm{A3}_m^{(n=1)}\right) + 2\,\Delta t\left(\mathrm{A4}_m^{(n=0)} + \mathrm{A4}_m^{(n=1)}\right) + \Delta t\left(\mathrm{A5}_m^{(n=0)} + \mathrm{A5}_m^{(n=1)}\right) \tag{E-63}$$

$$\left[2\ \Delta t\ \alpha_s^2\ \alpha_p\ \mathrm{A2}_{ml}^{(n)}\right]\sigma_l^{(n)} = \left(-3\ \mathrm{A1}_m^{(n)} + 4\ \mathrm{A1}_m^{(n-1)} - \mathrm{A1}_m^{(n-2)}\right) - 2\,\Delta t\ \mathrm{A3}_m^{(n)} - 4\,\Delta t\ \mathrm{A4}_m^{(n)} - 2\,\Delta t\ \mathrm{A5}_m^{(n)} \tag{E-64}$$

The isoparametric linear base is very simple, i.e.

$$\frac{\partial \phi_1}{\partial s} = -1 \qquad \frac{\partial \phi_2}{\partial s} = 1 \tag{E-65}$$

where

$$r = D_K\, s + R_K \qquad s = \frac{r - R_K}{R_{K+1} - R_K} \equiv \frac{r - R_K}{D_K}$$

$$det\ J = D_K \qquad ds = \frac{dr}{D_K} \tag{E-66}$$

$$\frac{\partial}{\partial r} = \frac{1}{det\ J}\frac{\partial}{\partial s}$$

For each element K the coefficients in Eq. (E-62) can be expanded as

$$^K\mathrm{A1}_m^{(n)} = \left[\int_0^1 {}^i\bar{\rho}\ \delta(s)\ (D_K\, s + R_K)\ \phi_m\ D_K\, ds\right]^{(n)}$$

$$^K\mathrm{A2}_m^{(n)} = \left[\int_0^1 \frac{{}^i\bar{\rho}}{{}^i\bar{\mu}}\ \delta^3(s)\ (D_K\, s + R_K)\frac{\partial \phi_l}{\partial s}\frac{\partial \phi_m}{\partial s}\frac{1}{D_K}\, ds\right]^{(n)} \tag{E-67}$$

$$^K\mathrm{A3}_m^{(n)} = \left[\int_0^1 {}^i\bar{\rho}\ \delta(s)\ (D_K\, s + R_K)\ \dot{R}(s)\frac{\partial \phi_m}{\partial s}\, ds\right]^{(n)}$$

$$^K\mathrm{A4}_m^{(n)} = \left[\int_0^1 \frac{{}^i\bar{\rho}}{{}^i\bar{\mu}}\ V_{loss}(s)\ (D_K\, s + R_K)\ \phi_m\ D_K\, ds\right]^{(n)} \tag{E-68}$$

$$
\begin{aligned}
{}^{1}A5_1^{(n)} &= -\,{}^{i-}\bar{\rho}\left[\frac{Q(R_w)}{2\pi} - R_w\,\delta(R_w)\,\dot{R}(R_w)\right]^{(n)} \\
{}^{L}A5_2^{(n)} &= {}^{i-}\bar{\rho}\left[\frac{Q(R_F)}{2\pi} - R_F\,\delta(R_F)\,\dot{R}(R_F)\right]^{(n)}
\end{aligned}
\tag{E-69}
$$

where the coefficients C_{ij} are defined below

$$
\begin{bmatrix} {}^{(K)}C_{11}^{(n=1)} & {}^{(K)}C_{12}^{(n=1)} \\ {}^{(K)}C_{21}^{(n=1)} & {}^{(K)}C_{22}^{(n=1)} \end{bmatrix}^{(n=1)} \begin{bmatrix} {}^{(K)}\sigma_1 \\ {}^{(K)}\sigma_2 \end{bmatrix}^{(n=1)} = \begin{bmatrix} {}^{(K)}E_1^{n=0,1} \\ {}^{(K)}E_2^{(n=0,1)} \end{bmatrix}
\tag{E-70}
$$

$$
\begin{bmatrix} {}^{(K)}C_{11}^{(n)} & {}^{(K)}C_{12}^{(n)} \\ {}^{(K)}C_{21}^{(n)} & {}^{(K)}C_{22}^{(n)} \end{bmatrix}^{(n)} \begin{bmatrix} {}^{(K)}\sigma_1 \\ {}^{(K)}\sigma_2 \end{bmatrix}^{(n)} = \begin{bmatrix} {}^{(K)}E_1^{(n,n-1,n-2)} \\ {}^{(K)}E_2^{(n,n-1,n-2)} \end{bmatrix}
\tag{E-71}
$$

$$
\begin{aligned}
{}^{(1)}C_{11}^{(n=1)} &= -\,\Delta t\,\alpha_s^2\,\alpha_p\,{}^{(1)}A2_{11} \\
{}^{(1)}C_{12}^{(n=1)} &= -\,\Delta t\,\alpha_s^2\,\alpha_p\,{}^{(1)}A2_{12} \\
{}^{(1)}C_{21}^{(n=1)} &= -\,\Delta t\,\alpha_s^2\,\alpha_p\,{}^{(1)}A2_{21} \\
{}^{(1)}C_{22}^{(n=1)} &= -\,\Delta t\,\alpha_s^2\,\alpha_p\,{}^{(1)}A2_{22}
\end{aligned}
\tag{E-72}
$$

$$
\begin{aligned}
{}^{(1)}C_{11}^{(n)} &= 2\,\Delta t\,\alpha_s^2\,\alpha_p\,{}^{(1)}A2_{11} \\
{}^{(1)}C_{12}^{(n)} &= 2\,\Delta t\,\alpha_s^2\,\alpha_p\,{}^{(1)}A2_{12} \\
{}^{(1)}C_{21}^{(n)} &= 2\,\Delta t\,\alpha_s^2\,\alpha_p\,{}^{(1)}A2_{21} \\
{}^{(1)}C_{22}^{(n)} &= 2\,\Delta t\,\alpha_s^2\,\alpha_p\,{}^{(1)}A2_{22}
\end{aligned}
\tag{E-73}
$$

$$
\begin{aligned}
{}^{(K)}C_{11}^{(n=1)} &= -\,\Delta t\,\alpha_s^2\,\alpha_p\,{}^{(K)}A2_{11} \\
{}^{(K)}C_{12}^{(n=1)} &= -\,\Delta t\,\alpha_s^2\,\alpha_p\,{}^{(K)}A2_{12} \\
{}^{(K)}C_{21}^{(n=1)} &= -\,\Delta t\,\alpha_s^2\,\alpha_p\,{}^{(K)}A2_{21} \\
{}^{(K)}C_{22}^{(n=1)} &= -\,\Delta t\,\alpha_s^2\,\alpha_p\,{}^{(K)}A2_{22}
\end{aligned}
\tag{E-74}
$$

$$
\begin{aligned}
{}^{(K)}C_{11}^{(n)} &= 2\,\Delta t\,\alpha_s^2\,\alpha_p\,{}^{(K)}A2_{11} \\
{}^{(K)}C_{12}^{(n)} &= 2\,\Delta t\,\alpha_s^2\,\alpha_p\,{}^{(K)}A2_{12} \\
{}^{(K)}C_{21}^{(n)} &= 2\,\Delta t\,\alpha_s^2\,\alpha_p\,{}^{(K)}A2_{21} \\
{}^{(K)}C_{22}^{(n)} &= 2\,\Delta t\,\alpha_s^2\,\alpha_p\,{}^{(K)}A2_{22}
\end{aligned}
\tag{E-75}
$$

$$
\begin{aligned}
{}^{(1)}E_1^{(n=0,1)} &= 2\left(-{}^{(1)}A1_1^{(n=0)} + {}^{(1)}A1_1^{(n=1)}\right) - \Delta t\ \alpha_s^2\ \alpha_p\ {}^{(1)}A2_{11}^{(n=0)}\ \sigma_1 + \Delta t\ \alpha_s^2\ \alpha_p\ {}^{(1)}A2_{12}^{(n=0)}\ \sigma_2 \\
&\quad + \Delta t\left({}^{(1)}A3_1^{(n=0)} + \Delta t\ {}^{(1)}A3_1^{(n=1)}\right) + 2\ \Delta t\left({}^{(1)}A4_1^{(n=0)} + {}^{(1)}A4_1^{(n=1)}\right) \\
&\quad + \Delta t\left({}^{(1)}A5_1^{(n=0)} + {}^{(1)}A5_1^{(n=1)}\right) \qquad \text{(E-76)} \\
{}^{(1)}E_2^{(n=0,1)} &= 2\left(-{}^{(1)}A1_2^{(n=0)} + {}^{(1)}A1_2^{(n=1)}\right) - \Delta t\ \alpha_s^2\ \alpha_p\ {}^{(1)}A2_{21}^{(n=0)}\ \sigma_1 + \Delta t\ \alpha_s^2\ \alpha_p\ {}^{(1)}A2_{22}^{(n=0)}\ \sigma_2 \\
&\quad + \Delta t\left({}^{(1)}A3_2^{(n=0)} + \Delta t\ {}^{(1)}A3_2^{(n=1)}\right) + 2\ \Delta t\left({}^{(1)}A4_2^{(n=0)} + {}^{(1)}A4_2^{(n=1)}\right)
\end{aligned}
$$

$$
\begin{aligned}
{}^{(1)}E_1^{(n,n-1,n-2)} &= -3\ {}^{(1)}A1_1^{(n)} + 4\ {}^{(1)}A1_1^{(n-2)} - {}^{(1)}A1_1^{(n-1)} - 2\ \Delta t\ {}^{(1)}A3_1^{(n)} \\
&\quad - 4\ \Delta t\ {}^{(1)}A4_1^{(n)} - 2\ \Delta t\ {}^{(1)}A5_1^{(n)} \qquad \text{(E-77)} \\
{}^{(1)}E_2^{(n,n-1,n-2)} &= -3\ {}^{(1)}A1_2^{(n)} + 4\ {}^{(1)}A1_2^{(n-2)} - {}^{(1)}A1_2^{(n-1)} - 2\ \Delta t\ {}^{(1)}A3_2^{(n)} - 4\ \Delta t\ {}^{(1)}A4_2^{(n)}
\end{aligned}
$$

$$
\begin{aligned}
{}^{(K)}E_1^{(n=0,1)} &= 2\left(-{}^{(K)}A1_1^{(n=0)} + {}^{(K)}A1_1^{(n=1)}\right) - \Delta t\ \alpha_s^2\ \alpha_p\ {}^{(K)}A2_{11}^{(n=0)}\ \sigma_1 + \Delta t\ \alpha_s^2\ \alpha_p\ {}^{(K)}A2_{12}^{(n=0)}\ \sigma_2 \\
&\quad + \Delta t\left({}^{(K)}A3_1^{(n=0)} + \Delta t\ {}^{(K)}A3_1^{(n=1)}\right) + 2\ \Delta t\left({}^{(K)}A4_1^{(n=0)} + {}^{(K)}A4_1^{(n=1)}\right) \\
&\quad + \Delta t\left({}^{(K)}A5_1^{(n=0)} + {}^{(K)}A5_1^{(n=1)}\right) \qquad \text{(E-78)} \\
{}^{(K)}E_2^{(n=0,1)} &= 2\left(-{}^{(K)}A1_2^{(n=0)} + {}^{(K)}A1_2^{(n=1)}\right) - \Delta t\ \alpha_s^2\ \alpha_p\ {}^{(K)}A2_{21}^{(n=0)}\ \sigma_1 + \Delta t\ \alpha_s^2\ \alpha_p\ {}^{(K)}A2_{22}^{(n=0)}\ \sigma_2 \\
&\quad + \Delta t\left({}^{(K)}A3_2^{(n=0)} + \Delta t\ {}^{(K)}A3_2^{(n=1)}\right) + 2\ \Delta t\left({}^{(K)}A4_2^{(n=0)} + {}^{(K)}A4_2^{(n=1)}\right)
\end{aligned}
$$

$$
\begin{aligned}
{}^{(K)}E_1^{(n,n-1,n-2)} &= -3\ {}^{(K)}A1_1^{(n)} + 4\ {}^{(K)}A1_1^{(n-2)} - {}^{(K)}A1_1^{(n-1)} - 2\ \Delta t\ {}^{(K)}A3_1^{(n)} \\
&\quad - 4\ \Delta t\ {}^{(K)}A4_1^{(n)} - 2\ \Delta t\ {}^{(K)}A5_1^{(n)} \qquad \text{(E-79)} \\
{}^{(K)}E_2^{(n,n-1,n-2)} &= -3\ {}^{(K)}A1_2^{(n)} + 4\ {}^{(K)}A1_2^{(n-2)} - {}^{(K)}A1_2^{(n-1)} - 2\ \Delta t\ {}^{(K)}A3_2^{(n)} - 4\ \Delta t\ {}^{(K)}A4_2^{(n)}
\end{aligned}
$$

The axisymmetrical problem consists in resolving the above set of equations, and a numerical minimization procedure, coupled to the above equations, to accurately track the movement of the boundaries

APPENDIX F
An Axisymmetrical Elasticity Algorithm

F-1 Numerically Removing Tip Singularities

Singularities for the crack opening and stress intensity factor, in the axisymmetrical case, can be numerically removed if the following transformations are assumed

$$(x-a)^{\gamma}$$
$$0 \le \gamma < 1$$
$$\int_a^b f(x)\,dx = \frac{1}{1-\gamma}\int_0^{(b-a)^{1-\gamma}} t^{\frac{\gamma}{1-\gamma}} f(t^{\frac{1}{1-\gamma}} + a)\,dt \tag{F-1}$$

$$(b-x)^{\gamma}$$
$$0 \le \gamma < 1$$
$$\int_a^b f(x)\,dx = \frac{1}{1-\gamma}\int_0^{(b-a)^{1-\gamma}} t^{\frac{\gamma}{1-\gamma}} f(b - t^{\frac{1}{1-\gamma}})\,dt \tag{F-2}$$

The crack opening is given as

$$\delta(r) = \left(\frac{2}{\pi}\right)\frac{1}{E}\int_r^R \frac{dl}{\sqrt{l^2-r^2}}\int_0^l \frac{\alpha\,\sigma(\alpha)}{\sqrt{l^2-\alpha^2}}\,d\alpha \tag{F-3}$$

$$\delta(r) = C_0\int_r^R \frac{g(l)}{\sqrt{l^2-r^2}}\,dl$$

$$C_0 = \frac{2}{\pi}\frac{1}{E} \tag{F-4}$$

$$g(l) = \int_0^l \frac{\alpha\,\sigma(\alpha)}{\sqrt{l^2-\alpha^2}}\,d\alpha$$

$$
\begin{aligned}
f(\alpha) &= \frac{\alpha\,\sigma(\alpha)}{\sqrt{l-\alpha}\,\sqrt{l+\alpha}} \\
g(l) &= \int_0^l f(\alpha)\,d\alpha \\
&= \frac{1}{1-0.5}\int_0^{\sqrt{l-0}} t^{\frac{0.5}{1-0.5}} f(l - t^{\frac{1}{1-0.5}})\,dt \\
g(l) &= \int_0^{\sqrt{l}} \frac{2(l-t^2)\,\sigma(l-t^2)}{\sqrt{2l-t^2}}\,dt
\end{aligned}
\tag{F-5}
$$

where the transformation given in Eq. (F-2) is used. Rewriting the above equation leads to

$$
\begin{aligned}
\delta(r) &= C_0 \int_r^R \frac{g(l)\,dl}{\sqrt{l-r}\,\sqrt{l+r}} \\
\delta(r) &= C_0 \int_0^{\sqrt{R-r}} \frac{2\,g(r+u^2)\,du}{\sqrt{2r+u^2}}
\end{aligned}
\tag{F-6}
$$

$$
\begin{aligned}
\delta(r) &= 4C_0 \int_0^{\sqrt{R-r}} \int_0^{h(u)} f(u,t;r)\,dt\,du \\
G(u;r) &= \int_0^{h(u)} f(u,t;r)\,dt \\
\delta(r) &= 4C_0 \int_0^{\sqrt{R-r}} G(u;r)\,du \\
h(u) &= \sqrt{r+u^2} \\
f(u,t;r) &= \frac{(r+u^2-t^2)\,\sigma(r+u^2-t^2)}{\sqrt{2r+u^2}\,\sqrt{2r+2u^2-t^2}}
\end{aligned}
\tag{F-7}
$$

This integration transformation gives excellent results. Convergence to square root of machine precision was achieved in average for approximately 20 integration points. Various load distributions were tested.

In addition the stress intensity factor in mode *1* can also be obtained

$$K(\sigma) = \frac{2}{\sqrt{\pi}} \frac{1}{\sqrt{R}} \int_0^R \frac{r\,\sigma(r)}{\sqrt{R^2 - r^2}} dr$$

$$K(\sigma) = \frac{4}{\sqrt{\pi}} \frac{1}{\sqrt{R}} \int_0^{\sqrt{R}} \frac{(R - t^2)\,\sigma(R - t^2)}{\sqrt{2R - t^2}} dt \qquad \text{(F-8)}$$

APPENDIX G
PARFES Simulation Results—Part 1

G-1 Half-Crack Simulation

Figure G-1 represents the initial configuration of a half-crack. The number of elements used is a function of the motion complexity—meshes are usually more refined than the one below. A downwards motion is shown in Figures **G-2** through **G-8**.

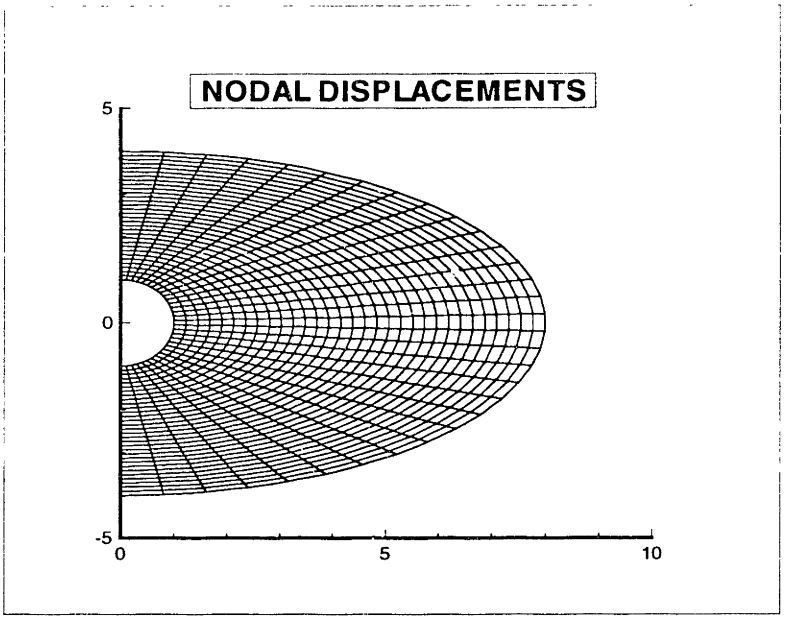

FIGURE G-1: Initial nodal location for elliptical crack

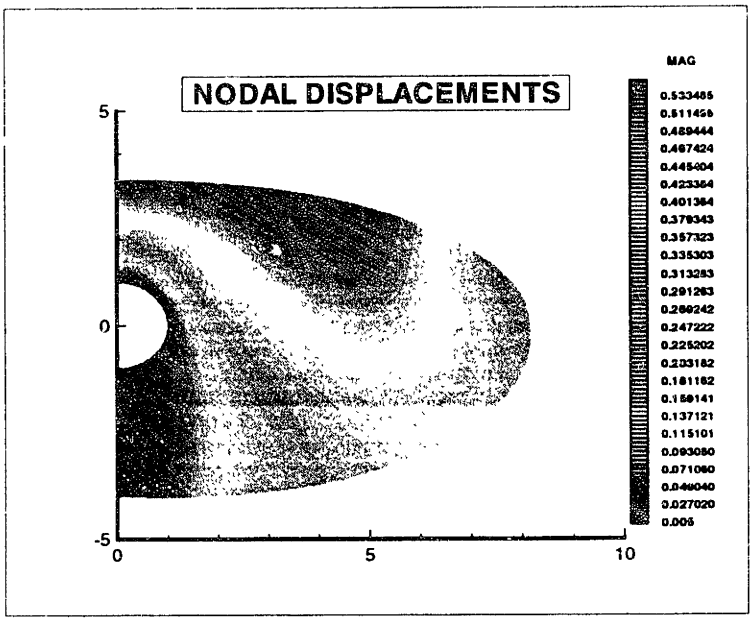

FIGURE G-2: Downwards displacement series—1

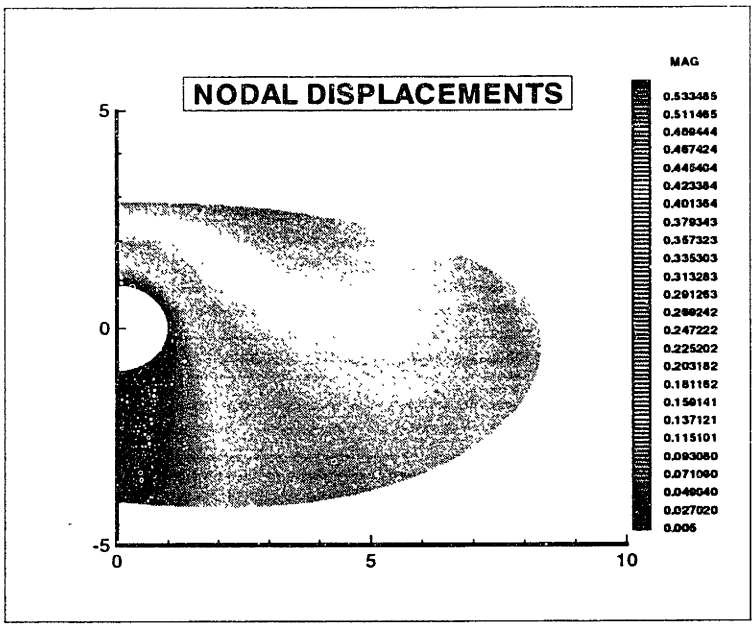

FIGURE G-3: Downwards displacement series—2

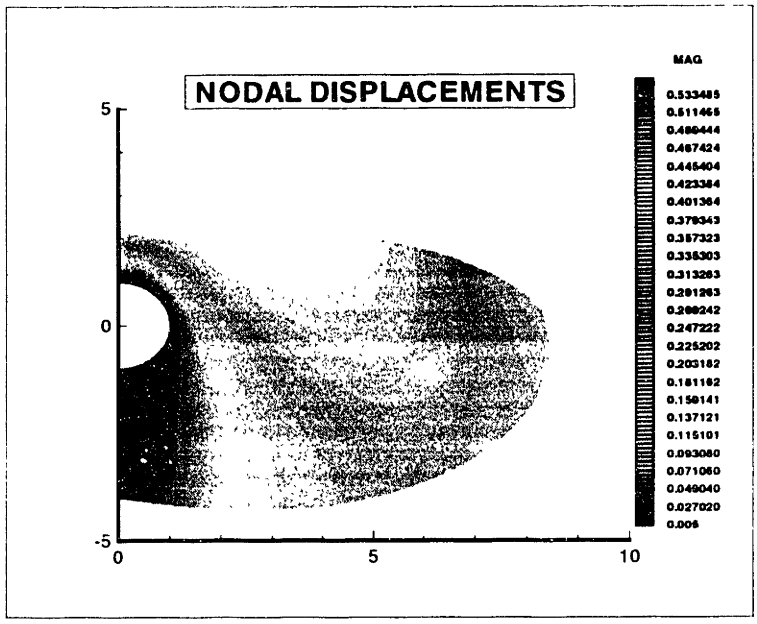

FIGURE G-4: Downwards displacement series—4

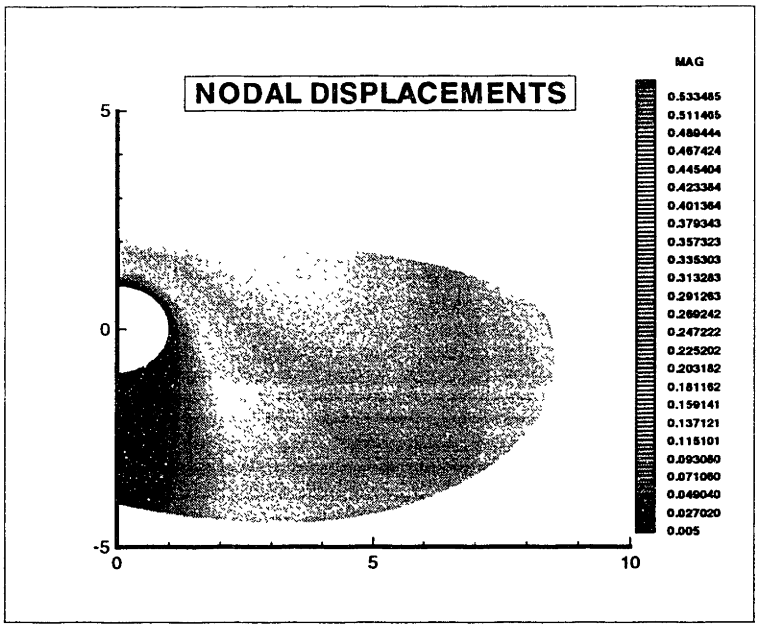

FIGURE G-5: Downwards displacement series—5

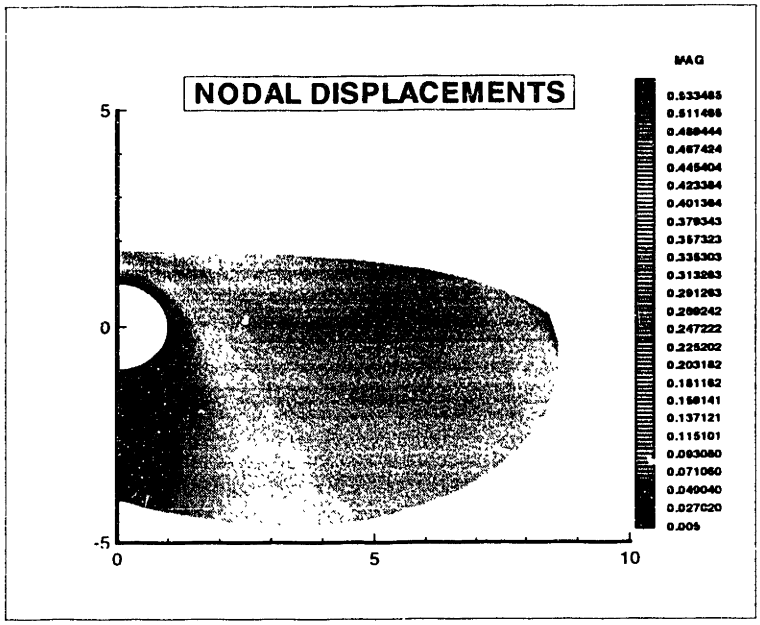

FIGURE G-6: Downwards displacement series—5

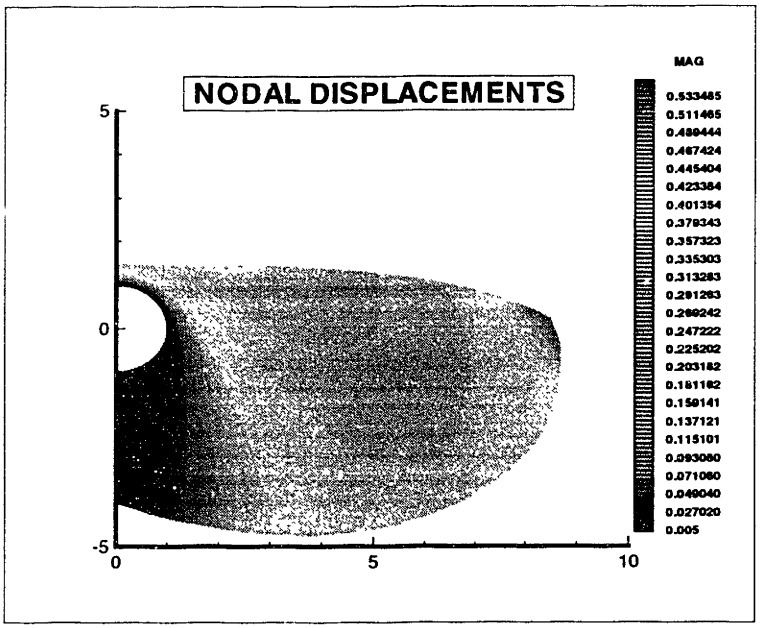

FIGURE G-7: Downwards displacement series—6

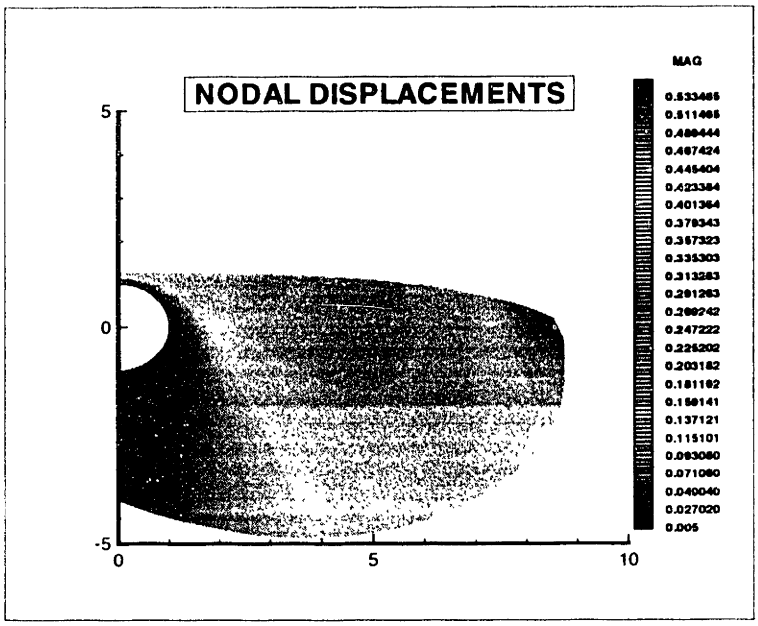

FIGURE G-8: Downwards displacement series—7

APPENDIX H
PARFES Simulation Results—Part 2

H-1 Blob Distortion Simulation

The following series—**Figures H-1** through **H-10**—of *blob* oblation and prolation motions, is used to predict boundary effects as a function of the external forces.

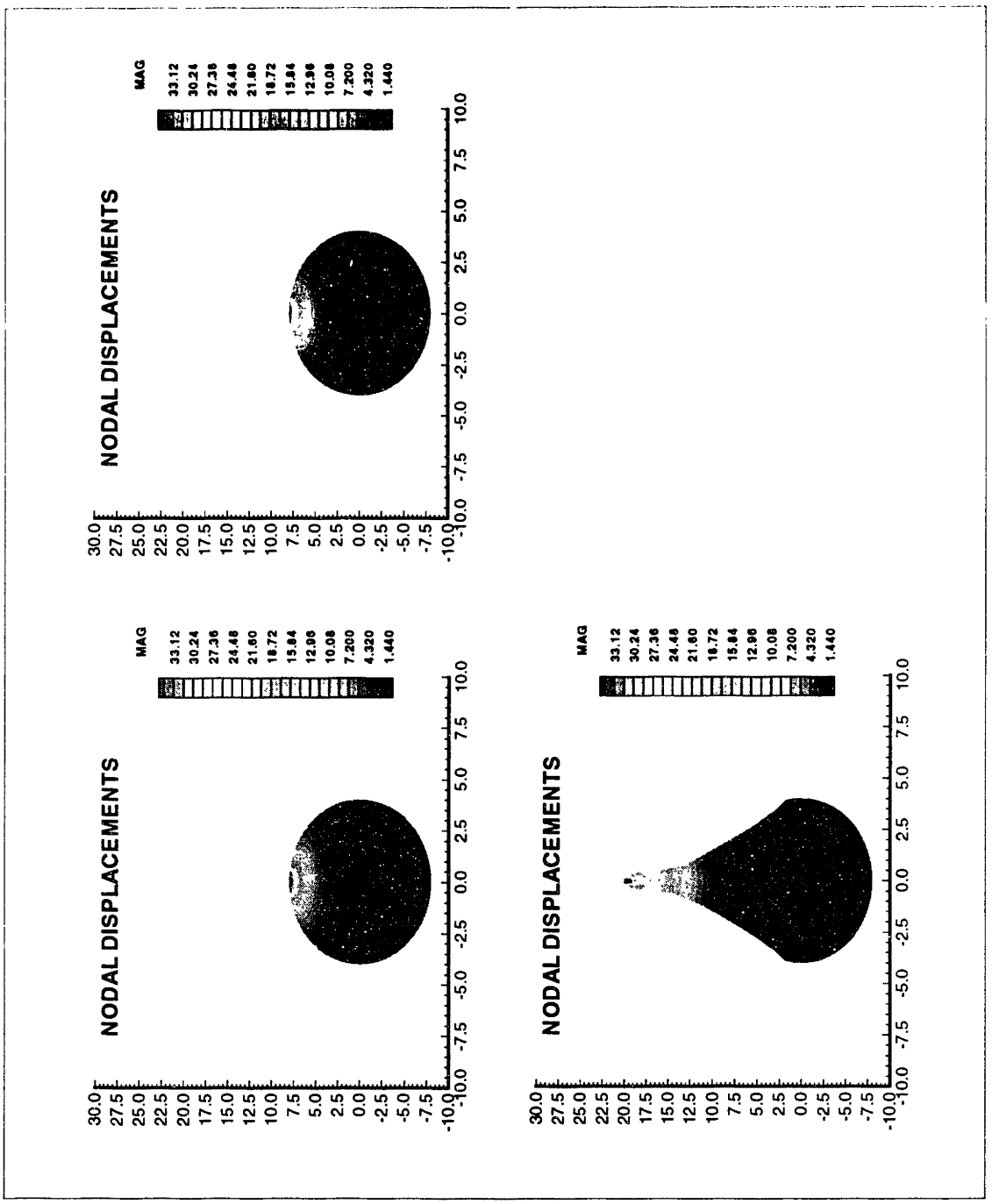

FIGURE H-1: Series of blob prolation displacements

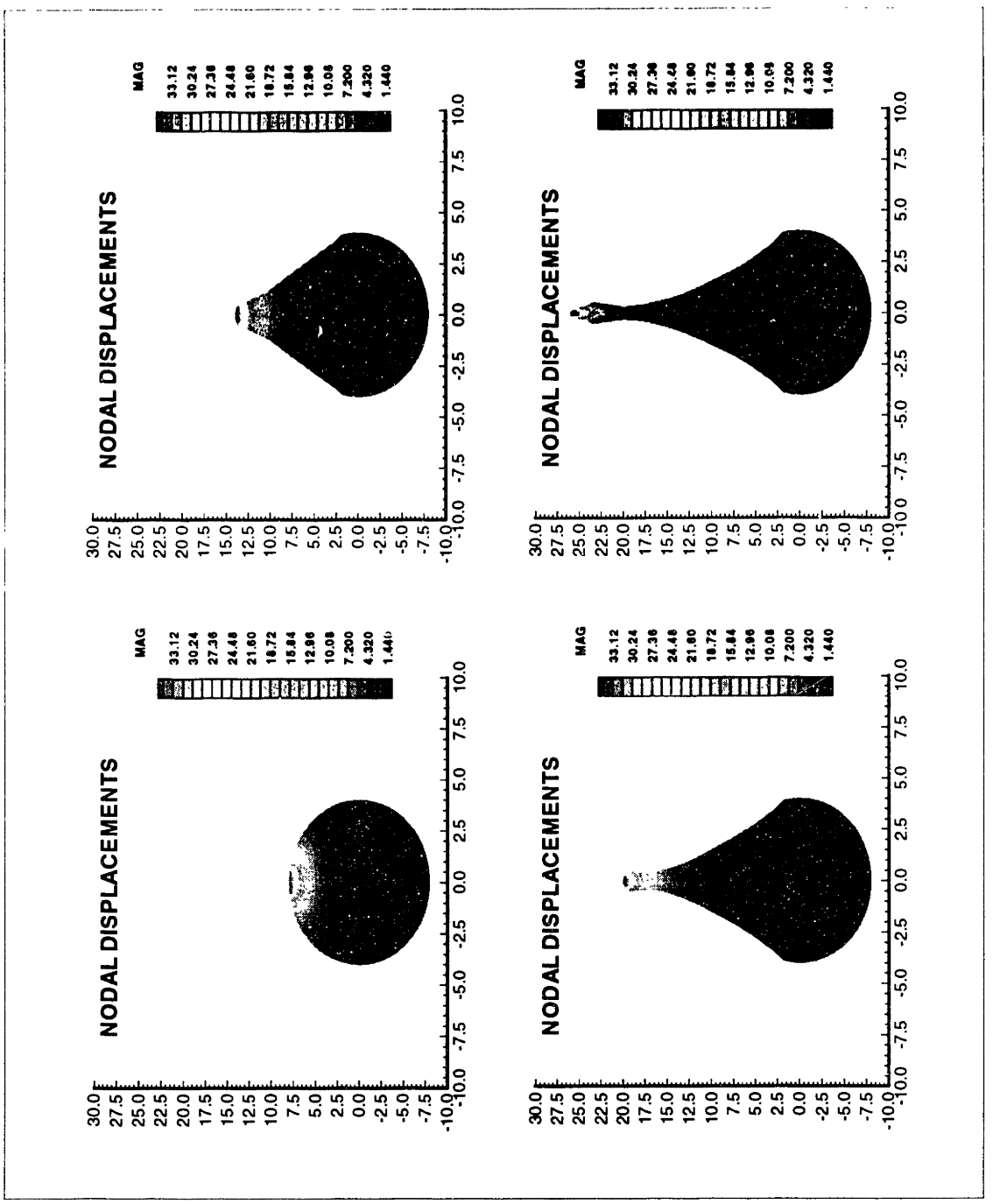

FIGURE H-2: Series of blob prolation displacements—2

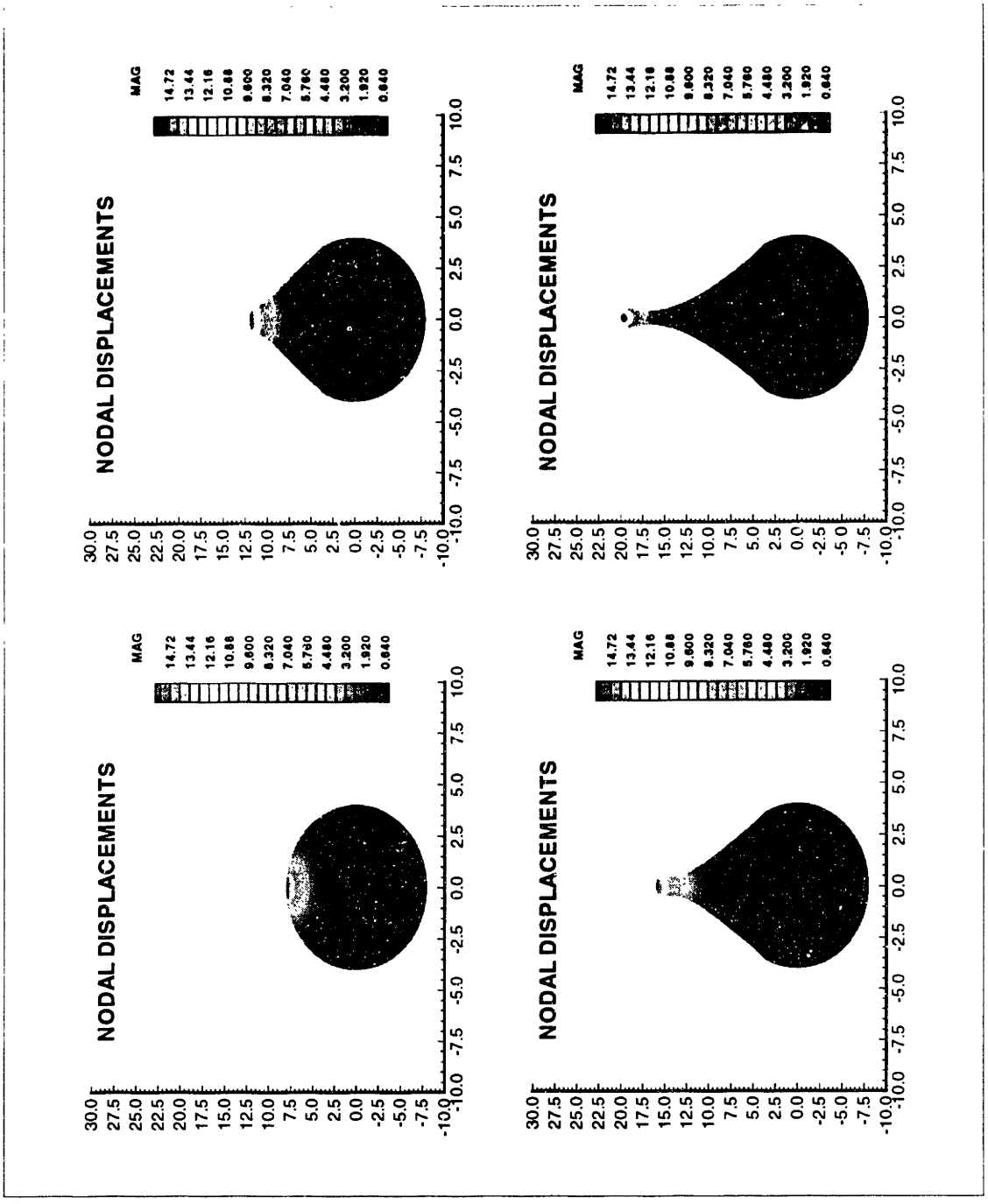

FIGURE H-3: Series of blob prolation displacements—3

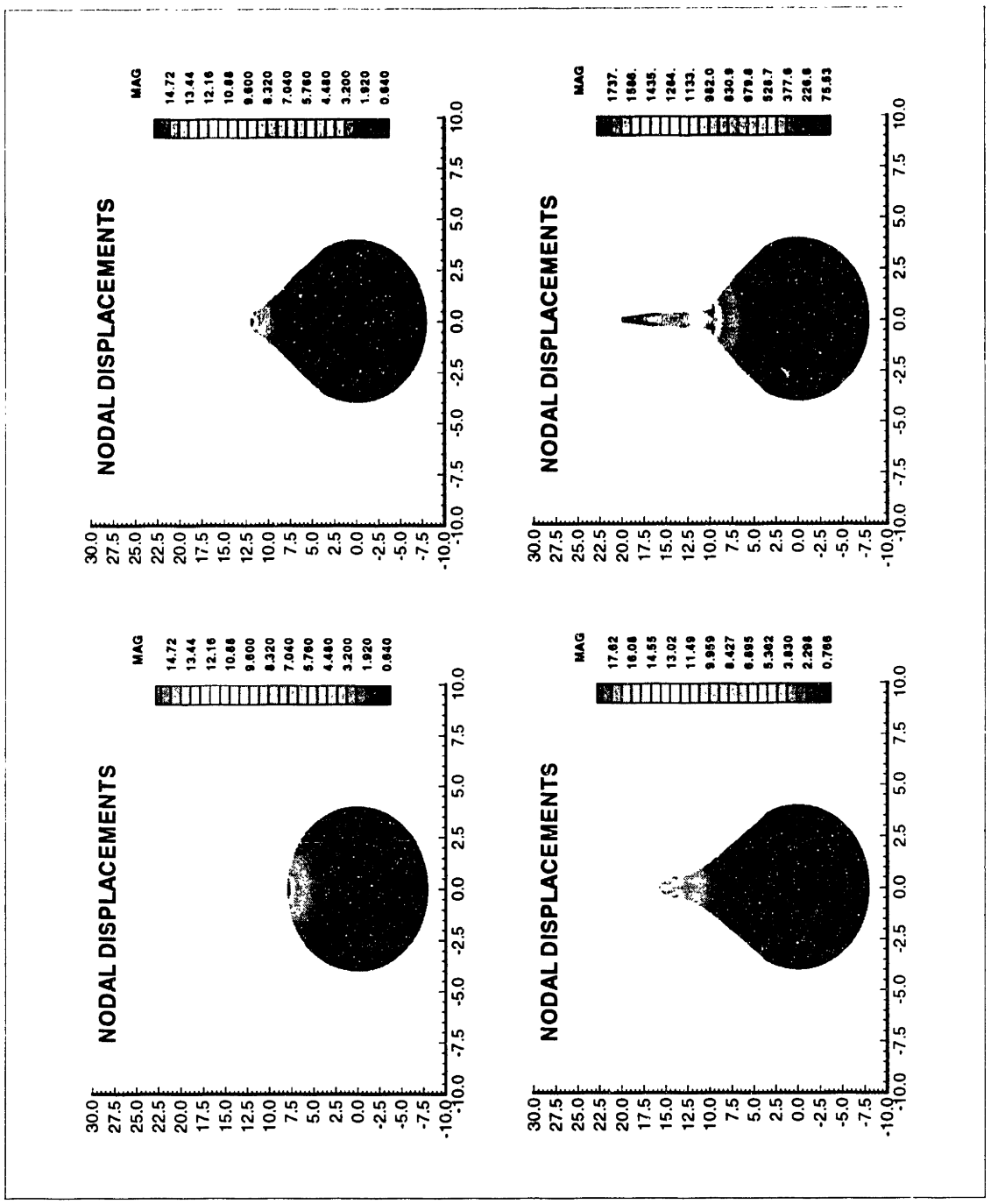

FIGURE H-4: Series of blob prolation displacements—4

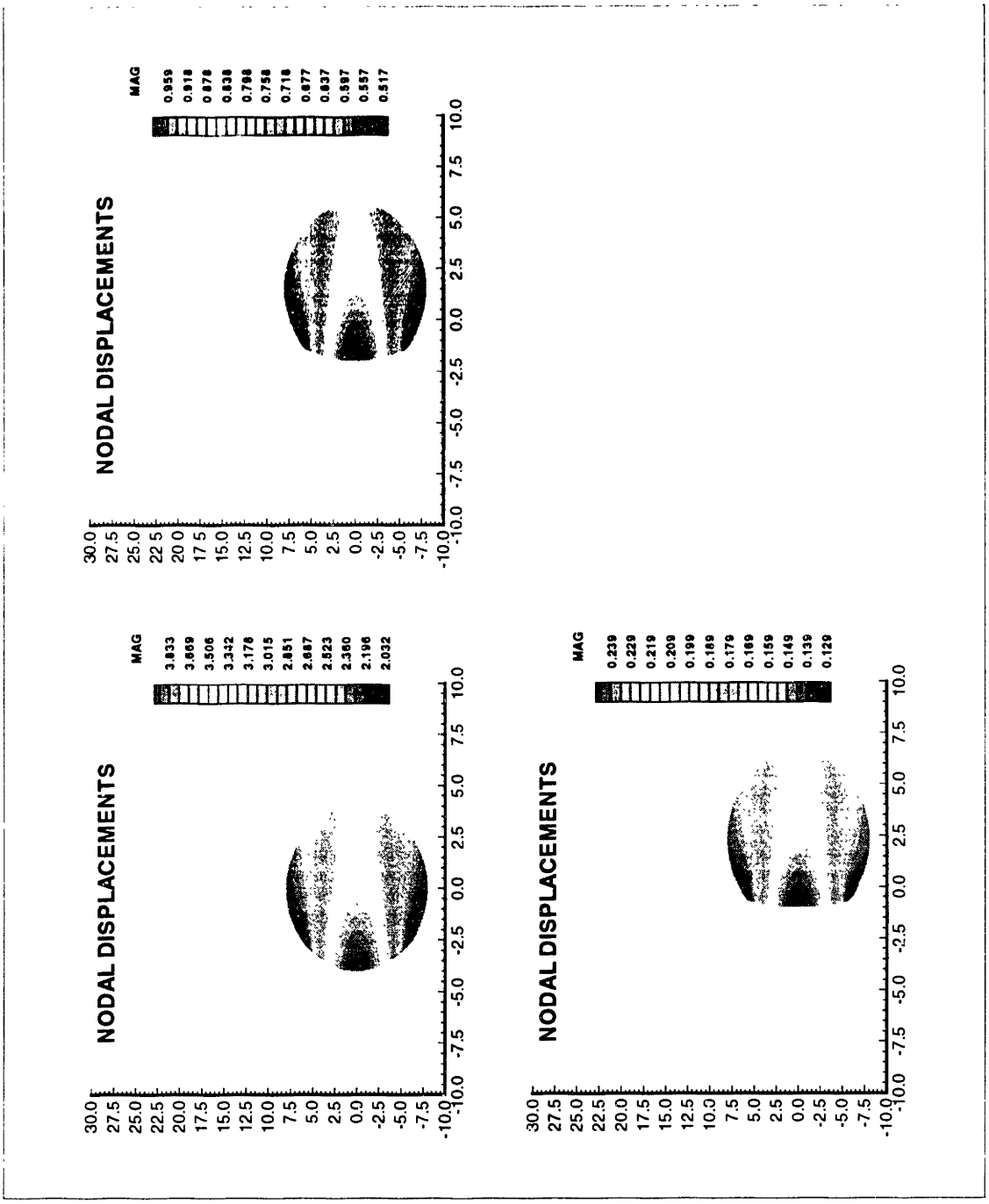

FIGURE H-5: Series of blob oblation displacements—1

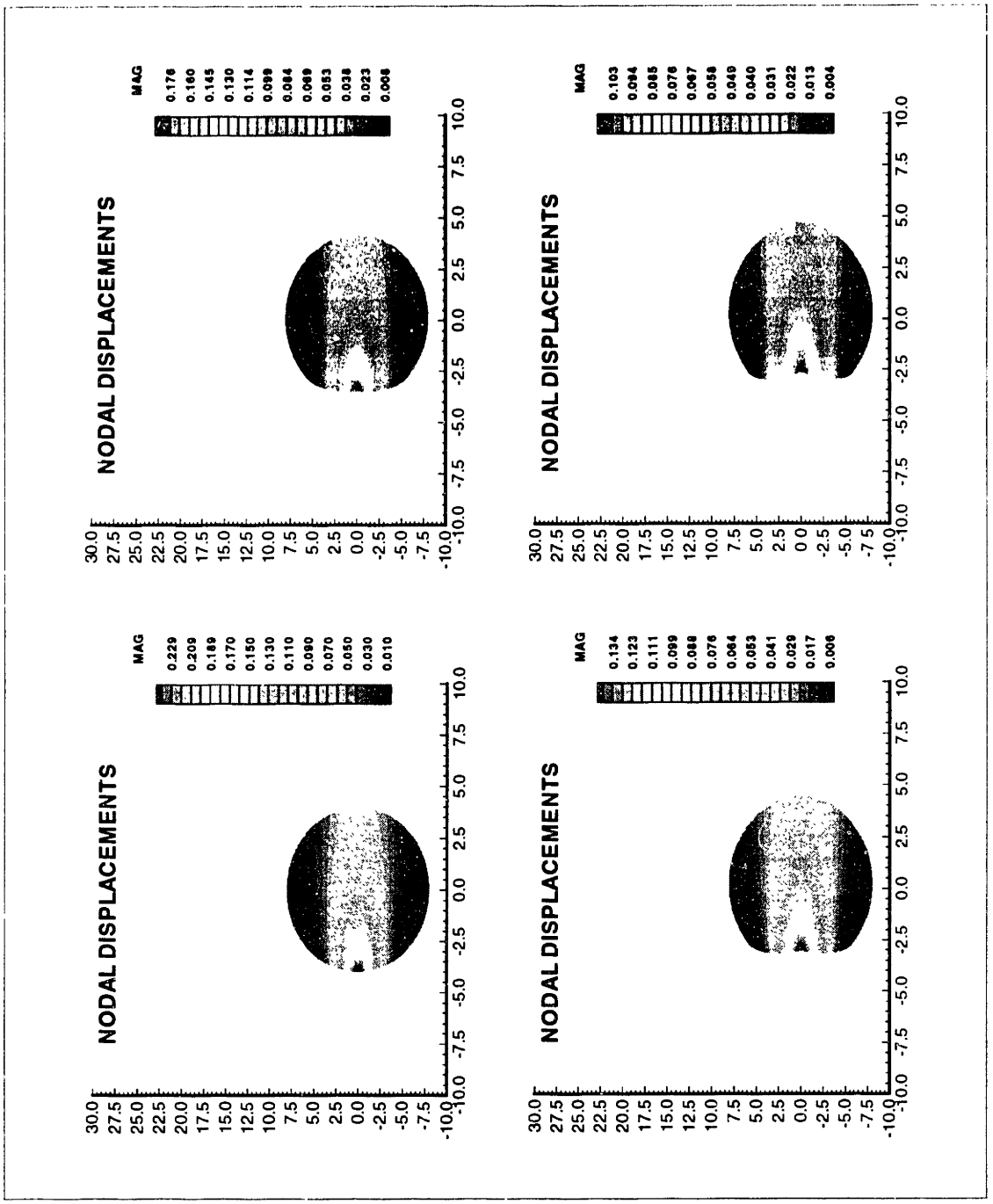

FIGURE H-6: Series of blob oblation displacements—2

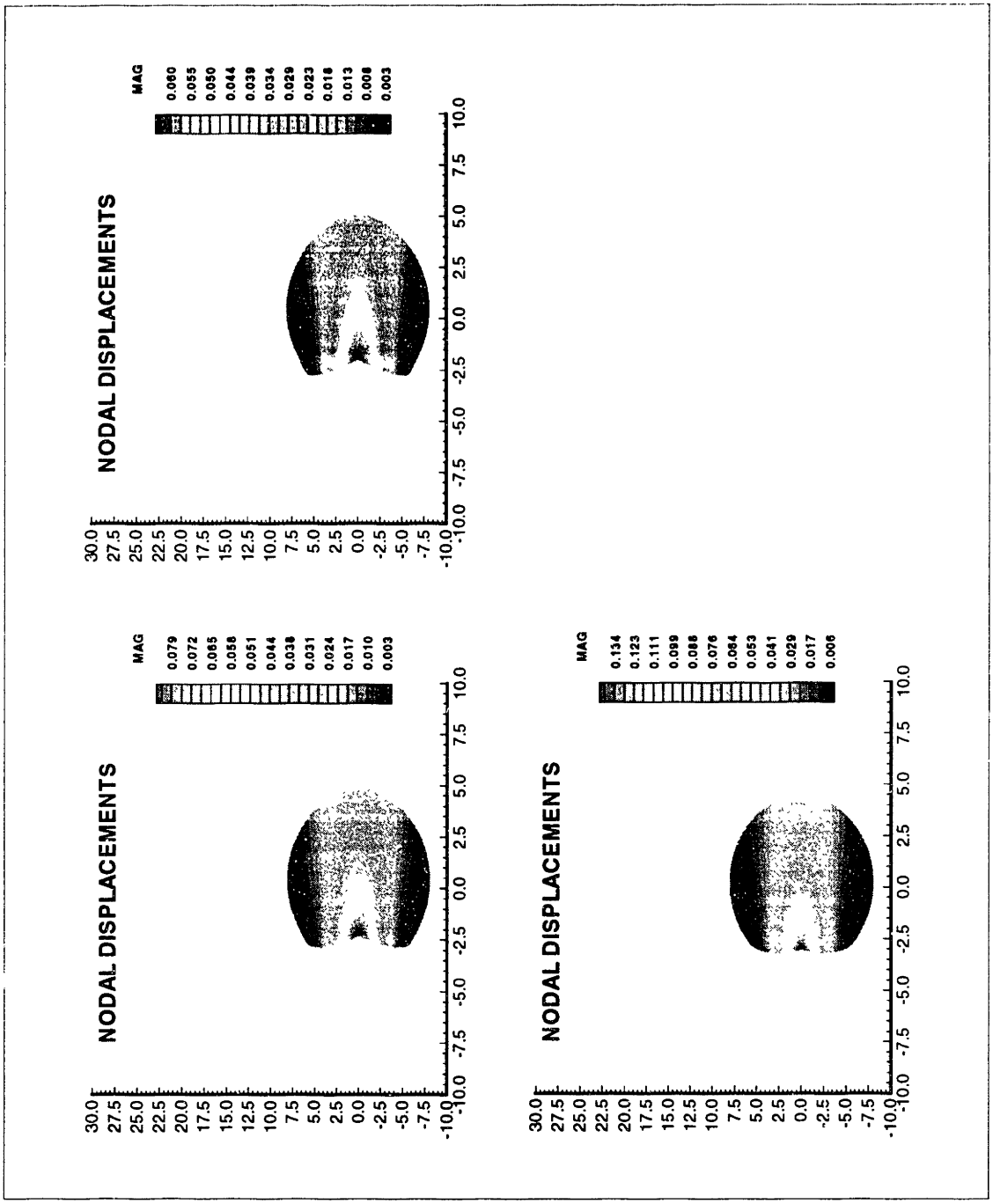

FIGURE H-7: Series of blob oblation displacements—3

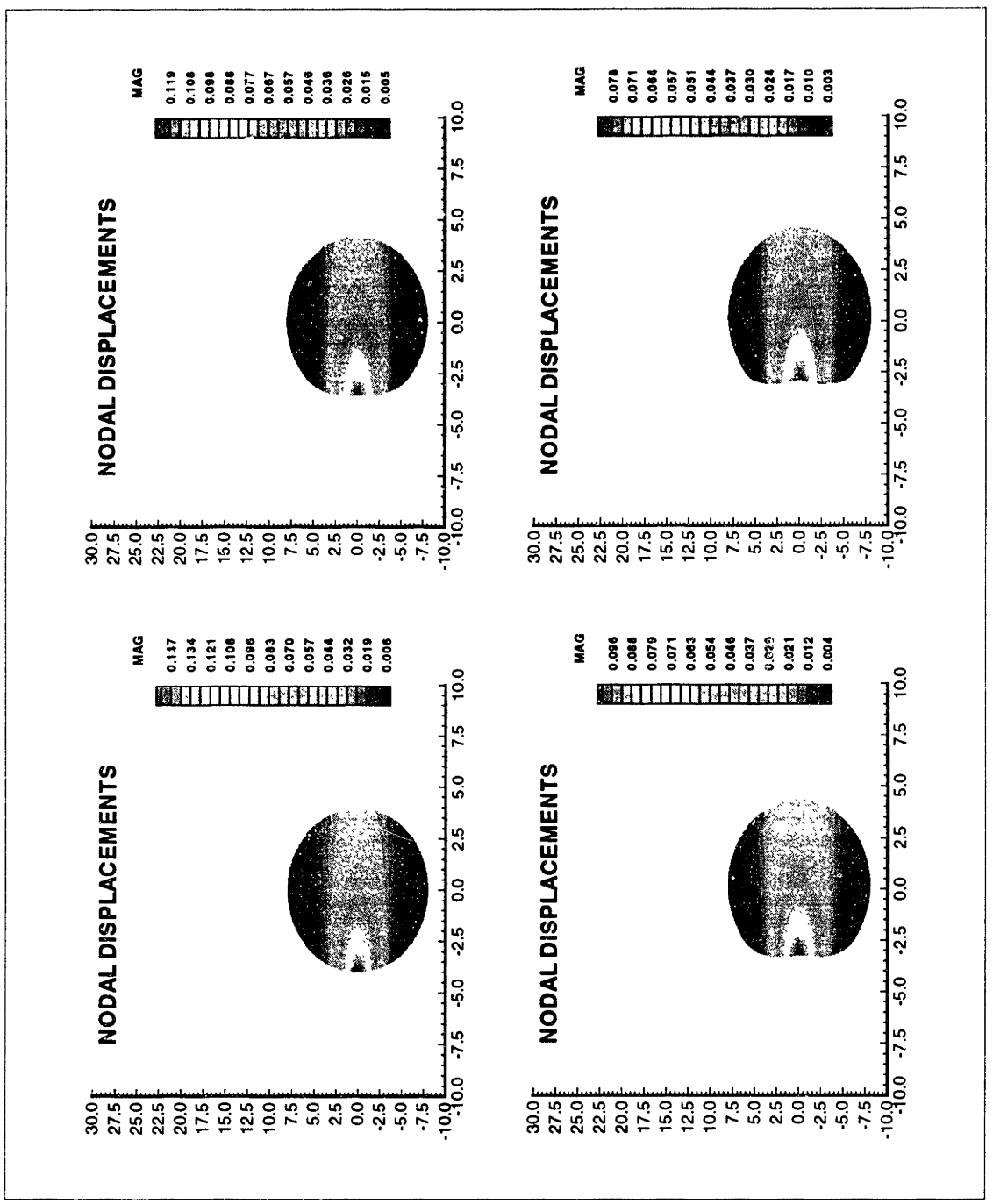

FIGURE H-8: Series of blob oblation displacements—4

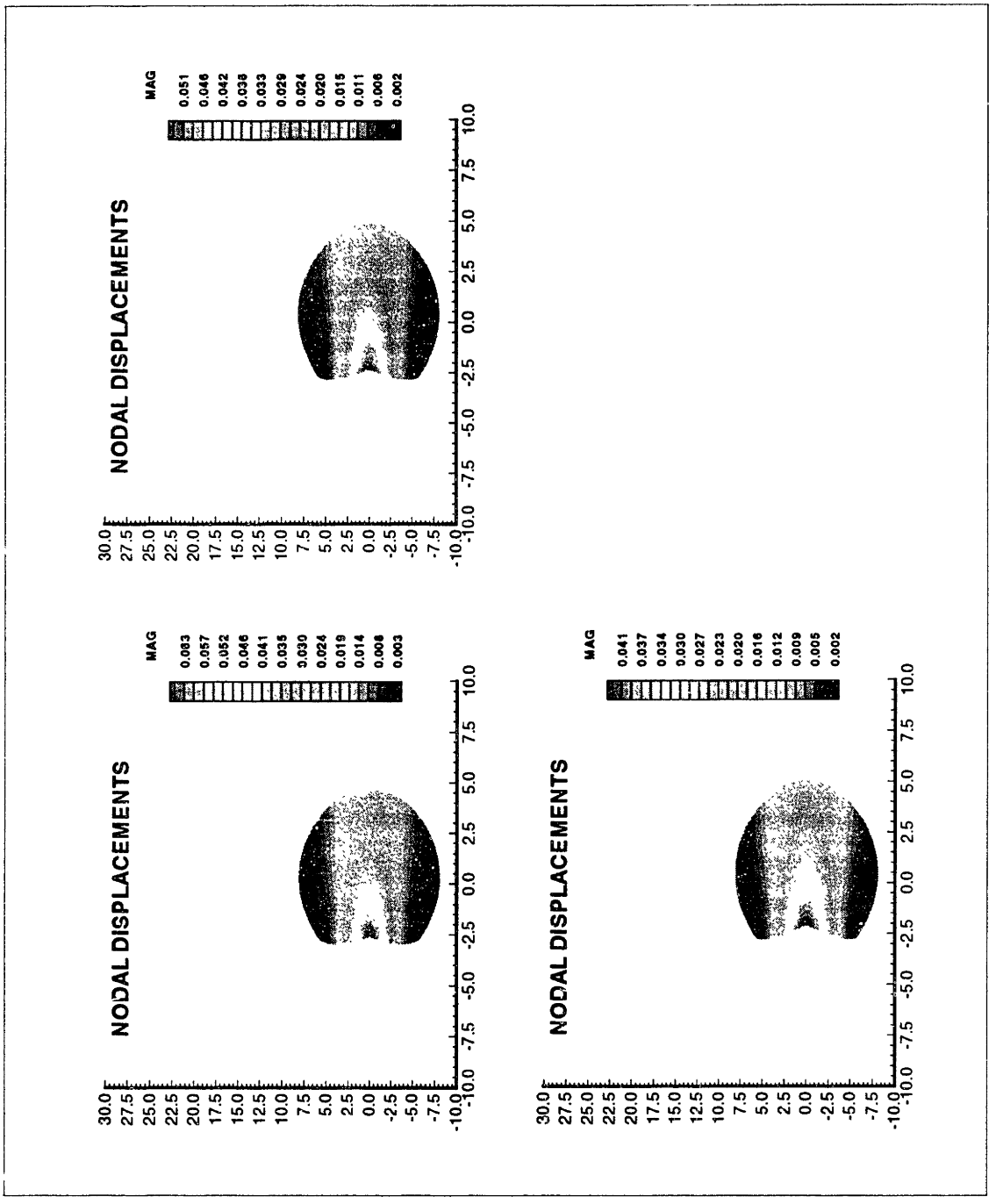

FIGURE H-9: Series of blob oblation displacements—5

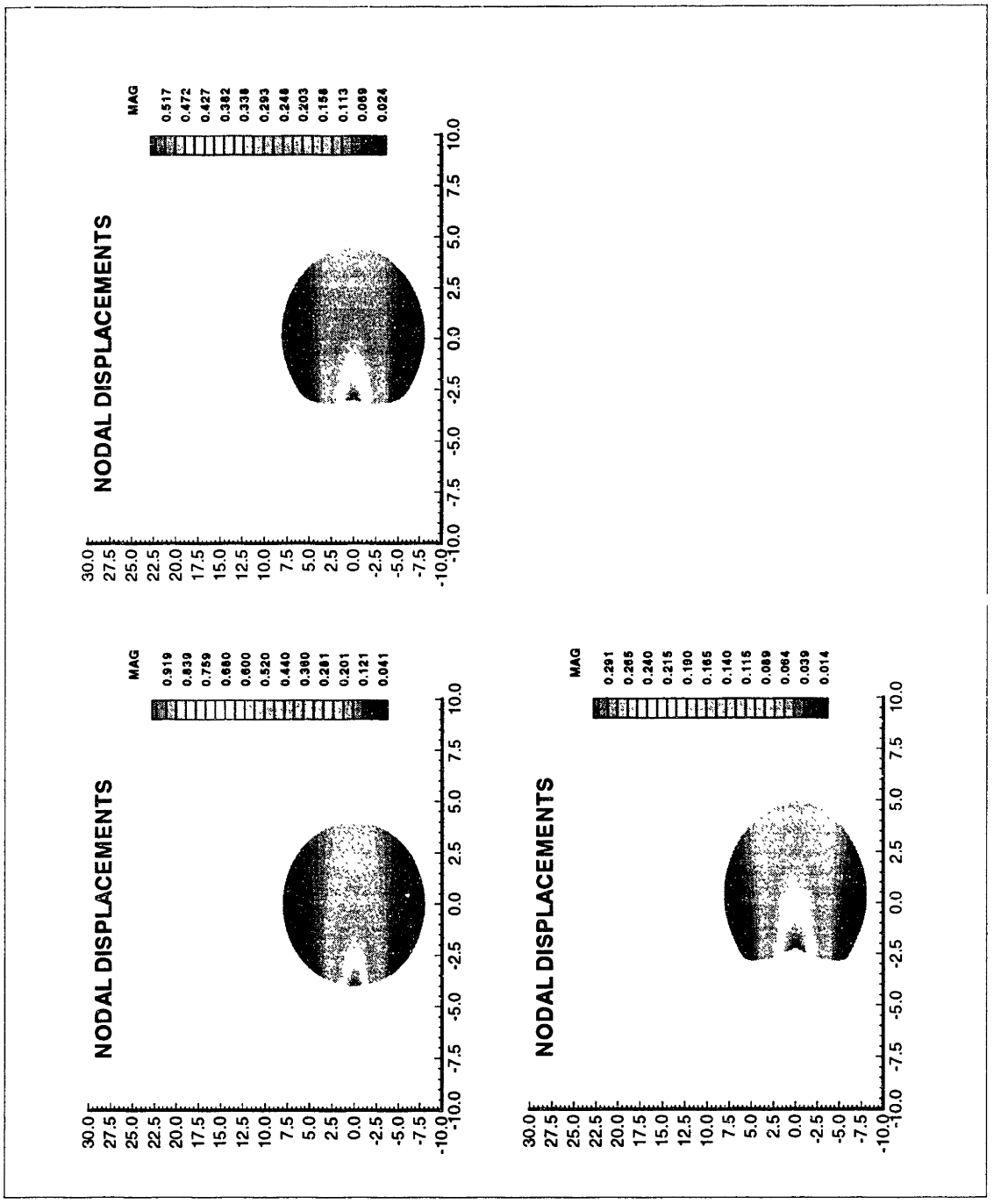

FIGURE H-10: Series of blob oblation displacements—6

APPENDIX I
PARFES Simulation Results—Part 3

I-1 Axisymmetrical Interface Tracking

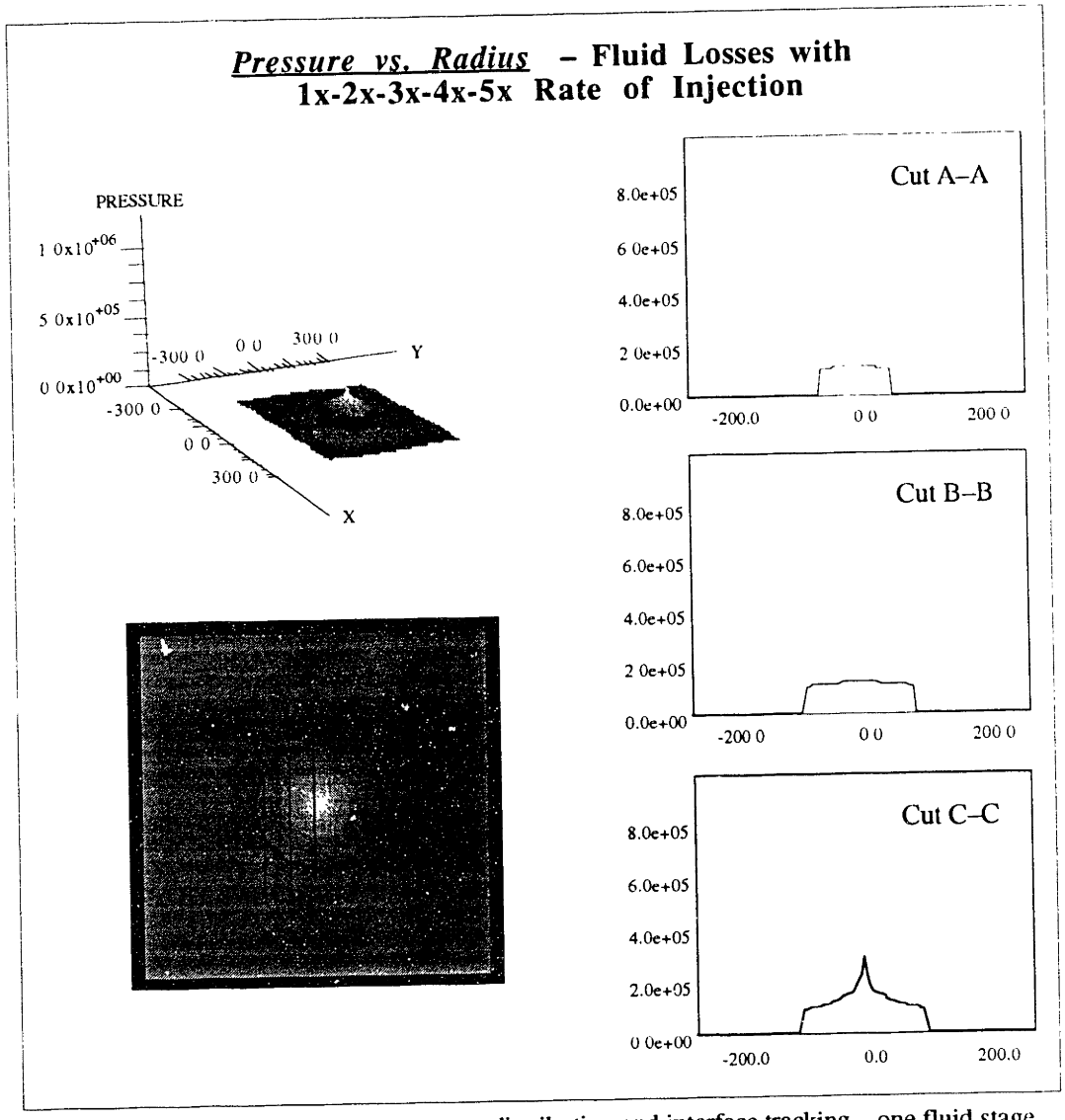

FIGURE I-1: Axisymmetrical pressure distribution and interface tracking—one fluid stage

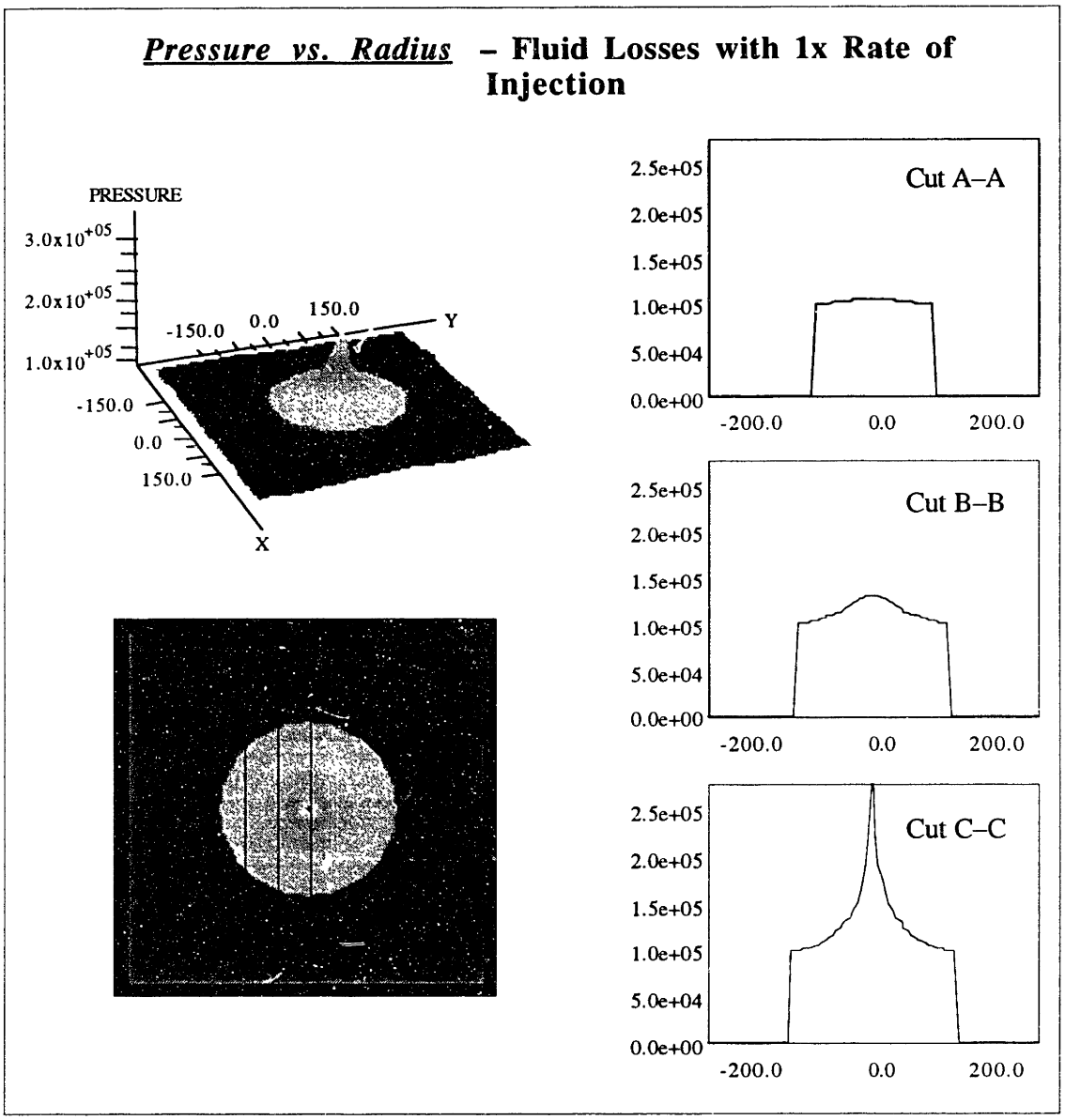

FIGURE I-2: Axisymmetrical pressure distribution and interface tracking—one fluid stage with fluid losses as a function of the rate of injection

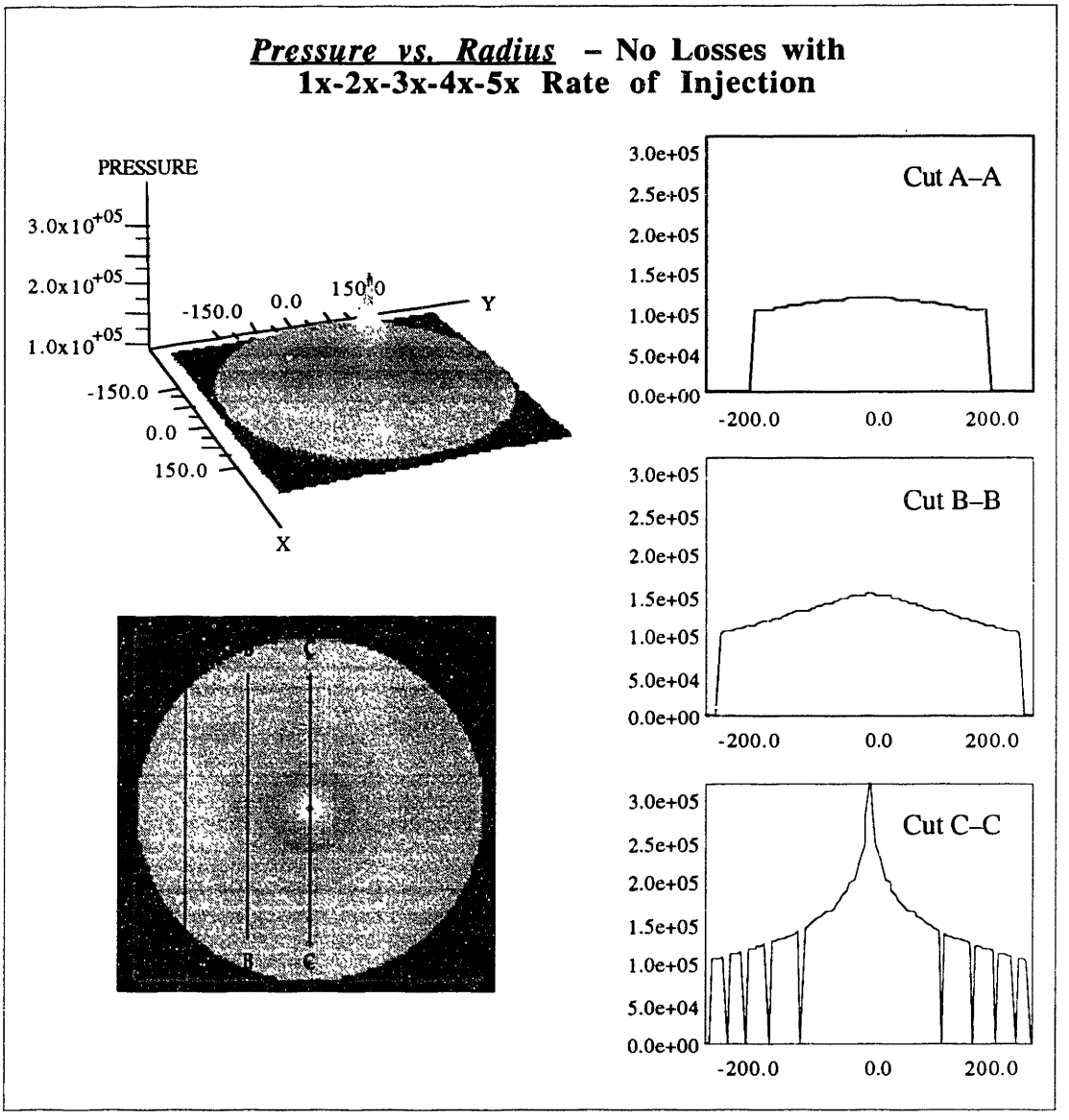

FIGURE I-3: Axisymmetrical pressure distribution and interface tracking—5 fluid stages. Valleys in Cut C-C represent the front location for each fluid stage

References

Abé, H., Keer, L. M. and Mura, T. (1979). *Theoretical Study of Hydraulically Fractured Penny-Shaped Cracks in Hot, Dry Rocks*. Int. J. Num. Anal. Meth. Geomech. **3**: p. 79-96.

Abé, H., Mura, T. and Keer, L. M. (1976). *Growth Rate of a Penny-Shaped Crack in Hydraulic Fracturing of Rocks*. J. Geophysycal Res. **10**

Adamson, A. W. (1967). *Physical Chemistry of Surfaces*. Interscience.

Ambwani, D. S. and Fort, T. (1974). *Pendant Drop Technique for Measuring Liquid Boundary Tensions*, in Surface & Colloid Science. R. J. Good and R. R. Stromberg Editor. Plenum Publishing Corp.: p. 93-119.

Anderson, T. B. and Jackson, R. (1967). *A Fluid Mechanical Description of Fluidized Beds*. Ind. Engng. Chem. Fundam. **6**: p. 527-539.

Anturkar, N. R., Papanastasiou, T. C. and Wilkes, J. O. (1990a). *Linear Stability Analysis of Multilayer Plane Poiseuille Flow*. Phys. Fluids A. **2**(4): p. 530-541.

Anturkar, N. R., Papanastasiou, T. C. and Wilkes, J. O. (1990b). *Lubrication Theory for n-Layer Thin-Film Flow with Applications to Multilayer Extrusion and Coating*. Chem. Eng. Sci. **45**(11): p. 3271-3282.

Apazidis, N. (1985). *On Two-Phase Flow in a Vertical Parallel-Plate Channel of Infinite Length*. J. Techn. Phys. **26**(3-4): p. 259-273.

Argyris, J., *et al.* (1985). *Finite Element Solution of Viscous Flow Problems*, in Finite Element in Fluids. R. H. Gallagher, *et al.* Editor. John Wiley & Sons: p. 89-114.

ASTM-D1331 (1989). *Standard Test Methods for Surface and Interfacial Tension of Solutions of Surface-Active Agents.* : p. 116-118.

ASTM-D971 (1982). *Standard Test Method for Interfacial Tension of Oil Against Water by the Ring Method.* : p. 321-323.

Bairstow, L., Cave, B. M. and Lang, E. D. (1922). *The Two-dimensional Slow Motion of Viscous Fluids.* Royal Soc. Proc. **A. 100**: p. 394-413.

Bairstow, L., Cave, B. M. and Lang, E. D. (1923). *The Resistance of a Cylinder Moving in a Viscous Fluid.* Phil. Trans. **A. 223**: p. 383-432.

Baker, G. R. and Moore, D. W. (1989). *The Rise and Distortion of a Two-Dimensional Gas Bubble in an Inviscid Liquid.* Phys. Fluids A. **1**(9): p. 1451-1459.

Barr, D. (1991). *Leading-Edge Analysis for Correct Simulation of Interface Separation and Hydraulic Fracturing.* Ph.D. Thesis, MIT.

Barr, D. T. and Cleary, M. P. (1984). *Instabilities of Fluid Flow and Coupled Solid Deformation in Permeable Media.* MIT REL-84-3 Report.

Barr, D. T. and Cleary, M. P. (1992). *Global versus Local Diffusion Phenomena in Underground Heat and Mass Transfer.* Geothermal Resources Council Annual Meeting - October 1992.

Behrens, R. A., *et al.* (1987). *Transient Free-Surface Flows: Motion of a Fluid Advancing in a Tube.* AIChE Journal. **33**(7): p. 1178-1186.

Bellman, R. (1973). *Methods of Nonlinear Analysis.* Mathematics in Science and Engineering. R. Bellman Editor. **2.** Academic Press.

Belytschko, T., Engelmann, B. E. and Liu, W. K. (1989). *A Review of Recent Developments in Time Integration*, in State-of-the-art Surveys on Computational Mechanics. A. K. Noor and J. T. Oden Editor. ASME: p. 185-235.

Belytschko, T., Smolinski, P. and Liu, W. K. (1984). *Multi-Stepping Implicit-Explicit Procedures in Transient Analysis*, in International Conference on Innovative Methods for Nonlinear Problems. W. K. Liu, *et al.* Editor. Pineridge Press. p. 135-153.

Ben-Amar, M., *et al.* (1991). *Self-Dilating Viscous Finger in Wedge-Shaped Hele-Shaw Cells*. Phys. Fluids A. **3**(9): p. 2039-2042.

Bensimon, D., *et al.* (1986). *Viscous Flow in Two Dimensions*. Reviews of Modern Physics. **58**(4): p. 977-999.

Bilicki, Z., *et al.* (1987). *Trajectories and Singular Points in Steady-State Models of Two-Phase Flows*. Int. J. Multiphase Flow. **13**(4): p. 511-533.

Bjørstad, P. E. and Hvidsten, A. (1987). *Iterative Methods for Substructured Elasticity Problems in Structural Analysis*, in First International Symposium on Domain Decomposition Methods for Partial Differential Equations. R. Glowinsky, *et al.* Editor. Paris, France. SIAM. p. 301-312.

Borst, R. d. (1984). *Application of Advanced Solution Techniques to Concrete Cracking and Non-Associated Plasticity*, in International Conference on Numerical Methods for Non-Linear Problems. C. Taylor, *et al.* Editor. Barcelona, Spain. Pineridge Press. p. 314-325.

Brener, E., Levine, H. and Tu, Y. (1991). *Nonsymmetric Saffman-Taylor Fingers*. Phys. Fluids A. **3**(4): p. 529-534.

Brochard, F. and de Gennes, P. G. (1991). *Collective Modes of a Contact Line*. Langmuir. **7**: p. 3216-3218.

Brochard-Wyart, F. and de Gennes, P. G. (1992). *Dynamics of Partial Wetting*. Adv. Colloid Interface Sci. **in press**: p. 1-10.

Bui, H. D. and Parnes, R. (1982). *A Reexamination of the Pressure at the Tip of a Fluid-filled Crack*. Int. J. Eng. Sci. **20**(11): p. 1215-20.

Burgess, D. and Foster, M. R. (1990). *Analysis of the Boundary Conditions for a Hele-Shaw Bubble*. Phys. Fluids A. **2**(7): p. 1105-1117.

Burgess, D. and Tanveer, S. (1991). *Infinite Stream of Hele-Shaw Bubbles*. Phys. Fluids A. **3**(3): p. 367-379.

Carey, G. F. and Jiang, B. N. (1984). *Element-by-Element Preconditioned Conjugate Gradient Algorithm for Compressible Flow*, in International Conference on Innovative Methods for Nonlinear Problems. W. K. Liu, *et al.* Editor. Pineridge Press. p. 41-49.

Carmignani, C., Cella, A. and Paulis, A. D. (1974). *Functional Minimization in Nonlinear Solid Mechanics*, in Computational Methods in Nonlinear Mechanics. J. T. Oden, *et al.* Editor. Texas, Austin. University of Texas at Austin. p. 617-626.

Chen, K. and Joseph, D. D. (1991). *Lubricated Pipelining: Stability of Core-Annular Flow. Part 4. Ginzburg-Landau Equations*. J. Fluid Mech. **227**: p. 587-615.

Christenson, H. K. (1988). *Adhesion between Surfaces in Undersaturated Vapors - A Reexamination of the Influence of Mensicus Curvature and Surface Forces*. J. Colloid Interface Sci. **121**(1): p. 170-178.

Chuoke, R. L., Meurs, P. v. and Poel, C. v. d. (1958). *The Instability of Slow, Immiscible, Viscous Liquid-Liquid Displacements in Permeable Media*. Petroleum Transactions of the AIME. **216**: p. 188-194.

Cleary, M. P. (1988). *The Engineering of Hydraulic Fractures – State of the Art and Technology of the Future*. SPE Distinguished Author Series – Journal of Petroleum Technology. (January): p. 13-21.

Cleary, M. P., Barr, D. T. and Willis, R. M. (1988). *Enhancement of Real-Time Hydraulic Fracturing Models With Full 3-D Simulation*. SPE Journal. **17713**: p. 79-93.

Cleary, M. P. and Junior, A. F. (1992). *Proppant Convection and Encapsulation in Hydraulic Fracturing: Pratical Implications of Computer and Laboratory Simulations*. SPE Journal. **24825**: (in press).

Cleary, M. P., Kavvadas, M. and Lam, K. Y. (1983). *Development of a Fully Three-Dimensional Simulator for Analysis and Design of Hydraulic Fracturing*. SPE/DOE Journal. **11631**: p. 271-282.

Cleary, M. P., Wright, C. A. and Wright, T. B. (1991). *Experimental and Modeling Evidence for Major Changes in Hydraulic Fracture Design and Field Procedures*. SPE Journal. **21494**: p. 131-146.

Clift, R., Grace, J. R. and Weber, M. E. (1978). *Bubbles, Drops, and Particles*. Academic Press.

Clifton, R. J. and Wang, J.-J. (1991). *Modelling of Poroelastic Effects in Hydraulic Fracturing*. SPE Journal. **21871** :

Cox, R. G. (1986). *The Dynamics of the Spreading of Liquids on a Solid Surfaces. Part 1. Viscous Flow*. J. Fluid Mech. **168**: p. 169-194.

Coyle, D. J., Blake, J. W. and Macosko, C. W. (1987). *The Kinematics of Fountain Flow in Mold-Filling*. AIChE Journal. **33**(7): p. 1168-1177.

Coyne, J. C. and Elrod, H. G. (1970). *Conditions for the Rupture of a Lubricating Film. Part 1: Theoretical Model.* Journal of Lubrication Technology - Trans. ASME F. **92**: p. 451-456.

Cuvelier, C. and Driessen, J. M. (1986). *Thermocapillary Free Boundaries in Crystal Growth.* J. Fluid Mech. **169**: p. 1-26.

Cuvelier, C. and Schulkes, R. M. S. M. (1990). *Some Numerical Methods for the Computation of Capillary Free Boundaries Governed by the Navier-Stokes Equations.* SIAM Review. **32**(3): p. 355-423.

de Gennes, P. G. (1985). *Wetting: Statics and Dynamics.* Reviews of Modern Physics. **57**(3): p. 827-863.

de Gennes, P. G. (1991). *The Dynamics of Wetting*, in Fundamentals of Adhesion. L.-H. Lee Editor. Plenum Publishing Corporation: p. 173-179.

Derby, J. J. and Brown, R. A. (1986). *A Fully Implicit Method for Simulation of the One-Dimensional Solidification of a Binary Alloy.* Chemical Engineering Science. **41**(1): p. 37-46.

Dodge, F. T. (1988). *The Spreading of Liquid Droplets on Solid Surfaces.* J. Colloid Interface Sci. **121**(1): p. 154-264.

Drazin, P. G. and Reid, W. H. (1981). *Hydrodynamic Stability.* Cambridge University Press.

Dussan, E. B. V. (1976). *The Moving Contact Line: The Slip Boundary Condition.* J. Fluid Mech. **77**: p. 665-684.

Dussan, E. B. V. (1979). *On the Spreading of Liquids on Solid Surfaces: Static and Dynamic Contact Lines.* Ann. Rev. Fluid Mechanics. **11**: p. 371-400.

Dussan, E. B. V., Ramé, E. and Garoff, S. (1991). *On Identifying the Appropriate Boundary Conditions at a Moving Contact Line: An Experimental Investigation*. J. Fluid Mech. **230**: p. 97-116.

El-Shimi, A. and Goddard, E. D. (1974a). *Wettability of Some Low Energy Surfaces - I. Air/Liquid/Solid Interface*. J. Colloid Interface Sci. **48**(2): p. 242-248.

El-Shimi, A. and Goddard, E. D. (1974b). *Wettability of Some Low Energy Surfaces - Oils on Solids Submerged in Water*. J. Colloid Interface Sci. **48**(2): p. 249-255.

Elliott, G. E. P. and Riddiford, A. C. (1967). *Dynamic Contact Angles - I. The Effect of Impressed Motion*. J. Colloid Interface Sci. **23**: p. 389-398.

Everage, A. E. J. (1973). *Theory of Stratified Bicomponent Flow of Polymer Melts. Part 1 - Equilibrium Newtonian Tube Flow*. Trans. Soc. Rheol. **17**(4): p. 629-646.

Everage, A. E. J. (1975). *Theory of Stratified Bicomponent Flow of Polymer Melts. Part 2 - Interface Motion in Transient Flow*. Trans. Soc. Rheol. **19**(4): p. 509-522.

Fellipa, C. A. (1984a). *Dynamic Relaxation and Quasi-Newton Methods*, in International Conference on Numerical Methods for Non-Linear Problems. C. Taylor, *et al.* Editor. Barcelona, Spain. Pineridge Press. p. 27-38.

Fellipa, C. A. (1984b). *Dynamic Relaxation Under General Increment Control*, in International Conference on Innovative Methods for Nonlinear Problems. W. K. Liu, *et al.* Editor. Pineridge Press. p. 103-133.

Fellipa, C. A. (1988). *Solution of Nonlinear Equations*, in Finite Element Analysis for Engineering Design. J. N. Reddy, *et al.* Editor. Springer-Verlag: p. 274-309.

Fellipa, C. A. and Park, K. C. (1978). *Direct Time Integration Methods in Nonlinear Structural Dynamics*, in International Conference in Finite Elements in Nonlinear Mechanics. K. S. Pister, *et al.* Editor. Stuttgart, Germany. North-Holland. p. 277-313.

Flügge, W. (1962). *Handbook of Engineering Mechanics.* McGraw-Hill.

Goodwin, R. and Homsy, G. M. (1991). *Viscous Flow Down a Slope in the Vicinity of a Contact Line*. Phys. Fluids A. **3**(4): p. 515-528.

Gray, W. G. and Hassanizadeh, S. M. (1989). *Averaging Theorems and Averaged Equations for Transport of Interface Properties in Multiphase Systems*. Int. J. Multiphase Flow. **15**(1): p. 81-95.

Griffiths, S. K., Nilson, R. H. and Morrison, F. A. J. (1986). *Hybrid Analytical/Numerical Computation of Heat Transfer in a Gas-Driven Fracture*. J. of Heat Transfer (ASME). **108**: p. 585-590.

Haisler, W. E. and Stricklin, J. A. (1974). *Computational Methods for Solving Nonlinear Structural Mechanics Problems*, in Computational Methods in Nonlinear Mechanics. J. T. Oden, *et al.* Editor. Texas, Austin. University of Texas at Austin. p. 393-403.

Haley, P. J. and Miksis, M. J. (1991). *The Effect of the Contact Line on Droplet Spreading*. J. Fluid Mech. **223**: p. 57-81.

Hamilton, W. C. (1972). *A Technique for the Characterization of Hydrophilic Solid Surfaces*. J. Colloid Interface Sci. **40**(2): p. 219-283.

Hayes, L. J. (1989). *Advances and Trends in Element-by-Element Techniques*, in State-of-the-art Surveys on Computational Mechanics. A. K. Noor and J. T. Oden Editor. ASME: p. 219-235.

Hayes, L. J. and Devloo, P. (1984). *An Element-by-Element Block Iterative Method for Large Non-Linear Problems*, in International Conference on Innovative Methods for Nonlinear Problems. W. K. Liu, *et al.* Editor. Pineridge Press. p. 51-62.

Hele-Shaw, H. S. (1898a). *The Flow of Water.* Nature. **58**(1489): p. 34-36.

Hele-Shaw, H. S. (1898b). *The Flow of Water - reply to O. Reynolds.* Nature. **58**(1509): p. 520 and 535.

Hele-Shaw, H. S. (1898c). *Investigation of the Nature of Surface Resistance of Water and of Stream-Line Motion under certain Experimental Conditions.* Trans. Institution of Naval Architects. **40**: p. 21-46 and figures addendum.

Hele-Shaw, H. S. (1898d). *Streamline Motion of a Viscous Fluid.* British Association for Science - Report. : p. 136-142.

Hele-Shaw, H. S. and Hay, A. (1900). *Lines of Induction in a Magnetic Field.* Proc. Royal Society **A. 67**: p. 234-236.

Herting, D. N. (1984). *A General Purpose Nonlinear Transient Integration System*, in International Conference on Innovative Methods for Nonlinear Problems. W. K. Liu, *et al.* Editor. Pineridge Press. p. 165-186.

Ho, L. W. (1989). *A Legendre Spectral Element Method for Simulation of Incompressible Unsteady Viscous Free-Surface Flow.* Ph.D. Thesis, MIT.

Hocking, L. M. (1977). *A Moving Fluid Interface. Part 2. The Removal of the Force Singularity by a Slip Flow.* J. Fluid Mech. **79**: p. 209-229.

Hoffman, R. L. (1975). *A Study of the Advancing Interface - I. Interface Shape in Liquid-Gas Systems.* J. Colloid Interface Sci. **50**(2): p. 228-241.

Homsy, G. M. (1987). *Viscous Fingering in Porous Media.* Ann. Rev. of Fluid Mechanics. **19**: p. 271-311.

Hooper, A. P. (1989). *The Stability of Two Superposed Viscous Fluids in a Channel.* Phys. Fluids A. **1**(7): p. 1133-1142.

Hooper, A. P. and Boyd, W. G. C. (1983). *Shear-Flow Instability at the Interface between Two Viscous Fluids.* J. Fluid Mech. **128**: p. 507-528.

Howison, S. D. (1986). *Fingering in Hele-Shaw Cells.* J. Fluid Mech. **167**: p. 439-453.

Hu, H. H. and Joseph, D. D. (1989). *Lubricated Pipelining: Stability of Core-Annular Flow. Part 2.* J. Fluid Mech. **205**: p. 359-396.

Hu, H. H. and Joseph, D. D. (1990). *Miscible Displacement in a Hele-Shaw Cell.* UMSI 90/155.: Univ. Minn. Supercomputer Institute.

Hughes, T. J. R. and Ferencz, R. M. (1987). *Fully Vectorized EBE Preconditioners for Nonlinear Solid Mechanics: Applications to Large-Scale Three-Dimensional Continuum, Shell and Contact/Impact Problems*, in First International Symposium on Domain Decomposition Methods for Partial Differential Equations. R. Glowinsky, *et al.* Editor. Paris, France. SIAM. p. 261-280.

Hughes, T. J. R., Pister, K. S. and Taylor, R. L. (1978). *Implicit-Explicit Finite Elements in Nonlinear Transient Analysis*, in International Conference in Finite Elements in Nonlinear Mechanics. K. S. Pister, *et al.* Editor. Stuttgart, Germany. North-Holland. p. 159-182.

Hughes, T. J. R., Raefsky, A. and Muller, A. (1984). *A Progress Report on EBE Solution Procedures in Solid Mechanics*, in International Conference on Numerical Methods for Non-Linear Problems. C. Taylor, *et al.* Editor. Barcelona, Spain. Pineridge Press. p. 18-26.

Huh, C. and Scriven, L. E. (1971). *Hydrodynamic Model of Steady Movement of a Solid/Liquid/Fluid Contact Line*. J Coll. Int. Sci. **35**: p. 85-101.

Huynh, Q. and Wong, Y. S. (1984). *Fast Iterative Methods for Nonlinear Problems*, in International Conference on Numerical Methods for Non-Linear Problems. C. Taylor, *et al.* Editor. Barcelona, Spain. Pineridge Press. p. 729-741.

Jansons, K. M. (1985). *Moving Contact Lines on a Two-Dimensional Rough Surface*. J. Fluid Mech. **154**: p. 1-28.

Jerrett, J. M. and J.R., d. B. (1992). *Fingering Instability of a Gravitationally Driven Contact Line*. Phys. Fluids A. **4**(2): p. 234-242.

Johnson, B. A., Kreuter, J. and Zografi, G. (1986). *Effects of Surfactants and Polymers on Advancing and Receding Contact Angles*. Colloids Surfaces. **17**: p. 325-342.

Johnson, E. and Cleary, M. P. (1991). *Implications of Recent Laboratory Experimental Results for Hydraulic Fractures*. SPE Journal. **21846**

Joseph, D. D. (1990). *Fluid Dynamics of Two Miscible Liquids with Diffusion and Gradient Stresses*. UMSI 90/156.: Univ. Minn. Supercomputer Institute.

Joseph, D. D., Nguyen, K. and Beavers, G. S. (1984). *Non-Uniqueness and Stability of the Configuration of Flow of Immiscible Fluids with Different Viscosities*. J. Fluid Mech. **141**: p. 319-345.

Joseph, D. D. and Preziosi, L. (1987). *Stability of Rigid Motions and Coating Films in Bicomponent Flows of Immiscible Liquids*. J. Fluid Mech. **185**: p. 323-351.

Joseph, D. D., Renardy, M. and Renardy, Y. (1984). *Instability of the Flow of Two Immiscible Liquids with Different Viscosities in a Pipe*. J. Fluid Mech. **141**: p. 309-317.

Junior, A. F. (1989). *An Adapted Finite Element Method for Massively Parallel Processors*, in The Fourth Conference on Hypercubes, Concurrent Computers, and Applications. Monterey, California. p. 1329-1333.

Kamal, M. R., Goyal, S. K. and Chu, E. (1988). *Simulation of Injection Mold Filling of Viscoelastic Polymer with Fountain Flow.* AIChE Journal. **34**(1): p. 94-106.

Kamat, K. P., Watson, L. T. and VandenBrink, D. J. (1984). *Comparison of a Globally Convergent Quasi-Newton Method with an EBE Method for Nonlinear Structural Problems*, in International Conference on Innovative Methods for Nonlinear Problems. W. K. Liu, *et al.* Editor. Pineridge Press. p. 63-82.

Kamat, M. P., VandenBrink, D. J. and Watson, L. T. (1985). *Quasi-Newton, Partitioned Variable Metric, EBE and Other Preconditioned Conjugate Gradient Methods for Nonlinear Problems of Structural Mechanics*, in Finite Elements in Computational Mechanics. T. Kant Editor. Bombay, India. Pergamon Press. p. 333-343.

Kamat, M. P. and Watson, L. T. (1984). *Determination of Multiple Equilibrium Solutions Through a Deflation Technique with Tunneling*, in International Conference on Numerical Methods for Non-Linear Problems. C. Taylor, *et al.* Editor. Barcelona, Spain. Pineridge Press. p. 39-51.

Kataoka, I. (1986). *Local Instant Formulation of Two-Phase Flow.* Int. J. Multiphase Flow. **12**(5): p. 745-758.

King, M. J. (1985). *Probabilistic Stability Analysis of Multiphase Flows in Porous Media.* SPE Journal. **14366**

Koh, C. J. and Leal, L. G. (1990). *An Experimental Investigation on the Stability of Viscous Drops Translating Through a Quiescent Fluid.* Phys. Fluids A. **2**(12): p. 2103-2109.

Krause, P. D. and Kildsig, D. O. (1972). *Mechanism of Dissolution II: Experimental Determination of Surface Tension of a Solid.* Journal of Pharmaceutical Sciences. **61**(2): p. 281-283.

Kwei, T. K., H., S. and H.L., F. (1969). *Kinetics of Wetting of Surfaces by Polymer Melts*, in Hydrophobic Surfaces. F. M. Fowkes Editor. Academic Press: San Fransisco. p. 201-204.

Lacey, A. A., *et al.* (1990). *Irregular Morphologies in Unstable Hele-Shaw Free-Boundary Problems.* Q. Jl. Mech. appl. Math. **43**(Pt. 3): p. 439-453.

Lam, K. Y. (1985). *The Development of a Fully Three-Dimensional Simulator for Analysis and Design of Hydraulic Fracturing.* Ph.D. Thesis, MIT.

Lamb, H. (1932). *Hydrodynamics.* Dover.

Lamperski, S. (1991). *Surface Tension and Adsorption from a Multicomponent Solution.* J. Colloid Interface Sci. **144**(1): p. 153-158.

Lee, B. L. and White, J. L. (1974). *An Experimental Study of Rheological Properties of Polymer Melts in Laminar Shear Flow and of Interface Deformation and Its Mechanisms in Two-Phase Stratified Flow.* Trans. Soc. Rheol. **18**(3): p. 467-492.

Lee, B. L. and White, J. L. (1975). *Experimental Studies of Disperse Two-Phase Flow of Molten Polymers Through Dies.* Trans. Soc. Rheol. **19**(3): p. 481-492.

Li, D. and Slattery, J. C. (1991). *Analysis of the Moving Apparent Common Line and Dynamic Contact Angle Formed by a Draining Film.* J. Colloid Interface Sci. **143**(2): p. 382-396.

Loewenherz, D. S. and Lawrence, C. J. (1989). *The Effect of Viscosity Stratification on the Stability of a Free Surface Flow at Low Reynolds Number.* Phys. Fluids A. **1**(10): p. 1686-1693.

Lowndes, J. (1980). *The Numerical Simulation of the Steady Movement of a Fluid Meniscus in a Capillary Tube.* J. Fluid Mech. **101**(3): p. 631-646.

Lynch, D. R. and Sidén, G. L. D. (1988). *Wave Equation Hydrodynamics on Deforming Elements.* International Journal for Numerical Methods in Fluids. **8**: p. 1071-1093.

MacLean, D. L. (1973). *A Theoretical Analysis of Bicomponent Flow and the Problem of Interface Shape.* Trans. Soc. Rheol. **17**(3): p. 385-399.

Maeder, R. (1990). *Programing in Mathematica™.* Addison-Wesley.

Manas-Zloczower, I., Blake, J. W. and Macosko, C. W. (1987). *Space-Time Distribution in Filling a Mold.* Polym. Eng. Sci. **27**(16): p. 1229-1235.

Marques, J. M. M. C. (1986). *Nonlinear Finite Element Solutions with Quasi- and Secant-Newton Methods*, in Numerical Methods for Non-Linear Problems. C. Taylor, *et al.* Editor. Dubrovnik, Yugoslavia. Pineridge Press. p. 1117-1147.

Mathur, K. K. (1989). *The Finite Element Method on a Data Parallel Architecture*, in Fifth International Symposium on Numerical Methods in Engineering. R. Gruber, *et al.* Editor. Springer-Verlag. p. 599-611.

Mavridis, H., Hrymak, A. N. and Vlachopoulos, J. (1986a). *Finite Element Simulation of Fountain Flow Injection in Molding.* Polymer Eng. and Science. **26**(7): p. 449-454.

Mavridis, H., Hrymak, A. N. and Vlachopoulos, J. (1986b). *Mathematical Modeling of Injection Mold Filling: A Review.* Adv. Polym. Tech. **6**(4): p. 457-466.

Mavridis, H., Hrymak, A. N. and Vlachopoulos, J. (1987). *Finite Element Simulation of Stratified Multiphase Flows.* A.I.Ch.E. Journal. **33**(3): p. 410-422.

Mavridis, H., Hrymak, A. N. and Vlachopoulos, J. (1988). *Transient Free-Surface Flows in Injection Mold Filling.* AIChE Journal. **34**(3): p. 403-410.

Maxworthy, T. (1991). *Bubble Rise Under an Inclined Plane.* J. Fluid Mech. **229**: p. 659-674.

Meiburg, E. (1989). *Bubbles in a Hele-Shaw Cell: Numerical Simulation of Three-Dimensional Effects.* Phys. Fluids A. **1**(6): p. 938-946.

Merchant, G. J. and Keeller, J. B. (1992). *Contact Angles.* Phys. Fluids A. **4**(3): p. 477-485.

Michael, D. H. (1981). *Meniscus Stability.* Ann. Rev. Fluid Mechanics. **13**: p. 189-215.

Miles, J. (1991). *Wave Motion in a Viscoud Fluid of Variable Depth. Part 2. Moving Contact Line.* J. Fluid Mech. **223**: p. 47-55.

Milinazzo, F. and Shinbrot, M. (1988). *A Numerical Study of a Drop on a Vertical Wall.* J. Colloid Interface Sci. **121**(1): p. 254-264.

Milne-Thomson, L. M. (1968). *Theoretical Hydrodynamics.* Mac-Millan.

Moriarty, J. A., Schwartz, L. W. and Tuck, E. O. (1991). *Unsteady Spreading of Thin Liquid Films with Small Surface Tension.* Phys. Fluids A. **3**(5): p. 733-742.

Muller, A. and Hughes, T. J. R. (1984). *Mixed Finite Element Methods and Iterative Solutions: An Algorithm for Structural Finite Element Analysis*, in International Conference on Innovative Methods for Nonlinear Problems. W. K. Liu, *et al.* Editor. Pineridge Press. p. 1-16.

Nakazawa, S. (1984). *Mixed Finite Elements and Iterative Solution Procedures*, in International Conference on Innovative Methods for Nonlinear Problems. W. K. Liu, *et al.* Editor. Pineridge Press. p. 389-417.

Nilson, R. H. (1981). *Gas-Driven Fracture Propagation*. J. App. Mech. **48**: p. 757-762.

Nilson, R. H. (1986). *An Integral Method for Predicting Hydraulic Fracture Propagation Driven by Gases or Liquids*. Int. J. Num. Anal. Meth. Geomechanics. **10**: p. 191-211.

Nilson, R. H. and Griffiths, S. K. (1982). *Numerical Analysis of Hydraulically-Driven Fractures*. SAND 81-2618.: Sandia National Labs.

Nilson, R. H. and Griffiths, S. K. (1986). *Similarity Analysis of Energy Transport in Gas-Driven Fractures*. Int. J. Fracture. **30**: p. 115-134.

Nilson, R. H. and Morrison, F. A. J. (1986). *Transient Gas or Liquid Flow Along a Preexisting or Hydraulically-Induced Fracture in a Permeable Medium*. J. Applied Mech. - Trans. of the ASME. **53**: p. 157-165.

Nilson, R. H., Proffer, W. J. and Duff, R. E. (1985). *Modelling of Gas-driven Fractures Induced by Propellant Combustion within a Borehole*. Int. J. Rock Mech. Min. Sci. and Geomech. Abst. **22**(1): p. 3-19.

Noor, A. K. (1987). *Parallel Computations and Their Impact on Mechanics*. ASME.

Nour-Omid, B. (1984). *A Preconditioned Conjugate Gradient Method for Solution of Finite Element Equations*, in International Conference on Innovative Methods for Nonlinear Problems. W. K. Liu, *et al.* Editor. Pineridge Press. p. 17-40.

Nour-Omid, B., Parlett, B. N. and Raefsky, A. (1987). *Comparison of Lanczos with Conjugate Gradient Using Element Preconditioning*, in First International Symposium on Domain Decomposition Methods for Partial Differential Equations. R. Glowinsky, *et al.* Editor. Paris, France. SIAM. p. 250-260.

Novy, R. A., Davis, T. H. and Scriven, L. E. (1989). *A Comparison of Synthetic Boundary Conditions for Continuous Flow Systems*. UMSI-89/214.: Univ. Minn. Supercomputer Institute.

Padday, J. F. (1969). *Effect of Temperature on the Wettability of Low-Energy Surfaces*, in Hydrophobic Surfaces. F. M. Fowkes Editor. Academic Press: San Fransisco. p. 215-222.

Park, C. W., Gorell, S. and Homsy, G. M. (1984). *Two-Phase Displacement in Hele Shaw Cells: Experiments on Viscous Driven Instabilities*. J. Fluid Mech. **141**: p. 257-287.

Park, C. W. and Homsy, G. M. (1984). *Two-Phase Displacement in Hele Shaw Cells: Theory*. J. Fluid Mech. **139**: p. 291-308.

Paterson, L. (1981). *Radial Fingering in a Hele-Shaw Cell*. J. Fluid Mech. **113**: p. 513-529.

Pearson, C. E. (1983). *Handbook of Applied Mathematics*. Van Nostrand.

Pelcé, P. (1988). *Dynamics of Curved Fronts*. Perspectives in Physics. H. Araki, *et al.* Editor. Academic Press.

Plesha, M. E. (1984). *Operator Splitting for the Dynamics of Discontinua*, in International Conference on Innovative Methods for Nonlinear Problems. W. K. Liu, *et al.* Editor. Pineridge Press. p. 215-231.

Pradhan, G. K. and Tripathy, U. K. (1986). *A Necessary and Sufficient Condition for the Instability of a Stratified Shear Flow.* Indian J. Tech. **24**(June): p. 340-341.

Pranckh, F. R. and Scriven, L. E. (1989). *Analysis of Membrane Coating Flow.* UMSI-89/85.: Univ. Minn. Supercomputer Institute.

Ramé-Hart (1992). *Contact Angle Goniometers - Instruction Manual.*

Reinelt, D. A. (1987). *Interface Conditions for Two-Phase Displacement in Hele-Shaw Cells.* J. Fluid Mech. **183**: p. 219-234.

Reinelt, D. A. and Saffman, P. G. (1985). *The Penetration of a Finger into a Viscous Fluid in a Channel and Tube.* SIAM J. Sci. Stat. Comput. **6**: p. 542-561.

Renardy, Y. (1989). *Weakly Nonlinear Behavior of Periodic Disturbances in Two-Layer Couette-Poiseuille Flow.* Phys. Fluids A. **1**(10): p. 1666-1676.

Reynolds, O. (1898). *Correspondence between Hele-Shaw and Reynolds.* Nature. **58**(1507): p. 467-468.

Riegels, F. (1938). *Zur Kritik des Hele-Shaw-Versuchs.* ZAMM. **18**(2): p. 95-106.

Ripa, P. (1991). *General Stability Conditions for a Multi-Layer Model.* J. Fluid Mech. **222**: p. 119-137.

Rose, W. (1961). *Fluid-Fluid Interfaces in Steady Motion.* Nature. **191**(July 15): p. 242-243.

Ruschak, K. J. (1985). *Coating Flows.* Ann. Rev. Fluid Mechanics. **17**: p. 65-89.

Sacher, E. (1988). *The Determination of the Surface Tensions of Solid Films*, in Surface Characterization of Biomaterials. B. D. Ratner Editor. Elsevier Science Publishers B.V.: Amsterdam. p. 53-64.

Saffman, P. F. and Tanveer, S. (1989). *Prediction of Bubble Velocity in a Hele-Shaw Cell: Thin Film and Contact Angle Effects*. Phys. Fluids A. **1**(2): p. 219-223.

Saffman, P. G. (1986). *Viscous Fingering in Hele-Shaw Cells*. J. Fluid Mech. **173**: p. 73-94.

Saffman, P. G. and Taylor, G. I. (1958). *The Penetration of a Fluid into a Porous Medium or Hele-Shaw Cell Containing a More Viscous Liquid*. Proceedings of the Royal Society of London, Series A. **245**: p. 312-329.

Salinas, D., Nguyen, D. H. and Southworth, T. W. (1974). *Finite Element Solutions of a Nonlinear Nuclear Reactor Dynamics Problem*, in Computational Methods in Nonlinear Mechanics. J. T. Oden, *et al.* Editor. Texas, Austin. University of Texas at Austin. p. 541-550.

Sand, J. and Østerby, O. (1979). *Regions of Absolute Stability*. 102.: Computer Science Department, Aarhus University, Denmark.

Schmidt, L. R. (1978). *Velocity Field Rearrangement in Stagnation Flow Leading to Diverging Radial Flow Between Parallel Plates*. J. Rheology. **22**(6): p. 571-588.

Schonhorn, H., H.L., F. and T.K., K. (1966). *Kinetics of Wetting of Surfaces by Polymer Melts*. Journal of Applied Physics. J. Appl. Phys. **37**(13): p. 4967-4973.

Schwartz, L. W. and Michaelides, E. E. (1988). *Gravity Flow of a Viscous Liquid Down a Slope with Injection*. Phys. Fluids. **31**(10): p. 2739-2741.

Shibata, M. and Mei, C. C. (1986a). *Slow Parallel Flows of a Water-Granule Mixture Under Gravity. Part 1: Continuum Modeling*. Acta Mech. **63**: p. 179-193.

Shibata, M. and Mei, C. C. (1986b). *Slow Parallel Flows of a Water-Granule Mixture Under Gravity. Part 2: Examples of Free-Surface and Channel Flows*. Acta Mech. **63**: p. 195-216.

Somasundaran, P. and Danitz, M. (1974). *A New Apparatus for Measurements of Dynamic Interfacial Properties*. J. Colloid Interface Sci. **48**(3): p. 410-416.

Sørensen, O. R. and Reffstrup, J. (1986). *Simulation of Generalized Newtonian Flow Using Finite Element Method with an Improved Iterative Procedure*, in Numerical Methods for Non-Linear Problems. C. Taylor, *et al.* Editor. Dubrovnik, Yugoslavia. Pineridge Press. p. 776-783.

Stokes, G. G. (1898). *Mathematical Proof of the Identity of the Stream Lines obtained by Means of a Viscous Film with those of a Perfect Fluid moving in Two Dimensions*. British Association for Science - Report. : p. 143-144.

Strang, G. (1980). *The Quasi-Newton Method in Finite Element Calculations*, in Computational Methods in Nonlinear Mechanics. J. T. Oden Editor. Austin, Texas. North-Holland. p. 451-456.

Strykowski, P. J. and Niccum, D. L. (1992). *The Influence of Velocity and Density Ratio on the Dynamics of Spatially Developing Mixing Layers*. Phys. Fluids A. **4**(4): p. 770-781.

Suarez, B., Oñate, E. and Albareda, R. (1984). *A Finite Element Formulation for the Analysis of the Nonlinear Transient Response of Natural Gas in Urban Pipe Networks*, in International Conference on Numerical Methods for Non-Linear Problems. C. Taylor, *et al.* Editor. Barcelona, Spain. Pineridge Press. p. 577-583.

Sullivan, J. M. J. and Lynch, D. R. (1987a). *Finite Element Simulation of Planar Instabilities during Solidification of an Undercooled Melt.* Journal of Computational Physics. **69**(1): p. 81-111.

Sullivan, J. M. J. and Lynch, D. R. (1987b). *Non-Linear Simulation of Dendritic Solidification of an Undercooled Melt.* International Journal for Numerical Methods in Engineering. **25**: p. 415-444.

Taylor, G. I. and Saffman, P. G. (1958). *Cavity Flows of Viscous Liquids in Narrow Spaces*, in 2nd Symposium on Naval Hydrodynamics. R. D. Cooper Editor. p. 277-291.

Tezduyar, T. E. and Liou, J. (1987). *Element-by-Element and Implicit-Explicit Finite Element Formulations for Computational Fluid Dynamics*, in First International Symposium on Domain Decomposition Methods for Partial Differential Equations. R. Glowinsky, *et al.* Editor. Paris, France. SIAM. p. 281-300.

Tezduyar, T. E., *et al.* (1988). *Adaptive Implicit and Parallel Element-By-Element Iteration Schemes*, in Second International Symposium on Domain Decomposition Methods. T. F. Chan, *et al.* Editor. Los Angeles, California. SIAM. p. 443-463.

Than, P. T., Rosso, F. and Joseph, D. D. (1987). *Instability of Poiseuille Flow of Two Immiscible Liquids with Different Viscosities in a Channel.* Int. J. Engng. Sci. **25**(2): p. 189-204.

Thomé, H., *et al.* (1989). *The Saffman-Taylor Instability: From the Linear to the Circular Geometry.* Phys. Fluids A. **1**(2): p. 224-240.

Truesdell, C. (1984). *Rational Thermodynamics.* Springer-Verlag.

Van Remoortere, P. and Joos, P. (1991). *The Kinetics of Wetting: The Motion of a Three Phase Contactline in a Capillary.* J. Colloid. Interface Sci. **141**(2): p. 348-359.

Weinstein, S. J., Dussan, V. E. B. and Ungar, L. H. (1991). *A Theoretical Study of Two-Phase Flow through a Narrow Gap with a Moving Contact Line: Viscous Fingering in a Hele-Shaw Cell.* J. Fluid Mech. **221**: p. 53-76.

White, J. L. and Lee, B. L. (1975). *Theory of Interface Distortion in Stratified Two-Phase Flow.* Trans. Soc. Rheol. **19**(3): p. 457-479.

Williams, M. C. (1975). *Migration of Two Liquid Phases in Capillary Extrusion: An Energy Interpretation.* A.I.Ch.E. Journal. **21**(6): p. 1204-1207.

Wolfram, S. (1988). *Mathematica™ - A System for Doing Mathematics by Computer.* Addison-Wesley.

Yang, Y. W., Zografi, G. and Miller, E. E. (1988a). *Capillary Flow Phenomena and Wettability in Porous Media - I. Static Characterestics.* J. colloid Interface Sci. **122**(1): p. 24-34.

Yang, Y. W., Zografi, G. and Miller, E. E. (1988b). *Capillary Flow Phenomena and Wettability in Porous Media - II. Dynamic Flow Studies.* J. colloid Interface Sci. **122**(1): p. 35-46.

Yiantsios, S. G. and Higgins, B. G. (1988). *Linear Stability of Plane Poiseuille Flow of Two Superposed Fluids.* Phys. Fluids. **31**(11): p. 3225-3238.

Yih, C. S. (1967). *Instability Due to Viscosity Stratification.* J. Fluid Mech. **27**(2): p. 337-352.

Yu, H. S. and Sparrow, E. M. (1967). *Stratified Laminar Flow in Ducts of Arbitrary Shape.* A.I.Ch.E. Journal. **13**: p. 10-16.

Zabaras, N. and Richmond, O. (1990). *Analysis and Finite Element Approximations of Deformations and Thermal Stresses in Solidifying Bodies.* UMSI-90/50.: Univ. Minn. Supercomputer Institute.

Zabaras, N. and Ruan, Y. (1989a). *Front Tracking Thermomechanical Model for Hypoelastic-Viscoplastic Behavior in a Solidifying Body.* UMSI-89/91.: Univ. Minn. Supercomputer Institute.

Zabaras, N. and Ruan, Y. (1989b). *Moving and Deforming Finite Element Simulation of Two-Dimensional Stefan Problems.* UMSI-89/190.: Univ. Minn. Supercomputer Institute.

Zabaras, N. and Ruan, Y. (1989c). *A Moving Finite Element Simulation of Two-Dimensional Stefan Problems.* UMSI-89/55.: Univ. Minn. Supercomputer Institute.

Zettlemoyer, A. C. (1969). *Hydrophobic Surfaces*, in Hydrophobic Surfaces. F. M. Fowkes Editor. Academic Press: San Fransisco. p. 1-27.

Zimmerman, W. B. and Homsy, G. M. (1991). *Nonlinear Viscous Fingering in Miscible Displacement with Anisotropic Dispersion.* Phys. Fluids A. **3**(8): p. 1859-1872.

Zisman, W. A. (1964). *Relation of Equilibrium Contact Angle to Liquid and Solid Constitution*, in Contact Angle - Wettability and Adhesion. R. F. Gould Editor. American Chemical Society: p. 1-51.